



THE HONG KONG  
POLYTECHNIC UNIVERSITY

香港理工大學

Pao Yue-kong Library

包玉剛圖書館

---

## Copyright Undertaking

This thesis is protected by copyright, with all rights reserved.

**By reading and using the thesis, the reader understands and agrees to the following terms:**

1. The reader will abide by the rules and legal ordinances governing copyright regarding the use of the thesis.
2. The reader will use the thesis for the purpose of research or private study only and not for distribution or further reproduction or any other purpose.
3. The reader agrees to indemnify and hold the University harmless from and against any loss, damage, cost, liability or expenses arising from copyright infringement or unauthorized usage.

If you have reasons to believe that any materials in this thesis are deemed not suitable to be distributed in this form, or a copyright owner having difficulty with the material being included in our database, please contact [lbsys@polyu.edu.hk](mailto:lbsys@polyu.edu.hk) providing details. The Library will look into your claim and consider taking remedial action upon receipt of the written requests.



**STRUCTURAL BEHAVIOR OF HYBRID  
FRP-CONCRETE-STEEL DOUBLE-SKIN  
TUBULAR COLUMNS**

**By**

**Tao YU**

**BEng**

**A Thesis Submitted in Partial Fulfilment of the Requirements for the  
Degree of Doctor of Philosophy**

**Department of Civil and Structural Engineering  
The Hong Kong Polytechnic University**

**August, 2006**

**To my parents**

## **CERTIFICATE OF ORIGINALITY**

I hereby declare that this thesis is my own work and that, to the best of my knowledge and belief, it reproduces no material previously published or written, nor material that has been accepted for the award of any other degree or diploma, except where due acknowledgement has been made in the text.

\_\_\_\_\_ (Signed)

Tao YU (Name of student)

## **ABSTRACT**

Hybrid FRP-concrete-steel double-skin tubular columns (DSTCs) are a new form of hybrid columns recently proposed by Prof. J.G. Teng of The Hong Kong Polytechnic University. The column consists of an outer tube made of fiber-reinforced polymer (FRP) and an inner tube made of steel, with the space between filled with concrete. In this new hybrid column, the three constituent materials are optimally combined to achieve several advantages not available with existing columns. This thesis presents a combined experimental and theoretical study aimed at developing a good understanding of the structural behavior of and reliable design methods for this new hybrid column to facilitate its acceptance in practical applications.

The first phase of the research was experimental, involving laboratory tests of DSTC specimens under axial compression, bending and eccentric compression to study the compressive, flexural and beam-column behavior of the new hybrid column. In addition to axial compression tests on short DSTCs, tests were also conducted on stub columns of circular solid and annular concrete sections confined with an outer FRP tube to gain a better understanding of how the three

components in a DSTC interact under axial compression. The test results have confirmed that the concrete in the new column is very effectively confined by the two tubes and local buckling of the inner steel tube is either delayed or suppressed by the surrounding concrete, leading to a very ductile response. The test results have also shown that the new DSTC is very ductile under both flexure and combined flexure and axial compression. The bending tests showed that when the new section form is employed as a beam, the outer FRP tube not only enhances the structural behavior by providing confinement to the concrete but also provides a significant contribution to the shear resistance.

Apart from the experimental study, finite element (FE) analysis of hybrid DTSCs under axial compression was also conducted. Existing Drucker-Prager (D-P) type concrete plasticity models for confined concrete were first critically assessed. It was found that D-P type plasticity models lead to reasonable predictions for both actively- and passively-confined concrete (e.g. FRP-confined concrete) only if the flow rule is suitably related not only to the confining pressure but also to the rate of increment of the confining pressure. A constitutive concrete model which takes into account the conclusions drawn from the assessment of existing D-P type models and other distinct characteristics of non-uniformly confined concrete was then proposed and verified with test results. A parametric study was next conducted using a finite element analysis incorporating the proposed constitutive

model, from which a simple one-dimensional stress-strain model for the concrete in DSTCs for design use was formulated.

Making use of the proposed one-dimensional stress-strain model for the concrete in DSTCs, a simple theoretical method based on section analysis was also developed for DSTCs under flexure or combined axial compression and flexure.

The section analysis method was then verified with test results and used in a parametric study to examine the beam-column behavior of hybrid DSTCs.

## LIST OF PUBLICATIONS

### Refereed Journal Papers:

Teng, J.G., Yu, T., Wong, Y.L. and Dong, S.L. (2007). “Hybrid FRP-concrete-steel tubular columns: concept and behavior”, *Construction and Building Materials*, Vol. 21, No. 4, pp. 846-854.

Yu, T., Wong, Y.L., Teng, J.G., Dong, S.L. and Lam, E.S.S. (2006). “Flexural behaviour of hybrid FRP-concrete-steel double-skin tubular members”, *Journal of Composites for Construction*, ASCE, Vol. 10, No. 5, pp. 443-452.

Teng, J.G., Yu, T., Wong, Y.L., Dong, S.L. and Yang, Y.F. (2006). “Experimental study and theoretical analysis of hybrid FRP-concrete-steel tubular columns”, *Progress in Steel Building Structures*, Vol. 8, No. 5, pp. 1-7. (in Chinese)

Wong, Y.L., Yu, T., Teng, J.G. and Dong, S.L. (2006). “Behavior of FRP-confined concrete in annular section columns”, submitted.

## **Conference Papers:**

Yu, T., Wong, Y.L., Teng, J.G. and Dong, S.L. (2004). “Structural behaviour of hybrid FRP-concrete-steel double-skin tubular columns”, *Proceedings of the 2004 ANCEER Annual Meeting*, July 28-30, Honolulu, Hawaii, USA, in CD-Rom.

Teng, J.G., Yu, T. and Wong, Y.L. (2004). “Hybrid FRP-concrete-steel double-skin tubular columns: Stub column tests”, *Proceedings of the Second International Conference on Steel & Composite Structures*, September 2-4, Seoul, Korea, in CD-Rom.

Teng, J.G., Yu, T. and Wong, Y.L. (2004). “Behaviour of hybrid FRP-concrete-steel double-skin tubular columns”, *Proceedings of the Second International Conference on FRP Composites in Civil Engineering*, December 8-10, Adelaide, Australia, pp. 811-818.

Teng, J.G., Yu, T., Wong, Y.L. and Dong, S.L. (2005). “Innovative FRP-concrete-steel hybrid columns”, *Proceedings of the Fourth International Conference on Advances in Steel Structures*, June 13-15, Shanghai, China, pp. 545-554.

Yu, T., Teng, J.G., Wong, Y.L. and Dong, S.L. (2007). “Finite element modeling of hybrid FRP-concrete-steel tubular columns under axial compression”, *Proceedings of the Eighth International Symposium on Fiber Reinforced Polymer Reinforcement for Concrete Structures*, Patras, Greece.

## **ACKNOWLEDGMENTS**

First and most importantly I would like to give my heartfelt thanks to my supervisor, Dr. Yuk-Lung Wong, and my three co-supervisors, Professor Jin-Guang Teng, Dr. Eddie Siu-Shu Lam and Professor Shi-Lin Dong, for their generous support and enlightening guidance throughout my PhD study.

I am grateful to The Hong Kong Polytechnic University for providing me with the opportunity of being a PhD candidate of this university and for providing me with the financial support.

It would have been much more difficult to complete the work without the help and generosity of many people. To acknowledge all those who contributed to my work in many different ways is clearly impossible, but a special mention must go to Dr. Lik Lam for his invaluable suggestions and constructive comments at the beginning of my study which benefited me greatly. I am also very grateful to all the technicians in the structures laboratories of the Department, especially, Messrs. S.W. Liauw, K.H. Wong, W.C. Chan, H.Y. Yau, K. Tam, M.C. Ng, C.F. Cheung,

C.S. Liu and T.T. Wai, for their support and assistance during the experimental program.

My sincere thanks also go to my friends and colleagues in the Department of Civil and Structural Engineering of The Hong Kong Polytechnic University, especially, Drs. Yang Zhao, Yu-Fang Fu, Xiang Lin, Hon-Ting Wong, Yuan-Feng Duan, Lei Zhang, Messrs. Yu-Li Huang, Tao Jiang, Yue-Ming Hu, Guang-Ming Chen, and Mss. Yu-Jie Wang and Jing Bao, not only for their constructive discussions, but also for their encouragement at difficult times in my study. Particularly, Mr. Tao Jiang and his wife Ms. Xiao Chen spent their valuable time helping to check and print the manuscript of this thesis, which is greatly appreciated.

Last but not the least, I wish to express my profound gratitude to my parents, to whom this thesis is dedicated. Without their everlasting love, support and encouragement I would never have embarked on my doctoral study and would not have had the opportunity to write this thesis. I am indebted to them for so many things which cannot be described in words. My heartfelt thanks also go to my sister Hong Yu and my brother-in-law Zhi-Fei Liang for their spiritual support. I would also like to thank my girlfriend, Xixi, for her devoted and dedicated help.

# CONTENTS

<b>CERTIFICATE OF ORIGINALITY</b> .....	I
<b>ABSTRACT</b> .....	II
<b>LIST OF PUBLICATIONS</b> .....	V
<b>ACKNOWLEDGMENTS</b> .....	VII
<b>LIST OF FIGURES</b> .....	XVI
<b>LIST OF TABLES</b> .....	XXI
<b>NOTATION</b> .....	XXII
<b>CHAPTER 1 INTRODUCTION</b> .....	1
1.1 HYBRID STRUCTURES INCORPORATING FIBER REINFORCED POLYMER.....	1
1.2 HYBRID FRP-CONCRETE-STEEL TUBULAR COLUMNS .....	4
1.2.1 Double-Skin Tubular Columns .....	4
1.2.2 New Form of Hybrid Columns .....	5
1.3 OBJECTIVES, SCOPE AND LAYOUT OF THIS THESIS .....	8
<b>CHAPTER 2 LITERATURE REVIEW</b> .....	17
2.1 INTRODUCTION .....	17
2.2 CONCRETE-FILLED FRP TUBES.....	18
2.2.1 Introduction.....	18
2.2.2 FRP Laminates.....	19
2.2.2.1 Constitutive equations.....	19

2.2.2.2 <i>Test methods</i> .....	23
2.2.3 FRP-Confined Concrete .....	25
2.2.3.1 <i>Introduction</i> .....	25
2.2.3.2 <i>Design-oriented model</i> .....	26
2.2.3.3 <i>Analysis-oriented model</i> .....	30
2.2.4 FRP-Confined Annular Concrete Cylinders .....	33
2.2.5 Beam-Column Behavior .....	36
2.3 DOUBLE-SKIN TUBULAR COLUMNS .....	38
2.3.1 Introduction.....	38
2.3.2 Experimental Behavior.....	39
2.3.3 Theoretical Modeling.....	40
2.4 CONSTITUTIVE MODELS FOR CONCRETE .....	42
2.4.1 Introduction.....	42
2.4.2 Concrete Plasticity .....	43
2.4.3 Plastic-Damage Models .....	46
2.4.4 Constitutive Models in ABAQUS.....	47
2.5 CONCLUDING REMARKS .....	49

## **CHAPTER 3 COMPRESSIVE BEHAVIOR OF HYBRID DSTC**

<b>COLUMNS</b> .....	54
3.1 INTRODUCTION .....	54
3.2 SPECIMEN DETAILS .....	54
3.3 MATERIAL PROPERTIES .....	57
3.4 PREPARATION OF SPECIMENS .....	59
3.5 EXPERIMENTAL SET-UP AND INSTRUMENTATION.....	60
3.6 BEHAVIOR OF HYBRID DSTC SPECIMENS .....	60
3.6.1 Overall Observations.....	60
3.6.2 Axial Load-Axial Strain Behavior .....	61
3.6.3 Buckling Behavior of Steel Tubes .....	62

3.6.3.1	<i>Hollow steel tubes</i> .....	62
3.6.3.2	<i>Steel tube inside hybrid DSTCs</i> .....	63
3.6.4	Interaction between the Concrete and the Steel Tube.....	66
3.7	CONCRETE BEHAVIOR .....	67
3.7.1	Comparison between FCSCs and FCHCs.....	67
3.7.1.1	<i>General behavior of FCHCs</i> .....	67
3.7.1.2	<i>Stress-strain behavior</i> .....	67
3.7.1.3	<i>Axial strain-hoop strain behavior</i> .....	73
3.7.2	Comparison between FCSCs and DSTCs.....	74
3.7.3	Comparison between DSTCs and FCHCs .....	76
3.7.4	Effect of Thickness of FRP Tube.....	78
3.8	CONCLUSIONS.....	79

## **CHAPTER 4 ASSESSMENT OF DRUCKER-PRAGER TYPE**

### **PLASTICITY MODELS FOR THE MODELING OF**

### **FRP-CONFINED CONCRETE..... 108**

4.1	INTRODUCTION .....	108
4.2	GENERAL BEHAVIOR OF CONFINED CONCRETE.....	110
4.3	DRUCKER-PRAGER (D-P) TYPE PLASTICITY MODELS .....	113
4.3.1	Introduction.....	113
4.3.2	Existing D-P Type Plasticity Models.....	114
4.3.2.1	<i>Yield criterion</i> .....	114
4.3.2.2	<i>Strain hardening and softening</i> .....	118
4.3.2.3	<i>Flow rule</i> .....	124
4.3.2.4	<i>Concluding remarks</i> .....	134
4.3.3	Proposed Modifications .....	135
4.3.3.1	<i>Extended Drucker-Prager model in ABAQUS</i> .....	137
4.3.3.2	<i>Solution-dependent field variables (SDFV) in ABAQUS</i>	138

4.3.3.3 <i>Implementation of the proposed modifications in ABAQUS</i>	139
4.3.4 Verification of the Proposed Modifications and Discussions....	141
<b>CHAPTER 5 FINITE ELEMENT MODELING OF HYBRID DSTCS .....</b>	<b>160</b>
5.1 INTRODUCTION .....	160
5.2 IMPROVED CONSTITUTIVE MODEL FOR CONCRETE.....	161
5.2.1 Introduction.....	161
5.2.2 Concrete Damaged Plasticity Model (CDPM) in ABAQUS .....	162
5.2.2.1 <i>Damage</i> .....	162
5.2.2.2 <i>Yield criterion</i> .....	164
5.2.2.3 <i>Hardening rule</i> .....	165
5.2.2.4 <i>Flow rule</i> .....	166
5.2.3 Proposed Modifications .....	166
5.2.3.1 <i>Damage variable</i> .....	167
5.2.3.2 <i>Yield criterion</i> .....	169
5.2.3.3 <i>Hardening rule</i> .....	170
5.2.3.4 <i>Flow rule</i> .....	170
5.2.3.5 <i>Concrete under non-uniform confinement</i> .....	171
5.2.4 Verifications of Improved Constitutive Model.....	174
5.3 MODELING OF HYBRID DSTCS .....	177
5.3.1 Model Description.....	177
5.3.2 Mesh Convergence Study .....	179
5.3.3 Results and Discussions .....	179
5.3.3.1 <i>Comparison with test results</i> .....	179
5.3.3.2 <i>Stress distribution in the radial direction</i> .....	181
5.3.3.3 <i>Interaction between the concrete and the steel tube</i> .....	182
5.3.3.4 <i>Comparison between FCSC and DSTC specimens</i> .....	183
5.3.3.5 <i>Concluding remarks</i> .....	185

5.4 PARAMETRIC STUDY.....	186
5.4.1 Introduction.....	186
5.4.2 Interaction between the Concrete and the Steel Tube.....	188
5.4.3 Compressive Strength.....	189
5.4.4 Ultimate Axial Strain.....	189
5.4.5 Axial Stress-Strain Curves.....	190
5.5 DESIGN-ORIENTED STRESS-STRAIN MODEL.....	191
5.5.1 Introduction.....	191
5.5.2 Modifications to Teng et al.'s (2006b) Model.....	192
5.6 CONCLUDING REMARKS AND DESIGN RECOMMENDATIONS	
.....	193
5.6.1 General.....	193
5.6.2 Design Recommendations.....	194
<b>CHAPTER 6 FLEXURAL BEHAVIOR OF HYBRID DSTCS.....</b>	<b>222</b>
6.1 INTRODUCTION.....	222
6.2 BENDING TESTS.....	223
6.2.1 Test Specimens.....	223
6.2.2 Material Properties.....	224
6.2.3 Preparation of Specimens.....	225
6.2.4 Experimental Set-up and Instrumentation.....	226
6.2.5 Test Results, Observations and Discussions.....	227
6.2.5.1 <i>General observations</i> .....	227
6.2.5.2 <i>Development of cracks</i> .....	228
6.2.5.3 <i>Effect of the FRP tube</i> .....	229
6.2.5.4 <i>FRP confinement of concrete</i> .....	230
6.2.5.5 <i>Slip between the concrete and the tubes</i> .....	232
6.2.5.6 <i>Effect of FRP bars</i> .....	234
6.2.5.7 <i>Effect of the steel tube</i> .....	234

6.3 THEORETICAL ANALYSIS .....	236
6.3.1 Analysis Model .....	236
6.3.2 Load-Strain Curves .....	237
6.3.2.1 Specimens without FRP bars .....	237
6.3.2.2 Specimens with FRP bars .....	240
6.3.3 Load-Deflection Curves .....	241
6.4 DESIGN RECOMMENDATIONS .....	242
6.5 CONCLUSIONS.....	243
<b>CHAPTER 7 BEAM-COLUMN BEHAVIOR OF HYBIRD DSTCS .....</b>	<b>259</b>
7.1 INTRODUCTION .....	259
7.2 EXPERIMENTAL STUDY.....	260
7.2.1 Specimen Details.....	260
7.2.2 Material Properties .....	261
7.2.3 Experimental Set-up and Instrumentation.....	262
7.2.4 Experimental Observations and Interpretations .....	263
7.2.5 Experimental Results and Discussions.....	265
7.2.5.1 Axial strain distribution over the section.....	265
7.2.5.2 Axial stress-strain curves of concrete in hybrid DSTCs under concentric compression .....	267
7.2.5.3 Axial load-shortening behavior .....	269
7.2.5.4 Hoop strain-axial strain behavior.....	272
7.3 THEORETICAL ANALYSIS .....	273
7.3.1 Analysis Model .....	273
7.3.2 Comparison with Test Results .....	277
7.3.3 Interaction Diagram .....	278
7.3.4 Parametric Study .....	280
7.4 CONCLUSIONS AND DESIGN RECOMMENDATIONS.....	281

<b>CHAPTER 8 CONCLUSIONS</b> .....	299
8.1 INTRODUCTION .....	299
8.2 AXIAL COMPRESSIVE BEHAVIOR.....	301
8.3 FLEXURAL BEHAVIOR .....	303
8.4 BEAM-COLUMN BEHAVIOR.....	304
8.5 THEORETICAL MODELING.....	306
8.6 FURTHER RESEARCH.....	309
<b>REFERENCES</b> .....	312

## LIST OF FIGURES

Figure 1.1 Cross section of hybrid FRP/concrete beam/slab (Burgueno et al. 2004) .....	14
Figure 1.2 Hybrid FRP-concrete beam (Nordin and Taljsten 2004).....	14
Figure 1.3 Concrete-filled FRP tube (Website of Queen’s university, Canada)...	15
Figure 1.4 Double-skin steel tube (Zhao and Grzebieta 2002) .....	15
Figure 1.5 Typical sections of new hybrid double-skin tubular members.....	16
Figure 1.6 Cross-sections of FCSCs and FCHCs .....	16
Figure 2.1 (a) Unidirectional lamina and (b) multidirectional laminate (Fam 2000) .....	50
Figure 2.2 Stress resultants acting on a general shell element (Fam 2000) .....	50
Figure 2.3 Typical test samples of FRP laminates (after Lam and Teng 2004)....	51
Figure 2.4 Classification of stress-strain curves of FRP-confined concrete .....	52
Figure 2.5 Variable confinement model (Fam et al. 2003) .....	53
Figure 3.1 Buckling of hollow steel tubes under axial compression .....	85
Figure 3.2 Forms for casting concrete .....	85
Figure 3.3 Formation of the FRP tube .....	86
Figure 3.4 Layout of strain gauges.....	86
Figure 3.5 Test in progress.....	87
Figure 3.6 Axial load-strain curves of DSTC specimens.....	87
Figure 3.7 DSTC specimen after test .....	90
Figure 3.8 Axial load-shortening curve of hollow steel tube under compression	90

Figure 3.9 Comparison between axial strains from strain gauges and from axial shortenings .....	91
Figure 3.10 Inner steel tubes of batch 1 after test .....	92
Figure 3.11 Comparison between axial strains from strain gauges and from axial shortenings .....	93
Figure 3.12 Steel tubes inside DSTC specimens of batch 2 after test.....	94
Figure 3.13 Axial strain-hoop strain curves of specimens D37-C3-I and D37-C3-II .....	95
Figure 3.14 Hoop strain-axial strain curves of steel tubes .....	95
Figure 3.15 FCHC specimens after test .....	97
Figure 3.16 Axial load-strain curves of FCHC specimens .....	98
Figure 3.17 Comparison of stress-strain curves between FCSCs and FCHCs ....	98
Figure 3.18 Axial stress-strain curves based on platen-to-platen deformations .	101
Figure 3.19 Theoretical stress variations in the radial direction .....	101
Figure 3.20 Comparison of axial strain-hoop strain curves between FCHCs and a corresponding FCSC .....	102
Figure 3.21 Comparison of stress-strain curves of concrete between FCSCs and DSTCs .....	102
Figure 3.22 Axial strain-hoop strain curves of FCHC and DSTC specimens ....	104
Figure 3.23 Effect of thickness of FRP tube on stress-strain curves of FCHCs .	107
Figure 3.24 Effect of thickness of FRP tube on stress-strain curves of concrete in DSTCs .....	107
Figure 4.1 Stress-strain curves of confined concrete (Teng and Lam 2004) .....	148
Figure 4.2 Dilation properties of confined concrete .....	148
Figure 4.3 Drucker-Prager yield surface in the meridian plane .....	149
Figure 4.4 Initial and subsequent yield surfaces in the meridian plane .....	150
Figure 4.5 Failure surfaces in the deviatoric plane .....	150
Figure 4.6 Axial stress-strain curve of concrete under uniaxial compression ....	151

Figure 4.7 Theoretical stress-strain curves of FRP- and actively-confined concrete (Teng et al. 2006a) .....	151
Figure 4.8 Theoretical axial stress-strain curves of unconfined and confined concrete .....	152
Figure 4.9 Axial stress-strain curves of FRP-confined concrete.....	152
Figure 4.10 Theoretical axial-lateral strain curves of actively-confined concrete .....	153
Figure 4.11 Dilation angle of FRP-confined concrete from Teng et al.'s (2006a) model.....	153
Figure 4.12 FE results from a D-P model with a constant dilation angle for Yu's test .....	154
Figure 4.13 Comparison between actively-confined and FRP-confined concrete .....	155
Figure 4.14 Failure surface of the Extended Drucker-Prager Model in ABAQUS .....	155
Figure 4.15 FE results for actively-confined concrete from numerical test I .....	156
Figure 4.16 FE results for FRP-confined concrete from numerical test II.....	158
Figure 4.17 FE results for FRP-confined concrete from numerical test III .....	159
Figure 5.1 Typical stress-strain curve of concrete under compression.....	196
Figure 5.2 Yield surface of Concrete Damaged Plasticity Model in ABAQUS .	196
Figure 5.3. D-P hyperbolic flow potential in the meridian plane.....	197
Figure 5.4 Actively-confined concrete.....	198
Figure 5.5 FRP-confined circular concrete cylinders .....	199
Figure 5.6 Concrete under biaxial compression.....	200
Figure 5.7 FRP-confined concrete in a square specimen.....	201
Figure 5.8 FE model for hybrid DSTCs.....	202
Figure 5.9 Results of mesh convergence study .....	202
Figure 5.10 Axial stress-strain curves of concrete in DSTCs .....	203
Figure 5.11 Hoop strain-axial strain curves of concrete in DSTCs.....	207

Figure 5.12 Axial stress distribution in the radial direction.....	212
Figure 5.13 Ratio of radial stress to circumferential stress.....	213
Figure 5.14 Interaction between the steel tube and the concrete .....	214
Figure 5.15 Comparison between FCSC and DSTC specimens.....	215
Figure 5.16 Effect of $D_o/t_s$ ratio of steel inner tube on stress-strain behavior.....	217
Figure 5.17 Compressive strength of concrete in DSTCs.....	218
Figure 5.18 Ultimate axial strain of concrete in DSTCs.....	218
Figure 5.19 Effect of confinement stiffness on stress-strain behavior.....	219
Figure 5.20 Effect of void ratio on stress-strain behavior.....	220
Figure 5.21 Compressive strength of concrete in DSTCs.....	221
Figure 5.22 Ultimate axial strain of concrete in DSTCs.....	221
Figure 6.1 Double-skin tubular members with an eccentric steel tube .....	246
Figure 6.2 Test set-up.....	246
Figure 6.3 Cross section of specimen with FRP bars .....	247
Figure 6.4 Formwork for casting concrete.....	247
Figure 6.5 Fabrication of FRP tube.....	248
Figure 6.6 Mid-span load-deflection curves .....	249
Figure 6.7 Specimens after testing .....	250
Figure 6.8 Compressive-tensile strain curves .....	251
Figure 6.9 Specimen B-D1-F after testing .....	252
Figure 6.10 Axial-hoop strain behavior .....	253
Figure 6.11 Typical stress-strain curve of steel tube in B-C1.....	253
Figure 6.12 Comparison of load-compressive strain curves.....	254
Figure 6.13 Comparison of mid-span load-deflection curves.....	257
Figure 6.14 Comparison between hoop strain-axial strain curves of DSTBs and DSTCs .....	258
Figure 7.1 Form for casting concrete .....	285
Figure 7.2 Buckling of hollow steel tube.....	285

Figure 7.3 Layout of strain gauges.....	286
Figure 7.4 Set-up for eccentric compression tests .....	286
Figure 7.5 Specimens after test .....	288
Figure 7.6 Axial strain distributions of specimens under eccentric compression.....	290
Figure 7.7 Comparisons between measured axial strains at extreme tensile and compressive fibers.....	292
Figure 7.8 Axial stress-strain curves of concrete.....	293
Figure 7.9 Experimental axial load-shortening curves of hybrid DSTCs.....	293
Figure 7.10 Comparison between specimens E-1-18-I and II.....	294
Figure 7.11 Hoop strain-axial strain curves .....	295
Figure 7.12 Comparisons between experimental and theoretical results.....	296
Figure 7.13 Column interaction diagram .....	297
Figure 7.14 Effect of confinement stiffness .....	297
Figure 7.15 Effect of void ratio.....	298
Figure 7.16 Design stress-strain curve for concrete in hybrid DSTCs .....	298

## LIST OF TABLES

Table 3.1 Details of specimens .....	81
Table 3.2 Material properties .....	82
Table 3.3 Key test results of DSTC specimens.....	83
Table 3.4 Peak concrete stresses and ultimate strains of all specimens.....	84
Table 4.1 Summary of existing D-P type models for FRP-confined concrete....	147
Table 6.1 Details of specimens and measured load capacities.....	245
Table 7.1 Details of test specimens.....	284
Table 7.2 Locations of tensile cracks and FRP rupture .....	284

## NOTATION

$A, B, C$	constants used in the yield criterion of the CDPM in ABAQUS
$[A]$	extensional stiffness matrix of an FRP laminate
$[B]$	coupling stiffness matrix of an FRP laminate
$C_1$	a constant used in Mander et al.'s (1988) model
$C_2$	a constant used in Fam et al.'s (2003) model
$C_3$	a constant used in Karabinis and Kiousis's (1996) model
$C_p$	a constant for the equivalent plastic strain
$d$	damage variable
$[D]$	flexural stiffness matrix of an FRP laminate
$D_{ijkl}^e$	initial (undamaged) elasticity matrix
$D_s$	outer diameter of a steel tube
$D_o$	outer diameter of a circular (or an annular) section
$e$	loading eccentricity
$E_1, E_2$	elastic moduli of an FRP laminate in two principal directions
$E_{2c}$	slope of the linear second portion of the stress-strain curve of for FRP-confined concrete in a column specimen

$E_{2ec}$	slope of the linear second portion of the stress-strain curve for FRP-confined concrete in a beam-column specimen
$E_c$	elastic modulus of unconfined concrete
$E_{f1}, E_{f2}$	elastic moduli of fibers in two principal directions
$E_{frp}$	elastic modulus of FRP
$E_m$	elastic modulus of polymer
$E_p, E'_p, f'_u, f'_y$	parameters used in the models of Karabinis and his coauthors
$E_s$	elastic modulus of steel
$E_{sec0}$	secant modulus at the compressive strength of unconfined concrete
$F$	yield function
$f'_b$	compressive strength of concrete under biaxial compression
$f'_{cc}$	compressive strength of FRP-confined concrete in a column specimen
$f_{cc}^*$	peak stress of concrete under a specific constant confining pressure
$\bar{f}_{cc}$	ultimate stress of FRP-confined concrete in a beam-column specimen, proposed in Fam et al. (2003)
$f'_{ch}$	unconfined concrete strength from hollow cylinder tests
$f'_{co}$	unconfined concrete strength from standard solid cylinder tests
$f'_{cu}$	ultimate stress of FRP-confined concrete in a column specimen
$f'_{cuo}$	stress corresponding to $\varepsilon_{cuo}$
$f_l$	maximum confining pressure provided by FRP

$f_o$	intercept of the stress axis by the linear second portion of the stress-strain curve of FRP-confined concrete
$f_u$	ultimate tensile strength of steel
$f_y$	yield strength of steel
$G$	flow potential
$G_{12}$	in-plane shear modulus of an FRP laminate
$G_{f12}$	shear modulus of fibers
$G_m$	shear modulus of polymer
$I_1$	the first stress invariant
$I_1^{'p}$	the first plastic strain invariant
$\bar{I}_1$	the first effective stress invariant
$I_{1c}$	the first stress invariant corresponding to the peak stress point of concrete under a specific constant confining pressure
$J_2$	the second deviatoric stress invariant
$J_2^{'p}$	the second deviatoric plastic strain invariant
$\bar{J}_2$	the second effective deviatoric stress invariants
$J_{2c}$	the second deviatoric stress invariant corresponding to $I_{1c}$
$J_3$	the third deviatoric stress invariant
$K$	shear strength ratio
$K_\alpha$	initial rate of change of $\alpha$ used in Karabinis and Kiouisis (2002)
$L_s$	length of a steel tube

$M_x$	resultant moment in the laminate global x-z plane per unit width
$M_y$	resultant moment in the laminate global y-z plane per unit width
$M_s$	resultant twisting moment per unit width
$N_x$	resultant force in the laminate global x-direction per unit width
$N_y$	resultant force in the laminate global y-direction per unit width
$N_s$	resultant shear force in the laminate global x-y plane per unit width
$P$	average load recorded by the load cells in four-point bending tests
$P_c$	ultimate load of hybrid DSTCs from a column test
$P_{co}$	calculated load capacity of concrete using its unconfined strength
$p_o$	outer pressure from FRP for a confined annular section
$P_s$	load capacity of a steel tube
$Q_{11}, Q_{22}, Q_{12}$	constants in the stiffness matrix of one-ply lamina
$Q_{21}, Q_{66}$	constants in the stiffness matrix of one-ply lamina
$r$	radius of a given point over a circular (or an annular) section
$R_o$	outer radius of a circular (or an annular) section
$R_i$	inner radius of an annular section
$s$	a function of the deviatoric stress invariants used in ABAQUS
$\bar{S}_{ij}$	effective deviatoric stress tensor
$S_r$	a function of the deviatoric stress invariants used in Karabinis and Kiouisis (1996)

$t_{frp}$	thickness of an FRP tube
$t_s$	thickness of a steel tube
$V_f$	volume ratio of fibers
$V_m$	volume ratio of polymer
$\alpha$	dilation rate
$\alpha_0, \alpha_u$	initial and ultimate values of $\alpha$
$\beta$	dilation parameter
$\arctan \beta$	dilation angle
$\gamma_6$	in-plane shear strain
$\varepsilon_1, \varepsilon_2, \varepsilon_3$	principal strains
$\varepsilon_1^p, \varepsilon_2^p, \varepsilon_3^p$	principal plastic strains
$\varepsilon_c$	axial strain of concrete
$\varepsilon_c^p$	axial plastic strain of concrete
$\bar{\varepsilon}_{cc}$	ultimate strain of FRP-confined concrete in a beam-column specimen, proposed in Fam et al. (2003)
$\varepsilon_{cc}^{*}$	axial strain corresponding to $f_{cc}^{*}$
$\varepsilon_{co}$	axial strain at the peak stress of unconfined concrete
$\varepsilon_{cu}$	ultimate axial strain of confined concrete
$\varepsilon_{cuo}$	ultimate axial strain of unconfined concrete
$\varepsilon_{h,rupt}$	hoop rupture strain of FRP
$\varepsilon_{ij}$	strain tensor

$\varepsilon_{ij}^p$	plastic strain tensor
$\varepsilon_l$	lateral strain
$\varepsilon_l^p$	lateral plastic strain
$\tilde{\varepsilon}_p$	equivalent plastic strain
$\tilde{\varepsilon}_{pc}$	equivalent compressive plastic strain
$\tilde{\varepsilon}_{pt}$	equivalent tensile plastic strain
$\varepsilon_t$	axial strain of the transition point of two portions of a stress-strain curve
$\varepsilon_x^0, \varepsilon_y^0, \gamma_s^0$	strain components on the reference plane for an FRP laminate
$\vec{\varepsilon}$	plastic strain trajectory
$\overline{\varepsilon}$	a function of the plastic strain trajectory
$\kappa_x, \kappa_y, \kappa_s$	laminate curvatures
$\theta$	friction parameter
$\arctan \theta$	friction angle
$\lambda$	scalar hardening parameter
$\nu_{12}, \nu_{21}$	Poisson's ratio of an FRP laminate in two principal directions
$\nu_c$	Poisson's ratio of concrete
$\nu_{f1}$	longitudinal Poisson's ratio of fibers
$\nu_m$	Poisson's ratio of polymer
$\rho_K$	confinement stiffness ratio
$\rho_\varepsilon$	strain ratio

$\sigma_1, \sigma_2, \sigma_3$	principal stresses
$\sigma_c$	axial stress of concrete
$\bar{\sigma}_{cn}$	effective compressive cohesion stress
$\bar{\sigma}_{ij}$	stress tensor
$\sigma_l$	confining pressure
$\sigma_{l,eff}$	effective confining pressure
$\bar{\sigma}_{max}$	peak stress of concrete
$\bar{\sigma}_{min}$	minimum effective principal stress
$\sigma_r$	radial stress
$\bar{\sigma}_m$	effective tensile cohesion stress
$\sigma_{to}$	uniaxial tensile stress at failure
$\sigma_\theta$	circumferential stress
$\tau_6$	in-plane shear stress
$\phi$	void ratio of an annular section
$\psi$	dilation angle measured in the meridian plane at high confining pressure for the D-P hyperbolic flow rule
$\varepsilon$	a constant defining the rate at which the function approaches the asymptote for the D-P hyperbolic flow rule

# **CHAPTER 1**

## **INTRODUCTION**

### **1.1 HYBRID STRUCTURES INCORPORATING FIBER REINFORCED POLYMER**

In recent years, fiber reinforced polymer (FRP) composites have found increasingly wide applications in civil engineering, both in the retrofit of existing structures and in new construction. FRP composites consist of fibers embedded in polymeric resins, and possess several advantages over steel, including their high strength-to-weight ratio and excellent corrosion resistance. As a result, the use of FRP composites as externally bonded reinforcement for the retrofit of structures has become very popular in recent years (Teng et al. 2002; Teng et al. 2003). These same advantages can also be exploited in new construction, and indeed a large amount of research around the world is currently under way examining the performance of various forms of structures made of FRP composites alone (i.e. all FRP structures) or FRP composites in combination with other materials (i.e. hybrid structures). Examples include FRP bridge decks, concrete-filled FRP tubes as columns and piles, and FRP cables.

Compared with the two primary modern structural materials, namely steel and concrete, FRP composites also have some disadvantages. These include their relatively high cost, linear-elastic-brittle stress-strain behavior, low elastic modulus-to-strength ratio, and poor fire resistance. In retrofit applications, cost savings arise from a number of aspects that offset the higher material cost, but this is more difficult to achieve in new construction at the present. The low elastic modulus-to-strength ratio is not critical in retrofit applications as the FRP is generally used to resist tension. The poor fire performance is also not an acute problem in retrofit applications either because the structure is in the open space (e.g. bridges) or because the FRP is not required to make a substantial contribution to structural resistance during a fire. When FRP composites are deployed in new construction, the consequences of their weaknesses need to be minimized as in retrofit applications. Based on these considerations, it may be concluded that the successful application of FRP composites in new construction requires the following three criteria to be met: (a) cost effectiveness at least in terms of a life-cycle cost assessment; (b) FRP to be used in areas subject to tension as much as possible; (c) fire resistance to be non-critical. It should be noted that criterion (c) is easily met for bridge structures and other outdoor structures, while the first two requirements very often mean that FRP composites should be used in combination with other materials to form hybrid structures.

Based on the above discussion, it is apparent that the area of hybrid structures should be a major research focus in the use of FRP composites in new construction. Within the area of hybrid structures, the aim shall be to optimally combine FRP with traditional structural materials such as steel and concrete to

create innovative structural forms that are cost-effective and of high-performance. To this end, simple duplications of existing structural systems are often inadequate.

Various forms of hybrid structures incorporating FRP have been proposed by previous researchers. Examples of hybrid flexural members with FRP include the hybrid FRP-concrete beam/slab (Figure 1.1) introduced by Burgueno et al. (2004) in the USA, and the hybrid FRP-concrete beams (Figure 1.2) introduced by Nordin and Taljsten (2004) in Sweden. The former consists of a concrete-filled FRP tube at the bottom and a reinforced concrete slab at the top, while the latter consists of concrete cast on the flat top surface of an FRP profile. It is evident that although these two members take different forms, the FRP is placed in the tension side of the member, which is desirable as discussed above.

The most popular example of hybrid compression members incorporating FRP is the concrete-filled FRP tube (CFFT) (Mirmiran and Shahawy 1997; Fam and Rizkalla 2001a, b; Hong et al. 2002; Zhang et al. 2000; Mirmiran 2003; Xiao 2004), as shown in Figure 1.3. When a concrete-filled FRP tube is under compression, the concrete is subjected to axial compression and confinement from the outer FRP tube, which is consequently subjected to tension in the circumferential direction. As a result, a very ductile structural member is formed from two brittle materials, namely, FRP and concrete. In addition to good ductility, the advantages of simple concrete-filled FRP tubes include their lightweight and excellent corrosion resistance. With these advantages, concrete-filled FRP tubes have been proposed for use as bridge columns and piles. However, it is noted that

concrete-filled FRP tubes have a number of disadvantages particularly when used as building columns. These include poor fire resistance, difficulty for connection to beams, inability to support substantial construction loads, brittle failure in bending, and high cost as the tube needs to be relatively thick in order to resist axial loads. As a bridge column, although the fire resistance and connection problems are not significant, it still suffers from the other disadvantages mentioned above.

## **1.2 HYBRID FRP-CONCRETE-STEEL TUBULAR COLUMNS**

### **1.2.1 Double-Skin Tubular Columns**

Double-skin tubular columns (DSTCs) are a variation of the conventional concrete-filled steel tubes which have been a common form of columns. The simplest form of concrete-filled steel tubes consists of a single hollow steel tube filled with concrete with or without internal steel reinforcing bars, while a double-skin tubular column consists of two generally concentric steel tubes with the space between filled with concrete (Figure 1.4). To the best of the authors' knowledge, such double-skin tubes were first reported in late 1980s (Shakir-Khalil and Illouli 1987). Since then, much research has been conducted on these columns (e.g. Shakir-Khalil 1991; Wei et al. 1995a, b; Han et al. 1995; Yagishita 2000; Zhao et al. 2002; Tao et al. 2003; Han et al. 2004). The inner void reduces the column weight without significantly affecting the flexural rigidity of the section and allows the easy passage of service ducts.

More recently, double-skin FRP tubes consisting of two FRP tubes and an annular concrete infill have been also been studied by Fam and Rizkalla (2001b). This structural form possesses the advantages of both concrete-filled FRP tubes and the structural form of DSTCs, but it also suffers from all the deficiencies of concrete-filled FRP tubes.

### **1.2.2 New Form of Hybrid Columns**

To overcome the existing disadvantages of concrete-filled FRP tubes, a new form of hybrid columns has recently been proposed by Prof. J.G. Teng of The Hong Kong Polytechnic University. The new column consists of a steel tube inside, an FRP tube outside and concrete in between (Figure 1.5). The inner void may be filled with concrete if desired. The FRP tube is provided with fibers which are predominantly oriented in the circumferential direction to provide confinement to the concrete and additional shear resistance. The new column form is an attempt to combine the advantages of all three constituent materials and those of the structural form of DSTCs, so as to achieve a high-performance structural member. While such a member may be used as a beam, its advantages are most obvious when used as a column so this new member may also be conveniently referred to as a hybrid FRP-concrete-steel double-skin tubular column (hybrid DSTC).

The novel feature of the new column form compared to existing forms of DSTCs is that the inner tube is made of steel but the outer tube is made of FRP with fibers oriented mainly in the hoop direction to provide confinement to the concrete for enhanced ductility. This simple change to the existing DSTC forms offers many

advantages, leading to a column which is easy to construct and highly resistant to corrosion and earthquakes. Direct comparisons can be made with a steel-concrete DSTC or an FRP-concrete DSTC.

Compared to the steel-concrete DSTC, the advantages of the new hybrid column include:

- (a) A more ductile response of concrete as it is well confined by the FRP tube which does not buckle. As mentioned above, the FRP tube is designed to have predominantly hoop fibers with its axial stiffness being nearly zero; by doing so, local buckling of the FRP tube due to axial compressive stresses, which is a common problem for steel tubes, is unlikely to happen.
- (b) No need for fire protection of the outer tube as the outer tube is required only as a form during construction and as a confining device and additional shear reinforcement during earthquakes. The FRP tube with negligible axial stiffness contributes little to the load-carrying capacity of the hybrid member and is not expected to affect the structural resistance during a fire. However, the outer steel tube of a steel-concrete DSTC takes considerable axial loading, and when its structural resistance is lost during a fire, the structural safety of the column is considerably compromised.
- (c) No need for corrosion protection as the steel tube inside is well protected by the concrete and the FRP tube. FRP, however, has excellent corrosion resistance.

Compared to the FRP-concrete DSTC, the advantages of the new hybrid column include:

- (a) Ability to support construction loading through the use of the inner steel tube.  
A steel tube is superior to an FRP tube in taking construction loading, as the latter is more susceptible to a buckling failure.
- (b) Ease for connection to beams due to the presence of the inner steel tube, which enables existing connection forms to be directly used.
- (c) Savings in fire protection cost as the outer tube is required only as a form during construction and as a confining device and additional shear reinforcement during earthquakes.
- (d) Better confinement of the concrete as a result of the increased rigidity of the inner tube.

Similarly, the new hybrid column also has significant advantages over other composite/hybrid columns including concrete-filled steel tubes, concrete-filled FRP tubes and concrete-encased steel columns in many applications.

The section form shown in Figure 1.5(a) consists of two circular tubes, but many different combinations of tubes are possible. Figures 1.5(b) and 1.5(c) show some of such variations. The section form can also be employed in a beam, in which case the inner steel tube may be shifted towards the tension side (Figure 1.5(d)). It should be noted that if the column section with two concentric tubes is deployed in situations where axial compression does not dominate under service loading, the column should be provided with some longitudinal reinforcement to avoid the development of large tensile cracks.

### **1.3 OBJECTIVES, SCOPE AND LAYOUT OF THIS THESIS**

As the hybrid DSTC columns are a new form of structural members, no existing studies have dealt with their behavior and design.

This thesis reports research carried out by the candidate over the last few years aimed at developing a good understanding of the structural behavior of and reliable design methods for this new form of hybrid columns. The thesis is mainly concerned with hybrid DSTCs with two concentrically placed circular tubes filled with concrete in between (Figure 1.5(a)), so hereafter the term “new hybrid DSTCs” or “hybrid DSTCs” is reserved for columns with a section shown in Figure 1.5(a) unless otherwise specified.

For columns, their compressive behavior is obviously the most important. Moreover, columns are normally also subjected to bending due to lateral loads, so that their beam-column behavior is also important. The flexural behavior of columns also needs to be understood within the overall picture of the beam-column behavior of columns. Therefore, this thesis deals with the compressive, flexural, and beam-column behaviour of hybrid DSTCs. The flexural behaviour of hybrid beams with a section as shown in Figure 1.5(d) is also treated.

The stress-strain behaviour of the confined concrete in this new form of hybrid structural members is the key to understanding their structural performance. To better understand the behaviour of concrete, it is important to understand how the

concrete is confined by the two tubes in these new columns and how the inner void and the steel tube affect the effectiveness of confinement. Direct comparisons of the behaviour of concrete between the new DSTCs, FRP-confined solid concrete cylinders (FCSC, see Figure 1.6(a)) and FRP-confined hollow concrete cylinders (FCHC, see Figure 1.6(b)) are presented in this thesis to clarify the differences and similarities.

Based on the above considerations, the research work presented in this thesis was carried out with the following six specific objectives:

- (a) To obtain a good understanding of the compressive, flexural and beam-column behavior of hybrid DSTCs through experimental work;
- (b) To clarify the confinement mechanism for the concrete in such DSTCs, through comparative tests of different section forms;
- (c) To develop a finite element (FE) model for predicting the axial compressive behavior of hybrid DSTCs;
- (d) To develop a simple one-dimensional stress-strain model for the concrete in such DSTCs for section analysis; and
- (e) To develop a sectional analysis method for predicting the flexural and beam-column behavior of hybrid DSTCs.

The research methodology adopted combines experimental investigations with theoretical modeling. The experimental program of the present study consisted of three series of tests: concentric compression tests, eccentric compression tests and

four-point bending tests to study the compressive behavior, beam-column behavior and flexural behavior of hybrid DSTCs. Comparative tests of DSTCs, FCHCs and FCSCs were also conducted to study the confinement mechanism of the concrete in hybrid DSTCs. These experimental results form a necessary basis for the theoretical modeling work. They also provide the means for verifying the theoretical models.

Since the proposed hybrid section has three constituents, it is important to understand the interaction between them, which is difficult to achieve through experiments alone. To this end, a three dimensional FE model was developed to study the behavior of this hybrid section under concentric axial compression. As a first step, existing Drucker-Prager (D-P) type concrete plasticity models for confined concrete were assessed. A constitutive model which takes into account the conclusions drawn from the assessment of existing D-P type models and other distinct characteristics of non-uniformly confined concrete was then proposed and verified with test results. A parametric study using the verified FE model was then conducted, from which a simple one-dimensional stress-strain model for the concrete in DSTCs was formulated. A sectional analysis method employing this simple stress-strain model was then developed based on the so-called fiber element approach. The proposed sectional analysis method was verified with test results and then deployed to study the behavior of hybrid DSTCs under pure flexure and combined axial compression and flexure.

The combined experimental and theoretical study is presented in this thesis in 8 chapters, details of which are summarized below.

Chapter 2 presents an extensive literature review of topics related to the present study. It starts with a discussion of existing research on concrete-filled FRP tubes, including both experimental and theoretical investigations. The behavior and analytical modeling of FRP-confined concrete, which depend on the unique properties of FRP tubes, are focused on in this discussion. Existing research on the experimental behavior and theoretical modeling of double-skin tubular columns is also discussed. Available three-dimensional constitutive models for concrete are then summarized, with an emphasis on their ability to model confined concrete.

Chapter 3 presents the experiment results of hybrid DSTCs subjected to concentric axial compression. Test results for two similar sections, namely, FCSCs and FCHCs, are also presented in this chapter. A brief introduction to the test program is first given. Details of the test specimens and the measured properties of the materials are then given. The main variables examined include the section configuration, the amount of FRP forming the outer tube, the type of the inner tube, and the inner void size. The procedure for the preparation of specimens is then described, including the formation of the mould for casting concrete and the wet-lay up process for forming the FRP tube. The test set-up and the instrumentation are next presented, followed by the experimental observations, results and discussions, with the focus being on the behavior of confined concrete and the steel tube. Based on the test results, comparisons are then made between the different types of sections. Through these comparisons, the effects of the key variables are clarified.

In Chapter 4, existing Drucker-Prager (D-P) type plasticity models for confined concrete are assessed. The effects of the three key components of a concrete plasticity model, namely, the yield criterion, the hardening rule and the flow rule, on the performance of the plasticity model in capturing the behavior of confined concrete, is assessed through a series of numerical tests. Conclusions are drawn from this assessment regarding the necessary attributes of a plasticity model for reasonable predictions of both actively- and passively-confined concrete (e.g. FRP-confined concrete). These conclusions also form the basis of the FE model for hybrid DSTCs presented in Chapter 5.

Chapter 5 presents an FE model for hybrid DSTCs subjected to concentric axial compression. This chapter starts with a description of the adopted concrete constitutive model, which takes due account of the conclusions reached in Chapter 4 and other distinct characteristics of non-uniformly confined concrete. The FE model is then presented in detail and verified with test results presented in Chapter 3. Results from a parametric study using the verified FE model are next presented to explore the behavior of hybrid DSTCs under axial compression. Finally, a simple stress-strain model is proposed based on both the FE and the test results.

Chapter 6 deals with the flexural behavior of hybrid DSTCs. Two series of four point bending tests are first presented. The test design, specimen details, material properties, preparation of specimens, test set-up and instrumentation are described in detail. The experimental results are next presented and discussed. The parameters examined in the experimental work include the section configuration,

the concrete strength, and the thicknesses of the steel tube and the FRP tube respectively. Finally, a sectional analysis method is presented. Comparisons between the predictions from the sectional analysis method and the test results confirm the accuracy of this method.

The beam-column behavior of hybrid DSTCs is investigated in Chapter 7. Eccentric compression tests, during which the specimens were subjected to combined axial compression and bending, are first described in this chapter. The load eccentricity is the main test variable. Experimental results are then discussed, with particular attention to the behavior of the mid-height section of the specimen. The sectional analysis method presented in Chapter 6 is extended for the prediction of DSTCs under eccentric compression. Results from a parametric study conducted using this extended section analysis method are also presented.

The thesis closes with Chapter 8, where the conclusions drawn from previous chapters are reviewed, and areas in need of further research highlighted.

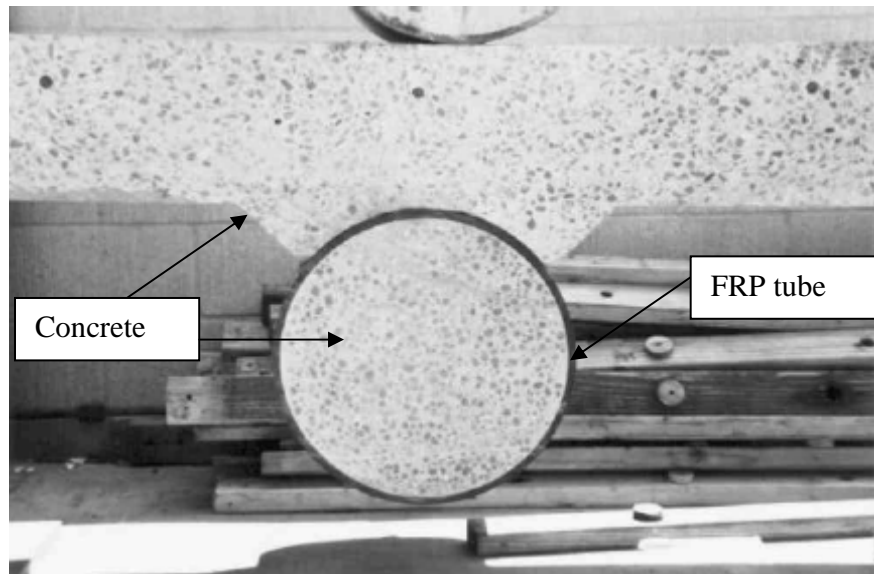


Figure 1.1 Cross section of hybrid FRP/concrete beam/slab (Burgueno et al. 2004)

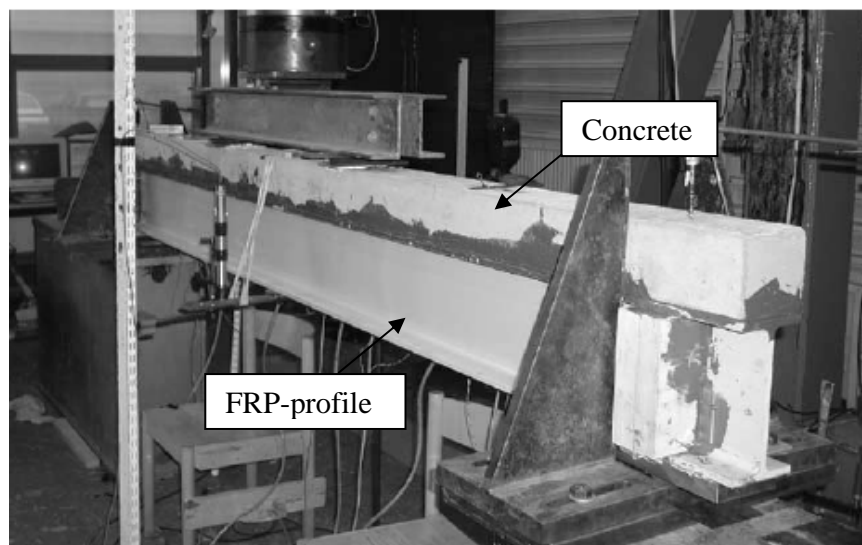


Figure 1.2 Hybrid FRP-concrete beam (Nordin and Taljsten 2004)

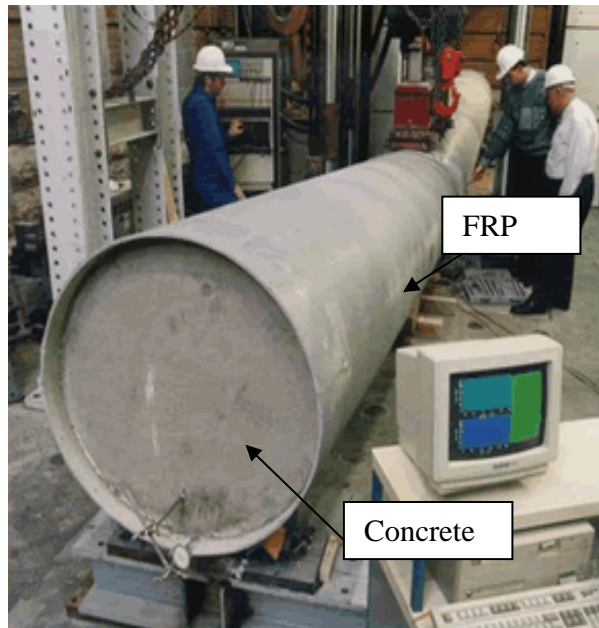


Figure 1.3 Concrete-filled FRP tube (Website of Queen's university, Canada)

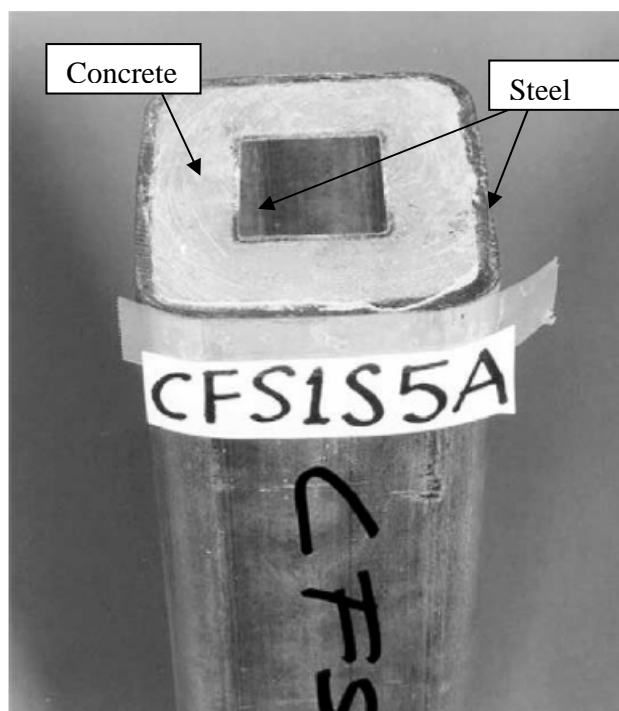


Figure 1.4 Double-skin steel tube (Zhao and Grzebieta 2002)

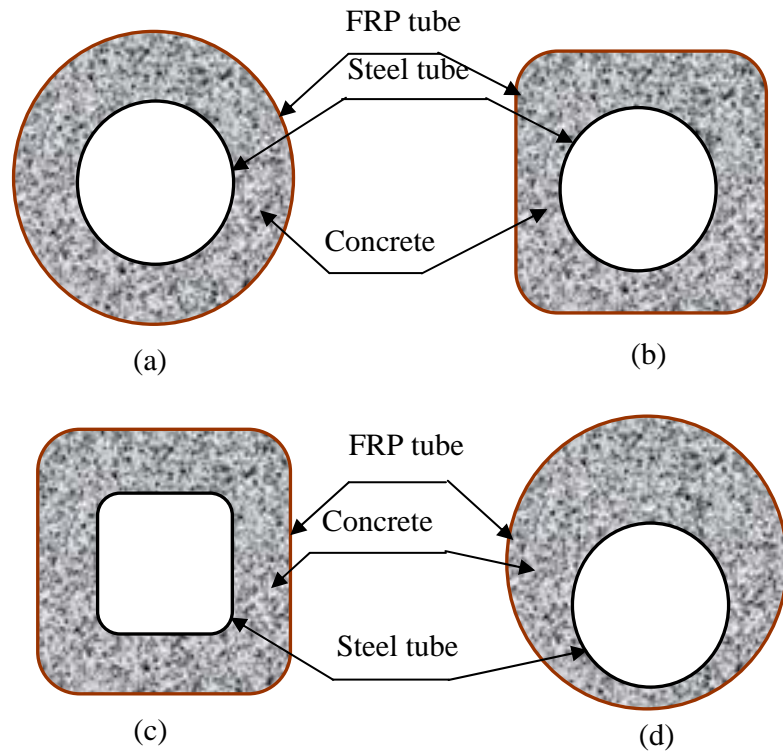


Figure 1.5 Typical sections of new hybrid double-skin tubular members

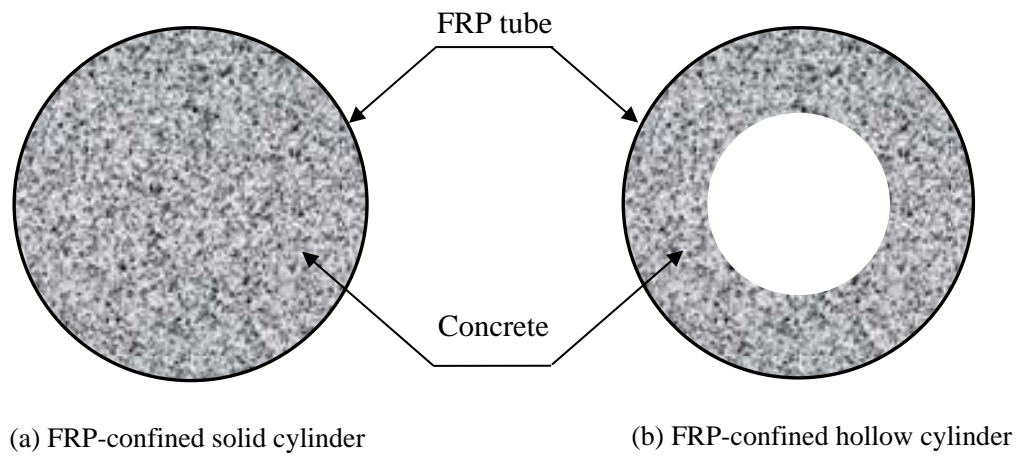


Figure 1.6 Cross-sections of FCSCs and FCHCs

## **CHAPTER 2**

### **LITERATURE REVIEW**

#### **2.1 INTRODUCTION**

This chapter presents a review of existing knowledge pertinent to the new hybrid FRP-concrete-steel double-skin tubular column (DSTC). As pointed out in Chapter 1, existing structural forms that are closely similar to this new member form are concrete-filled FRP tubes (CFFTs) and two forms of DSTCs, including steel-concrete DSTCs and FRP-concrete DSTCs. Therefore, existing knowledge of these structural forms, including both experimental and theoretical findings, are reviewed in this chapter. In addition, previous research on the constitutive modeling of confined concrete is briefly summarized and commented on. This existing work provides the basis for the three dimensional finite element (FE) modeling work presented later in the thesis.

The chapter starts with a discussion of previous research on CFFTs with or without an inner void. In these structural members, the concrete is confined by an FRP tube which has properties different from traditional confining materials such as steel. Consequently, FRP-confined concrete behaves differently from actively-confined concrete (i.e. concrete subject to constant confinement) or

steel-confined concrete. This different behavior has been widely investigated both experimentally and theoretically. In addition, the unique properties of the FRP tube are also important for a better understanding of the structural behavior of these members.

Existing research on the structural performance of steel-concrete DSTCs and FRP-concrete DSTCs, with an emphasis on the concrete behavior in such hybrid sections, is then described. The concrete in these two types of hybrid members is subjected to constraints from both the inside and the outside, a situation which also exists in the new hybrid DSTC. Previous experimental work on these two DSTCs is introduced, followed by a summary of analytical modeling work.

Existing constitutive models for confined concrete are described towards the end of this chapter; their unique characteristics are a particular focus of the discussions presented here.

## **2.2 CONCRETE-FILLED FRP TUBES**

### **2.2.1 Introduction**

Fiber reinforced polymer (FRP) is composed of fibers embedded in a polymeric resin. In this section, the properties of FRP laminates, formed from a number of laminae with fibers oriented in different directions, are discussed based on available research. Both constitutive equations and standard test methods are described. Following this, the unique properties of FRP-confined concrete, together with existing analytical and design models, are presented. For simplicity,

hereafter in this chapter the term “FRP-confined concrete” is used to refer to concrete in circular solid cylinders confined with an FRP jacket, unless otherwise specified.

## **2.2.2 FRP Laminates**

### *2.2.2.1 Constitutive equations*

It is widely acknowledged that the stress-strain behavior of FRP is predominantly linear elastic, especially when it is loaded in the direction of the fibers (Shao 2003; Daniel and Ishai 1994). Consequently, most of the previous research (e.g. Fam 2000; Samaan 1997; Davol 1998; Flisak 2004; Bhide 2002; Becque 2000; Zhu 2004) adopted a linear elastic constitutive law based on the lamination theory of FRP laminates.

An FRP laminate (Figure 2.1(b)) is made up of two or more unidirectional laminae, which are plane (or curved) plies of unidirectional fibers in a matrix and stacked together at various orientations. The unidirectional lamina (Figure 2.1(a)) is an orthotropic material with the three principal material axes being in the direction of the fibers (longitudinal), normal to the fibers in the plane of the lamina (in-plane transverse), and normal to the plane of the lamina. Consequently, the mechanical analysis of FRP laminates generally includes two steps (Daniel and Ishai 1994): (i) micro-mechanical analysis to find the properties of a unidirectional lamina (a one-ply material) and (ii) macro-mechanical analysis to find the properties of an FRP laminate.

The micro-mechanical analysis of the in-plane elastic constants of a unidirectional lamina is based on the mechanical properties of the two constituents (i.e. fiber and polymer), their volume ratio and Eqns 2.1-2.4 shown below.

$$E_1 = E_{f1}V_f + E_m V_m \quad (2.1)$$

$$E_2 = \frac{E_{f2} E_m}{E_{f2}V_m + E_m V_f} \quad (2.2)$$

$$\nu_{12} = \nu_{f1}V_f + \nu_m V_m \quad (2.3)$$

$$G_{12} = \frac{G_{f12} G_m}{G_{f12}V_m + G_m V_f} \quad (2.4)$$

in which  $E_1$  and  $E_2$  are the elastic moduli of an FRP laminate in the two principal directions,  $\nu_{12}$  is the longitudinal Poisson's ratio of an FRP laminate, and  $G_{12}$  is the in-plane shear modulus of an FRP laminate;  $E_{f1}$  and  $E_{f2}$  are the elastic moduli of fibers in the two principal directions;  $G_{f12}$  is the shear modulus of fibers;  $\nu_{f1}$  is the longitudinal Poisson's ratio of fibers;  $E_m$ ,  $G_m$  and  $\nu_m$  are the elastic modulus, the shear modulus and the Poisson's ratio of polymer respectively, and  $V_f$  and  $V_m$  are the volume ratio of fibers and polymer respectively.

The in-plane stress-strain relationship of a one-ply FRP lamina can be expressed by Eqn 2.5.

$$\begin{bmatrix} \sigma_1 \\ \sigma_2 \\ \tau_6 \end{bmatrix} = \begin{bmatrix} Q_{11} & Q_{12} & 0 \\ Q_{21} & Q_{22} & 0 \\ 0 & 0 & Q_{66} \end{bmatrix} \begin{bmatrix} \varepsilon_1 \\ \varepsilon_2 \\ \gamma_6 \end{bmatrix} \quad (2.5)$$

in which

$$Q_{11} = \frac{E_1}{1 - \nu_{12}\nu_{21}} \quad (2.6)$$

$$Q_{22} = \frac{E_2}{1 - \nu_{12}\nu_{21}} \quad (2.7)$$

$$Q_{12} = Q_{21} = \frac{\nu_{12}E_2}{1 - \nu_{12}\nu_{21}} = \frac{\nu_{21}E_1}{1 - \nu_{12}\nu_{21}} \quad (2.8)$$

$$Q_{66} = G_{12} \quad (2.9)$$

The macro-mechanical analysis is based on the mechanical properties of the laminae, the stacking sequence and the lamination theory. The lamination theory leads to Eqn 2.10 for a laminate with an arbitrary structure (Figure 2.2).

$$\begin{bmatrix} N_x \\ N_y \\ N_s \\ M_x \\ M_y \\ M_s \end{bmatrix} = \begin{bmatrix} A_{xx} & A_{xy} & A_{xs} & B_{xx} & B_{xy} & B_{xs} \\ A_{yx} & A_{yy} & A_{ys} & B_{yx} & B_{yy} & B_{ys} \\ A_{sx} & A_{sy} & A_{ss} & B_{sx} & B_{sy} & B_{ss} \\ B_{xx} & B_{xy} & B_{xs} & D_{xx} & D_{xy} & D_{xs} \\ B_{yx} & B_{yy} & B_{ys} & D_{yx} & D_{yy} & D_{ys} \\ B_{sx} & B_{sy} & B_{ss} & D_{sx} & D_{sy} & D_{ss} \end{bmatrix} \begin{bmatrix} \varepsilon_x^0 \\ \varepsilon_y^0 \\ \gamma_s^0 \\ \kappa_x \\ \kappa_y \\ \kappa_s \end{bmatrix} = \begin{bmatrix} [A] & [B] \\ [B] & [D] \end{bmatrix} \begin{bmatrix} \varepsilon_x^0 \\ \varepsilon_y^0 \\ \gamma_s^0 \\ \kappa_x \\ \kappa_y \\ \kappa_s \end{bmatrix} \quad (2.10)$$

Where,

$N_x$ ,  $N_y$  and  $N_s$  are the resultant force in the laminate global x-direction per unit width, the resultant force in the laminate global y-direction per unit width, and the resultant shear force in the laminate global x-y plane per unit width respectively;

$M_x$ ,  $M_y$  and  $M_s$  are the resultant moment in the laminate global x-z plane per unit width, the resultant moment in the laminate global y-z plane per unit width, and the resultant twisting moment per unit width respectively;

$\varepsilon_x^0$ ,  $\varepsilon_y^0$  and  $\gamma_s^0$  are the strain components on a reference plane equidistant from the top and bottom of the laminate, in the laminate global coordinate system;

$\kappa_x$ ,  $\kappa_y$  and  $\kappa_s$  are the laminate curvatures;

$[A]$  is the extensional stiffness matrix, relating in-plane loads to in-plane strains;

$[B]$  is the coupling stiffness matrix, relating in-plane loads to curvatures and moments to in-plane strains;

$[D]$  is the flexural stiffness matrix, relating moments and curvatures.

$[A]$ ,  $[B]$  and  $[D]$  can be obtained through the lamination theory, based on the properties of each lamina and the stacking sequence (see Daniel and Ishai 1994).

As special cases, a laminate is referred to as a symmetric laminate when for each ply on one side of the reference plane (i.e. the middle plane) there is a corresponding ply at an equal distance from the reference plane on the other side with an identical thickness, fiber orientation and properties; a laminate is called a cross-ply laminate when it only consists of plies with principal material axes coinciding with the laminate axes; a laminate is called a balanced laminate when it consists of pairs of plies with identical thicknesses and elastic properties but has  $+\theta$  and  $-\theta$  orientations of their principal material axes with respect to the laminate reference axes. For a symmetric laminate, the coupling stiffness matrix  $B$  is zero; for a cross-ply or balanced laminate,  $A_{xx} = A_{yy} = 0$ . Therefore, for a symmetric balanced or symmetric cross-ply laminate, Eqn 2.11 can be obtained, which is very similar to that of an orthotropic material.

$$\begin{Bmatrix} N_x \\ N_y \\ N_s \end{Bmatrix} = \begin{bmatrix} A_{xx} & A_{xy} & 0 \\ A_{yx} & A_{yy} & 0 \\ 0 & 0 & A_{ss} \end{bmatrix} \begin{Bmatrix} \varepsilon_x^0 \\ \varepsilon_y^0 \\ \gamma_s^0 \end{Bmatrix} \quad (2.11)$$

The effective engineering constants (i.e. elastic modulus, Poisson's ratio, shear modulus) can then be easily defined for such laminates.

In existing research (Hahn and Tsai 1973; Lifshitz 1988; Haj-Ali and Kilic 2002; Yuan et al. 2002; Shao 2003; ASTM D3518/D3518M-94 1994), deviations from linearity were observed when FRP was loaded under in-plane transverse loading and in-plane shear, although the linear elastic behavior of fibers is generally the dominant behavior in the response of unidirectional FRP materials loaded in the direction of the fibers (Shao 2003; Daniel and Ishai 1994). The non-linearity of FRP under in-plane shear is much more significant than that of FRP under in-plane transverse loading.

#### *2.2.2.2 Test methods*

The classical lamination theory provides a feasible method to evaluate the mechanical properties of FRP tubes. This theory, however, involves complicated calculations for FRP laminates, especially those with asymmetric unbalanced laminate structures. In addition, non-linear behavior may be dominant for FRP tubes with angle-ply laminate structures, which cannot be predicted by the lamination theory. Moreover, some previous research (e.g. Fam 2000) showed that the error of predictions of the lamination theory may be up to 40% for the ultimate strength, up to 25% for the elastic modulus and up to 50% for the Poisson's ratio. Therefore, standard material tests are important for more accurate evaluation of the mechanical properties of FRP tubes.

The most popular test standards for the tensile properties of FRP appear to be ASTM D3039/D3039M-00 (2000) and ASTM D2290-00 (2000), or the earlier versions of these two standards. ASTM D3039/D3039M-00 (2000) provides a test

method for the tensile properties of FRP using flat coupon tests. A typical test sample following this standard is shown in Figure 2.3(a). ASTM D2290-00 (2000) provides a test method for the tensile properties of an FRP ring through the split disk method (i.e. ring splitting tests). A typical test sample following this standard is shown in Figure 2.3(b). Lam and Teng (2004) compared results from flat coupon tests and ring splitting tests and concluded that the ultimate strength obtained by the ring splitting test is in general lower than that obtained from the corresponding flat coupon test, mainly due to the effect of curvature. Despite the difference in the ultimate strength, Lam and Teng (2004) also found that the elastic moduli obtained from these two test methods are almost the same.

The most popular test standards for the compressive properties of FRP include ASTM D3410/D3410M-95 (1995) which provides a test method for the compressive properties of FRP through shear loading tests, and ASTM D695-02a (2002) which is specifically for rigid plastics, or the earlier versions of these two standards.

In the present research, the FRP tubes used had all the fibers oriented in the hoop direction. Consequently, only the tensile properties of FRP in the hoop direction were of interest. Flat coupon tests following ASTM D3039/D3039M-00 (2000) were conducted as described in the following chapters.

### **2.2.3 FRP-Confined Concrete**

#### *2.2.3.1 Introduction*

Extensive research has been conducted on the compressive strength and stress-strain behavior of FRP-confined circular concrete cylinders (e.g. Fardis and Khalili 1981; Mirmiran and Shahawy 1996; Saafi et al. 1999; Fam and Rizkalla 2001a, b; Toutanji 1999; Xiao and Wu 2000; Lam and Teng 2003a; Teng et al. 2006a, b), through experimental work, theoretical analysis or FE analysis. The following unique properties have emerged from existing research on FRP-confined concrete: (1) due to the linear elastic behavior of FRP, the concrete is subjected to a continuously increasing confining pressure provided by the FRP jacket, and reaches its ultimate state by the hoop rupture of FRP when its tensile strength is reached; this is different from concrete under a constant active confining pressure and that confined by a steel tube which provides an almost constant confinement after yielding; (2) the axial stress-strain curve of FRP-confined concrete exhibits an approximately bilinear shape with a continuously increasing axial stress until ultimate failure (Figure 2.4(a)) when the level of confinement from the FRP jacket is sufficiently large, but otherwise has a descending branch following the initial ascending branch (Figures 2.4(b) and (c)); (3) the behavior of FRP-confined concrete, including its stress-strain curve and ultimate state, depends strongly on the stiffness of FRP and the column size, among other parameters.

Many stress-strain models have been proposed for predicting the behavior of FRP-confined concrete based on test results, including design-oriented models in

closed-form expressions (e.g. Lam and Teng 2003a) and analysis-oriented models (e.g. Teng et al. 2006a) which predict stress-strain curves by an incremental procedure (Teng and Lam 2004; Teng et al. 2006a).

#### *2.2.3.2 Design-oriented model*

Design-oriented models are based on the interpretation of experimental results and regression analysis, and adopt closed-form equations to express the stress-strain curve. Consequently, the accuracy of these equations depends on whether the test database is reliable and sufficiently large, and whether the variables selected for inclusion in the closed-form equations are reasonable and sufficient to reflect the mechanical behavior of FRP-confined concrete. Some typical stress-strain models of this category include those presented in Lam and Teng (2003a), Xiao and Wu (2000), Toutanji (1999), Saffi et al. (1999), and Samaan et al. (1998).

Different researchers adopted different approximations to a typical bilinear stress-strain curve. Examples include Xiao and Wu's (2000) model which approximates the bilinear curve using two straight lines, Toutanji's (1999) model and Saafi et al.'s (1999) model which approximates the bilinear curve using two curved lines, and Samaan et al.'s (1998) model which approximates the bilinear curve using a single equation of complex form. In particular, Lam and Teng's (2003a) model describes the typical bilinear stress-strain curve using a parabola for the first portion and a straight line for the second portion, with the various parameters being dependent on the FRP properties. The parabola is similar to that in stress-strain equations for unconfined concrete in codes of practice such as BS 8110 (1997) and Eurocode 2 (1991), and is thus familiar to engineers. In addition,

Lam and Teng (2003a) selected suitable variables for the proposed equations, based on a large database containing the test results of 76 FRP-confined specimens. Test results of FRP-confined circular concrete cylinders can be closely predicted by Lam and Teng's (2003a) model, which is briefly presented below.

Lam and Teng's (2003a) design-oriented stress-strain model is based on the following assumptions: (i) the stress-strain curve consists of a parabolic first portion and a linear second portion; (ii) the slope of the parabola at zero axial strain (the initial slope) is the same as the elastic modulus of unconfined concrete; (iii) the nonlinear part of the first portion is affected to some degree by the presence of an FRP jacket; (iv) the parabolic first portion meets the linear second portion smoothly (i.e. there is no change in slope between the two portions where they meet); (v) the linear second portion terminates at a point where both the compressive strength and the ultimate axial strain of confined concrete are reached.

Based on these assumptions, Lam and Teng's (2003a) stress-strain model for FRP-confined concrete is described by the following expressions:

$$\sigma_c = E_c \varepsilon_c - \frac{(E_c - E_{2c})^2}{4f_o} \varepsilon_c^2 \quad \text{for} \quad 0 \leq \varepsilon_c < \varepsilon_t \quad (2.12)$$

and

$$\sigma_c = f_o + E_{2c} \varepsilon_c \quad \text{for} \quad \varepsilon_t \leq \varepsilon_c \leq \varepsilon_{cu} \quad (2.13)$$

where  $\sigma_c$  and  $\varepsilon_c$  are the axial stress and the axial strain,  $E_c$  is the elastic modulus of unconfined concrete,  $E_{2c}$  is the slope of the linear second portion,

$f_o$  is the intercept of the stress axis by the linear second portion, and  $\varepsilon_{cu}$  is the ultimate axial strain of confined concrete. The parabolic first portion meets the linear second portion with a smooth transition at  $\varepsilon_t$  which is given by

$$\varepsilon_t = \frac{2f_o}{(E_c - E_{2c})} \quad (2.14)$$

The slope of the linear second portion  $E_{2c}$  is given by

$$E_{2c} = \frac{f'_{cc} - f_o}{\varepsilon_{cu}} \quad (2.15)$$

where  $f'_{cc}$  is the compressive strength of confined concrete.

This model allows the use of test values or values specified by design codes for the elastic modulus of unconfined concrete  $E_c$ . For example, it is suggested in ACI 318-95 (1999) that the elastic modulus of unconfined concrete  $E_c = 4730\sqrt{f'_{co}}$ . Lam and Teng (2003a) proposed that  $f_o$  be equal to the compressive strength of unconfined concrete  $f'_{co}$ , Eqn 2.16 be used to predict the ultimate axial strain  $\varepsilon_{cu}$ , and Eqns 2.17 and 2.18 be used to predict the compressive strength of FRP-confined concrete  $f'_{cc}$ .

$$\frac{\varepsilon_{cu}}{\varepsilon_{co}} = 1.75 + 12 \left( \frac{E_{frp} t_{frp}}{E_{sec} R_o} \right) \left( \frac{\varepsilon_{h,rupt}}{\varepsilon_{co}} \right)^{1.45} \quad (2.16)$$

$$\frac{f'_{cc}}{f'_{co}} = 1 + 3.3 \frac{f_l}{f'_{co}} \quad \text{when } f_l / f'_{co} \geq 0.07 \quad (2.17)$$

$$\frac{f'_{cc}}{f'_{co}} = 1 \quad \text{when } f_l / f'_{co} < 0.07 \quad (2.18)$$

where  $E_{frp}$  is the elastic modulus of FRP in the hoop direction,  $t_{frp}$  is the thickness of the FRP jacket,  $\varepsilon_{h,rupt}$  is the hoop strain of FRP at the rupture of the

jacket due to hoop tensile stresses,  $R_o$  is the outer radius of the confined concrete core,  $E_{\text{sec}o}$  and  $\varepsilon_{co}$  are the secant modulus and the axial strain at the compressive strength of unconfined concrete, with  $E_{\text{sec}o} = f'_{co} / \varepsilon_{co}$ . The term  $E_{\text{frp}t_{\text{frp}}} / (E_{\text{sec}o} R_o)$  is referred to as the confinement stiffness ratio and  $\varepsilon_{h,\text{rup}} / \varepsilon_{co}$  is the strain ratio.  $f_l$  is the maximum confining pressure provided by an FRP jacket which is defined by

$$f_l = \frac{E_{\text{frp}t_{\text{frp}}} \varepsilon_{h,\text{rup}}}{R_o} \quad (2.19)$$

The ratio of maximum confining pressure to unconfined concrete strength  $f_l / f'_{co}$  has been commonly referred to as the confinement ratio.

Teng et al. (2006b) refined Lam and Teng's (2003a) model based on additional test data and proposed the following equations for  $f'_{cc}$  and  $\varepsilon_{cu}$ .

$$\frac{f'_{cc}}{f'_{co}} = \begin{cases} 1 + 3.5(\rho_K - 0.01) \cdot \rho_\varepsilon & \text{if } \rho_K \geq 0.01 \\ 1 & \text{if } \rho_K < 0.01 \end{cases} \quad (2.20)$$

$$\frac{\varepsilon_{cu}}{\varepsilon_{co}} = 1.75 + 6.5 \rho_K^{0.8} \rho_\varepsilon^{1.45} \quad (2.21)$$

where  $\rho_K = E_{\text{frp}t_{\text{frp}}} / (E_{\text{sec}o} R_o)$  is the confinement stiffness ratio and  $\rho_\varepsilon = \varepsilon_{h,\text{rup}} / \varepsilon_{co}$  is the strain ratio.

With these refinements, the modified version of Lam and Teng's (2003a) model provides closer predictions of test stress-strain curves than the original model, especially for concrete confined by a relatively weak FRP tube.

### *2.2.3.3 Analysis-oriented model*

While design-oriented models are given in closed-form expressions which are derived directly from test results, analysis-oriented models consider the responses of the concrete and the FRP jacket as well as their interaction in an explicit manner. Analysis-oriented models provide a unified treatment of both well-confined concrete with a bilinear stress-strain curve and weakly-confined concrete with a stress-strain curve featuring a descending branch, and can potentially be used to predict the behavior of concrete confined with other materials (Teng et al. 2006a). These features make analysis-oriented models more versatile and powerful than design-oriented models (Teng et al. 2006a). While some of the models (e.g. Becque et al. 2003) are based on alternative methods, most of the analysis-oriented models (e.g. Teng et al. 2006a; Fam and Rizkalla 2001a; Mirmiran and Shahawy 1996; Spoelstra and Monti 1999) are based on an active confinement model for concrete, force equilibrium and displacement compatibility in the radial direction between the concrete core and the FRP jacket. The accuracy of this category of models consequently depends on whether the active confinement model is appropriate, whether the relationship between the axial and the lateral strains of concrete is accurate and whether the failure criterion is reliable. Becque et al.'s (2003) model is based on Gerstle's (1981a, b) octahedral stress-strain model with some modifications, and is discussed later in Subsection 2.2.4.

The common procedure of this kind of models for developing axial stress-strain curves is: (1) for a given axial strain of concrete, find the corresponding lateral strain; (2) based on the force equilibrium and the displacement compatibility in

the radial direction between the concrete core and the FRP jacket, find the corresponding lateral pressure; (3) based on the axial strain and the obtained lateral pressure, find the axial stress using an active confinement model, and thus obtain a point on the stress-strain curve; (4) repeat steps (1)-(3) and develop the whole curve.

Although most existing analysis-oriented models (e.g. Teng et al. 2006a; Mirmiran and Shahawy 1996; Spoelstra and Monti 1999; Fam and Rizkalla 2001a) employ Mander et al.'s (1988) model, which was originally proposed for steel-confined concrete, as the active confinement model, different models employ quite different methods for step (1) (i.e. to find the lateral strain corresponding to an axial strain). This also produces the most significant differences between the various models.

Some researchers (e.g. Spoelstra and Monti 1999) adopted an implicit and iterative method for step (1), which appears to be very complex and time-consuming. As an improvement, some researchers (e.g. Teng et al. 2006a; Mirmiran and Shahawy 1996) proposed an explicit equation for the relationship between the axial strain and the lateral strain, with the variables in this equation being material properties such as the confinement stiffness and the strength of FRP. Teng et al.'s (2006a) analysis-oriented model is the latest one based on a large test database of concrete under different types of confinement, namely, active confinement and passive confinement (i.e. FRP confinement and steel confinement). Teng et al.'s (2006a) model has shown good agreement with numerous test results and is briefly presented below.

Eqn 2.22 was proposed by Teng et al. (2006a) for the relationship between the axial strain and the lateral strain.

$$\Phi\left(\frac{-\varepsilon_l}{\varepsilon_{co}}\right) = \frac{\varepsilon_c}{\varepsilon_{co}} \left/ \left(1 + 8 \frac{\sigma_l}{f'_{co}}\right) \right. = 0.85 \left\{ \left[ 1 + 0.75 \left( \frac{-\varepsilon_l}{\varepsilon_{co}} \right) \right]^{0.7} - \exp \left[ -7 \left( \frac{-\varepsilon_l}{\varepsilon_{co}} \right) \right] \right\} \quad (2.22)$$

where  $\sigma_l$  is the confining pressure and can be related to the lateral strain  $\varepsilon_l$  by

$$\sigma_l = -\frac{E_{frp} t_{frp} \varepsilon_l}{R_o}. \text{ The axial strain } \varepsilon_c \text{ and the lateral strain } \varepsilon_l \text{ are the only two}$$

variables in this equation with their relationship being implicit.

With Eqn 2.22, the axial stress-strain response of FRP-confined concrete can be predicted without difficulty following the procedure stated earlier, base on an active confinement model. Teng et al. (2006a) adopted the following axial stress-axial strain equation for the active confinement model, which was originally proposed by Popovics (1973) and used in Mander et al.'s (1988) model for steel-confined concrete.

$$\frac{\sigma_c}{f_{cc}^*} = \frac{\left(\varepsilon_c / \varepsilon_{cc}^*\right) C_1}{C_1 - 1 + \left(\varepsilon_c / \varepsilon_{cc}^*\right)^{C_1}} \quad (2.23)$$

where  $\sigma_c$  is the axial stress of concrete,  $f_{cc}^*$  and  $\varepsilon_{cc}^*$  are respectively the peak axial stress and the corresponding axial strain of concrete under a specific constant confining pressure. The constant  $C_1$  in Eq. 2.23, approximately accounting for the brittleness of concrete, is defined in Carreira and Chu (1985) as

$$C_1 = \frac{E_c}{E_c - f_{cc}^* / \varepsilon_{cc}^*} \quad (2.24)$$

Teng et al. (2006b) also proposed Eqns 2.25 and 2.26 for the peak stress and strain, instead of the original equations adopted in Mander et al. (1988).

$$\frac{f_{cc}^*}{f_{co}} = 1 + 3.5 \frac{\sigma_l}{f_{co}} \quad (2.25)$$

$$\frac{\varepsilon_{cc}^*}{\varepsilon_{co}} = 1 + 17.5 \frac{\sigma_l}{f_{co}} \quad (2.26)$$

#### 2.2.4 FRP-Confined Annular Concrete Cylinders

As introduced in Subsection 2.2.3, test results of FRP-confined circular concrete cylinders can now be closely predicted by some of the existing stress-strain models such as those proposed by Lam and Teng (2003a) and Teng et al. (2006a). However, the behavior of FRP-confined concrete in sections other than circular sections is not yet well understood. In non-circular FRP-confined sections such as annular sections, the concrete is non-uniformly confined. Only a very limited amount of research is available on the behaviour of FRP-confined concrete in annular sections (e.g. Fam and Rizkalla 2001a, b; Becque et al. 2003).

Fam and Rizkalla (2001b) reported the test results of four FRP-confined hollow concrete cylinders (FCHCs) and showed that FRP confinement is less effective for concrete in FCHCs than for concrete in FRP-confined solid concrete cylinders (FCSCs). Fam and Rizkalla (2001b) also reported two tests on FRP-concrete DSTCs with both the inner and the outer tube being made of FRP. Such FRP-concrete DSTCs were reported to be superior to FCHCs in terms of the effectiveness of FRP confinement on the concrete, due to the existence of the FRP inner tube. It was also observed from the test results that corresponding to a given

axial strain, the lateral strain of an FRP-concrete DSTC specimen is lower than that of the corresponding FCSC specimen but is higher than that of the corresponding FCHC specimen. However, the effect of many parameters which may affect the behavior of FCHCs and DSTCs were not clarified by these limited test results.

Fam and Rizkalla (2001a) and Becque et al. (2003) presented their attempts to model FCHCs and FRP-concrete DSTCs. These models were shown to provide reasonable predictions of the limited test results and are summarized below.

Fam and Rizkalla (2001a) adopted the same procedure as that for FRP-confined circular concrete cylinders (see Subsection 2.2.3.3) to develop the stress-strain curve of FRP-confined concrete in an annular section. Fam and Rizkalla (2001a) proposed the following equation for steps (1) and (2) of this procedure, based on the linear elasticity theory:

$$\sigma_l = \frac{(R_o - R_i)v_c}{\frac{R_o^2}{E_{frp}t_{frp}} + \frac{R_o \left( \frac{R_o^2 + R_i^2}{R_o^2 - R_i^2} - v_c \right)}{E_c}} \varepsilon_c \quad (2.27)$$

where  $R_o$  and  $R_i$  are the outer radius and the inner radius of the annular section respectively, and  $v_c$  is the Poisson's ratio of concrete. Fam and Rizkalla (2001a) related the Poisson's ratio of confined concrete to the axial strain and the confining pressure based on test results of actively-confined and unconfined concrete presented in Gardner (1969).

Fam and Rizkalla (2001a) adopted the  $\sigma_l$  value found through Eqn 2.27 for a given axial strain, and subsequently found the axial stress of the annular section based on Mander et al.'s (1988) active confinement model. By doing so, it was implicitly assumed that the confining stress and consequently the axial stress are uniform over the annular section. This is not consistent even with the results from the linear elasticity theory adopted to produce Eqn 2.27, as is shown later in Chapter 3. In addition, the equation for  $\nu_c$  in this paper is based on the test results of actively-confined concrete, and its validity for FRP-confined concrete has not been appropriately justified. In Chapter 3, it is shown that Fam and Rizkalla's (2001a) analysis-oriented model does not provide reasonable predictions of the results of FCHC specimens tested in the present research.

Becque et al.'s (2003) analysis-oriented model employs Gerstle's (1981a, b) octahedral stress-strain model with some modifications for FRP-confined concrete in a circular or an annular section. For FCHCs, it was assumed that the concrete stress remains constant when the axial strain exceeds the value of 0.004. This is not consistent with the test results from the present study as shown in Chapter 3. In addition, Becque et al. (2003) neglected the effect of the coupling modulus, which accounts for the experimental observation that the deviatoric stress causes a decrease in volume. This may cause considerable errors when the hydrostatic pressure is large. Furthermore, it is necessary to always assume a stress increment at the first step for a given confining pressure when developing the stress-strain curve through the octahedral model. By doing so, the descending branch of concrete stress-strain curves cannot be predicted. Becque et al.'s (2003) model also implicitly assumes a uniform axial stress over the annular section, which is

thus incapable of accounting for the variation of stresses over the section and does not reflect the true behavior. In Chapter 3, it is shown that Becque et al.'s (2003) analysis-oriented model does not provide reasonable predictions of the results of the FCHC specimens tested in the present research.

### **2.2.5 Beam-Column Behavior**

The beam-column behavior of concrete-filled FRP tubes (CFFTs) has also been extensively investigated (e.g. Flisak et al. 2001; Parvin and Wang 2001; Davol et al. 2001; Fam and Rizkalla 2002; Fam et al. 2003; Mirmiran et al. 1999). The experimental work presented in these papers includes pure bending tests (e.g. Fam and Rizkalla 2002), eccentric compression tests (e.g. Flisak et al. 2001; Parvin and Wang 2001; Fam et al. 2003) and tests of CFFTs under a constant axial load and a monotonically increased lateral load (e.g. Mirmiran et al. 1999).

While some researchers directly adopted the stress-strain curve of FRP-confined concrete obtained from axial compression tests for the modeling of beam (and beam-column) specimens (e.g. Davol et al. 2001), other researchers (e.g. Fam and Rizkalla 2002; Fam et al. 2003; Mirmiran et al. 1999) found from their experiments that the confining effectiveness is lower in beam (and beam-column) specimens than in column specimens. Consequently, they recommended to adopt different stress-strain curves for the confined concrete in column and beam (and beam-column) specimens.

Fam et al. (2003) suggested that the stress-strain curve of unconfined concrete should be adopted for the concrete in the compression zone when a CFFT specimen is under pure flexure. When a CFFT specimen is under axial compression, the stress-strain model proposed by Fam and Rizkalla (2001a) was suggested for use. When a CFFT specimen is under eccentric compression, a so-called variable confinement model was recommended (Eqns 2.28-2.30) which produces stress-strain curves lying between that for column specimens and that of unconfined concrete which was proposed for use in modeling beam specimens (Figure 2.5). The proposed variable confinement model for the concrete in beam-column specimens is represented by Eqn 2.28, which is similar to Eqn 2.23.

$$\frac{\sigma_c}{f'_{co}} = \frac{\left(\frac{\varepsilon_c}{\varepsilon_{co}}\right)(C_1 C_2)}{(C_1 C_2) - 1 + \left(\frac{\varepsilon_c}{\varepsilon_{co}}\right)^{C_1 C_2}} \quad (2.28)$$

with the ultimate stress  $\bar{f}_{cc}$  and strain  $\bar{\varepsilon}_{cc}$  being defined as follows:

$$\bar{f}_{cc} = (f'_{cc} - f'_{cuo}) \frac{D_o}{D_o + e} + f'_{cuo} \quad (2.29)$$

$$\bar{\varepsilon}_{cc} = (\varepsilon_{cuo} - \varepsilon_{cu}) \sqrt{1 - \left(\frac{\bar{f}_{cc} - f'_{cuo}}{f'_{cc} - f'_{cuo}}\right)^2} + \varepsilon_{cu} \quad (2.30)$$

where  $C_1 = E_c / (E_c - E_{sec o})$ ;  $E_{sec o}$  is the secant modulus of unconfined concrete and can be estimated by  $f'_{co} / \varepsilon_{co}$ .  $\varepsilon_{cuo}$  is the ultimate strain of unconfined concrete for beam specimens which is assumed to be equal to the ultimate compressive strain of the FRP tube;  $f'_{cuo}$  is the stress corresponding to  $\varepsilon_{cuo}$ ;  $f'_{cc}$  and  $\varepsilon_{cu}$  are the ultimate concrete stress and strain for column specimens;  $D_o$  and  $e$  are the outer diameter of the CFFT specimens and the loading eccentricity;  $C_2$  can be calculated when  $\bar{f}_{cc}$  and  $\bar{\varepsilon}_{cc}$  are found.

Mirmiran et al. (1999) noticed that the effect of confinement increased with the level of axial load and suggested that the strain hardening of concrete, i.e. the slope of the linear second portion of the stress-strain curve of confined concrete  $E_{2c}$ , is a function of the axial load level. An upper bound of  $E_{2c}$  was set to be equal to that of the confined concrete in a CFFT column specimen and a lower bound of  $E_{2c}$  was set to be equal to zero. Rochette and Labossiere (1996) also proposed a lower bound of 0 for  $E_{2c}$ . A similar approach was suggested by Ziara et al. (1995) for conventional RC beams with considerable transverse reinforcement.

## **2.3 DOUBLE-SKIN TUBULAR COLUMNS**

### **2.3.1 Introduction**

Extensive research has been carried out on double-skin tubular columns (DSTCs), both on steel-concrete DSTCs (e.g. Zhao et al. 2002; Zhao and Grzebieta 2002; Elchalakani et al 2002; Wei et al. 1995a, b; Han et al. 1994; Tao et al. 2002) and FRP-concrete DSTCs (e.g. Fam and Rizkalla 2001b; Becque et al. 2003; Fam and Rizkalla 2002). While some of the research was concerned with the beam-column behavior (e.g. Tao et al. 2002) or the flexural behavior of DSTCs (e.g. Fam and Rizkalla 2002), most of the research was focused on the concentric compressive behavior (e.g. Zhao et al. 2002; Zhao and Grzebieta 2002; Elchalakani et al 2002; Wei et al. 1995a, b; Han et al. 1994; Fam and Rizkalla 2001b; Becque et al. 2003). Cross sections with two concentrically placed circular tubes and with concrete filled between were investigated in most of existing studies (e.g. Wei et al. 1995a,

b; Han et al. 1994; Zhao et al. 2002; Fam and Rizkalla 2001b; Becque et al. 2003; Fam and Rizkalla 2002), although other sections have also been studied to a more limited extent (e.g. Tao et al. 2002; Elchalakani et al. 2002; Zhao and Grzebieta 2002). Both experimental and theoretical research have been conducted.

### **2.3.2 Experimental Behavior**

While some theoretical models were proposed for the prediction of DSTCs, most existing research has been experimental. The ultimate load of DSTCs and the buckling behavior of steel tubes (for steel-concrete DSTCs only) have been the two aspects of greatest concern in existing research.

The conclusions drawn by different researchers on the load capacity of DSTCs are controversial. For steel-concrete DSTCs, Zhao et al (2002) suggested that the ultimate load of the hybrid member could be estimated by the sum of the section capacities of the unconfined concrete, the outer steel tube and the inner steel tube. However, Wei et al. (1995a, b) found from their experiments that the sum of the load capacity of each component could be increased by 10-30% in a DSTC. For FRP-concrete DSTCs, Fam and Rizkalla (2001b) found that the existence of an inner tube significantly increased the concrete strength.

In most existing studies on steel-concrete DSTCs, steel tubes with a relatively small  $D_s/t_s$  value (e.g.  $D_s/t_s = 17-33$  for the inner tube in Zhao et al. 2002) were adopted. Therefore, the “elephant foot” buckling mode was the most often observed mode of buckling failure when such tubes were tested under

compression. In this case, buckling normally took place after yielding. The axial deformation at the occurrence of buckling depends significantly on the  $D_s/t_s$  value. Buckling occurs earlier in steel tubes with a relatively large  $D_s/t_s$  value. For the steel inner tube of a steel-concrete DSTC, it was reported that buckling was delayed or prevented because of the restraint of concrete (e.g. Wei et al 1995a, b) and that the buckling mode changed from the “elephant foot” mode to a “distorted diamond” mode. Consequently, the axial deformation capacity of the steel tube was enlarged.

### **2.3.3 Theoretical Modeling**

Various theoretical models were proposed for the prediction of the behavior of concrete in steel-concrete DSTCs (e.g. Wei et al 1995b; Han et al. 1994) or that in FRP-concrete DSTCs (e.g. Becque et al. 2003).

Wei et al. (1995a) based their model on a previously proposed model for steel-confined solid concrete cylinders. It was assumed that there is no interaction between the concrete and the steel inner tube. This assumption may be suitable for steel-concrete DSTCs, as the dilation of steel-confined concrete becomes divergent after the yielding of the steel tube, and the outward expansion of the concrete thus becomes larger than that of the inner steel tube. However, for concrete confined with a strong FRP jacket, the ratio of the lateral strain to the axial strain may be less than 0.5 and interaction may exist between the concrete and the inner steel tube. Actually, such interaction was found in the tests of Fam and Rizkalla (2001b) on FRP-concrete DSTCs. In addition, Wei et al. (1995a)

made the assumption that the stresses, including the axial and the lateral stresses, are uniform over the section. This assumption is also undesirable as it has no theoretical basis and cannot account for the stress variation over the section. Therefore, although Wei et al.'s (1995a) model provided good predictions of his limited test results on steel-concrete DSTCs, its wide validity for such DSTCs is doubtful and it cannot be used for the prediction of other DSTCs (e.g. FRP-concrete DSTCs and hybrid DSTCs investigated in the present research).

Han et al. (1994) based their model on the linear elastic theory. A Poisson's ratio equal to 0.4 was adopted for concrete. However, it has been shown by many researchers (e.g. Teng et al. 2006a) that the Poisson's ratio varies not only with the axial deformation but also with the confining pressure. In addition, Han et al.'s (1994) model suffers from the same problem as Wei et al. (1995a), since it is based on the assumption that no interaction exists between the concrete and the steel inner tube, and a uniform axial stress exists over the section. Becque et al.'s (2003) model also suffers from many problems as discussed in Subsection 2.2.4.

It may be concluded from the above discussions that most existing research on DSTCs has been experimental and has been concerned with the overall structural behavior. The confining mechanism for the concrete in DSTCs has not yet received an in-depth treatment. All existing theoretical models cannot account for stress variations over the annular section. These models are not based on and do not lead to a good understanding of the behavior of concrete in DSTCs.

## **2.4 CONSTITUTIVE MODELS FOR CONCRETE**

### **2.4.1 Introduction**

The finite element (FE) method has frequently been employed to predict the results of experiments for hybrid structural members (e.g. concrete-filled FRP tubes), due to its capability of capturing complex stress variations within the entire member and predicting interactions between components. The success of an FE model depends significantly on the employment of an appropriate constitutive model for each constituent material. Many different concrete constitutive models have been published for the modeling of FRP-confined concrete, including plasticity models (e.g. Karabinis and Kiousis 1994, 1996; Karabinis and Rousakis 2002; Oh 2002; Mirmiran et al. 2000; Lan 1998; Fang 1999; Mahfouz et al. 2001; Shahawy et al. 2000) and plastic-damage models (e.g. Luccioni and Rougier 2005; Huang 2005). Despite the inclusion of damage in some models (e.g. Luccioni and Rougier 2005; Huang 2005), all of these constitutive models involve concrete plasticity. The inclusion of plasticity in the concrete constitutive model is generally based on the experimental observation that concrete can flow like a ductile material under triaxial compression (Chen 1982). In this thesis, a material is defined to be under triaxial compression when it is subjected to equal confining pressures in two lateral directions and axial compression in the loading direction, unless otherwise specified. Most, if not all of the existing concrete plasticity models (e.g. Karabinis and Kiousis 1994, 1996; Karabinis and Rousakis 2002; Oh 2002; Mirmiran et al. 2000; Lan 1998) adopt the flow or incremental theory of plasticity, in which the yield criterion can be modified at every state of plastic deformation (Chen 1982; Oh 2000). Hereafter in this thesis a concrete plasticity

model refers to a concrete model within the theoretical framework of the flow theory of plasticity.

### **2.4.2 Concrete Plasticity**

The key components of a concrete plasticity model include the yield criterion, the hardening rule and the flow rule. The yield criterion is normally defined by a yield function  $F$ , which is a function of the current stress and one or more other parameters. When  $F$  is less than zero, the material is in the elastic range; when  $F$  is equal to zero, yielding and inelastic deformation occur. The yield function can be understood as a surface in the three-dimensional stress space, which is called a yield surface. When strain hardening/softening is included in a yield criterion, it represents a series of surfaces in the stress space, including the initial yield surface and subsequent yield surfaces (i.e. loading surfaces) which evolve with the plastic deformation. The hardening rule is normally defined by a hardening function, which defines the relationship between the subsequent yield surfaces and the magnitude of plastic deformation (or plastic work per unit volume). It is apparent that a hardening function at least includes the magnitude of plastic deformation (or plastic work per unit volume) as one parameter. The flow rule is defined using a so-called potential function, which defines the direction of the plastic deformation. When the potential function is the same as the yield function, the flow rule is called an associated flow rule; otherwise the flow rule is called a non-associated flow rule. While the associated flow rule is often adopted for ductile materials such as metals, the non-associated flow rule is extensively adopted for soil and granular materials (Oh 2000).

Many yield functions have been proposed for concrete. The number of parameters included in these functions ranges from one (e.g. Von Mises criterion) to five (Chen 1982). Except for the von Mises criterion, which is used widely for metal plasticity, most of the yield criteria developed for concrete incorporate a dependence of the shear strength (i.e. the peak value of the second deviatoric stress invariant) on the hydrostatic pressure (i.e. the first stress invariant). This dependence was widely observed in experiments (Chen 1982). Although more advanced functions that fit the experimental evidence better have also been suggested (e.g. William-Wranke criterion with five parameters), the Drucker-Prager (D-P) (Drucker and Prager 1952) criterion with two parameters is widely used for the modeling of confined concrete (e.g. Lan 1998; Karabinis and Kioussis 1994, 1996; Karabinis and Rousakis 2002; Oh 2002; Mirmiran et al. 2000; Fang 1999; Mahfouz et al. 2001; Shahawy et al. 2000), not only because it is simple in form but also because it is sufficiently accurate for concrete under triaxial compression when the hydrostatic pressure is within the practical engineering range. It has, however, been noted by some researchers (e.g. Chen 1982; Lan 1998; Huang 2005) that the shear strength is different for concrete under biaxial compression and that under triaxial compression, even when the hydrostatic pressure for the two cases is the same. The original D-P criterion with two parameters cannot reflect this test observation. In this thesis, a material is defined to be under biaxial compression when it is subjected to equal compression in two principal directions, unless otherwise specified. Karabinis and Kioussis (1996) modified the D-P criterion by including the third deviatoric stress invariant

to reflect this difference in the shear strength, although the accuracy of the parameters they adopted is doubtful (see Chapter 4).

Although some researchers (e.g. Mirmiran et al. 2000; Fang 1999; Shahawy et al. 2000) assumed an elastic-perfectly plastic model for confined concrete, the strain hardening/softening behavior has long been observed in experiments (Chen 1982). While the classical hardening rule with the plastic deformation as the only parameter without involving any hydrostatic (or confining) stresses has been adopted by many researchers (e.g. Mahfouz et al. 2001), it was recently noted (e.g. Lan 1998; Oh 2002; Karabinis and Kiousis 1994; Chen and Lan 2004) that, such a hardening rule cannot lead to reasonable predictions of the ductility of confined concrete. These authors also proposed modified hardening rules in which the confining pressure was taken as another parameter, and announced good predictions of test results.

It was noted by many researchers (e.g. Chen and Lan 2004; Huang 2005; Mirmiran 2000; Oh 2002) that the associated flow rule leads to an overestimation of the expansion of confined concrete. Mirmiran (2000) and Karabinis and Kiousis (1994, 1996) adopted a non-associated flow rule with a constant dilation angle for the modeling of confined concrete. Karabinis and Rousakis (2002) recently related the dilation angle to the plastic deformation, and the dilation angles they adopted imply volume compaction of concrete throughout the deformation process. Oh (2002) related the dilation angles to both the confining pressure and the plastic deformation, based on empirical equations for

actively-confined concrete, but the wide validity of Oh's (2002) model for FRP-confined concrete has yet to be established.

In Chapter 4, the performance of existing D-P type plasticity models for the modeling of confined concrete is assessed numerically, with the focus on the three key components: the yield criterion, the hardening rule and the flow rule.

### **2.4.3 Plastic-Damage Models**

Despite the good performance of concrete plasticity models in modeling concrete under monotonic loadings, it is difficult for such models to represent the stiffness gradation of concrete (Lee and Fenves 1998), which was observed in concrete subjected to cyclic loadings (Karsan and Jirsa 1969; Gopalaratnam and Shah 1985; Maekawa et al. 2003). In addition, the adoption of a plasticity model to simulate the post-peak descending (strain softening) behavior of concrete has long been controversial (Chen 1982). The modeling of strain softening using a plasticity model involves the retraction of yield surface in the stress space and may cause numerical difficulty during the FE analysis. In order to model the stiffness degradation, some researchers (e.g. Mazars 1986; Cervera et al. 1995) adopted continuum damage mechanics in which the stiffness degradation can be modeled by defining the relationship between stresses and effective stresses. However, without plastic strains the continuum damage mechanics theory cannot provide an appropriate dilatancy control, which is very important for simulating concrete structures under multi-axial loading (Lee and Fenves 1998). Therefore, some researchers (e.g. Simo and Ju 1987; Lubliner et al. 1989; Lee and Fenves 1989)

imbedded the continuum damage mechanics concept in a plasticity model, leading to the so-called plastic-damage model.

It is obvious that the only difference between a plastic-damage model and a plasticity model is the inclusion of damage. The description of damage, however, is very complicated, not only because there are many different damage states such as tensile cracking and compressive failure, but also because of the recovery of degraded stiffness during a cyclic loading process, which is a consequence of the closing of previously open cracks (Reinhardt 1984; Lee and Fenves 1998). Nevertheless, the definition of damage could be relatively simple for some special cases, such as concrete under monotonic compression in which tensile damage and stiffness recovery are not of concern. Lee and Fenves (1998) proposed a plastic-damage model using the concepts of scalar damaged elasticity. For the simple case of concrete under monotonic compression, the parameters of a plastic-damage model such as Lee and Fenves's (1998) model can be easily calibrated using a compressive stress-strain curve with a known unloading stiffness.

#### **2.4.4 Constitutive Models in ABAQUS**

In general, an FE model built within a commercially available software package, such as ABAQUS, is often easily accessible, well maintained and possibly extendable (Chen and Lan 2004). On the other hand, as commercially software packages are programmed for general purposes, they may not necessarily have all the capabilities required to accurately model the application of interest.

The Extended Drucker-Prager (D-P) Model provided in ABAQUS is a D-P type plasticity model. It adopts a modified D-P yield criterion which includes the third deviatoric stress invariant. However, this model includes a limit for the shear strength ratio of the material under biaxial compression to that for triaxial compression, which seems not appropriate for normal concrete (see Chapter 4). This model also allows the user definition of strain hardening/softening and the adoption of a non-associated flow rule. In Chapter 4, the assessment of existing D-P type models and the verification of proposed modifications using this model as a tool are presented.

The Concrete Damaged Plasticity Model (CDPM) in ABAQUS is a plastic-damage model. It uses concepts of isotropic damaged elasticity in combination with isotropic tensile and compressive plasticity to represent the inelastic behavior of concrete. The yield criterion proposed in Lee and Fenves (1998) is adopted in this model, which reduces to the D-P yield condition for the special case of concrete under triaxial compression. The third deviatoric stress invariant is also included in the yield criterion, with a larger range of allowed shear strength ratio which covers the normal experimental values of concrete (see Chapter 4). The degradation of elastic stiffness can be captured by this model using a scalar damage variable which varies with the plastic deformation. This model also allows the definition of strain hardening/softening and the adoption of a non-associated flow rule. In Chapter 5, the use of this model, with suitable modifications, for the modeling of the hybrid DSTCs is examined.

ABAQUS allows the inclusion of modifications to its constitutive models, within their general theoretical frameworks. Modifications can be implemented using the Solution-Dependent Field Variable (SDFV) option with a user subroutine, as noted by Lan (1998). In Chapters 4 and 5, modifications to the two models mentioned above using this option are presented.

## **2.5 CONCLUDING REMARKS**

This chapter has provided a review of existing research relevant to the new hybrid DSTCs. A summary of theoretical models for predicting the behavior of FRP-confined concrete, either in solid circular sections or in annular sections, has been presented. It is clear that the existing knowledge provides an important basis for understanding the behavior of hybrid DSTCs. It is also clear the behavior of confined concrete in annular sections is not yet well understood, although test results of FRP-confined concrete in circular solid cylinders can now be closely predicted by some of the existing stress-strain models. The validity of existing three-dimensional concrete constitutive models for FRP-confined concrete is either doubtful or has not been well established. For the new hybrid DSTCs to be widely accepted in practice, it is therefore imperative to carry out rigorous experimental investigations into their behavior, and to develop suitable modeling techniques and design methods.

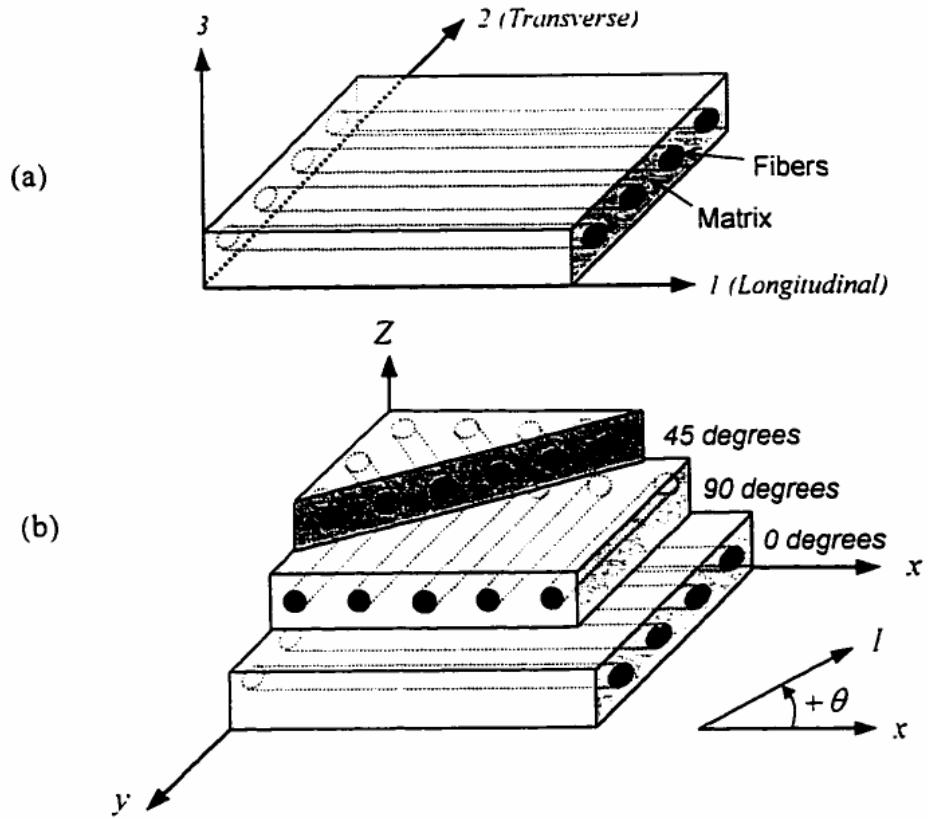


Figure 2.1 (a) Unidirectional lamina and (b) multidirectional laminate (Fam 2000)

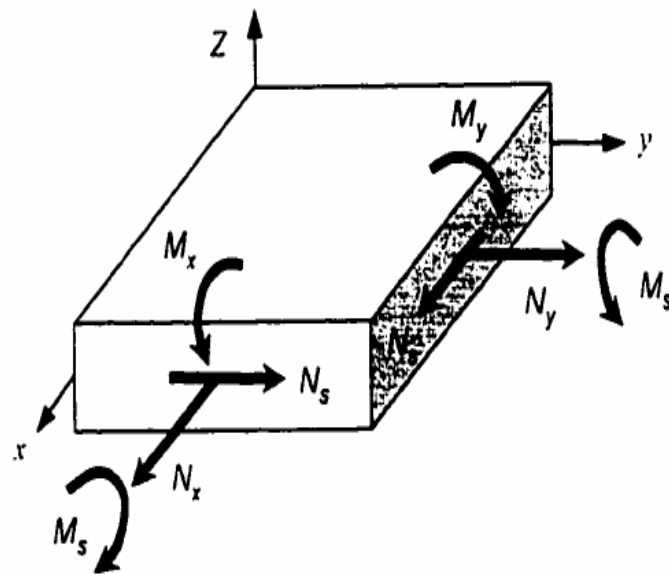
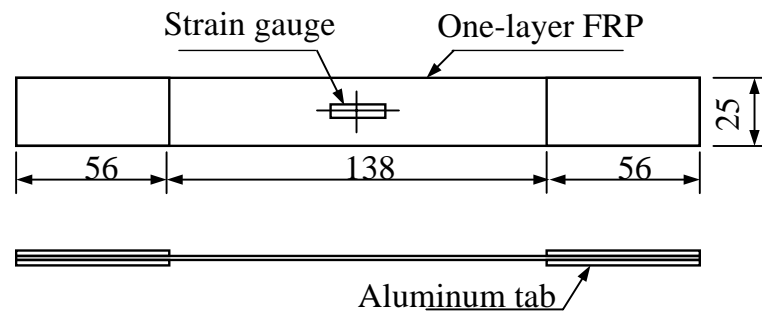
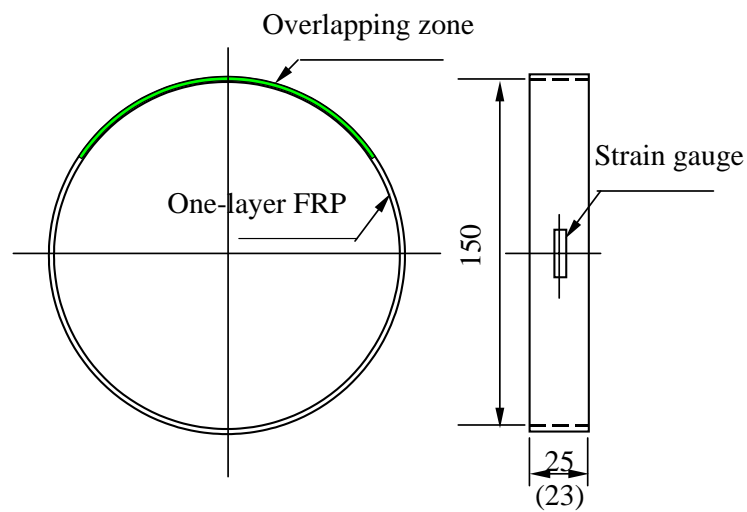


Figure 2.2 Stress resultants acting on a general shell element (Fam 2000)



(a) Test sample following ASTM D3039/D3039M-00



(b) Test sample following ASTM D2290-00

Figure 2.3 Typical test samples of FRP laminates (after Lam and Teng 2004)

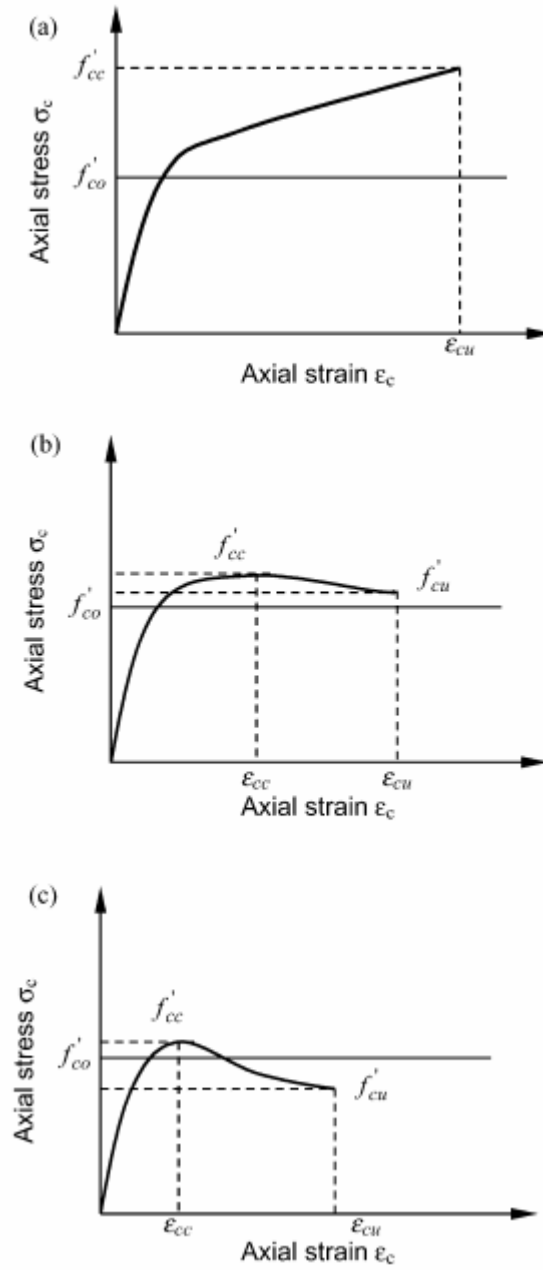


Figure 2.4 Classification of stress-strain curves of FRP-confined concrete

(a) Increasing type; (b) Decreasing type with  $f'_{cu} > f'_{co}$

(c) Decreasing type with  $f'_{cu} < f'_{co}$

(Lam and Teng 2003a)

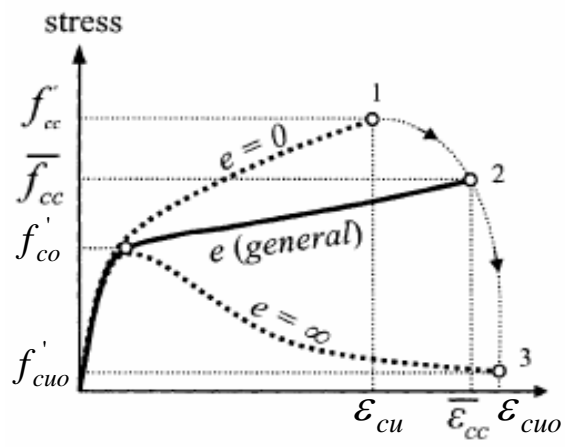


Figure 2.5 Variable confinement model (Fam et al. 2003)

# **CHAPTER 3**

## **COMPRESSIVE BEHAVIOR OF HYBRID DSTC COLUMNS**

### **3.1 INTRODUCTION**

As explained in Chapter 1, the advantages of the new hybrid DSTCs are most obvious when used as a column, for which the compressive behavior is the main behavioral aspect to be understood. This chapter presents a systematic study on the compressive behavior of these hybrid members. In addition, compressive tests on specimens of other similar section forms were also conducted for comparison, in order to reach a better understanding of the structural behavior and confining mechanism of this new type of members. These other columns forms include FRP-confined solid cylinders (FCSC) which consists of a circular solid concrete section confined by an outer FRP tube, and FRP-confined hollow cylinders (FCHC) which consists of an annular concrete section confined by an outer FRP tube (Figure 1.6).

### **3.2 SPECIMEN DETAILS**

In total, 43 specimens were prepared and tested, including 18 DSTC specimens, 11 FCSC specimens and 14 FCHC specimens. The specimens all had an outer

diameter of 152.5 mm and a height of 305 mm. Other details of the specimens are summarized in Table 3.1. The specimens were cast in seven batches (“1-7”) with the same concrete mix ratio except batch 4. In batch 4, a smaller water-to-cement ratio was adopted in order to produce a higher concrete grade. The resulting concrete strengths varied within the narrow range of 36.5 MPa to 40.1 MPa except for batch 4 which had a concrete strength of 46.7 MPa.

Batches 1 and 2 were designed mainly to investigate the behavior of DSTC specimens and the effect of a different outer FRP tube and a different inner steel tube. Batch 1 included three pairs of DSTC specimens with the only variable being the thickness of outer FRP tube, and three pairs of corresponding FCSC specimens for comparison. Each pair were nominally identical, and the three pairs of either DSTCs or FCSCs covered three different FRP tube thicknesses, being composed of one ply, two plies and three plies of FRP respectively. Batch 2 included three pairs of DSTCs only. Again, each pair of specimens was nominally identical, and the three pairs of DSTCs had one-ply, two -ply and three-ply FRP tubes respectively. The void ratio  $\phi$  (ratio between the inner diameter and the outer diameter of the annular concrete section) of the DSTCs in batch 1 is 0.5 which is similar to that of the DSTCs in batch 2 which is 0.58. The only major difference between the DSTCs of these two batches lies in the steel tubes used. The steel tubes in batch 1 had a diameter-to-thickness ratio of 23 while this ratio was 42 for batch 2. A comparison of the test results of DSTCs of batch 1 with those from batch 2 can be expected to show the effect of a thicker steel inner tube.

Batches 3, 4 and 5 were designed to clarify the difference in behavior between FCSC, DSTC and FCHC specimens and the effect of the void ratio. Each batch consisted of two nominally identical DSTC specimens, two nominally identical FCHC specimens and one FCSC specimen, with the DSTC and FCHC specimens having the same void ratio. The void sizes of the three batches of specimens (see Table 3.1) were chosen so that their void ratios cover a considerable range (approximately equal to 1/4, 1/2 and 3/4 respectively). Despite the different void ratios, the  $D_s/t_s$  ratios of the steel inner tubes were similar for these three batches (see Table 3.1). In batch 4, a higher concrete grade was designed in order to avoid repetitions of specimens in batch 1 and to investigate the effect of concrete strength, although the difference in the concrete strength between the two batches turned out to be much smaller than intended.

Batches 6 and 7 were designed to investigate the behavior of FCHC specimens, including the effect of void ratio and the effect of FRP tube thickness. Each batch included two nominally identical two-ply and two nominally identical three-ply FCHC specimens. The main difference between these two batches of specimens is the different void sizes. The void ratios of these two batches of specimens were designed to be equal to 0.58 and 0.75 respectively, for easy comparisons with specimens of batches 2 and 3. In addition, one two-ply and one three-ply FCSC specimens were included in batch 7 for comparison purposes.

Each specimen is given a name, which starts with a letter (“D”, “S” or “H”) to represent the type of specimen (see Table 3.1), followed by a two-digit number to represent the concrete strength, and then a letter (from “A” to “D”) to represent

the void ratio (0.28, 0.50, 0.58 and 0.75) for DSTC and FCHC specimens only (see Table 3.1) together with a number which defines the number of plies in the FRP tube. The last Roman number is used to differentiate the two nominally identical specimens of a pair. For example, specimen D40-B1-II is the second DSTC specimen of a pair that had a one-ply FRP tube, a void ratio of 0.50, and a concrete cylinder compressive strength of 40 MPa.

### 3.3 MATERIAL PROPERTIES

Tensile tests on six FRP coupons were conducted following the ASTM standard (ASTM D3039 2000). The test results showed that the FRP used in the study had an average tensile strength of 1825.5 MPa and an average elastic modulus of 80.1 GPa, based on a nominal thickness of 0.17 mm per ply.

Three plain concrete cylinders (152.5 mm x 305 mm) were tested for each batch to determine the concrete cylinder compressive strength. The average concrete strengths obtained from these concrete cylinder tests are given in Table 3.1, while other concrete properties are given in Table 3.2. In these tables,  $E_c$ ,  $f'_{co}$  and  $\epsilon_{co}$  denote the elastic modulus, the peak stress (i.e. the cylinder compressive strength) and the axial strain at peak stress respectively. For batch 7, the unconfined concrete properties for specimens H33-C2-I and H33-C3-I are different from those for specimens H37-C2-I and H37-C3-I because these two sets of FCHCs were tested on 29 days and 47 days of age respectively, and their unconfined concrete properties were obtained on the day of testing the FCHCs by having the

3 plain concrete cylinders and 2 plain hollow cylinders shared by the two sets of FCHC specimens (see footnote in Table 3.2).

In each of batches “3” to “7”, two plain hollow concrete cylinders (outer dimensions of 152.5 mm x 305 mm) with the same inner void size as that of the FCHC specimens in the same batch were tested to clarify whether and how the inner void affected the compressive strength of concrete. The concrete strength so determined is denoted by  $f'_{ch}$  in Table 3.2. The results in Table 3.2 show that the inner void had little or very limited effect on the concrete strength, and this effect appears to increase with the concrete strength.

Tensile tests on three steel coupons were conducted for each type of steel tubes. The coupons were cut from a steel tube along the longitudinal direction and were tested following the BS 18 (1987) standard. The average values of the elastic modulus  $E_s$ , yield strength  $f_y$ , and ultimate tensile strength  $f_u$  for each type of steel tubes are listed in Table 3.2.

In addition, for each type of steel tubes, three hollow steel tubes cut from the same long steel tube that provided the steel tubes for the DSTCs and for tensile coupons were tested under axial compression. The steel tubes had the same height as those in the DSTC specimens (305 mm). All these steel tubes except the three tubes for batch 5 showed large plastic deformation until local buckling in the elephant’s foot mode took place (Figure 3.1(a)). The steel tubes for batch 5 also showed large plastic deformation but failed by a combination of overall buckling and local buckling (Figure 3.1(b)). This is because these tubes had a larger  $L/D_s$  ratio

compared with the other tubes. The average axial load capacities of all steel tubes ( $P_s$ ) are listed in Table 3.3.

### **3.4 PREPARATION OF SPECIMENS**

The preparation process of the DSTC specimens included the following steps: (1) fabrication of the form, which consisted of a PVC tube outside and a steel tube inside; strain gauges on the steel tube were installed before the casting of concrete (Figure 3.2(a)), for specimens in batches 1 and 2; (2) casting the concrete; (3) wet-layup formation of the FRP tube after the concrete had hardened and the PVC form had been removed (Figure 3.3). A similar preparation process was adopted for the FCSC and FCHC specimens except step (1). For the FCSC specimens, standard 152.5 mm x 305 mm steel moulds were used for casting concrete. For the FCHC specimens, standard steel moulds with an inner insertion were used (Figure 3.2(b)).

It should be noted that the FRP tubes were formed by the wrapping and resin impregnation of fiber sheets on hardened concrete as is done in retrofit applications, instead of the use of prefabricated FRP tubes into which concrete is cast. The wrapping process was used as prefabricated FRP tubes with fibers oriented mainly in the hoop direction were not readily available to the authors. It is believed that there is little difference between the two methods of forming the FRP tube in terms of the performance of the hybrid column, based on previous research by Shahawy et al. (2000).

### **3.5 EXPERIMENTAL SET-UP AND INSTRUMENTATION**

For each specimen, four bi-directional strain rosettes with a gauge length of 20 mm were installed at the mid-height of the FRP tube. For the specimens in batches 1 and 2, two additional bi-directional strain rosettes with a gauge length of 10 mm were attached at the mid-height of the inner steel tube. The circumferential layout of the strain gauges is shown in Figure 3.4, in which the overlapping zone spans a circumferential distance of 150 mm.

In addition, two linear variable displacement transducers (LVDTs) were used to measure the axial deformation of the middle region of 120 mm (Figure 3.5) for each specimen. All compression tests were carried out using an MTS machine with a displacement control rate of 0.003 mm/sec. All test data, including the strains, loads, and displacements, were recorded simultaneously by a data logger.

### **3.6 BEHAVIOR OF HYBRID DSTC SPECIMENS**

#### **3.6.1 Overall Observations**

All DSTC specimens failed by the rupture of the FRP tube under hoop tension. The load kept increasing for the two- and three-ply specimens; for the one-ply specimens, the load remained nearly constant in the second stage of deformation, as shown in Figure 3.6. The axial strains were calculated from the LVDT readings in this figure and elsewhere in this chapter unless otherwise specified. In this chapter, the following sign convention is adopted: compressive loads, stresses and strains are positive while tensile strains are negative. During the loading process,

snapping noises, which were attributed to the micro-cracking of concrete and movements of aggregates, were heard after the unconfined concrete strength was reached. White patches on the FRP outer tube then occurred when the load was close to the ultimate value. With the development of white patches, several large noises were heard and FRP rupture took place. Specimen D40-B2-I after test is shown in Figure 3.7.

### 3.6.2 Axial Load-Axial Strain Behavior

The key test results of all 18 DSTC specimens are summarized in Table 3.3. In this table,  $P_c$  is equal to the ultimate load of the hybrid column from the test,  $P_{co}$  is equal to the unconfined concrete strength times the area of the annular concrete section,  $P_s$  is equal to the average ultimate load of the three hollow steel tubes of a given type, and  $(P_{co}+P_s)$  represents the ultimate load of the DSTC if the constituent parts do not interact and the confinement effect of the FRP tube is ignored. The ultimate experimental strain, which is the strain at the rupture of the FRP tube, is denoted by  $\varepsilon_{cu}$  and listed in Table 3.4. The strain of unconfined concrete at peak stress  $\varepsilon_{co}$  found from tests on three 152.5 mm x 305 mm concrete cylinders is also used to normalize the measured ultimate strain in Table 3.4. Table 3.3 shows that the provision of a two- or three-ply FRP tube significantly enhanced the load-carrying capacity of hybrid DSTCs (by up to 62%), but a one-ply FRP tube did not affect the load-carrying capacity. All 18 specimens achieved much larger ultimate strains than the strain at peak stress of the unconfined concrete, with the largest value of the former being 10.58 times the latter. It can be concluded that when all other parameters are the same, a

thicker FRP tube leads to greater increases in the ultimate load and the ductility of DSTCs.

Typical axial load-axial strain curves of the DSTC specimens are shown in Figure 3.6. For the three specimens of batch 2, the axial load-axial strain curves of the steel tube and the annular concrete section and their sum are also shown in Figure 3.6(b) for comparison. The direct contribution of the FRP tube to the axial load capacity is not included in this sum as it had no longitudinal fibers.

Figure 3.6 shows that the two-ply DSTC and three-ply DSTC had a bilinear load-strain curve while the one-ply DSTC had an almost elastic-perfectly plastic load-strain curve. Similar curves can be obtained from FCSC specimens with appropriate levels of confinement (Lam and Teng 2003a). It is also obvious that the DSTCs reached ultimate loads and ultimate strains which are significantly higher than may be expected from the simple addition of those of the axial load-strain curves of steel and concrete, even for DSTC specimens with a one-ply FRP tube. It can also be found from Figure 3.6 that although the two-ply DSTC specimens had void ratios ranging from 0.28 to 0.75, they all showed a bilinear monotonically ascending load-strain curve.

### **3.6.3 Buckling Behavior of Steel Tubes**

#### *3.6.3.1 Hollow steel tubes*

Figure 3.8 shows a typical axial load-deformation curve for the hollow steel tubes in batch 1 specimens under axial compression; those for the hollow steel tubes in

other batches are similar. It is clear from Figure 3.8 that local buckling, after which the load began to drop, occurred after the yielding of steel. Figure 3.9 shows a comparison between the axial strains obtained from strain gauges at the mid-height section and those calculated from the platen-to-platen displacements which represent the axial shortenings of the steel tube. It can be seen from Figure 3.9 that a linear relationship between the two strain values is observed initially, but when the axial strain exceeds about 0.016, the difference between these two strain values begins to increase, indicating the development of local buckling deformation outside the mid-height section. When the axial strain reaches about 0.019, which corresponds to the occurrence of buckling, the axial strain measured by strain gauges begins to reduce slowly while the axial strain from platen-to-platen shortenings keeps increasing.

#### *3.6.3.2 Steel tube inside hybrid DSTCs*

Due to the existence of the external concrete in the DSTCs, the inner steel tube was prevented from buckling outwards. As a result, its likeliness to buckle was reduced. The buckling behavior of the steel tubes inside the DSTC specimens of batches 1 and 2 is discussed below. The steel tubes inside the DSTCs of batches 3 to 5 were designed to be so thick that no local buckling was found after test.

For the DSTC specimens of batch 1, local buckling of the steel tube ( $D_s/t_s = 76/3.3$ ) did not occur in those with a one- or a two-ply FRP tube. For the two-ply DSTCs, when failure occurred by the tensile rupture of FRP, the axial compressive strain reached about 0.022, which is significantly higher than the value of about 0.019 at the buckling of the hollow steel tubes. This observation indicates that the external

concrete at least delayed the occurrence of local buckling of the steel tubes in these DTSC specimens. In the DSTC specimens with a three-ply FRP tube, local buckling of the steel tube did occur but the buckling mode was different. The corresponding hollow steel tubes tested under compression failed in the “elephant foot” mode (Figure 3.1(a)), which is the commonly reported buckling mode for steel tubes with relatively small diameter-to-thickness ratios. However, small inward ripples developed on the steel tubes of the three-ply DSTC specimens (Figure 3.10(b)). In order to clarify when steel tube buckling took place in the three-ply specimens, the axial strain values obtained from the strain gauges on the steel tube are compared with those calculated from the platen-to-platen deformations for specimen D40-B3-I in Figure 3.11. Figure 3.11 shows that a linear relationship is maintained between the two strain values until an axial strain of about 0.025, after which the axial strain value found from the strain gauges begins to increase faster than that calculated from the platen-to-platen shortenings, indicating the development of significant local deformations. Therefore, it can be concluded that steel tube local buckling took place at an axial strain value not smaller than 0.025, which is much higher than the buckling strain from the hollow steel tube tests. It is also noted that this strain value (0.025) is higher than the ultimate axial strain of the DSTC specimen when rupture of the FRP tube occurred.

The DSTC specimens of batch 2 had steel tubes with a larger  $D_s/t_s$  ratio than those in batch 1, which made local buckling a more likely event. Test observations revealed that local buckling took place in specimens with a two- or three-ply FRP tube but not in specimens with a one-ply FRP tube. It is not surprising that a steel

tube in a DSTC with a thicker FRP tube experiences more severe local buckling deformations (Figure 3.12(a)), as in such a DSTC, the steel tube experiences larger axial straining before failure of the specimen and the confining pressure is larger. It should be noted that even in two nominally identical DSTCs, the buckling deformations of the two steel tubes may be significantly different. Figure 3.12(b) contrasts the different deformations of the two steel tubes in two nominally identical three-ply DSTCs (D37-C3-I and D37-C3-II). This difference is due to the sensitivity of these tubes to small imperfections and external disturbances such as the movements of the adjacent concrete. As a result of these different deformations, the two DSTC specimens showed significant difference in the recorded strains. Figure 3.13 shows the axial strain-hoop strain curves of these two specimens, in which the axial and hoop strains were obtained from the strain gauges at the mid-height of the FRP tube. The axial strains were averaged from all four strain gauges, while the hoop strains were averaged from the three gauges outside the overlapping zone. It is seen that as the axial strain increases, the hoop strain of specimen D37-C3-II, in terms of the absolute value, becomes increasingly smaller than that of D37-C3-I. This is because that the hoop strain of the FRP tube in the DSTC varied over the height of the specimen and had the highest values at the locations of buckling deformation of the steel tube. In specimen D37-C3-I, the buckling deformations were located at approximately the mid-height, therefore the hoop strain gauges at the mid-height recorded relatively high values. In specimen D37-C3-II, the buckling deformations were located away from the mid-height of the FRP tube.

### **3.6.4 Interaction between the Concrete and the Steel tube**

The interaction between the concrete and the steel tube in a DSTC can be revealed by a comparison of the axial strain-hoop strain curves of the steel tubes inside the DSTCs and those from the hollow steel tube tests, as any lateral stresses caused by this interaction are expected to cause variations in the axial strain-hoop strain curve. In this subsection, such comparisons are made (Figure 3.14) for the specimens of batch 1. The strain rosettes on the steel tubes inside the DSTC specimens remained functional throughout the loading process for these specimens, so that the entire axial strain-hoop strain curves are available, making such comparisons possible. In Figure 3.14, the strain values were averaged from the readings of these strain rosettes which were attached at the mid-height of the steel tubes.

It is evident from Figure 3.14 that there is little difference between the curves of the steel tubes inside the one- or two-ply DSTC specimens and that of the steel tube under pure axial compression. This suggests that the interaction between the steel tube and the concrete did not exist or is negligible for the one- and two-ply DSTC specimens. For the three-ply specimens, the steel tube inside specimen D40-B3-II had almost the same curve as that under pure compression, while the steel tube inside specimen D40-B3-I showed a slightly lower curve, which suggests that this interaction existed in specimen D40-B3-I but not in specimen D40-B3-II. It may therefore be concluded that the interaction between the concrete and the steel tube in a hybrid DSTC does not exist when the FRP outer tube is relatively weak and may exist when the FRP outer tube is sufficiently strong.

## **3.7 CONCRETE BEHAVIOR**

### **3.7.1 Comparison between FCSCs and FCHCs**

#### *3.7.1.1 General behavior of FCHCs*

In general, the FCHC specimens showed quite different behavior (see Figure 3.16) from the DSTC and FCSC specimens. Specimens with a small void (void ratio = 0.28) exhibited load-strain curves similar to those of the FCSC and DSTC specimens; those specimens with a two-ply FRP tube showed monotonically increasing load-strain behavior until they failed by the rupture of the FRP tube. FCHC specimens with intermediate void ratios of 0.5 and 0.58 showed a descending branch with a slowly decreasing load, until failure occurred by the rupture of the FRP tube, after which the load decreased rapidly. Specimens with a large void (void ratio = 0.75) also had a smooth descending branch after the peak load, but exhibited no clear failure point: no explosive FRP rupture was observed during the test but considerable concrete damage on the inner surface was found at the end of test. Specimens H37-C2-I and H37-D2-II after test are also shown in Figure 3.15.

#### *3.7.1.2 Stress-strain behavior*

The stress-strain curves of FCSCs and FCHCs of different void ratios are compared in Figure 3.17. The axial stress was found by dividing the axial load by the concrete area. The hoop strain was averaged from the three strain gauge readings outside the overlapping zone. The predictions of the two models

proposed by Fam and Rizkalla (2001a) and Becque et al. (2003) respectively are also shown in Figure 3.17 for comparison. All specimens covered by Figure 3.17 had a two-ply FRP tube.

The key test results are also summarized in Table 3.4, in which  $\sigma_{\max}$  is the peak concrete stress, which is equal to the peak load resisted by the concrete divided by the concrete area,  $f'_{cc}$  is the peak concrete stress of a corresponding FCSC specimen with the same amount of FRP and the same unconfined concrete strength, and  $\varepsilon_{cu}$  is the concrete strain at the rupture of the FRP tube. For FCHC specimens with a large inner void (i.e. void ratio = 0.75), as no explosive FRP rupture was observed, the strain at the peak concrete stress is listed instead. This is why the  $\varepsilon_{cu}$  values of FCHC specimens in these two batches are obviously lower than those of the corresponding FCSC specimens.

Figure 3.17(a) shows a comparison between two nominally identical FCHCs with a small void (i.e. void ratio = 0.28) and a corresponding FCSC. The two FCHCs showed very similar behavior. The effect of FRP confinement is obvious for such FCHC specimens, as the compressive strength and ultimate strain of the concrete are substantially higher than those of the unconfined concrete (also see Table 3.4). These FCHC specimens also displayed approximately bilinear stress-strain curves until failure. Their curves, however, are always lower than that of the corresponding FCSC specimen and end at a lower (by about 11%, see Table 3.4) ultimate strength. However, there is no clear difference between the  $\varepsilon_{cu}$  values of these two FCHCs and that of the corresponding FCSC. Figure 3.17(a) also

shows that for these FCHCs, the model of Becque et al. (2003) substantially underestimates the ultimate concrete stress; Fam and Rizkalla's (2001a) model predicts the general trend much better but substantially overestimate the ultimate axial strain.

Figures 3.17(b)-(c) show comparisons between FCSCs and FCHCs with intermediate void ratios of 0.5 and 0.58 respectively. The stress-strain curves of these FCHC specimens have a descending branch before failure by the rupture of the FRP tube. After the peak stress, the FRP hoop strain continues to increase while the concrete stress steadily decreases. Rupture of the FRP tube can be easily identified, as it corresponds to a rapid decrease in stress on the stress-strain curve. While the peak axial stresses of these FCHC specimens are significantly lower (by about 20%, see Table 3.4) than those of the corresponding FCSC specimens, the differences between their ultimate axial strains are much smaller (see Table 3.4). However, the ultimate hoop strains of these FCHC specimens are generally lower (by about 25% or more) than those of corresponding FCSC specimens, which is mainly due to a much more non-uniform deformation state in these FCHC specimens. Figures 3.17(b) and (c) also show that for these FCHCs, Fam and Rizkalla's (2001a) model predicts an incorrect trend. Becque et al.'s (2003) model assumes a constant concrete stress if the axial strain exceeds 0.004, which differs considerably from the test results.

Figures 3.17(d)-(e) show comparisons between FCSCs and FCHCs with a void ratio of 0.75. The peak axial stresses of concrete in these FCHC specimens are significantly lower (by about 20-30%) than those of the corresponding FCSC

specimens (Table 3.4) though higher than the unconfined concrete strength. In addition, these peak stresses of FCHCs occur at a relatively low axial strain (about 1.7 times the peak strain of unconfined concrete), after which the axial stress decreases rapidly. These figures also show that the hoop strain in these FCHC specimens remains almost unchanged at a low value or increases only slowly in the post-peak regime. This explains why explosive FRP rupture was not observed in these FCHC specimens. Figures 3.17(d) and (e) show that for these FCHCs, Fam and Rizkalla's (2001a) model provides reasonable predictions of the general trend but considerably underestimates the ultimate concrete stress. Again, the flat second branch of the curve from Becque et al.'s (2003) model differs greatly from the test results.

It is of interest to note that for each of the two pairs of nominally identical FCHC specimens covered by Figures 3.17(d) and 11(e), the two specimens displayed significantly different stress-strain curves. Inspections of the failed specimens revealed that this was due to the localization of deformation at different heights in these specimens. For instance, specimen H40-D2-I experienced localized deformations outside the 120 mm mid-height region covered by the LVDTs which delivered almost constant axial strains in the descending regime (Figure 3.17(e)). Specimen H40-D2-II however experienced localized deformations near the mid-height, which are thus reflected by the LVDT readings. If axial strains are calculated from platen-to-platen shortenings instead, the axial stress-strain curves of these two specimens are quite similar (Figure 3.18).

It is also worth noting that those FCHC specimens (e.g. specimens H37-D2-I and H37-D2-II in Figure 3.17(d)) with a relatively low unconfined concrete strength (36.5 MPa) displayed stiffer stress-strain curves in the early stage than the corresponding FCSC specimen. This may be due to the higher hoop stresses in these FCHC specimens than in the corresponding FCSC specimen. This phenomenon, however, is not obvious (e.g. specimen H40-D2-II in Figure 3.17(e)) or does not exist (e.g. specimen H40-D2-I in Figure 3.17(e)) when the unconfined concrete strength is higher (40.1 MPa). This could be explained by the fact that the unconfined concrete strength of these FCHC specimens from hollow cylinder tests was slightly lower (by about 5%) than that of the corresponding FCSC specimens from solid cylinder tests (see Table 3.2), which might counteract the beneficial effect of the higher hoop stresses.

The difference in behavior between FCSC specimens and FCHC specimens could be explained by their different stress and deformation states. In FCSC specimens, after the outer FRP tube is activated by the expansion of the concrete core, the concrete is subjected to axial stresses and uniform confinement over the whole section. In FCHC specimens, however, the two lateral confining stresses, the radial stress and the hoop stress, are not equal and both vary in the radial direction.

Based on the classical theory of elasticity, when a hollow concrete cylinder is subjected to an outer pressure  $p_o$  only, the circumferential stress  $\sigma_\theta$  and radial stress  $\sigma_r$  at any point with radius  $r$  can be found from the following equations:

$$\sigma_{\theta} = \frac{p_o R_o^2 (R_i^2 + r^2)}{r^2 (R_o^2 - R_i^2)} \quad (3.1)$$

$$\sigma_r = \frac{p_o R_o^2 (r^2 - R_i^2)}{r^2 (R_o^2 - R_i^2)} \quad (3.2)$$

where  $R_o$  and  $R_i$  are the outer and the inner diameters of the annular section respectively.

According to Eqns 3.1 and 3.2, the hoop stress increases while the radial stress decreases from the outer edge to the inner edge, as shown in Figure 3.19 where the stresses are normalized by the outer pressure  $p_o$ . In particular, the concrete at the inner edge is confined by the hoop stress only, where the radial stress is zero. It can thus be hypothesized that in FCHCs, as the outer pressure provided by the FRP tube increases, the concrete near the inner edge is damaged first and its axial load resistance consequently decreases. If the concrete near the outer edge is able to resist at least the stresses released by the damaged concrete near the inner edge, then the average stress on the section keeps increasing. Otherwise, the peak stress is reached and the stress-strain curve follows a descending branch. In general, this peak stress point occurs earlier in FCHC specimens with a larger inner void as they are subjected to a more non-uniform stress state. This hypothesis explains well the observation that the FCHC specimens with a larger inner void reached their peak stress before the rupture of the FRP tube, while those with a small inner void had a continuously increasing stress-strain curve.

### *3.7.1.3 Axial strain-hoop strain behavior*

It is now well established that the axial strain-hoop strain relationship of confined concrete is the key parameter controlling the effectiveness of FRP confinement and has been investigated by many researchers (e.g. Fam and Rizkalla 2001b; Teng et al. 2006a).

As stated earlier, the concrete in FCHCs is subjected to a non-uniform stress and deformation state. A full understanding of the deformation state requires strain information across the concrete section. Due to technical difficulties, hoop strain gauges were only installed on the FRP tube in the tests. Nevertheless, these strain readings still provide useful insight into the deformation state of FCHC specimens.

The axial strain-hoop strain curves of some of the FCSC specimens and the FCHC specimens are shown in Figure 3.20, where the hoop strains were averaged from the readings of the three strain gauges outside the overlapping zone of the outer FRP tube. All these specimens had very similar unconfined concrete strengths (the differences are less than 1%) and a two-ply FRP tube. Therefore the differences observed in this figure are only due to the different inner void sizes. It is seen that the axial strain-hoop strain curve of the FCHC specimen with the smallest inner void (specimen H37-A2-I) is almost the same as that of the corresponding FCSC specimen, while those of other two FCHC specimens are higher. This observation indicates that for a given axial strain, the outer hoop strain of the annular concrete section, in terms of the absolute value, decreases with the inner void size. This is

easy to understand as in FCHCs, no pressure acts on the inner surface, leading to a reduced outward expansion of the concrete section.

### 3.7.2 Comparison between FCSCs and DSTCs

To evaluate the effectiveness of confinement of the concrete in DSTCs, the behavior of the concrete in the DSTC specimens is compared with that of the corresponding FCSC specimens. The axial stress of the concrete in the DSTCs is defined as the load carried by the annular concrete section divided by its cross-sectional area. The load carried by the concrete section is assumed to be equal to the difference between the load carried by the DSTC specimen and the load carried by the steel tube at the same axial strain; the latter was found from the compression tests on hollow steel tubes. When the axial strain of a DSTC specimen exceeds the buckling strain of the corresponding hollow steel tube tests, it is assumed that the load resisted by the steel inner tube is equal to  $P_s$ , as in a DSTC specimen, the buckling of the steel inner tube is prevented or delayed by the constraint from the concrete, and the decrease in the load carried by the tube may be expected to be limited. The peak concrete stress deduced from this process and the ultimate strain for all DSTC specimens are summarized in Table 3.4.

Figures 3.21(a)-(c) show the comparisons between the stress-strain curves of DSTC and FCSC specimens for different unconfined concrete strengths. For specimens D40-D2-I and II, as the concrete area is relatively small, considerable errors may exist in the deduced axial stresses of concrete when the load taken by the steel tube cannot be accurately evaluated. Therefore, the last part of the

stress-strain curves for specimen D40-D2-I (after the axial buckling strain from the hollow steel tube tests) is not shown. For the same reason, the compressive strengths of confined concrete of these two specimens cannot be deduced.

Figures 3.21(a)-(c) show that in general, for the same unconfined concrete strength, the stress-strain curves of the DSTC specimens are similar to those of the corresponding FCSC specimen. This observation indicates that the inner steel tube in the DSTC specimens provided effective constraint to the inner edge of the annular concrete section. The DSTC specimens shown in Figure 3.21 cover different  $D_s/t_s$  ratios of the inner steel tube (from 18 to 42), different void ratios (from 0.28 to 0.75) and different unconfined concrete strengths (from 36.5 MPa to 46.7 MPa). The variations of these parameters, however, do not significantly affect the effectiveness of confinement of the concrete in the DSTCs.

Some small differences do exist in the stress-strain curve between some of the DSTCs and the corresponding FCSCs. Compared with the corresponding FCSC specimen, the axial stress-strain curve of specimen D37-C2-I with a void ratio of 0.58 has a smaller slope of its second part, which however ends with a larger axial strain (Figure 3.21(a)). Similarly, the curve of specimen D40-D2-I with a void ratio of 0.75 is slightly lower than that of S40-2-I. However, the ultimate axial strain of specimen D40-D2-I is considerably larger than that of the corresponding FCSC specimens (see Table 3.4). For specimens with smaller void ratios (e.g. D37-A2-I and D40-B2-I), such differences from the corresponding FCSC specimens are not seen. Therefore, the void ratio is a significant parameter affecting the behavior of concrete in DSTC specimens.

### **3.7.3 Comparison between DSTCs and FCHCs**

It is evident from Table 3.4 that the concrete in DSTCs has greater compressive strengths and ultimate strains than that in the corresponding FCHCs, regardless of the type of steel tubes in the DSTCs. The stress-strain behavior of concrete in DSTCs is thus superior to that of concrete in FCHCs (Figures 3.17 and 3.21). In FCHCs, the concrete near the inner edge suffers from early loss of resistance as a result of local spalling failure, but in DSTCs, the steel inner tube effectively restrains the inner edge concrete against local spalling failure. As a result, the concrete in DSTCs can resist increasing axial stresses until failure occurs by the rupture of the FRP tube.

As mentioned earlier, the axial strain-hoop strain relationship is the key parameter controlling the effectiveness of FRP confinement of concrete. Figures 3.22(a)-(e) show comparisons between the axial strain-hoop strain curves of FCHC and DSTC specimens. The curves of FCSC specimens are also shown for reference. The axial strains in these figures were averaged from the four axial strain readings at the mid-height, which is believed to reflect more closely the axial deformation at the mid-height in cases when the axial deformation was non-uniform down the height. The curves of any two nominally identical specimens were found to be very similar except specimens D37-C3-I and II, so only one of the two curves is shown for each of the other pairs. The obvious difference in the axial strain-hoop strain curve between specimens D37-C3-I and II is explained earlier.

It is interesting to find that the axial strain-hoop strain curves of DSTC specimens in batch 2, with a void ratio of 0.58, agree well with those of the corresponding FCHC specimens, and the curves of both DSTCs and FCHCs are higher than those of the corresponding FCSC specimens (Figures 3.22(a)-(b)). By contrast, the axial strain-hoop strain curves of all three types of specimens in batch 5, with a void ratio of 0.28, are similar (Figure 3.22(c)), indicating that a small void produces little difference between FCHCs, DSTCs and FCSCs. The curves of DSTCs in batches 3 and 4, with a void ratio of 0.75, are similar to those of FCHCs when the axial strain is less than about 0.005 (Figures 3.22(d)-(e)). However, the curves of FCHCs in these two batches do not follow a bilinear path in the later stage and thus deviate from those of DSTCs. This is due to the occurrence of significant local deformations in the later stage of loading of the FCHC specimens, which were not captured by the four strain rosettes.

It may be concluded from the above discussions that the axial strain-hoop strain relationships of FCHCs and the DSTCs are almost the same before significant local deformations take place in the FCHCs, and that the radial expansion of the outer FRP tube in both DSTCs and FCHCs is less than that in FCSCs for the same axial strain. This observation suggests that the inner steel tube in DSTCs has only a negligible effect on the lateral expansion of the outer concrete surface and that overall, the radial interaction between the steel tube and concrete is insignificant before the concrete starts to spall at the inner edge. It is, however, noted earlier in the chapter that significant differences exist between the stress-strain curves of DSTC and FCHC specimens. Taken all factors into consideration, it may be concluded that the inner steel tube works mainly as an inner support to prevent the

local damage and inward spalling of the concrete near the inner edge. The FCHC specimens were indeed found to fail by local damage and loss of part of concrete near the inner edge (Figures 3.15(b) and (c)).

#### **3.7.4 Effect of Thickness of FRP Tube**

It has been well established that the behavior of FCSC specimens depends on the amount of confining FRP. When all other parameters are the same, a thicker FRP tube leads to greater increases in strength and ductility. For example, specimens S40-3-I and S40-3-II with a three-ply FRP tube are superior to specimens S40-2-I and S40-2-II with a two-ply FRP tube, in both strength and ductility (Table 3.4). The thickness of the FRP tube also significantly affects the stress-strain curve of confined concrete, especially its second portion. The thicker the FRP tube, the stiffer the response of the second stage (Teng et al. 2006a).

For FCHC specimens, especially those with a large void ratio, the effect of the thickness of the FRP tube is not as significant as the effect for FCSC specimens. Comparisons between specimens H37-D2-I, H37-D2-II and H37-D3-I, H37-D3-II (Table 3.4) show that specimens with a two-ply FRP tube have almost the same peak concrete stress and corresponding strain as those with a three-ply FRP tube. Their stress-strain curves also show little differences (Figure 3.23). Two reasons are possible for this phenomenon: 1) the concrete in FCHCs is subjected to non-uniform confinement and the overall effect of confinement is less significant than that in FCSC specimens; 2) the failure of FCHCs with a large void ratio is controlled by the local damage and spalling of concrete near the inner edge

instead of the rupture of the FRP tube. Therefore, the FRP tube is not fully utilized and the use of a thicker FRP tube does not bring obvious benefits. Figure 3.23 shows that in specimens H37-D3-I and H37-D2-II, the hoop strains of the FRP tubes reached only low values (about 0.005 or less) compared with the hoop rupture strain of the FRP tubes (about 0.018).

The thickness of the FRP tube in general has similar effect on DSTCs and FCSCs (Figure 3.24). The three-ply specimen developed the highest curves and achieved the highest concrete strength and the largest ductility. This is easy to understand as the steel inner tube helps to prevent the damage and spalling of concrete and thus all the DSTC specimens in the present study failed by the rupture of the FRP tube.

### **3.8 CONCLUSIONS**

This chapter has presented and interpreted the results of a large number of axial compression tests on hybrid DSTC specimens, and on specimens of other similar section forms, i.e. FCSCs and FCHCs, to examine the behavior of concrete in such FRP-confined annular sections. The main parameters examined include the section configuration, the void ratio, the diameter-to-thickness ratio of the inner steel tube, and the thickness of the FRP tube. Two existing stress-strain models (Fam and Rizkalla 2001a; Becque et al. 2003) were used to predict the stress-strain behavior of FRP-confined concrete in FCHCs. Based on the test results and discussions presented in the chapter, the following conclusions may be drawn:

- (1) The concrete in the new hybrid DSTCs is very effectively confined by the two tubes and local buckling of the inner steel tube is either delayed or suppressed by the surrounding concrete, leading to a very ductile response. The load-axial shortening behavior of concrete in DSTCs is very similar to that of FCSCs.
- (2) DSTCs are superior to FCHCs in both the general behavior and the effectiveness of confinement of concrete. The inner steel tube plays an important role by preventing the concrete near the inner edge from inward spalling.
- (3) The behavior of FCHCs, including their stress-strain curves, deformation properties and failure mechanisms, depends significantly on the void ratio.
- (4) The behavior of concrete in DSTCs is generally similar to that in FCSCs provided the void ratio and the  $D_s/t_s$  ratio of the steel inner tube are within a reasonable range. This range is at least from 0.28 to 0.75 for the void ratio and from 20 to 42 for the  $D_s/t_s$  ratio of the steel tube, as found from the tests.
- (5) The thickness of the outer FRP tube has a significant effect on the behavior of concrete in FCSCs and DSTCs, but a smaller significant effect on the behavior of concrete in FCHCs, especially when the void ratio is large.
- (6) The concrete in FCHCs or DSTCs is subjected to unequal lateral confining stresses in the radial and hoop directions. This produces non-uniform axial stresses over the section and accounts for the difference in behavior between these annular sections and FCSCs.
- (7) The two stress-strain models (Fam and Rizkalla 2001a; Becque et al. 2003) do not provide accurate predictions of the test results of FCHCs. Therefore, new, accurate stress-strain models for concrete in DSTCs and FCHCs need to be developed for use in theoretical models for such columns.

Table 3.1 Details of specimens

Specimen		FRP outer tube thickness	Void size (mm) (void ratio $\phi$ )	Steel tube $D_s(t_s)$ (mm)	Concrete cylinder strength $f'_{co}$ (MPa)	Batch
Type	Number					
D (DSTC)	D37-A2-I, II	2 plies	42(0.28)	42(2.1)	36.7	5
	D40-B1-I, II	1 ply	76(0.50)	76(3.3)	39.6	1
	D40-B2-I, II	2 plies				
	D40-B3-I, II	3 plies				
	D47-B2-I, II	2 plies	76(0.50)	76(3.5)	46.7	4
	D37-C1-I, II	1 ply	88(0.58)	88(2.1)	36.9	2
	D37-C2-I, II	2 plies				
	D37-C3-I, II	3 plies				
D40-D2-I, II	2 plies	115(0.75)	115(5.2)	40.1	3	
S (FCSC)	S40-1-I, II	1 ply	/	/	39.6	1
	S40-2-I, II	2 plies	/	/		
	S40-3-I, II	3 plies	/	/		
	S40-2-III	2 plies	/	/	40.1	3
	S47-2-I	2 plies	/	/	46.7	4
	S37-2-I	2 plies	/	/	36.7	5
	S37-2-II	2 plies	/	/	36.5	6
	S37-3-I	3 plies	/	/	36.5	6
H (FCHC)	H37-A2-I, II	2 plies	42(0.28)	/	36.7	5
	H47-B2-I, II	2 plies	76(0.50)	/	46.7	4
	H33-C2-I	2 plies	88(0.58)	/	33.6	7
	H37-C2-I	2 plies	88(0.58)	/	36.8	7
	H33-C3-I	3 plies	88(0.58)	/	33.6	7
	H37-C3-I	3 plies	88(0.58)	/	36.8	7
	H40-D2-I, II	2 plies	115(0.75)	/	40.1	3
	H37-D2-I, II	2 plies	115(0.75)	/	36.5	6
	H37-D3-I, II	3 plies	115(0.75)	/	36.5	6

Table 3.2 Material properties

Batch	Concrete				Steel		
	Elastic modulus $E_c$ (GPa)	Strain at peak stress $\varepsilon_{co}$	Peak stress from hollow cylinders $f'_{ch}$ (MPa)	$\frac{f'_{ch}}{f'_{co}}$	Elastic modulus $E_s$ (MPa)	Yield stress $f_y$ (MPa)	Ultimate stress $f_u$ (MPa)
1	30.2	0.00263	/	/	207.3	352.7	380.4
2	29.5	0.00262	/	/	208.9	337.8	387.5
3	28.2	0.00259	38.1	95.1%	199.7	353.7	396.3
4	30.7	0.00287	42.4	90.9%	198.7	406.2	475.5
5	27.8	0.00274	36.7	100.3%	201.7	365.2	410.9
6	30.1	0.00256	36.6	100.2%	/	/	/
7*	27.8*	0.00258*	33.1*	98.6%*			
7^	27.9^	0.00289^	/	/	/	/	/

\* For specimens H33-C2-I and H33-C3-I, obtained from one plain solid cylinder and two plain hollow cylinders

^ For specimens H37-C2-I and H37-C3-I, obtained from two plain solid cylinders

Table 3.3 Key test results of DSTC specimens

Specimen	Ultimate load $P_c$ (kN)	Average $P_c$ (kN)	Ultimate load of steel tube $P_s$ (kN)	Ultimate load of concrete section $P_{co}$ (kN)	$\frac{P_c}{(P_{co} + P_s)}$
D37-A2-I	942.1	986.7	113.9	618.7	1.35
D37-A2-II	1031.3				
D40-B1-I	793.8	811.5			0.99
D40-B1-II	829.3				
D40-B2-I	1044.2	1034.5	273.8	543.5	1.27
D40-B2-II	1024.8				
D40-B3-I	1214.0	1208.0			1.48
D40-B3-II	1201.9				
D47-B2-I	1207.0	1165.9	378.3	640.4	1.14
D47-B2-II	1124.7				
D37-C1-I	704.3	692.2			1.10
D37-C1-II	680.2				
D37-C2-I	861.3	843.3	184.7	447.1	1.33
D37-C2-II	825.4				
D37-C3-I	1025.6	1024.2			1.62
D37-C3-II	1022.7				
D40-D2-I	1221.8	1214.6	722.7	315.6	1.17
D40-D2-II	1207.5				

Table 3.4 Peak concrete stresses and ultimate strains of all specimens

Specimen	$\sigma_{\max}$ (MPa)	Average $\sigma_{\max}$ (MPa)	$\frac{\sigma_{\max}}{f'_{co}}$	$\frac{\sigma_{\max}}{f'_{cc}}$	$\epsilon_{cu}$	Average $\epsilon_{cu}$	$\frac{\epsilon_{cu}}{\epsilon_{co}}$
D40-A2-I	54.6	52.1	1.42	0.98	0.0192	0.0175	6.37
D40-A2-II	49.6				0.0157		
D40-B1-I	41.5	40.8	1.03	0.99	0.0148	0.0145	5.53
D40-B1-II	40.1				0.0141		
D40-B2-I	56.3	55.6	1.40	0.99	0.0220	0.0202	7.69
D40-B2-II	55.0				0.0183		
D40-B3-I	68.7	68.2	1.72	1.08	0.0234	0.0235	8.96
D40-B3-II	67.8				0.0237		
D47-B2-I	60.0	57.9	1.24	1.00	0.0223	0.0184	6.41
D47-B2-II	55.7				0.0145		
D37-C1-I	42.9	42.2	1.14	N/A	0.0166	0.0150	5.71
D37-C1-II	41.4				0.0133		
D37-C2-I	55.9	54.4	1.48	1.02	0.0235	0.0212	8.07
D37-C2-II	52.9				0.0188		
D37-C3-I	69.4	69.3	1.88	1.10	0.0241	0.0259	9.89
D37-C3-II	69.2				0.0277		
D40-D2-I	N/A	N/A	N/A	N/A	0.0296	0.0274	10.58
D40-D2-II	N/A				0.0252		
S40-1-I	41.5	41.1	1.04	1.00	0.00825	0.00884	3.36
S40-1-II	40.8				0.00942		
S40-2-I	56.3	56.4	1.42	1.00	0.0183	0.0177	6.74
S40-2-II	56.5				0.0170		
S40-3-I	65.7	63.3	1.60	1.00	0.0256	0.0212	8.05
S40-3-II	61.0				0.0167		
S40-2-III	54.6	54.6	1.36	1.00	0.0213	0.0213	8.22
S47-2-I	58.0	58.0	1.24	1.00	0.0177	0.0177	6.17
S37-2-I	53.1	53.1	1.45	1.00	0.0153	0.0153	5.58
S37-2-II	53.8	53.8	1.48	1.00	0.0154	0.0154	6.02
S37-3-I	63.1	63.1	1.73	1.00	0.0215	0.0215	8.40
H37-A2-I	46.8	47.3	1.29	0.89	0.0171	0.0162	5.89
H37-A2-II	47.8				0.0152		
H47-B2-I	45.8	46.0	0.98	0.79	0.0173	0.0180	6.27
H47-B2-II	46.2				0.0186		
H33-C2-I	44.8	44.8	1.33	/	0.0150	0.0150	5.81
H37-C2-I	42.6	42.6	1.16	0.80	0.0218	0.0218	7.54
H33-C3-I	50.7	50.7	1.52	/	0.0424	0.0424	16.4
H37-C3-I	48.3	48.3	1.31	0.76	0.0253	0.0253	8.73
H37-D2-I	42.6	43.5	1.19	0.81	0.00371*	0.00421	1.65
H37-D2-II	44.4				0.00471*		
H37-D3-I	42.7	44.0	1.21	0.70	0.00325*	0.00413	1.61
H37-D3-II	45.3				0.00500*		
H40-D2-I	39.9	42.3	1.06	0.78	0.00249*	0.00442	1.70
H40-D2-II	44.8				0.00634*		

\* Strain at peak stress, as no explosive FRP rupture occurred in these specimens.

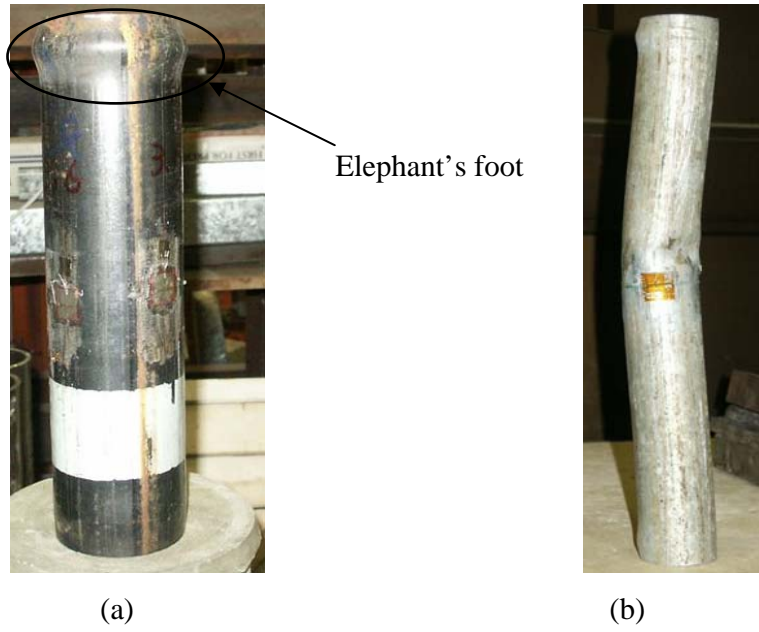


Figure 3.1 Buckling of hollow steel tubes under axial compression

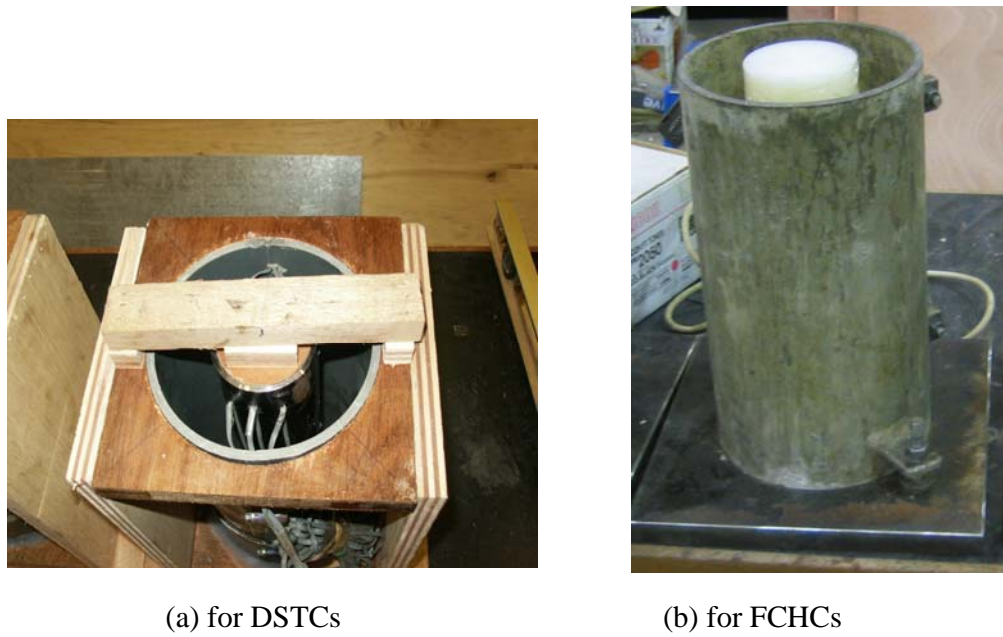


Figure 3.2 Forms for casting concrete



Figure 3.3 Formation of the FRP tube

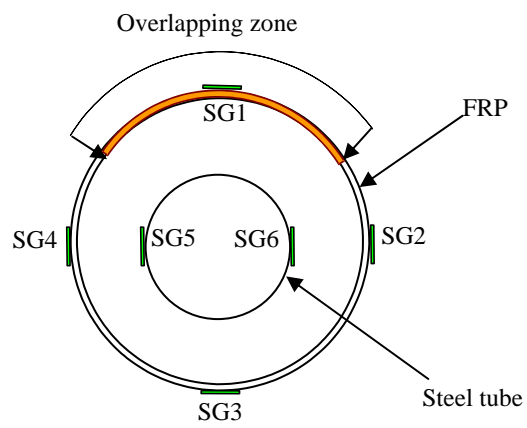
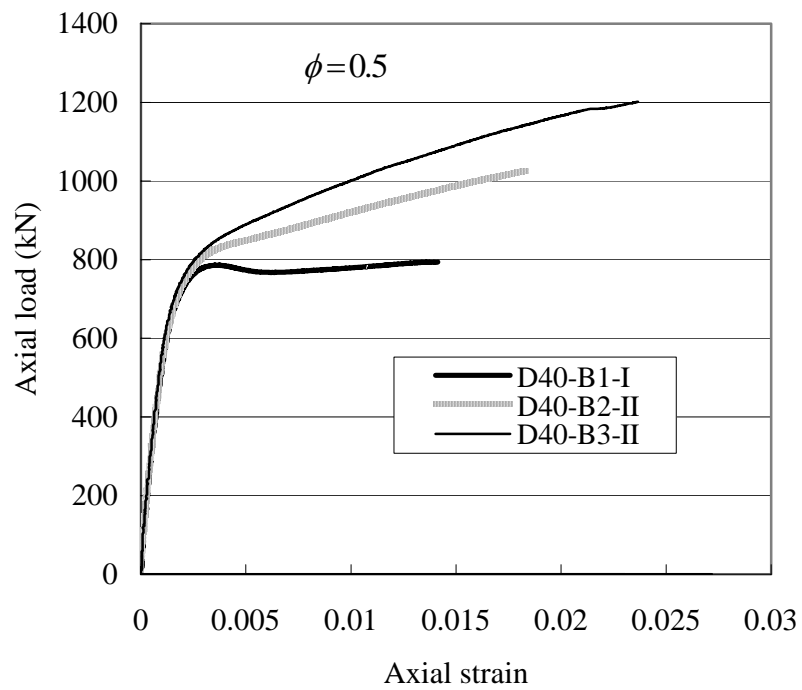


Figure 3.4 Layout of strain gauges

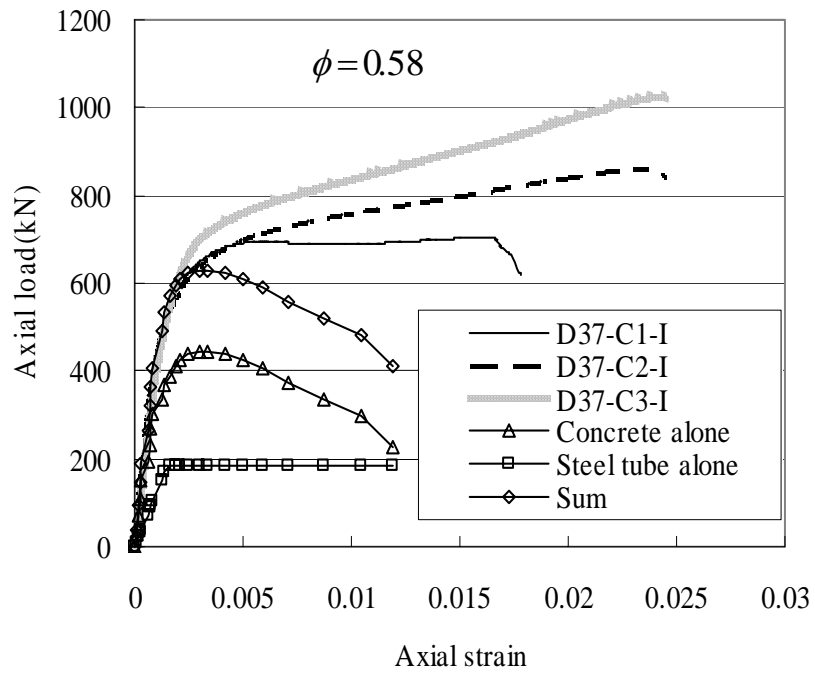


Figure 3.5 Test in progress

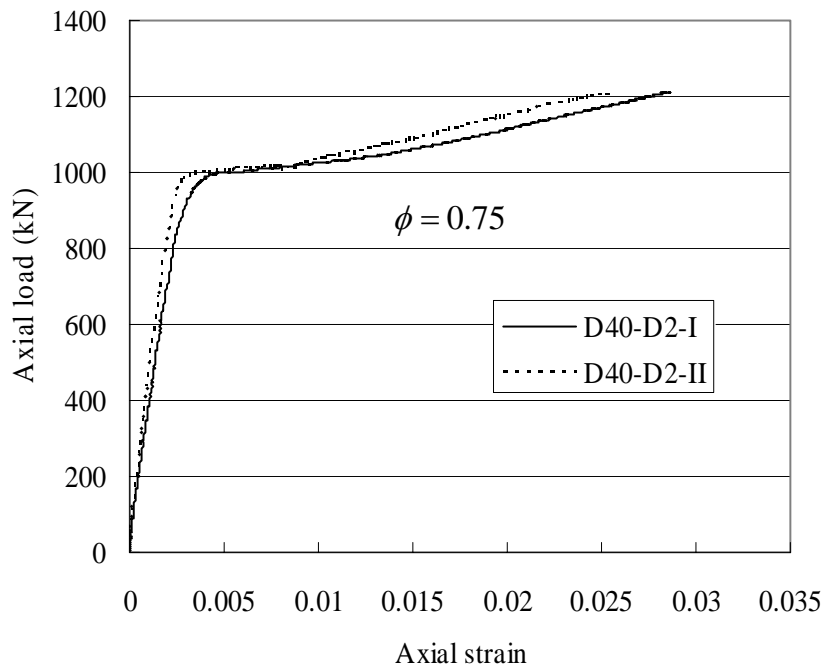


(a) Specimens of batch 1

Figure 3.6 Axial load-strain curves of DSTC specimens

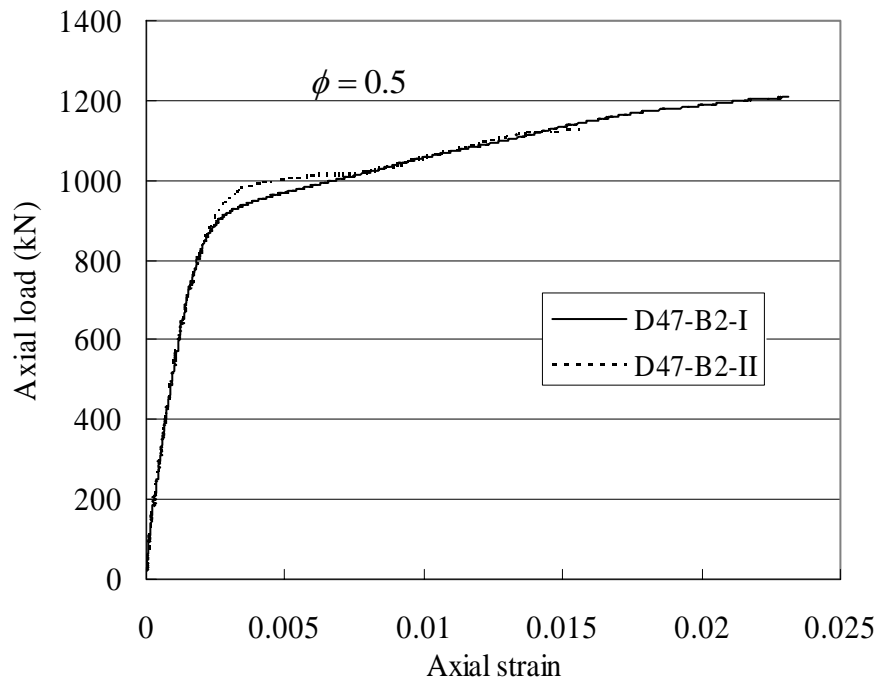


(b) Specimens of batch 2

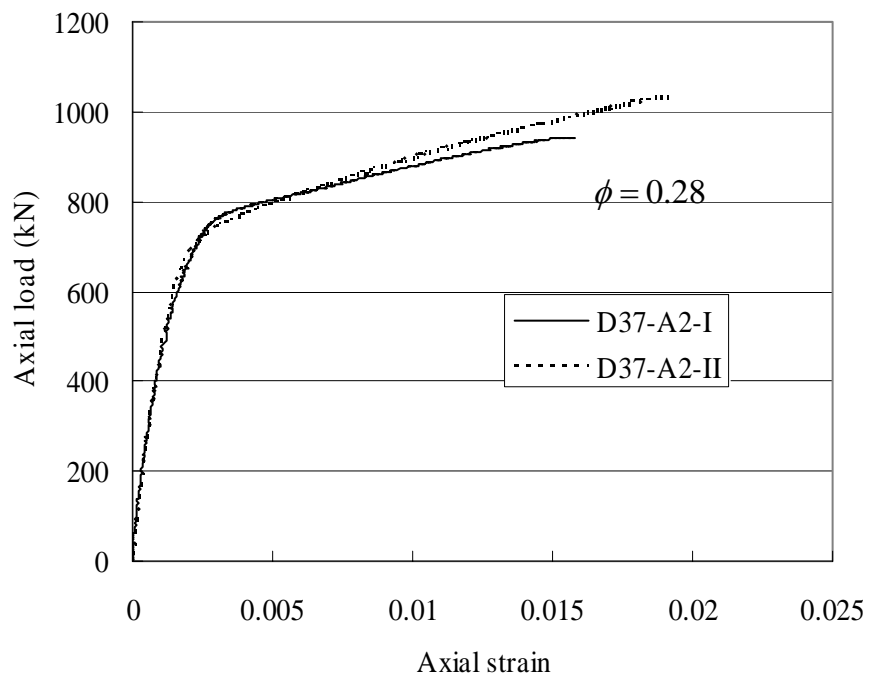


(c) Specimens of batch 3

Figure 3.6 Axial load-strain curves of DSTC specimens (Cont'd)



(d) Specimens of batch 4



(e) Specimens of batch 5

Figure 3.6 Axial load-strain curves of DSTC specimens (Cont'd)



Figure 3.7 DSTC specimen after test

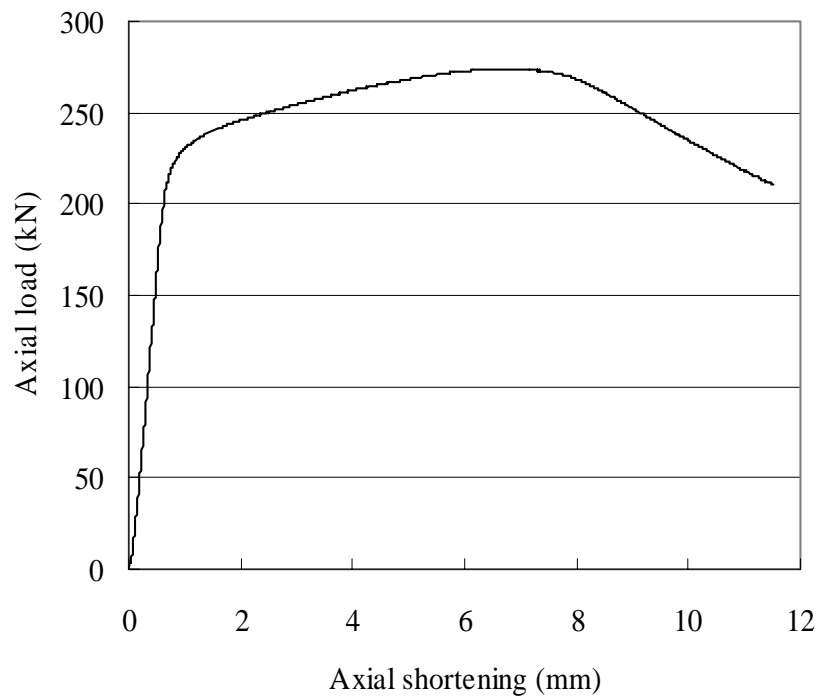


Figure 3.8 Axial load-shortening curve of hollow steel tube under compression

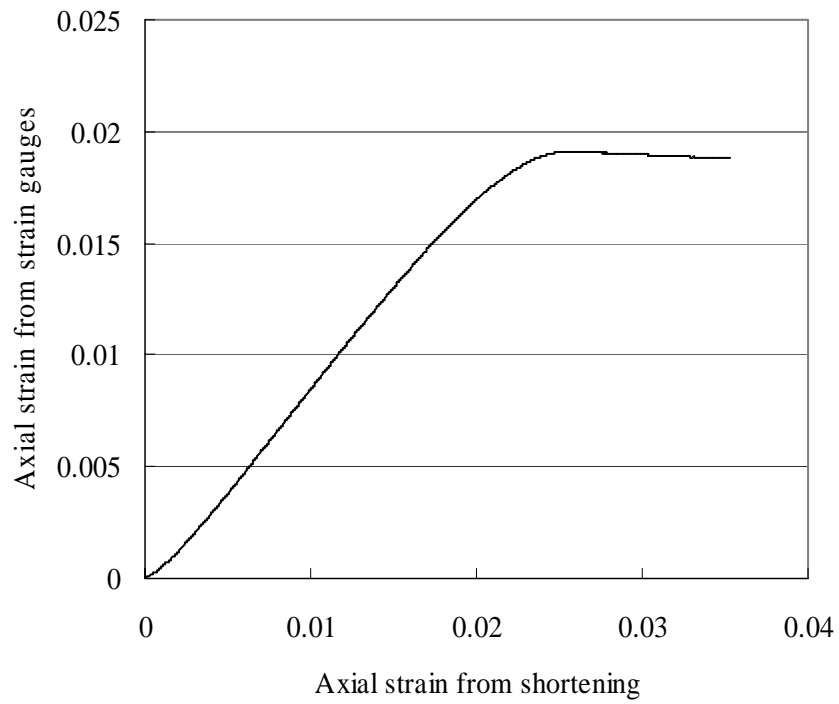


Figure 3.9 Comparison between axial strains from strain gauges and from axial shortenings



(a) Specimen D40-B2-I after test



(b) Specimen D40-B3-I after test

Figure 3.10 Inner steel tubes of batch 1 after test

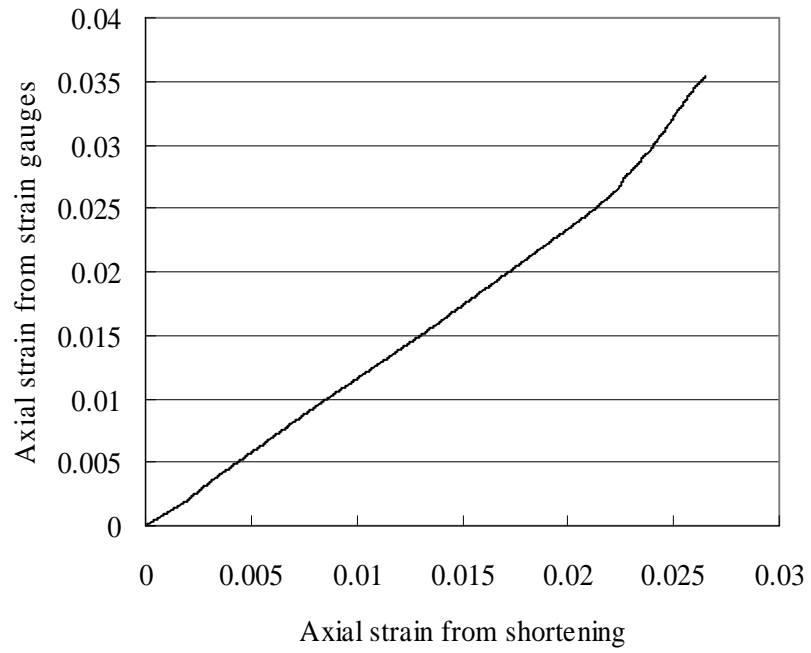
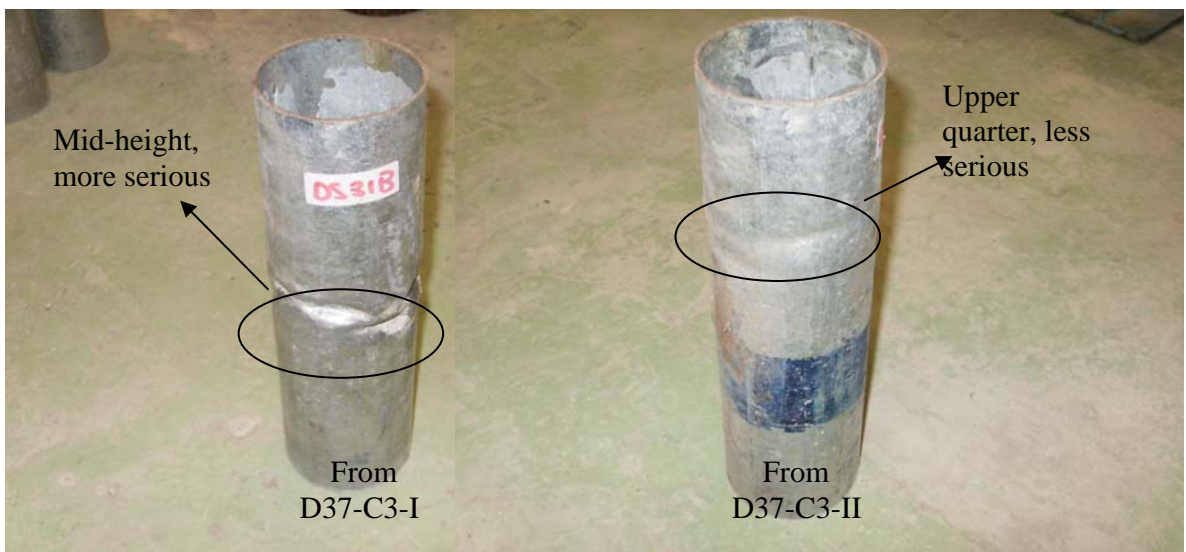


Figure 3.11 Comparison between axial strains from strain gauges and from axial shortenings



(a) Steel tubes from different DSTCs



(b) Steel tubes from two identical three-ply specimens

Figure 3.12 Steel tubes inside DSTC specimens of batch 2 after test

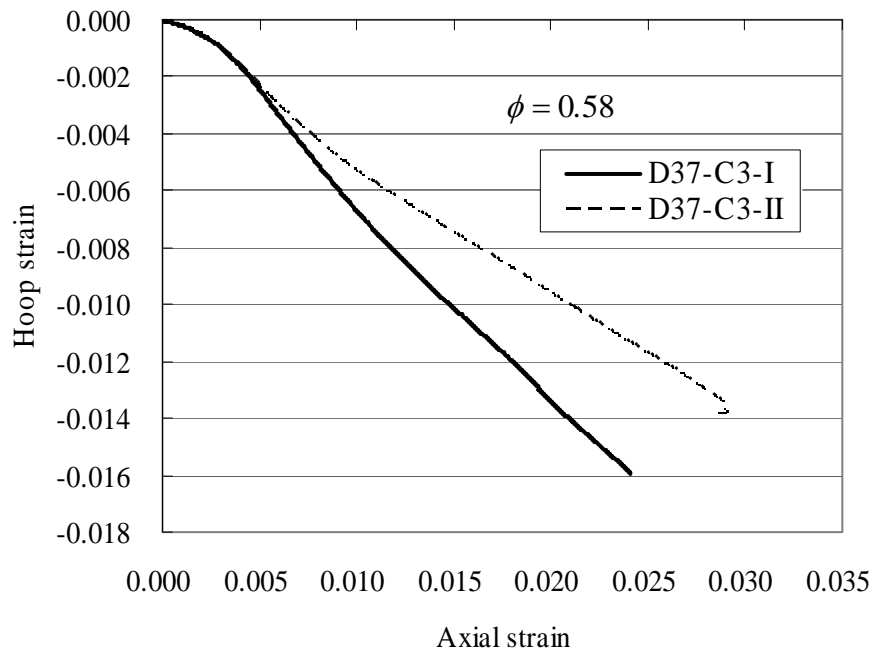
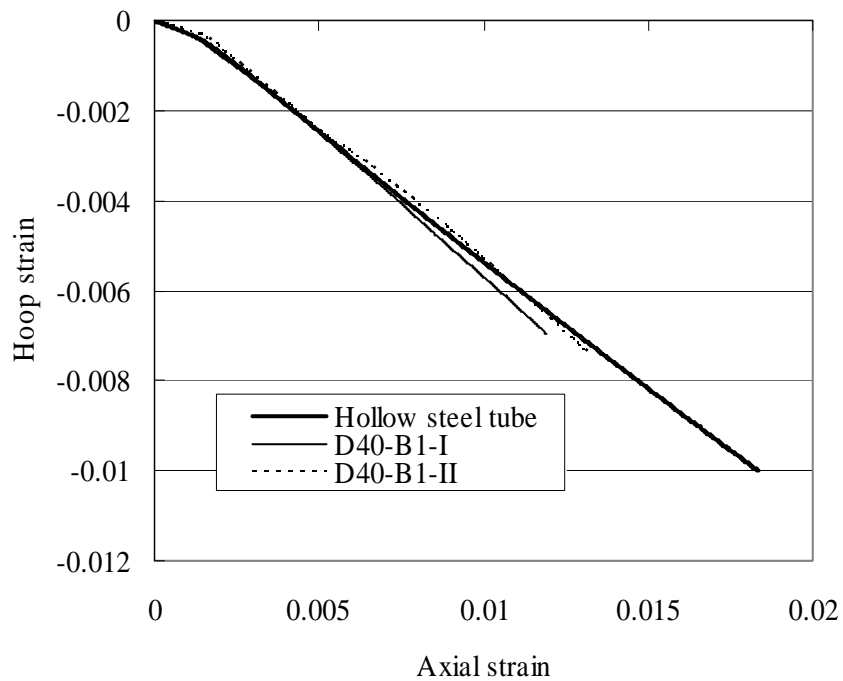
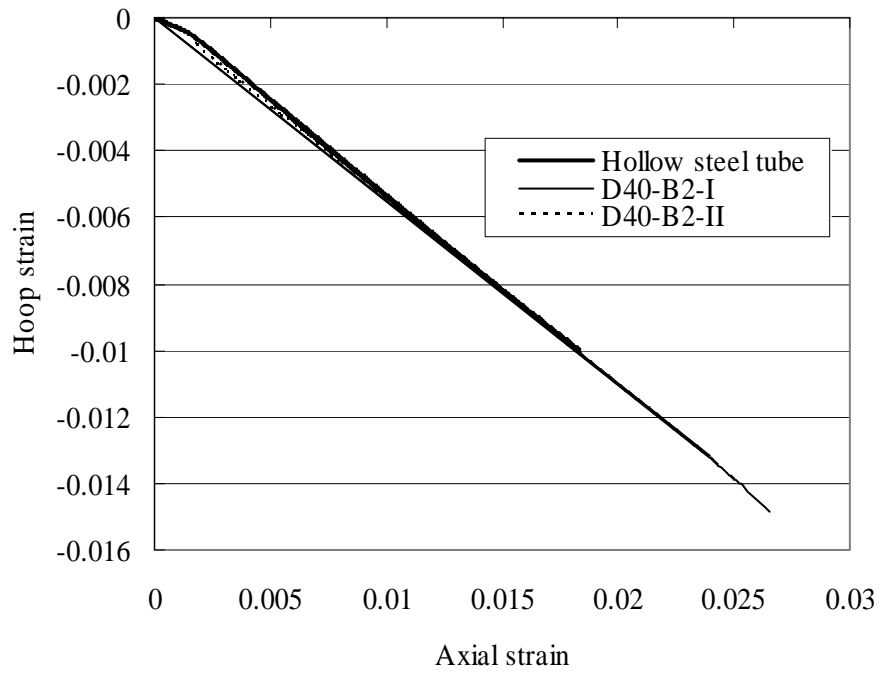


Figure 3.13 Axial strain-hoop strain curves of specimens D37-C3-I and D37-C3-II

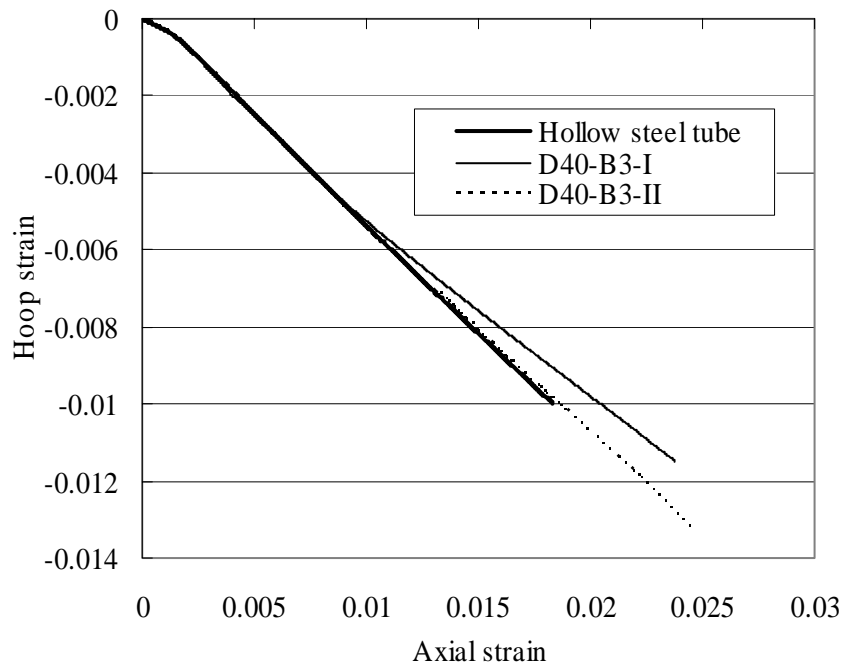


(a) One-ply specimens

Figure 3.14 Hoop strain-axial strain curves of steel tubes



(b) Two-ply specimens



(c) Three-ply specimens

Figure 3.14 Hoop strain-axial strain curves of steel tubes (Cont'd)



(a) Specimen H37-C2-I



(b) Specimen H37-D2-I

Figure 3.15 FCHC specimens after test

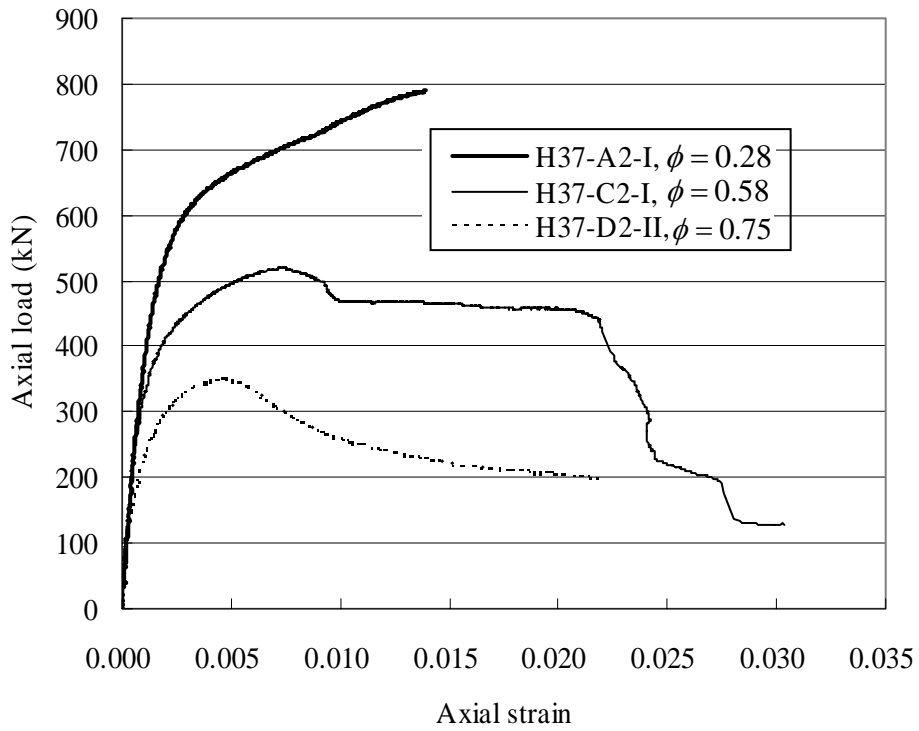
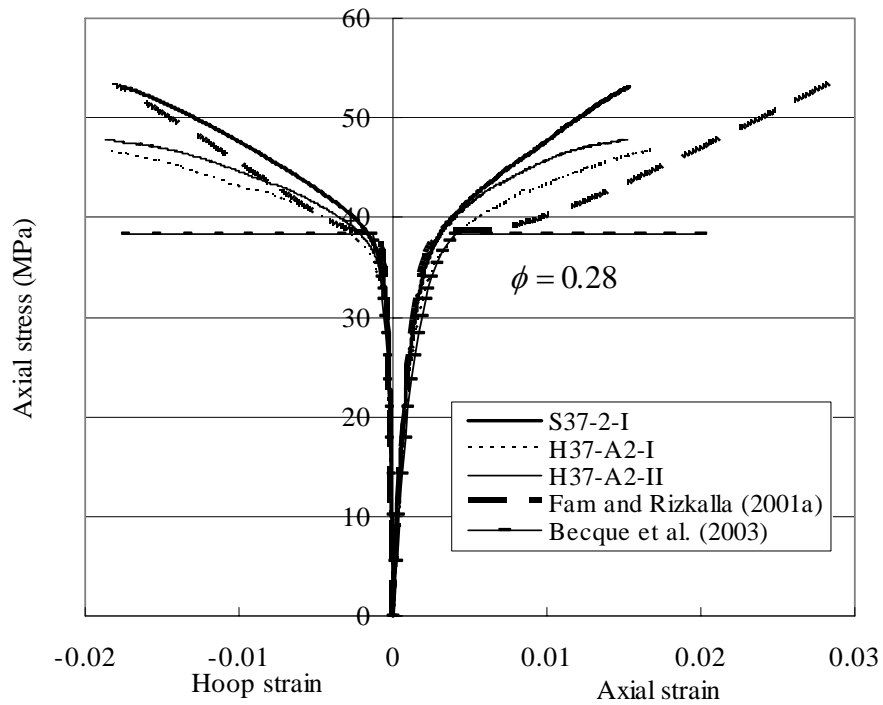


Figure 3.16 Axial load-strain curves of FCHC specimens



(a) Void ratio  $\phi = 0.28$

Figure 3.17 Comparison of stress-strain curves between FCSCs and FCHCs

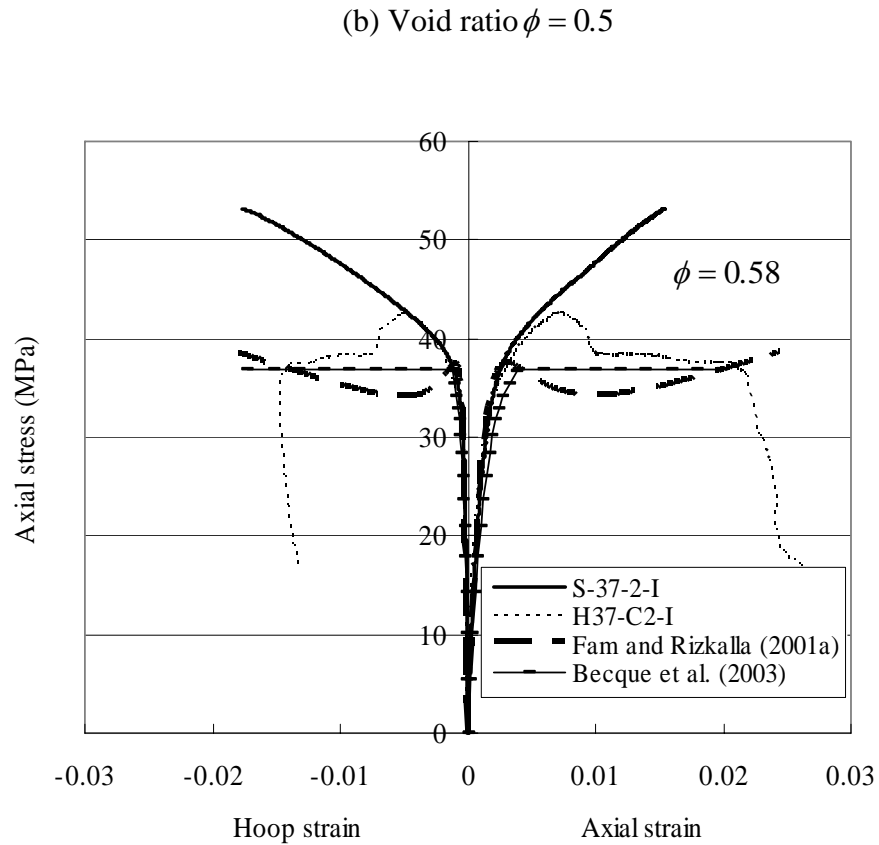
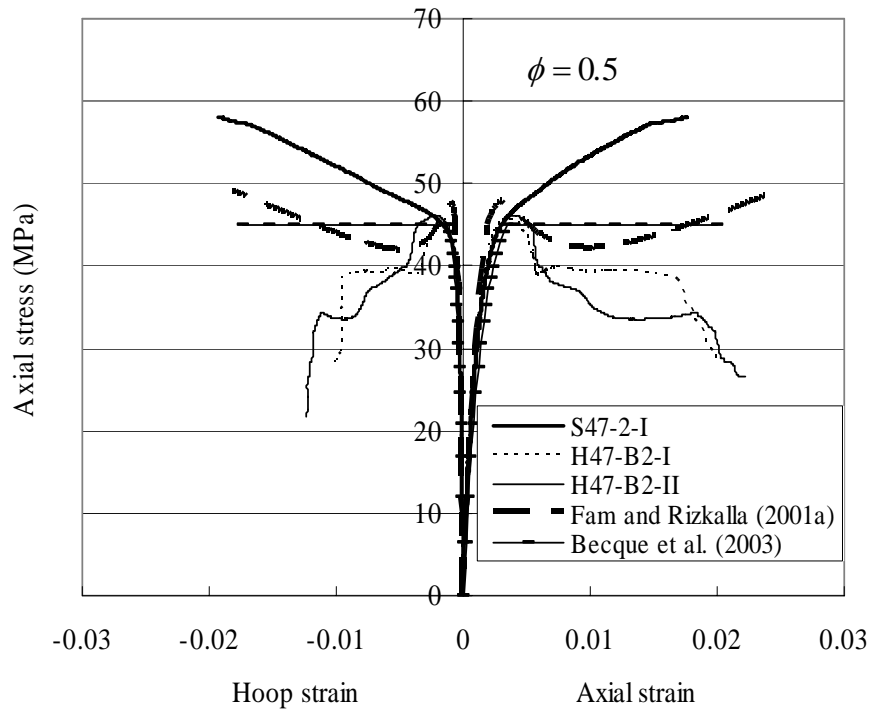
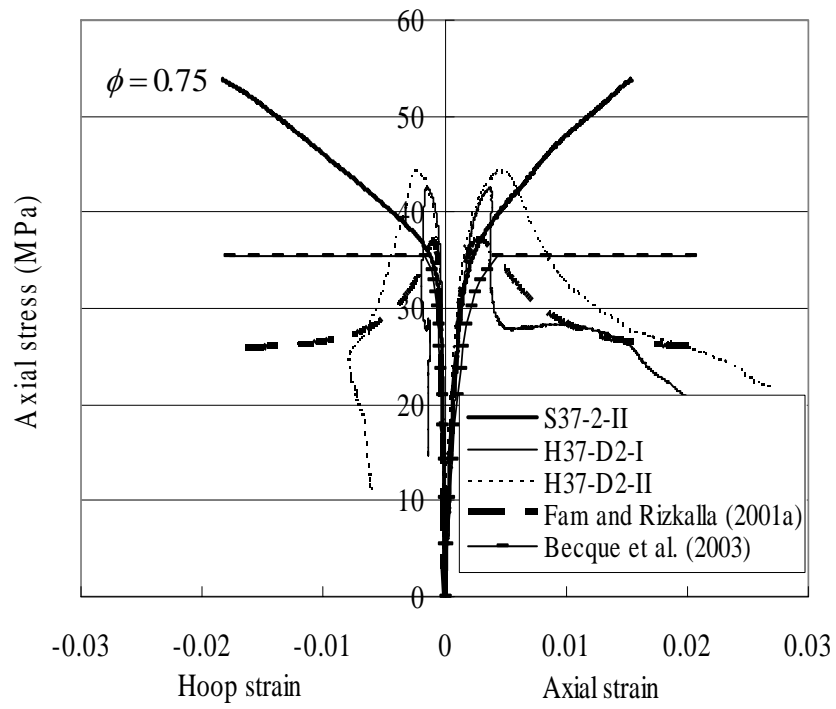
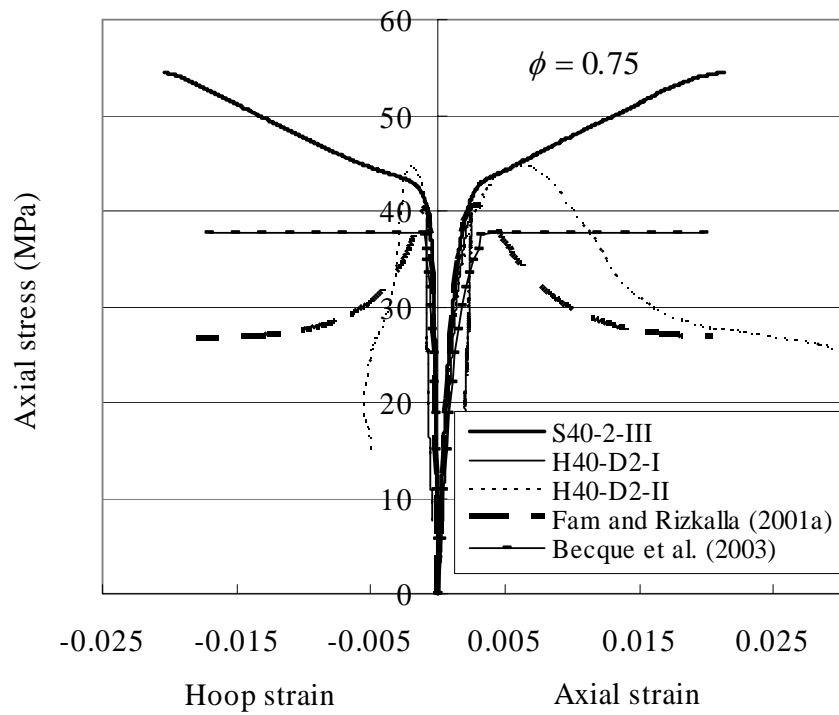


Figure 3.17 Comparison of stress-strain curves between FCSCs and FHCs

(Cont'd)



(d) Void ratio  $\phi = 0.75$ ,  $f'_{co} = 36.5$  MPa



(e) Void ratio  $\phi = 0.75$ ,  $f'_{co} = 40.1$  MPa

Figure 3.17 Comparison of stress-strain curves between FCSCs and FCHCs (Cont'd)

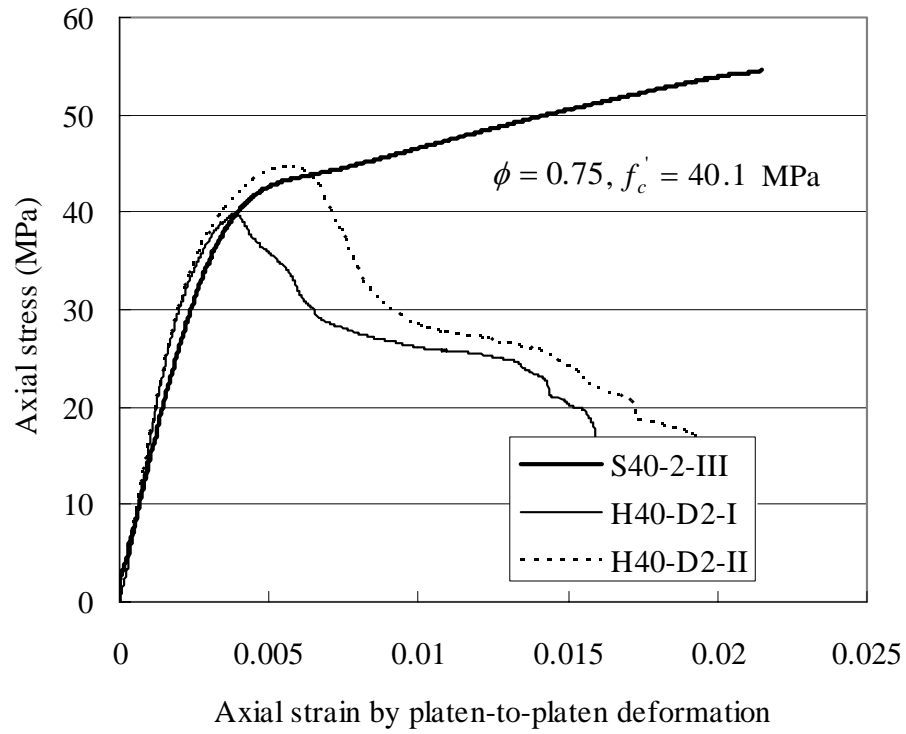


Figure 3.18 Axial stress-strain curves based on platen-to-platen deformations

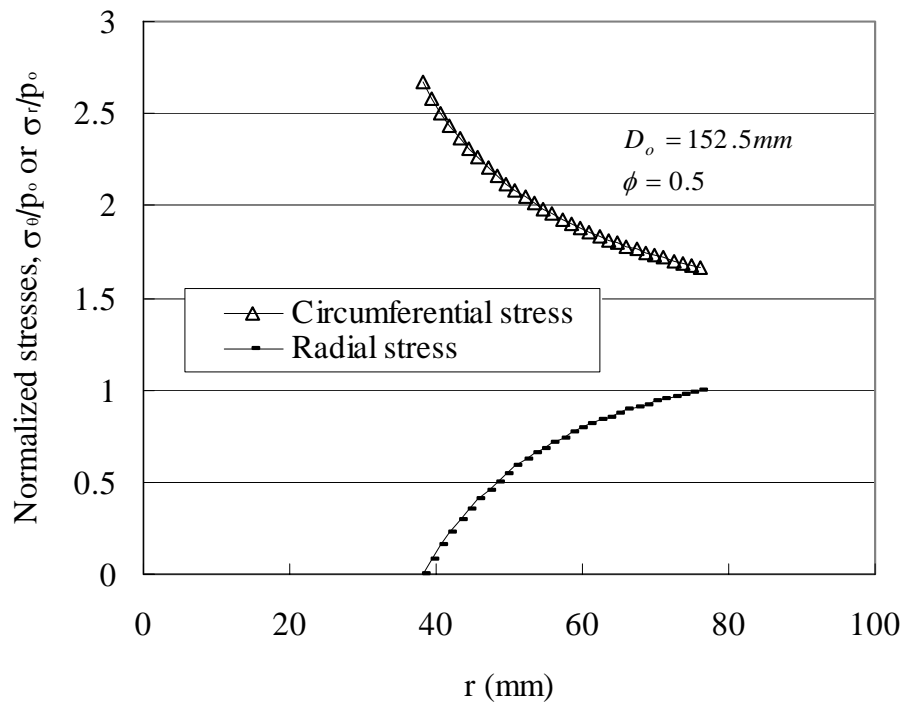


Figure 3.19 Theoretical stress variations in the radial direction

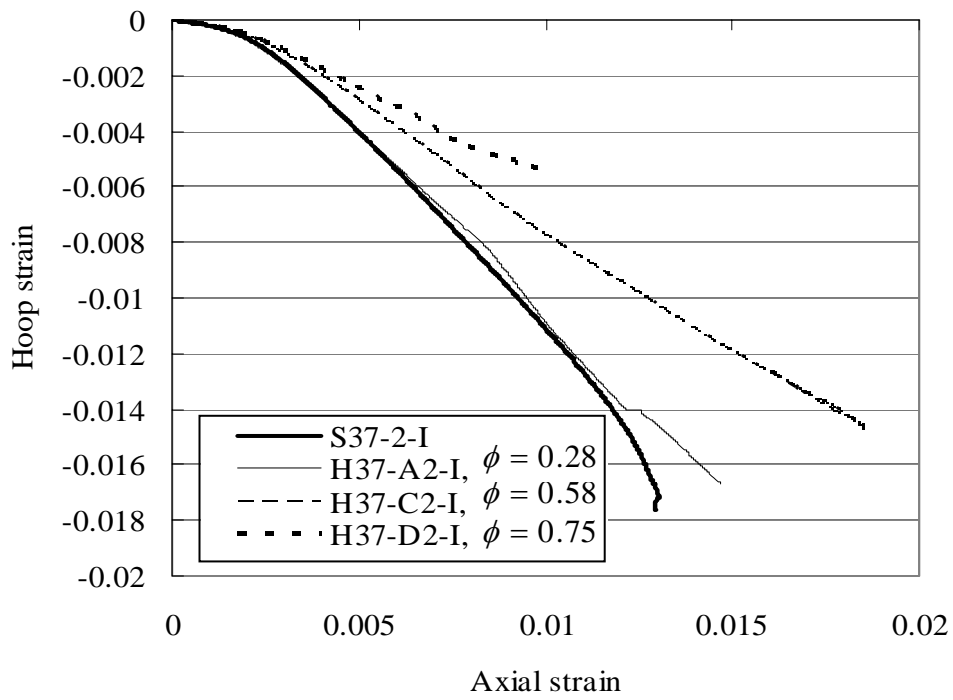
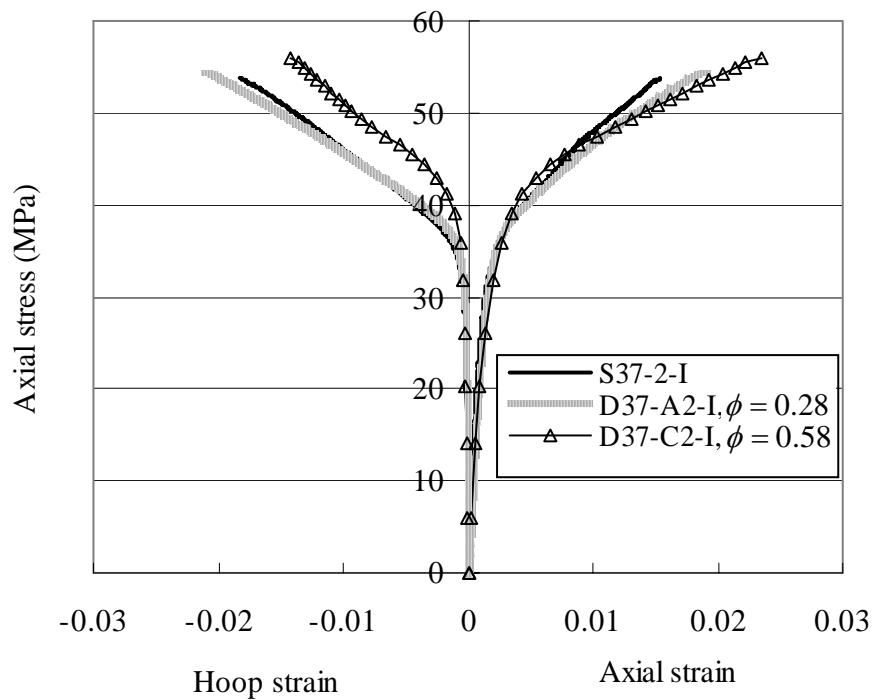
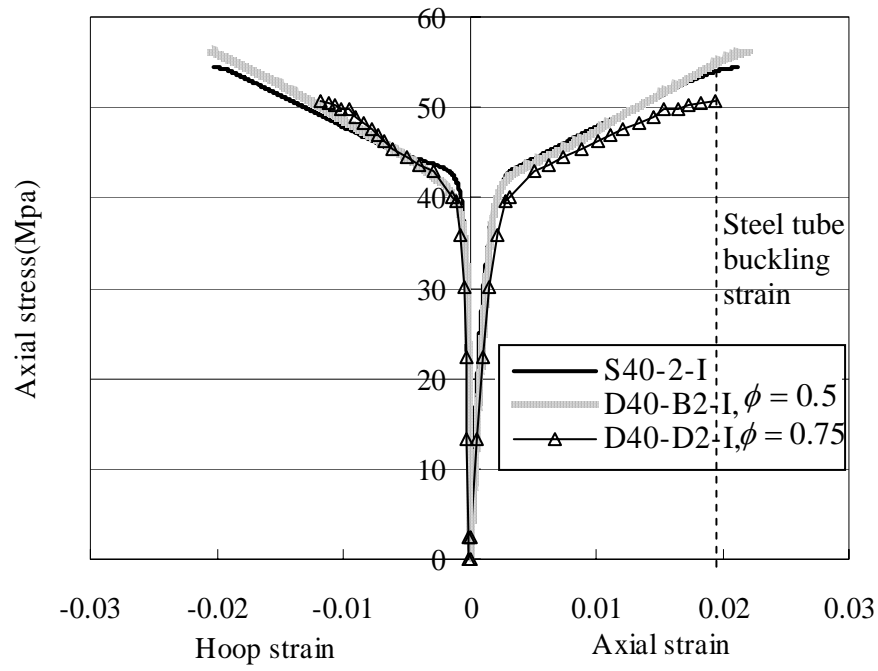


Figure 3.20 Comparison of axial strain-hoop strain curves between FCHCs and a corresponding FCSC

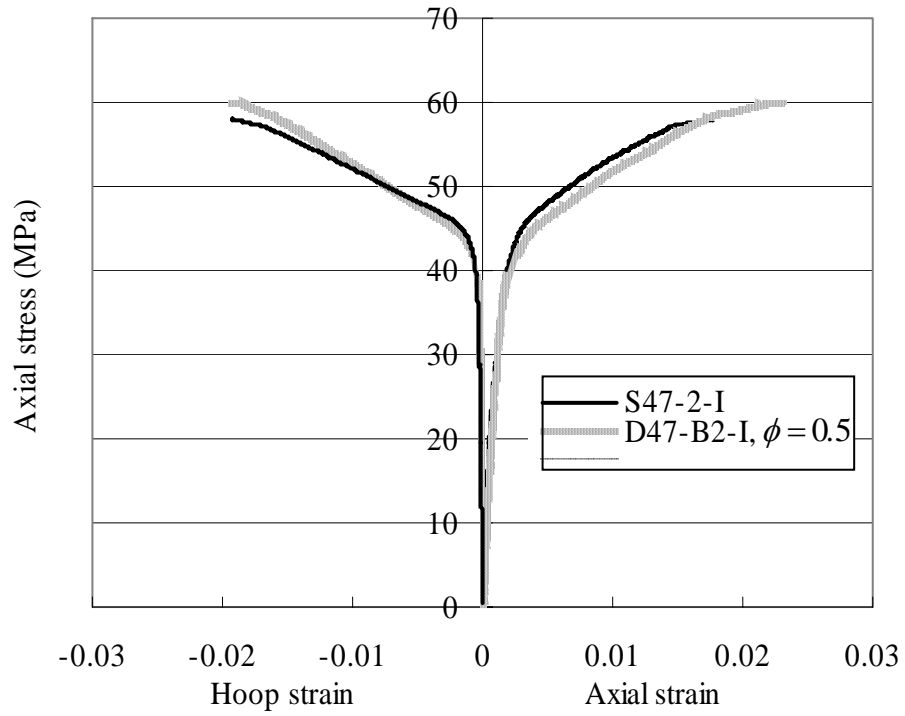


(a)  $f'_{co} = 37$  MPa

Figure 3.21 Comparison of stress-strain curves of concrete between FCSCs and DSTCs

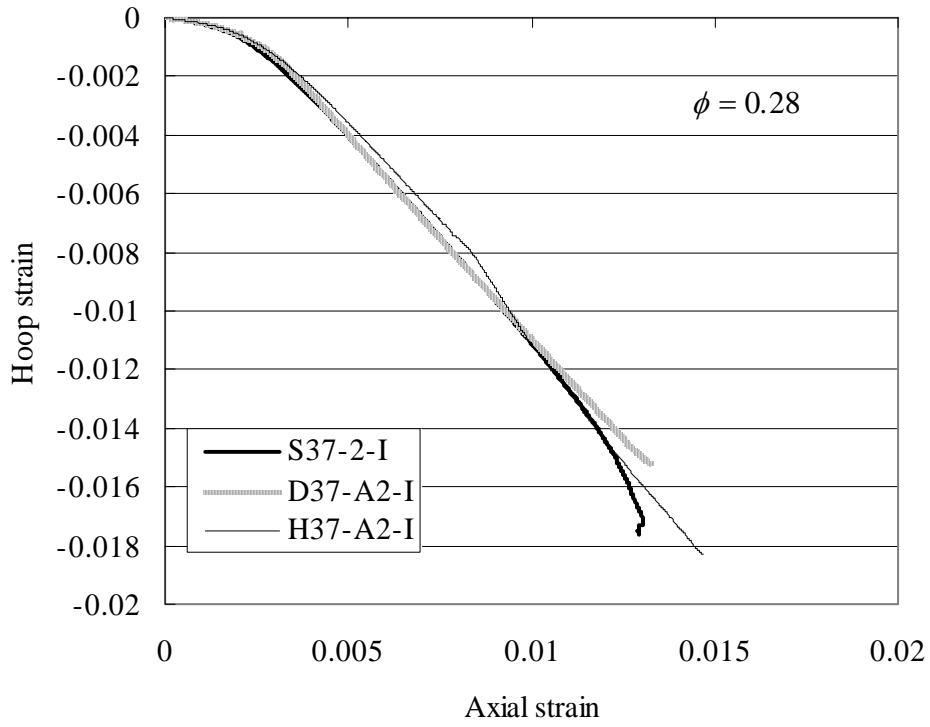


(b)  $f'_{co} = 40$  MPa

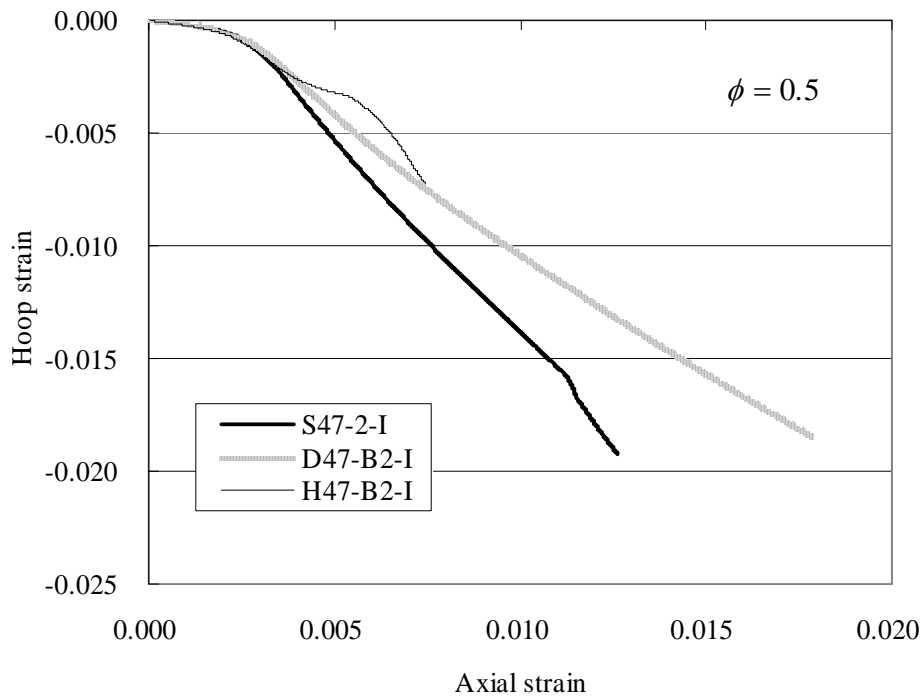


(c)  $f'_{co} = 47$  MPa

Figure 3.21 Comparison of stress-strain curves of concrete between FCSCs and DSTCs (Cont'd)

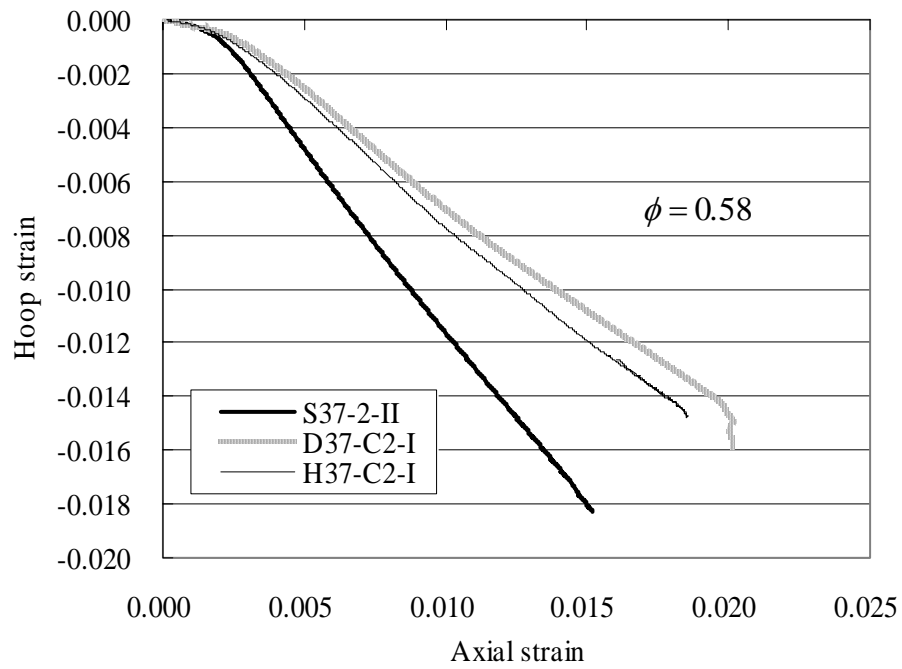


(a) Void ratio  $\phi = 0.28$

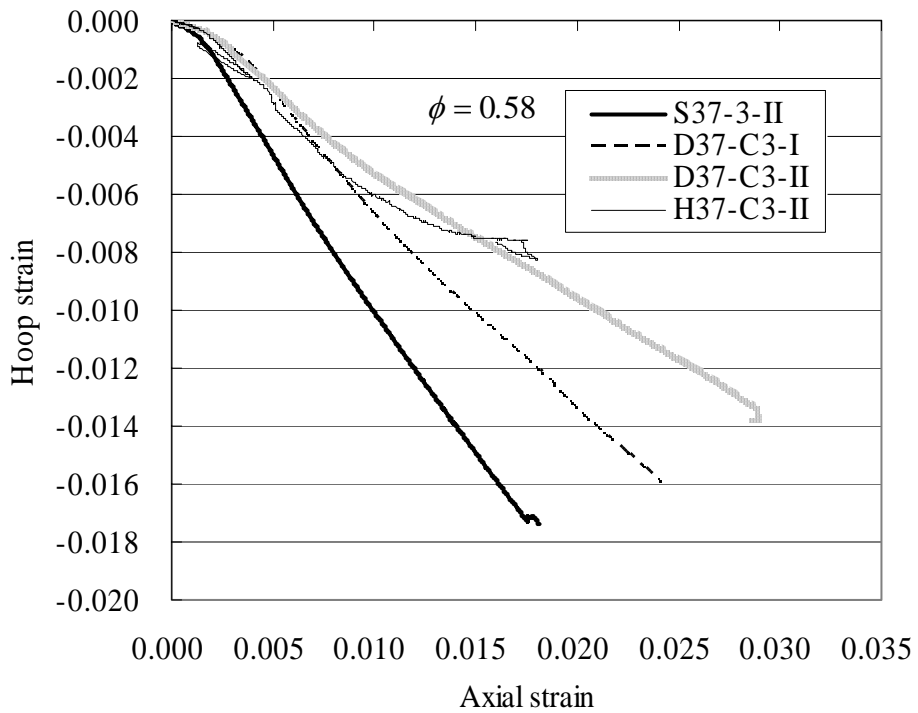


(b) Void ratio  $\phi = 0.5$

Figure 3.22 Axial strain-hoop strain curves of FCHC and DSTC specimens

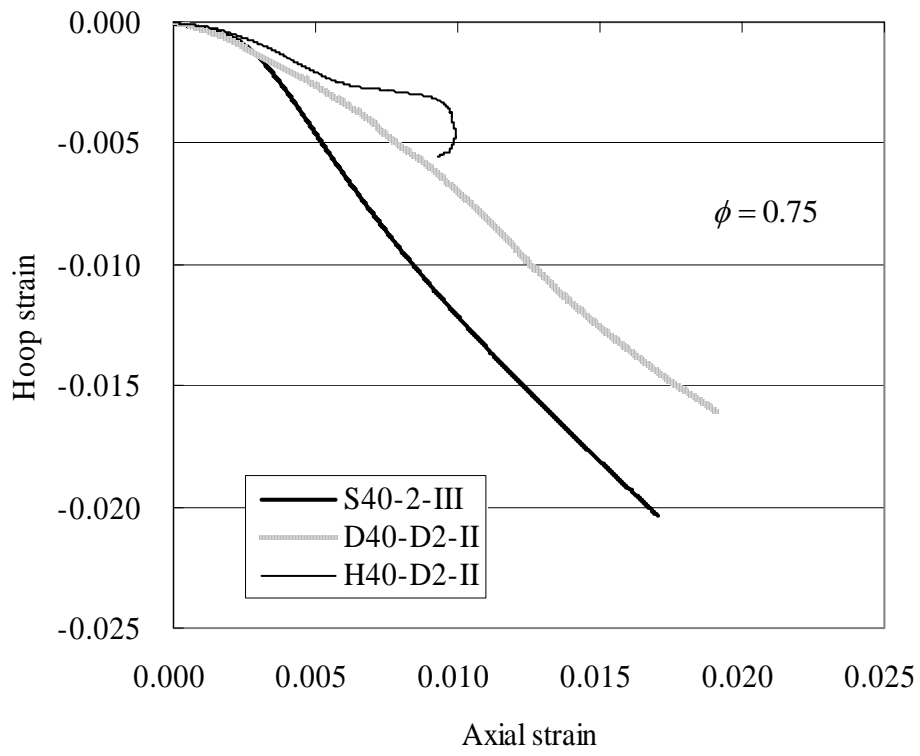


(c) Void ratio  $\phi = 0.58$ , with a two-ply FRP tube



(d) Void ratio  $\phi = 0.58$ , with a three-ply FRP tube

Figure 3.22 Axial strain-hoop strain curves of FCHC and DSTC specimens (Cont'd)



(e) Void ratio  $\phi = 0.75$

Figure 3.22 Axial strain-hoop strain curves of FCHC and DSTC specimens (Cont'd)

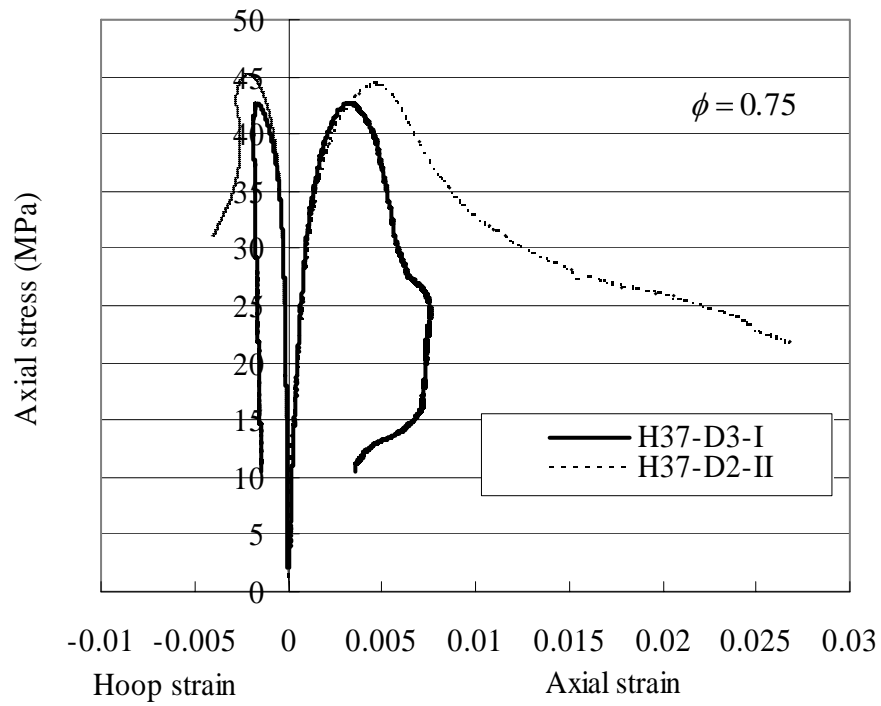


Figure 3.23 Effect of thickness of FRP tube on stress-strain curves of FCHCs

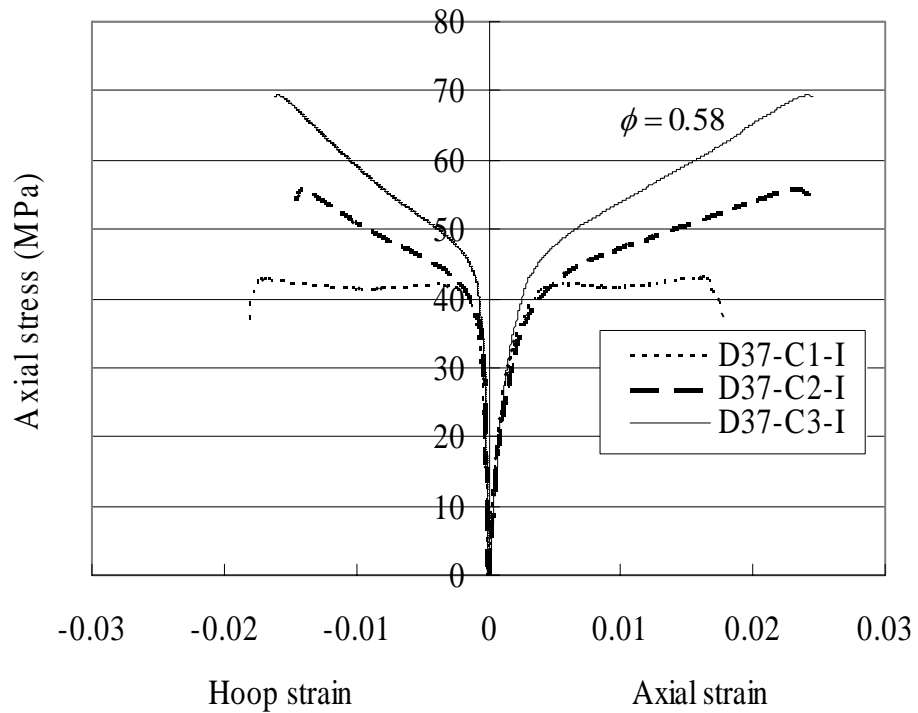


Figure 3.24 Effect of thickness of FRP tube on stress-strain curves of concrete in DSTCs

## **CHAPTER 4**

# **ASSESSMENT OF DRUCKER-PRAGER TYPE PLASTICITY MODELS FOR THE MODELING OF FRP-CONFINED CONCRETE**

### **4.1 INTRODUCTION**

Extensive research has been conducted on FRP-confined concrete using circular solid cylinders confined with an FRP jacket, and the behavior of such uniformly-confined concrete is now well understood, as reviewed in Chapter 2. Many stress-strain models have been proposed for concrete in FRP-confined solid cylinders (FCSCs) based on test results, including design-oriented models in closed-form expressions (e.g. Lam and Teng 2003a) and analysis-oriented models (e.g. Teng et al. 2006a) which predict stress-strain curves by an incremental procedure. Test results can now be closely predicted by some of the existing stress-strain models such as those proposed by Lam and Teng (2003a) and Teng et al. (2006a). By contrast, the behavior of FRP-confined concrete in sections other than circular sections is not yet well understood. In non-circular FRP-confined sections such as rectangular sections and annular sections, the concrete is non-uniformly confined. A substantial amount of work has been conducted on FRP-confined concrete in rectangular sections (e.g. Lam and Teng 2003b), but only a very limited amount of information is available on the behaviour of

FRP-confined concrete in annular sections (Fam and Rizkalla 2001a, b; Becque et al. 2003). Fam and Rizkalla (2001a) and Becque et al. (2003) presented their attempts to model FCHCs or FRP-concrete DSTCs using analysis-oriented models. These models are based on the assumption that the axial concrete stresses are uniform over the section which does not reflect the true behavior. It has also been shown in Chapter 3 that these models do not provide reasonable predictions of the test results obtained in the present study.

It is well known that stresses in an annular section are non-uniform in the radial direction when it is subjected to axial compression applied through a rigid plate, as shown by the results from the classical theory of elasticity (see Chapter 3 for details). The analysis-oriented models introduced earlier for FCSCs (e.g. Teng et al.'s (2006a) model expressed by Eqns 2.22-2.26) cannot predict the behavior of hybrid DSTCs, not only because they are proposed for concrete under uniform confinement but also because they are one-dimensional models which do not provide complete multi-axial stress-strain relationships. These models, however, can be used to calibrate the material parameters in constitutive models because of their ability to predict the behavior of FCSCs.

Many different FE studies have been published on FRP-confined concrete. The constitutive models for concrete adopted in previous research include plasticity models (e.g. Karabinis and Kioussis 1994, 1996; Karabinis and Rousakis 2002; Oh 2002; Mirmiran et al. 2000; Lan 1998; Fang 1999; Mahfouz et al. 2001; Shahawy et al. 2000) and plastic-damage models (e.g. Luccioni and Rougier 2005; Huang 2005). Despite the inclusion of damage in some models (Luccioni and Rougier

2005; Huang 2005), all these constitutive models involve concrete plasticity. In this chapter, the effects of three key components of a plasticity model, namely, the yield criterion, the hardening rule and the flow rule, on its performance in predicting the behavior of confined concrete are assessed numerically. As a basis for this assessment, the general behavior of confined concrete is reviewed first. The assessment is mainly focused on the Drucker-Prager (D-P) type concrete plasticity models, not only because they are widely used (e.g. Karabinis and Kioussis 1994, 1996; Karabinis and Rousakis 2002; Oh 2002; Mirmiran et al. 2000; Lan 1998; Fang 1999; Mahfouz et al. 2001; Shahawy et al. 2000) but also because the conclusions reached for such models are relevant to other plasticity models. The conclusions drawn in this chapter will be taken into account in the modeling of hybrid DSTCs presented in Chapter 5.

## **4.2 GENERAL BEHAVIOR OF CONFINED CONCRETE**

The behavior of concrete under a constant active confining pressure has been widely investigated (Richart et al. 1928; Mander et al. 1988; Canadppa et al. 2001; Sfer et al. 2002). Extensive research on the behavior of FRP-confined concrete, which is subjected to a varying passive confining pressure, has also been conducted, as reviewed in Chapter 2. Figure 4.1 (Teng and Lam 2004) shows the typical stress-strain curves of actively-confined and FRP-confined concrete respectively, and Figure 4.2 (Teng et al. 2006a; Teng and Lam 2004) illustrates the dilation properties of them. In these figures, compressive stresses/strains are defined to be positive while tensile strains/stresses are defined to be negative. These definitions are adopted throughout this chapter unless otherwise specified.

The curves of carbon FRP-(CFRP-) confined concrete were obtained by Lam and Teng (2004) from compression tests on 152 mm × 305 mm concrete cylinders. The CFRP had a nominal thickness of 0.165 mm per ply, an elastic modulus of 250 GPa and a tensile strength of 3800 MPa. The curves of actively-confined concrete were obtained either by Canadppa et al. (2001) or Sfer et al. (2002) from concrete cylinders with active confinement at different lateral pressures. The unconfined concrete cylinder strengths of these specimens were in the range of 32.8 MPa-42 MPa. In these figures, the axial stress  $\sigma_c$  is normalized by the compressive strength of unconfined concrete  $f'_{co}$  while the axial strain  $\varepsilon_c$  or lateral strain  $\varepsilon_l$  is normalized by the axial strain of unconfined concrete at its peak stress  $\varepsilon_{co}$ .

It can be seen from Figures 4.1 and 4.2 that actively-confined concrete has the following properties: (1) the peak stress of concrete and the corresponding strain increases with an increase in the confining pressure; (2) the curve of concrete confined by a larger confining pressure has a more gradual descending branch; (3) corresponding to the same axial strain, the lateral expansion of concrete under a larger confining pressure is less; and (4) actively-confined concrete exhibits continuous volume dilation after volume compaction, and the volumetric strain of the transition point increases with an increase in the confining pressure. It can also be found from simple calculations that the shear strength of concrete, which refers to the peak value of the second deviatoric stress invariant, increases with an increase in the confining pressure.

The main characteristics of FRP-confined concrete include: (1) an approximately bilinear axial stress-strain curve, the first part of which differs only slightly from the curve of unconfined concrete while the second part of which depends on the circumferential stiffness and strength of the outer FRP jacket; (2) corresponding to the same axial strain, the lateral strain of concrete confined by a stronger FRP jacket is less; and (3) the volumetric change depends significantly on the FRP jacket stiffness  $\frac{E_{frp}t_{frp}}{R_o}$  in which  $E_{frp}$  and  $t_{frp}$  are the elastic modulus and thickness of the FRP jacket respectively, and  $R_o$  is the radius of the cylinder. Figure 4.2(b) shows that the concrete cylinder confined by a one-ply FRP jacket exhibits continuous volume dilation after volume compaction; the concrete cylinder confined by a two-ply FRP jacket exhibits volume compaction initially followed by volume dilation which however is replaced by volume compaction afterwards until final failure; the concrete cylinder confined by a three-ply FRP jacket exhibits continuous volume compaction. Teng et al. (2006a) also concluded from test results that although the lateral strain-axial strain paths of actively-confined concrete and FRP-confined concrete are very different, the axial strain at a given lateral strain depends mainly, if not completely, on the current confinement ratio defined as the ratio between the lateral confining pressure  $\sigma_l$  and the strength of unconfined concrete  $f'_{co}$ . This conclusion means that at the interception points in Figure 4.2(a) both FRP-confined concrete and actively-confined concrete are with the same confinement ratio.

## **4.3 DRUCKER-PRAGER (D-P) TYPE PLASTICITY MODELS**

### **4.3.1 Introduction**

Concrete plasticity models are generally based on the same framework of plasticity theory for metals, but with necessary modifications to include the unique properties of concrete. The key aspects of a plasticity model include the yield surface (including the initial and subsequent yield surfaces), the flow rule and the hardening rule. The initial yield surface determines when plastic deformation begins; the flow rule determines the direction of plastic deformation; and the hardening rule defines the relationship between the subsequent yield surfaces and the magnitude of plastic deformation.

Many yield functions have been proposed for concrete. The number of parameters included in these functions ranges from one (e.g. Von Mises criterion) to five (Chen 1982). Among these yield functions, the Drucker-Prager (D-P) criterion has been widely adopted for the modeling of confined concrete (e.g. Karabinis and Kioussis 1994, 1996; Karabinis and Rousakis 2002; Oh 2000; Mirmiran et al. 2000; Lan 1998; Fang 1999; Mahfouz et al. 2001; Shahawy et al. 2000) because of its simplicity (involving only two parameters) and its capability to capture shear strength increases as a result of hydrostatic pressure increases, which is a unique property of concrete under confinement. In this section, the ability of this type of models to simulate the behavior of both actively-confined and FRP-confined concrete is discussed by examining the three key aspects mentioned above, namely, the yield criterion, the flow rule and the hardening rule. Various existing

D-P type models are examined. Several numerical tests are introduced to illustrate and verify the conclusions drawn.

Based on the critical assessment of existing models, a modified D-P type plasticity model is proposed and implemented in the general purpose FE program ABAQUS. Numerical tests are then introduced to verify the suitability of the proposed model for actively-confined and FRP-confined concrete.

### **4.3.2 Existing D-P Type Plasticity Models**

The Drucker-Prager yield/failure criterion is one of the pressure-sensitive criteria which reflect the experimental observation that the shear strength of concrete increases with an increase in the hydrostatic pressure. The difference between the Drucker-Prager failure criterion and pressure-insensitive criteria (e.g. Von Mises criterion) is obvious in the meridian plane of the stress space (Figure 4.3). The latter is a line parallel to the abscissa while the former is an inclined line. When a plasticity model is based on the Drucker-Prager yield/failure criterion, it is referred to as a Drucker-Prager type plasticity model.

#### *4.3.2.1 Yield criterion*

##### (i) General equations

The Drucker-Prager yield criterion takes the following form (Chen 1982; Oh 2000).

$$F = \sqrt{J_2} - \theta I_1 - k \quad (4.1)$$

where  $\theta$  and  $k$  are parameters to be determined,  $J_2$  and  $I_1$  are respectively the second deviatoric stress invariant and the first stress invariant. When  $k$  is not a constant and is related to plastic deformations (Eqn 4.2), it is known as the hardening-softening function and Eqn 4.1 represents both the initial and the subsequent yield surfaces.

$$k = k(\tilde{\varepsilon}_p) = k(\int d\tilde{\varepsilon}_p) \quad (4.2)$$

$$d\tilde{\varepsilon}_p = C_p \sqrt{d\varepsilon_j^p d\varepsilon_j^p} \quad (4.3)$$

where  $d\tilde{\varepsilon}_p$  is the equivalent plastic strain increment. When the D-P yield criterion with an associated flow rule is adopted,  $C_p$  is given by the following equation for concrete under triaxial compression:

$$C_p = \frac{\frac{1}{\sqrt{3}} - \theta}{\sqrt{3\theta^2 + 0.5}} \quad (4.4)$$

The classical metal plasticity model can be regarded as a special case of the D-P type models, with  $\theta=0$  and consequently  $C_p = \sqrt{\frac{2}{3}}$ .

It is evident from Eqn 4.1 that the initial and the subsequent yield surfaces have the same shape in the stress space, provided that  $\theta$  is a constant for a given material. The subsequent yield surfaces are a series of straight lines in the meridian plane. These lines are all parallel to that representing the initial yield surface as shown in Figure 4.4. The only difference between these lines is the point of interception with the  $\sqrt{J_2}$  axis, and this interception point is dependent

on the hardening/softening function  $k$ . It is also evident from Eqn 4.1 that the D-P yield surface has a circular shape in the deviatoric plane, as shown in Figure 4.5.

Although many researchers directly adopted Eqn 4.1 as the yield criterion for concrete (e.g. Mirmiran et al. 2000; Karabinis and Kioussis 1994; Karabinis and Rousakis 2002; Oh 2000; Lan 1998; Fang 1999; Mahfouz et al. 2001; Shahawy et al. 2000), some others (Chen 1982; Karabinis and Kioussis 1996; Huang 2005) found from test results that the third deviatoric stress invariant should also be included in the yield criterion to better reflect the experimental observations. Karabinis and Kioussis (1996) modified the D-P criterion by including the third deviatoric stress invariant, although the accuracy of the parameters they adopted is doubtful. The yield criteria adopted in existing D-P type models (Table 4.1) are assessed below, with an emphasis on the importance of the inclusion of the third deviatoric stress invariant, and the determination of constants in the yield criterion.

## (ii) Discussions

It has been noted by many researchers (e.g. Chen 1982; Lan 1998; Huang 2005) that the shear strength of concrete under biaxial compression and that under triaxial compression is different, even when the hydrostatic pressures of the two cases are the same. Based on the plasticity theory, it is known that the stress states of concrete under biaxial compression and triaxial compression correspond to different circumferential positions on the deviatoric plane respectively (Figure 4.5). The shear strength ratio between these two cases (i.e. between biaxial compression and triaxial compression) can be found from experimental results or

empirical equations for the strengths of concrete under biaxial compression and triaxial compression (see Appendix 4.2). If the experimental results of Kupfer et al. (1969) are adopted for concrete under biaxial compression and the empirical equation proposed by Richart et al. (1928) is adopted for concrete under triaxial compression, this strength ratio is around 0.7 (Appendix 4.2), much less than 1 as implied by the circular failure curve. Therefore, a failure surface which aims at reflecting the experimental behavior of concrete should take into account the effect of the third deviatoric stress invariant and adopt a non-circular failure curve in the deviatoric plane. A possible shape of such failure surfaces is shown in Figure 4.5.

It can also be expected that the peak stress of concrete under non-uniform confinement cannot be accurately predicted by Eqn 4.1. The stress state of non-uniformly confined concrete corresponds to a circumferential position between that of triaxial and biaxial compression on the deviatoric plane (Figure 4.5). Therefore, the peak stress of this case cannot be accurately predicted as the two extreme cases (i.e. biaxial compression and triaxial compression) are not accurately defined.

In Eqn 4.1,  $\theta$  is known as the friction parameter and  $\arctan\theta$  is defined as the friction angle in the  $\sqrt{J_2}$ - $I_1$  plane. The value of  $\theta$  can be found through calibration using empirical equations for concrete under triaxial compression. Among many such equations, the most popular are those proposed by Richart et al. (1928) and Mander et al. (1988). Teng et al. (2006a) recently proposed an equation which has been verified by a large amount of test data. The friction

parameter is calculated to be 0.2934 using the equation proposed by Richart et al. (1928) and to be 0.2634 using the equation proposed by Teng et al. (2006a), as explained in Appendix 4.1.

Mirmiran et al. (2000), Shahawy et al. (2000), Karabinis and Kioussis (1994), Karabinis and Rousakis (2002) and Oh (2000) directly adopted the D-P yield criterion and calibrated the  $\theta$  value using empirical equations for the triaxial compressive strength of concrete. Fang (1999) and Mahfouz et al. (2001) simulated concrete using the smeared concrete model in ABAQUS, which has a yield criterion similar to Eqn 4.1 for concrete in compression. Therefore, these models cannot give accurate predictions for the strength of concrete under non-uniform confinement. In Karabinis and Kioussis (1996), the term  $\sqrt{J_2}$  in Eqn 4.1 is replaced by  $\sqrt{J_2} \sqrt[4]{1-C_3 S_r}$  where  $S_r = \frac{J_3}{(J_2)^{3/2}}$  is a function of the second and the third deviatoric stress invariants, and  $C_3$  is a constant. This replacement causes the shape of the yield surface in the deviatoric plane to be non-circular. It is suggested that  $C_3 = 2.3$  in Karabinis and Kioussis (1996). By doing so,  $\sqrt[4]{1-C_3 S_r}$  is equal to 1.17 for triaxial compression and equal to 0.58 for biaxial compression. The shear strength ratio is approximately 0.5, which is lower than the experimental value (about 0.7) as discussed earlier.

#### 4.3.2.2 Strain hardening and softening

##### (i) General equations

Although some researchers (e.g. Mirmiran et al. 2000; Shahawy et al. 2000) assumed an elastic-perfectly plastic model for confined concrete, the strain hardening/softening behavior has long been observed in experiments (Chen 1982). In classical metal plasticity models,  $k$  is only a function of the equivalent plastic strain (Eqn 4.2). If this concept is adopted with the D-P yield criterion, the strain hardening/softening rule can be determined by any single uniaxial stress-strain curve of concrete, either with or without confinement. It is evident that the task is to determine the value of  $k$  corresponding to a given value of  $\tilde{\varepsilon}_p$  based on Eqn 4.2. It can be easily shown that  $d\tilde{\varepsilon}_p$  is equal to  $d\varepsilon_1^p$  for concrete under uniaxial compression based on Eqns 4.2-4.4 and Eqn 4.11 presented later in this chapter, where  $\varepsilon_1^p$  is the plastic strain in the loading direction. The hardening/softening function can then be determined by the following procedure with a uniaxial stress-strain curve:

(1) obtain the axial stress-plastic strain curve using

$$\varepsilon_1^p = \varepsilon_1 - \frac{\sigma_1}{E_c} \quad (4.5)$$

and the  $\sigma_1 - \varepsilon_1$  relationship;

(2) find the relationship between the plastic strain and both  $J_2$  and  $I_1$  based on the axial stress-plastic strain curve obtained in step (1);

(3) find the relationship between  $k$  and the plastic strain based on Eqn 4.1 and the results of step (2).

While the classical hardening rule takes the plastic deformation as the only parameter, it has recently been noted (Lan 1998; Oh 2002; Karabinis and Kioussis 1994; Chen and Lan 2004; Huang 2005) that without involving the confining pressure, the hardening rule cannot lead to reasonable predictions of the ductility of confined concrete. Some of these authors (e.g. Lan 1998; Oh 2002) have also proposed modified hardening rules in which the confining pressure is taken as another parameter, and announced good predictions of test results. The hardening rules adopted in existing D-P models (Table 4.1) are assessed below. The importance of the inclusion of strain hardening/softening, and that of the inclusion of confining pressures in the hardening rules are numerically illustrated.

#### (ii) Discussions

As is evident from numerous compression tests on concrete (e.g. Figure 4.6), an elastic-perfectly plastic model cannot reflect the true behavior of concrete in compression. Therefore a plasticity model including strain hardening and softening is necessary to capture the experimental phenomenon. Mirmiran et al. (2000) and Shahawy et al. (2000) adopted an elastic-perfectly plastic model, which is obviously incapable of close predictions of the behavior of actively-confined concrete. However, Mirmiran et al. (2000) and Shahawy et al. (2000) believed that an elastic-perfectly plastic model can provide reasonably close predictions of the axial stress-strain behavior of FRP-confined concrete. The following discussion is an attempt to clarify this issue.

It is known that FRP-confined concrete is subjected to a varying confining pressure. In order to determine a point on the stress-strain curve of FRP-confined

concrete, it is necessary to, (1) find the confining pressure under a given axial strain, (2) find the axial stress based on the known axial strain and confining pressure. Step (1) above relates to the flow rule which is discussed in Subsection 4.3.2.3, while step (2) relates directly to the strain hardening/softening rule. Researchers (e.g. Mirmiran and Shahawy 1996; Spoelstra and Monti 1999; Fam and Rizkalla 2001a; Chun and Park 2002; Harries and Kharel 2002 and Teng et al. 2006a) generally believe that the axial stress of FRP-confined concrete at a given axial strain and confining pressure is equal to that of actively-confined concrete with the same confining pressure and axial strain. Figure 4.7, which is produced using Teng et al.'s (2006a) model, illustrates that the stress-strain curve of FRP-confined concrete crosses a series of stress-strain curves of actively-confined concrete at points where both the FRP-confined concrete and the actively-confined concrete have the same confining pressure. The locations of these interception points, however, depend on the stiffness of the FRP jacket. When the FRP jacket stiffness is higher, these interception points are at smaller axial strains. As the assumption of elastic-perfectly plastic behavior can only correctly capture the peak stress point of actively-confined concrete (i.e. cannot predict the post peak softening behavior), it would lead to inaccurate predictions of the stress-strain behavior of FRP-confined concrete when the interception points do not coincide with the peak stress points. The farther these interception points are from the peak stress points, the larger the prediction errors. It can therefore be concluded that the assumption of elastic-perfectly plastic behavior generally cannot lead to close predictions of the stress-strain behavior of FRP-confined concrete, but may produce reasonable predictions when the FRP

jacket stiffness is within a certain range, provided that the dilation of confined concrete is closely predicted.

If the equivalent plastic strain is taken as the only variable in the strain hardening/softening function, the axial stress-strain curves of both actively-confined and FRP-confined concrete cannot be closely predicted, as pointed out by previous researchers (Lan 1998; Oh 2002; Karabinis and Kiousis 1994; Chen and Lan 2004; Huang 2005). Two numerical tests were conducted in the present study to clarify this issue. Figure 4.8 shows the FE results from such a D-P type model for the stress-strain curves of unconfined concrete and concrete confined by a constant active pressure equal to 6 MPa and 12 MPa respectively. The unconfined concrete strength is 39.6 MPa. The hardening/softening function was obtained from the uniaxial stress-strain curve of unconfined concrete produced by Teng et al.'s (2006a) model, following the procedure stated earlier. The Extended Drucker-Prager Model of ABAQUS, which is introduced in detail later in this chapter, was employed to conduct this FE analysis. It can be seen in Figure 4.8 that the slopes of the strain softening branch of all three curves are almost identical. This is not consistent with the experimental observation that the stress-strain curve of actively-confined concrete has a less steep descending branch than unconfined concrete (Figure 4.1). Figure 4.9 shows the FE results from the same D-P model with a constant dilation angle equal to  $8^\circ$  (the dilation angle is discussed in detail in Subsection 4.3.2.3) for FRP-confined concrete. The concrete cylinder has an outer diameter of 152.5 mm and is confined by a two-ply GFRP jacket with an elastic modulus of 80,100 MPa and a thickness of 0.17 mm per ply. It is obvious that the FE results are quite different from the test results.

The inappropriate strain hardening/softening function is again one of the major reasons. As such a strain hardening/softening function leads to an underestimation of the post-peak stress of actively-confined concrete (see Figure 4.8), the stresses of FRP-confined concrete, which is subjected to continuously varying confining pressures, are consequently underestimated. It may therefore be concluded that the strain hardening/softening function should also be dependent on the confining pressure, in order to closely predict the behavior of confined concrete. In Subsection 4.3.4, it is verified through numerical tests that a strain hardening/softening function dependent on the confining pressure leads to close predictions of the behavior of confined concrete.

Some researchers (e.g. Lan 1998; Oh 2000; Karabinis and Kiousis 1994) included the confining pressure into the hardening/softening function. Lan (1998) included the effect of confining pressure based on a set of experimental stress-strain curves of actively-confined concrete with different confining pressures. Oh (2000) proposed a set of complicated equations to determine the  $k$  function. These equations included six parameters and twenty subordinate parameters and were obtained from nonlinear regression analysis of data produced from an empirical axial stress-strain model developed by the same author for concrete under triaxial compression. Despite the complicated form, the major hardening parameters were still the plastic deformation and the confining pressure, for concrete with a given unconfined strength.

Karabinis and Kiousis (1994) adopted the following form for the  $k$  function:

$$k = \left( \frac{1}{\sqrt{3}} - \theta \right) \left( \frac{\bar{\varepsilon}}{\frac{1}{E_p} + \frac{\bar{\varepsilon}}{f_u' - f_y'}} - R(\sigma_l) E_p' \bar{\varepsilon} + f_y' \right) \quad (4.6)$$

in which  $\bar{\varepsilon}$  is a function of the plastic strain trajectory which is an indirect representation of the equivalent plastic strain;  $R(\sigma_l)$  is a function of the confining pressure; the other parameters, including  $E_p$ ,  $E_p'$ ,  $f_u'$ , and  $f_y'$ , are constants that can be determined using the unconfined concrete strength. This equation, although complicated, indicates the dependence of the hardening function on both the confining pressure and the plastic deformation.

The above three approaches are conceptually correct and can be expected to provide close predictions of the axial stress-strain behavior of actively-confined concrete, if their material parameters are suitably selected. However, in order to closely predict the behavior of FRP-confined concrete, an appropriate flow rule is another important issue, as discussed below.

#### 4.3.2.3 Flow rule

##### (i) General equations

When the associated flow rule is adopted, the flow potential is the same as the yield function and the plastic strain increments can be calculated using Eqn 4.7 (Chen 1982; Oh 2000).

$$d\varepsilon_{ij}^p = \lambda \frac{\partial G}{\partial \sigma_{ij}} = \lambda \frac{\partial F}{\partial \sigma_{ij}} \quad (4.7)$$

where  $F$  is the yield function defined by Eqn 4.1 and  $\lambda$  is a scalar hardening parameter which can vary throughout the straining process.

For concrete subjected to triaxial compression, Eqn 4.7 can be written as

$$d\varepsilon_1^p = \lambda \left( \frac{1}{2\sqrt{J_2}} \frac{2\sigma_1 - \sigma_2 - \sigma_3}{3} - \theta \right) \quad (4.8)$$

$$d\varepsilon_2^p = \lambda \left( \frac{1}{2\sqrt{J_2}} \frac{2\sigma_2 - \sigma_3 - \sigma_1}{3} - \theta \right) \quad (4.9)$$

$$d\varepsilon_3^p = \lambda \left( \frac{1}{2\sqrt{J_2}} \frac{2\sigma_3 - \sigma_1 - \sigma_2}{3} - \theta \right) \quad (4.10)$$

Eqn 4.11 can be obtained from Eqns 4.8-4.10.

$$\theta = \frac{\sqrt{3}}{6} \frac{d\varepsilon_1^p + 2d\varepsilon_2^p}{d\varepsilon_1^p - d\varepsilon_2^p} = \frac{1}{6} \frac{dI_1^p}{d\sqrt{J_2^p}} = \frac{1}{6} \alpha \quad (4.11)$$

where  $\alpha$  is the dilation rate,

$$I_1^p = \varepsilon_1^p + \varepsilon_2^p + \varepsilon_3^p \quad (4.12)$$

and

$$\sqrt{J_2^p} = \sqrt{\frac{1}{6} [(\varepsilon_1^p - \varepsilon_2^p)^2 + (\varepsilon_2^p - \varepsilon_3^p)^2 + (\varepsilon_3^p - \varepsilon_1^p)^2]} \quad (4.13)$$

Eqn 4.11 clearly shows how the flow rule determines the direction of plastic deformation. For concrete under triaxial compression, the flow rule determines the ratio of the lateral (or volume) plastic strain to the axial plastic strain.

While the associated flow rule was adopted in some research (e.g. Fang 1999; Mahfouz et al. 2001), it has been found by many researchers (e.g. Chen and Lan 2004; Huang 2005; Mirmiran et al. 2000; Oh 2002) to lead to an overestimation of the expansion of confined concrete. Consequently, these authors suggested the use of the non-associated flow rule.

When the non-associated flow rule is adopted, a flow potential  $G$  different from the yield function is defined (Eqn 4.14) to find the plastic strain increments (Oh 2000). That is,

$$d\varepsilon_{ij}^p = \lambda \frac{\partial G}{\partial \sigma_{ij}}; \quad G = \sqrt{J_2} - \beta I_1 \quad (4.14)$$

where  $\beta$  is the dilation parameter and  $\arctan \beta$  is defined as the dilation angle. A positive  $\beta$  value indicates volume dilation while a negative  $\beta$  value indicates volume compaction.

By adopting Eqn 4.14, Eqn 4.11 can be rewritten as

$$\beta = \frac{\sqrt{3}}{6} \frac{d\varepsilon_1^p + 2d\varepsilon_2^p}{d\varepsilon_1^p - d\varepsilon_2^p} = \frac{1}{6} \frac{dI_1^p}{d\sqrt{J_2^p}} = \frac{1}{6} \alpha \quad (4.15)$$

Mirmiran et al. (2000), Shahawy et al. (2000) and Karabinis and Kiousis (1994, 1996) adopted a non-associated flow rule with a constant dilation angle for the modeling of confined concrete. Karabinis and Rousakis (2002) recently related the dilation angle to the plastic deformation. Oh (2002) noted the complicated deformation properties of concrete and related the dilation angle to both the confining pressure and the plastic deformation based on empirical equations for actively-confined concrete. The flow rules adopted in existing D-P type models (Table 4.1) are numerically assessed below, including (1) the associated flow rule; (2) the non-associated flow rule with a constant dilation angle; (3) the non-associated flow rule with a dilation angle varying with the plastic

deformation; (4) the non-associated flow rule with a dilation angle varying with both plastic deformation and confining pressure.

## (ii) Discussions

As stated earlier, the flow rule determines the ratio of lateral (volume) plastic strain to axial plastic strain. When the associated flow rule is used, continuous volume dilation after yielding is predicted, as the dilation angle is set to be equal to the friction angle which is a positive constant (e.g. 16.3 degrees, see Appendix 4.1). However, experimental observations show that actively-confined concrete exhibits volume compaction followed by volume dilation, while concrete strongly confined by an FRP jacket exhibits continuous volume compaction (Figure 4.2(b)). An experimental axial-lateral strain curve of actively-confined concrete is compared with FE results in Figure 4.10. The experimental curve, from a concrete cylinder with an unconfined strength of 41.9 MPa and confined by a constant pressure equal to 12 MPa, was obtained by Canadppa et al. (2001). The FE results are from the D-P model with the associated flow rule. It is obvious that the FE results overestimate the lateral expansion of actively-confined concrete, as found by Chen and Lan (2004), Huang (2005), Mirmiran et al. (2000) and Oh (2002).

Mirmiran et al. (2000) and Shahawy et al. (2000) explored the use of a non-associated flow rule with a constant dilation angle not equal to the friction angle for the modeling of FRP-confined concrete. Although Mirmiran et al. (2000) and Shahawy et al. (2000) found that the dilation tendencies of FRP-confined concrete could not be properly established by such a flow rule, they showed that the stress-strain curves of FRP-confined concrete could be reasonably closely

predicted by assuming the dilation angle to be equal to zero. The inability of such an assumption in predicting the dilation properties of FRP-confined concrete is evident from available test results. Based on test results, FRP-confined concrete (see Figure 4.2(b)) exhibits a varying dilation angle during the loading process (e.g. volume compaction occurs after volume dilation), while the assumption of a zero dilation angle corresponds to no volume change.

To understand the success of Mirmiran et al.'s (2000) model in predicting the stress-strain behavior of FRP-confined concrete and to explore its wider validity, Teng et al.'s (2006a) analysis-oriented stress-strain model is employed for the following discussion. Figure 4.11 shows the dilation angles of FRP-confined concrete calculated from Teng et al.'s (2006a) model for two specimens tested respectively by Mirmiran et al. (2000) and the author. In Mirmiran et al.'s (2000) test, the concrete had an unconfined strength of about 30 MPa, the cylinder had a diameter of 152.5 mm and the FRP tube had an elastic modulus of 40,336 MPa, a thickness of 2.21 mm and a tensile strength of 579 MPa in the circumferential direction. In the Yu's test, the concrete had an unconfined strength of 36.7 MPa and a corresponding strain of 0.0026, the cylinder had a diameter of 152.5 mm and the FRP tube had an elastic modulus of 80,100 MPa, a thickness of 0.34 mm and a hoop rupture strain of 0.0019. It is obvious from Figure 4.11 that the dilation angle of FRP-confined concrete not only varies with the plastic deformation, but also depends on the stiffness of the FRP jacket. FRP-confined concrete with a weaker jacket (Yu's test) has a larger dilation angle. Therefore, the adoption of a constant dilation angle cannot lead to reasonable predictions of the behavior of FRP-confined concrete of different jacket stiffnesses. Mirmiran et

al.'s (2000) conclusion is reasonable for his own test as the actual dilation angle of his specimen is seen in Figure 4.11 to vary from about 3 degrees to negative 5 degrees (Figure 4.11). In addition, Mirmiran et al. (2000) assumed the elastic-perfectly plastic behavior. The good performance of his FE model in predicting the axial stress-strain curve is also partly because the effect of underestimating lateral expansion at the beginning of the loading process counteracts the effect of overestimating the stress of confined concrete due to the assumption of elastic-perfectly plastic behavior. The zero-degree dilation angle assumption obviously does not lead to close predictions of Yu's test results (see Figure 4.12(a)). Using a trial-and-error procedure, it was found that a constant dilation angle equal to 8 degrees can produce reasonable predictions for Yu's test, as shown in Figure 4.12(a). By doing so, the lateral dilation of FRP-confined concrete can also be reasonably but not accurately predicted, as indicated in Figure 4.12(b). It can be found from Figure 4.12(b) that the FE results underestimate the lateral expansion. This is consistent with Figure 4.11 as at the beginning of the loading process the dilation angle is larger than 8 degrees. Based on the above discussion, it can be concluded that the assumption of a constant dilation angle not only does not lead to reasonable predictions of the complicated dilation properties of FRP-confined concrete (see Figure 4.2(b)), but also fails to predict the stress-strain behavior of FRP-confined concrete accurately. The above discussions also suggest that adopting the associated flow rule, which implies a constant dilation angle equal to the friction angle, does not provide close predictions of the behavior of FRP-confined concrete.

Karabinis and Rousakis (2002) recently related the dilation angle to the plastic deformation, but assumed it to be a constant in their earlier studies (Karabinis and Kioussis 1994, 1996). The following equation was given by them:

$$\alpha = \alpha_0 - \frac{\vec{\varepsilon}}{\frac{1}{K_\alpha} - \frac{\vec{\varepsilon}}{\alpha_u - \alpha_0}} \quad (4.16)$$

where  $\alpha_0$  and  $\alpha_u$  are the initial and ultimate values of  $\alpha$  and  $K_\alpha$  is the initial rate of change of  $\alpha$  as a function of  $\vec{\varepsilon}$  which is known as the plastic strain trajectory and is an indirect representation of the equivalent plastic strain. Eqn 4.16 describes the variation of  $\alpha$  which parallels the variation of plastic deformation. Karabinis and Rousakis (2002) proposed that the values of  $\alpha_0$  and  $\alpha_u$  be equal to -0.6 and -1.732 respectively.

Karabinis and Kioussis (1994, 1996) assumed a constant dilation angle and thus could not closely predict the behavior of confined concrete as explained earlier. Karabinis and Rousakis (2002) related the dilation angle to the plastic deformation but the negative dilation angle values they used are not consistent with experimental observations. As explained earlier, a negative value of  $\alpha$  indicates volume compaction. However, experimental observations showed that actively-confined concrete exhibits volume compaction followed by volume dilation with plastic deformation. In addition, Karabinis and Rousakis (2002) did not take into account the variation of dilation angle with the confining pressure. This variation, however, is evident from numerous tests (e.g. Figure 4.2(b)). In Figure 4.2(b), it is obvious that concrete confined with a larger confining pressure begins to dilate at a larger axial strain.

Oh (2002) noted the complicated deformation properties of concrete and related the dilation angle to both the plastic deformation and the confining pressure. Several equations were proposed to express the dilation angle based on an empirical transverse deformation model, proposed by the same author, and non-linear regression analysis. These equations, although complicated, include the variation of the dilation angle with both the confining pressure and the plastic deformation. Therefore, it can be expected that the equations of Oh (2002) are capable of close predictions of the dilation behavior of actively-confined concrete, provided that his empirical model has sufficient accuracy. However, it is believed that Oh's (2000) equations cannot provide close predictions of FRP-confined concrete, as explained below.

Figure 4.2(a) shows the curve of FRP-confined concrete crossing those of actively-confined concrete. Existing test results show that at the points of interception, the confining pressures of both types of specimens are almost the same for a given concrete (Teng et al. 2006a). However, in a plasticity model, the direction of plastic flow determines the ratio of the increment of lateral plastic strain to the increment of axial plastic strain. Figure 4.2(a) shows clearly that the tangent Poisson's ratio (i.e. the ratio of the increment of lateral strain to the increment of axial strain) of actively-confined concrete is different from that of FRP-confined concrete at the interception point, where the axial strain and the confining pressure are however almost the same for both cases. It should be noted that Figure 4.2(a) shows the axial-lateral strain curves, but it is reasonable to expect that the axial-lateral plastic strain curves are similar. Therefore, a plasticity

model, which relates the flow rule to the confining pressure and thus can predict the behavior of actively-confined concrete closely is likely to give unreliable predictions for FRP-confined concrete.

Teng et al.'s (2006a) analysis-oriented model is employed to further clarify this issue. The results from this model are shown in Figure 4.13, in which the horizontal axis is the axial plastic strain and the vertical axis is the dilation angle. The solid black curve in Figure 4.13 represents the results for a solid circular concrete cylinder ( $f'_{co} = 39.6$  MPa, diameter=152.5 mm) confined by an FRP jacket with an elastic modulus of 80,100 MPa and a thickness of 0.34 mm. The two dashed curves in Figure 4.13 represent the results for actively-confined concrete with the confining pressures equal to 6 MPa and 10 MPa respectively. The vertical dotted line on the left represents the axial plastic strain value of FRP-confined concrete when the confining pressure provided by the FRP jacket is equal to 6 MPa, while the right vertical dotted line represents the axial plastic strain value when the confining pressure is 10 MPa. It is evident from Figure 4.13 that the dilation angle of actively-confined concrete is different from that of FRP-confined concrete even when both have the same axial plastic strain and confining pressure. The black regions marked in Figure 4.13 indicate the differences in the dilation angle at the two key values of axial plastic strain. These results again suggests that a plasticity model, which relates the flow rule to the confining pressure and can accurately predict the behavior of actively-confined concrete, tends to overestimate the lateral dilation of FRP-confined concrete and in turn overestimate the axial stress-strain behavior. This point is further examined in Subsection 4.3.4 through FE results.

The difference in the dilation angle can be explained by the difference between actively-confined concrete and FRP-confined concrete which is under passive confinement. For actively-confined concrete, the confining pressure is constant and is not related to the deformation of concrete. For passively-confined concrete, however, the confinement level varies with the increment of deformation and in turn controls the deformation. Therefore, the dilation angle of passively-confined concrete may be related not only to the confining pressure but also to the ratio of the confining pressure increment to the lateral strain increment (i.e. the rate of confining pressure increment). For FRP-confined concrete, this ratio is directly related to the FRP jacket stiffness. The variation of dilation angle with this ratio is clearly illustrated in Figure 4.11 which shows the variations of dilation angle with the axial plastic strain for concrete confined by two different FRP jackets.

The above discussions indicate that all flow rules adopted in existing D-P type models cannot lead to close predictions for FRP-confined concrete. Considering the dilation properties of passively-confined concrete discussed above, the flow rule should also include the rate of confining pressure increment, beside the plastic deformation and the confining pressure, in order to reach reasonably accurate predictions. In Subsection 4.3.4, it is verified through numerical tests that such a flow rule leads to reasonable predictions of the behavior of both actively-confined and FRP-confined concrete.

#### 4.3.2.4 Concluding remarks

It can be concluded from the above discussions that in order to provide reasonably accurate predictions of the behavior of both actively-confined and passively-confined concrete, the D-P type plasticity models should at least include the following modifications: (1) a yield criterion dependent on the third deviatoric stress invariant; (2) a confinement-dependent hardening rule; (3) a confinement-dependent non-associated flow rule, in which the dilation angle is related not only to the confining pressure but also to the rate of confining pressure increment. When (1) is appropriately applied, the strength of concrete under non-uniform confinement can be accurately predicted; when (2) is appropriately applied, the axial stress-strain curve of actively-confined concrete can be accurately predicted; when (3) is appropriately applied, the lateral deformation of both passively-confined and actively-confined concrete can be accurately predicted.

None of the existing models includes all three modifications mentioned above. Fang (1999) and Mahfouz et al. (2001) directly adopted the smeared crack concrete model in ABAQUS, which has an associated flow rule and does not include the third deviatoric stress invariant in the yield criterion. Fang's (1999) model also did not consider strain hardening/softening. The models proposed by Karabinis and his coauthors (Karabinis and Kioussis 1994, 1996; Karabinis and Rousakis 2002) do not include the effect of confining pressure on the flow rule and provide unreasonable values for the dilation angle. Therefore, their models cannot provide reasonable predictions of the lateral deformation of confined concrete. In addition, the shear strength ratio was either set to be 1 (Karabinis and

Kiousis 1994; Karabinis and Rousakis 2002) or set to be a value smaller than common experimental values (Karabinis and Kiousis 1996), as discussed earlier. The model proposed by Oh (2000) is conceptually correct for actively-confined concrete, except that it does not include the effect of the third deviatoric stress invariant and thus is not suitable for use with concrete under non-uniform confinement. However, it cannot provide reasonable predictions of the behavior of FRP-confined concrete as discussed earlier. The model adopted in Mirmiran et al. (2000) and Shahawy et al. (2000) do not include any of the three required modifications. Therefore it cannot be expected to predict the behavior of either actively-confined or passively-confined concrete with reasonable accuracy.

In the next subsection, it is illustrated that a D-P type model including all the above three modifications can lead to accurate predictions for both actively-confined and FRP-confined concrete.

### 4.3.3 Proposed Modifications

The proposed modifications are summarized below in Eqns 4.17-4.19.

#### (1) Yield criterion related to the third deviatoric stress invariant

The yield criterion is related to the third deviatoric stress invariant, as also suggested by Chen (1982), Karabinis and Kiousis (1996), and Huang (2005).

Eqn 4.1 is modified into

$$F = F(I_1, J_2, J_3) \quad (4.17)$$

#### (2) Confinement-dependent hardening rule

The hardening function is related to the confining pressure, as also suggested by Lan (1998), Oh (2002), Karabinis and Kiousis (1994) and Chen and Lan (2004). Eqn 4.2 is modified into

$$k = k(\sigma_l, \tilde{\varepsilon}_p) \quad (4.18)$$

where  $\sigma_l$  is the confining pressure.

### (3) Confinement-dependent non-associated flow rule

A non-associated flow rule with a flow potential different from the yield function is adopted (Eqn 4.14). The dilation parameter  $\beta$  is related to the plastic deformation, the confining pressure and the rate of confining pressure increment.

$$\beta = \beta\left(\sigma_l, \frac{\Delta\sigma_l}{\Delta\varepsilon_l}, \tilde{\varepsilon}_p\right) \quad (4.19)$$

where  $\varepsilon_l$  is the lateral strain.

For actively-confined concrete,  $\frac{\Delta\sigma_l}{\Delta\varepsilon_l} = 0$  and Eqn 4.19 reduces to

$$\beta = \beta(\sigma_l, \tilde{\varepsilon}_p) \quad (4.20)$$

For FRP-confined concrete in which the concrete is confined by a linear

elastic confining device,  $\frac{\Delta\sigma_l}{\Delta\varepsilon_l} = \frac{\sigma_l}{\varepsilon_l}$  and  $\sigma_l$  can be determined from  $\tilde{\varepsilon}_p$  and

$\varepsilon_l$ . Eqn 4.19 thus reduces to

$$\beta = \beta\left(\frac{\sigma_l}{\varepsilon_l}, \tilde{\varepsilon}_p\right) \quad (4.21)$$

The FE program ABAQUS was adopted to conduct FE analyses. The proposed modifications were made to a D-P type plasticity model available in ABAQUS,

which is referred to as the Extended Drucker-Prager Model. The facility of user defined solution-dependent field variables (SDFV) available in ABAQUS was used to implement these modifications.

#### 4.3.3.1 Extended Drucker-Prager model in ABAQUS

The Extended Drucker-Prager Model in ABAQUS is a D-P type plasticity model with a modified yield criterion. In this model, an additional parameter  $K$  is adopted to take into account the effect of the third deviatoric stress invariants. The physical meaning of  $K$  is that it represents the shear strength ratio of materials between biaxial compression and triaxial compression. In the Extended Drucker-Prager Model, the yield criterion takes the following form:

$$F = s - \theta I_1 - k \quad (4.22)$$

where

$$s = \frac{1}{2} \sqrt{J_2} \left[ 1 + \frac{1}{K} + \left( 1 - \frac{1}{K} \right) \left( \frac{\sqrt{3} \sqrt[3]{J_3/2}}{\sqrt{J_2}} \right)^3 \right] \quad (4.23)$$

where  $J_3$  is the third deviatoric stress invariant. By using “ $s$ ” in Eqn 4.22 instead of  $\sqrt{J_2}$  in Eqn. 4.1, the shape of the yield surface in the deviatoric plane

is changed and is no longer circular. Based on Eqn 4.23, when  $\frac{\sqrt{3} \sqrt[3]{J_3/2}}{\sqrt{J_2}} = 1$

(corresponding to the triaxial compression case),  $s = \sqrt{J_2}$  ; when

$\frac{\sqrt{3} \sqrt[3]{J_3/2}}{\sqrt{J_2}} = -1$  (corresponding to the biaxial compression case),  $s = \frac{1}{K} \sqrt{J_2}$  .

Therefore, if suitable parameters are selected so that Eqn 4.22 represents the same failure curve as Eqn 4.1 in the meridian plane for the case of triaxial compression,

the failure surface for the case of biaxial compression can be represented by the following equation:

$$F = \sqrt{J_2} - K\theta_1 - Kk \quad (4.24)$$

The modified yield surface in the deviatoric plane and that in the meridian plane are shown in Figure 4.14. However, in the Extended Drucker-Prager Model of ABAQUS, the  $K$  value is limited between 0.778 and 1.0 to ensure the convexity of the yield surface. The lower limit of  $K$  value is larger than the experimental value (about 0.7, see Appendix 4.2) and thus this model tends to overestimate the strength of concrete under biaxial compression. Nevertheless, the  $K$  value does not affect the results for concrete under triaxial compression, as long as the  $\theta$  value is calibrated with empirical equations for triaxial compression.

The Extended Drucker-Prager Model also allows the user to define the strain hardening/softening function and input a dilation angle, either the same as or different from, the friction angle to allow either the associated or the non-associated flow rule to be used.

#### *4.3.3.2 Solution-dependent field variables (SDFV) in ABAQUS*

In ABAQUS, the material properties can be set to be dependent on the solution-dependent field variables using the user-defined subroutine USDFLD. A solution-dependent field variable is a field variable that varies throughout the solution process (such as the displacement and the stresses). This facility provides the possibility for the material models in ABAQUS to account for additional material characteristics.

In the present study, the option of SDFV was adopted to define the dependence of strain hardening/softening on the confining pressure, and the dependence of the flow rule on the confining pressure, the plastic deformation and the rate of confining pressure increment. By doing so, the variations of the material properties during the loading process can be appropriately captured.

#### *4.3.3.3 Implementation of the proposed modifications in ABAQUS*

##### (1) Yield criterion

The yield criterion of the Extended Drucker-Prager Model was directly adopted, with  $\theta = 0.2624$  which was found using Teng et al.'s (2006a) equations (see Appendix 4.1), and  $K = 0.78$ . The use of this  $K$  instead of 0.725 found from empirical equations (see Appendix 4.2) is due to the limitation of the Extended Drucker-Prager Model in ABAQUS as explained earlier.

##### (2) Hardening rule

The confinement-dependent hardening rule was implemented in ABAQUS through the following procedure:

- (a) obtain a series of axial stress-strain relationships of concrete for various active confining pressures using Teng et al.'s (2006a) model, based on given values of the unconfined concrete strength and the corresponding strain of concrete;

(b) obtain the corresponding axial stress-plastic strain relationships of concrete for different confining pressures based on the initial elastic modulus, the initial Poisson's ratio and the equation below:

$$\varepsilon_c^p = \varepsilon_c - \frac{\sigma_c}{E_c} + 2 \frac{\sigma_l}{E_c} \nu_c \quad (4.25)$$

where  $E_c$  and  $\nu_c$  are the initial values of the elastic modulus and Poisson's ratio of concrete respectively. The empirical equations below were adopted for  $E_c$  and  $\nu_c$  when experimental values were not available.

$$E_c = 4730 \sqrt{f'_{co}} \quad (4.26)$$

$$\nu_c = 0.18 \quad (4.27)$$

(c) input these relationships into ABAQUS in the required format, in which the association of the stress-strain relationship with the confining pressure is defined using the SDFV option.

A computer program was developed to produce the input material data. The only parameters needed for the program are the unconfined concrete strength and the corresponding strain as stated earlier.

### (3) Flow rule

The confinement-dependent flow rule was implemented through the following procedure:

(a) obtain a series of axial strain-lateral strain relationships of concrete for various confining pressures using Teng et al.'s (2006a) model;

(b) obtain a series of axial strain-lateral strain relationships of FRP-confined concrete for different  $\frac{E_{frp}t_{frp}}{R_o}$  values using Teng et al.'s (2006a) model;

for FRP-confined concrete 
$$\frac{\Delta\sigma_l}{\Delta\varepsilon_l} = \frac{\sigma_l}{\varepsilon_l} = \frac{E_{frp}t_{frp}}{R_o};$$

(c) calculate the dilation angles under different conditions based on the axial strain-lateral strain relationships obtained from steps (a) and (b) and Eqns 4.15, 4.25 and the following equation:

$$\varepsilon_l^p = \varepsilon_l - \frac{\sigma_l}{E_c}(1 - \nu_c) + \frac{\sigma_c}{E_c}\nu_c \quad (4.28)$$

(d) input the variation of the dilation angle with the plastic deformation, the confining pressure and the rate of confining pressure increment into ABAQUS in the required format, in which the SDFV option was once again adopted.

A computer program was again developed to produce the input material data.

#### 4.3.4 Verification of the Proposed Modifications and Discussions

Since the material parameters for the modified D-P model proposed here were obtained from the analysis-oriented model of Teng et al. (2006a), it can be expected that the proposed model has the same accuracy as Teng et al.'s (2006a) model. Several numerical tests (i.e. FE analyses) were conducted for verification as shown below. For the concrete under a uniform active confining pressure, only

a single 8-node solid element was used. For the FCSC specimen, the FE model was for a vertical slice of the specimen and consisted of a single-layer of 8-node solid elements for the concrete tied to 4-node shell elements for the FRP jacket. The FRP jacket was simulated to behave in a linear elastic manner with stiffness in the hoop direction only.

(1) Numerical test I: actively-confined concrete

Figure 4.15 shows a comparison between the predictions obtained from the proposed model and the test results reported by Sfer et al. (2002) for actively-confined concrete. The concrete has an unconfined strength of 32.8 MPa and a corresponding strain of 0.0018, and is confined by a constant pressure of 9 MPa. Results from Teng et al.'s (2006a) analysis-oriented model are also shown in Figure 4.15 for reference. It is evident that the FE results are almost identical to the predictions of Teng et al.'s (2006a) model, and are very close to the experimental stress-strain curve.

(2) Numerical test II: FRP-confined concrete

In this numerical test, a two-ply FRP-confined solid concrete cylinder, which has been denoted as "S40-2-II" in Chapter 3, was simulated using the proposed D-P type model. The cylinder had a diameter of 152.5 mm; the concrete had an unconfined strength of 39.6 MPa and a corresponding strain of 0.0026; the FRP jacket had an elastic modulus of 80100 MPa, and a thickness of 0.17 mm per ply. The FE results are compared with the test results and the predictions from Teng et al.'s (2006a) model in Figure 4.16. It is evident that they are in close agreement with each other.

### (3) Numerical test III: Oh's (2002) approach for FRP-confined concrete

This numerical test was conducted to demonstrate that the confining pressure-dependent non-associated flow rule proposed by Oh (2000), which is capable of accurate predictions of the behavior of actively-confined concrete, cannot provide reasonably close predictions of the behavior of FRP-confined concrete. A D-P model with the flow rule related to the confining pressure and the plastic deformation but not the rate of confining pressure increment, following the work of Oh (2000), was employed in this numerical test. The FE results obtained with this D-P model, denoted as "FE results (Oh)", are compared with the test results in Figure 4.17. The FE results from the model adopted in numerical test II, denoted as "FE results", are also shown in Figure 4.17 for reference. It is clear from Figure 4.17 that there are considerable differences between "FE results (Oh)" and the test results. The FE analysis with a D-P model following Oh's (2000) approach overestimates the dilation of FRP-confined concrete and thus overestimates its axial stress-strain behavior. This further demonstrates the importance of including the dependence of the flow rule on the rate of confining pressure increment in modeling passively-confined concrete.

The preceding comparisons show that the modified D-P type plasticity model proposed here can accurately predict the behavior of both actively-confined and FRP-confined concrete. However, this model still has its limitations. Firstly, the softening behavior of confined concrete is simulated using the hardening/softening function  $k$ , which involves the retraction of the yield surface

in the stress space. This may cause numerical difficulty during the finite element analysis. Secondly, the D-P type plasticity model cannot simulate the reduction of elastic stiffness during the loading process, which however has been widely observed in previous experimental work (Maekawa et al. 2003). This limitation does not affect the numerical simulation results of monotonic tests but does affect those of cyclic tests. Thirdly, the shear strength ratio allowed in the Extended D-P Model of ABAQUS are significantly higher than the typical experimental values of concrete and tends to overestimate the strength of concrete under non-uniform confinement. Lastly, the proposed modifications are calibrated with empirical equations for concrete under uniform confinement and improvements may be necessary when they are applied to concrete under non-uniform confinement.

The first two limitations mentioned above can be overcome by including damage into a concrete plasticity model, forming a so-called plastic-damage model, as mentioned in Chapter 2. By doing so, both strain softening and the degradation of elastic constants can be simulated as the damage of concrete. In the next chapter, an improved plastic-damage model, which is within the theoretical framework of the Concrete Damaged Plasticity Model (CDPM) in ABAQUS and takes due account of the conclusions reached in this chapter, will be presented. The CDPM provided in ABAQUS allows a wider range of shear strength ratios to be used and thus does not suffer from the third limitations mentioned above. The distinct deformation characteristics of non-uniformly confined concrete are also taken into account in this improved model so that it can be applied to concrete under various non-uniform confinement. Numerical results for the new hybrid DSTCs, obtained using this plastic-damage model, will also be presented in Chapter 5.

## Appendix 4.1

Based on Richart et al. (1928),

$$f'_{cc} = f'_{co} + 4.1\sigma_l \quad (4.A.1)$$

Therefore,

$$I_1 = f'_{co} + 6.1\sigma_l \quad (4.A.2)$$

and

$$\sqrt{J_2} = \frac{(f'_{co} + 3.1\sigma_l)}{\sqrt{3}} \quad (4.A.3)$$

at the peak concrete stress. Consequently,

$$\frac{(f'_{co} + 3.1\sigma_l)}{\sqrt{3}} - \theta(f'_{co} + 6.1\sigma_l) - k = 0 \quad (4.A.4)$$

and

$$\left(\frac{1}{\sqrt{3}} - \theta\right)f'_{co} - \left(6.1\theta - \frac{3.1}{\sqrt{3}}\right)\sigma_l - k = 0 \quad (4.A.5)$$

As  $\theta$  is a constant not related to the current stress state, it is necessary that

$$6.1\theta - \frac{3.1}{\sqrt{3}} = 0 \quad (4.A.6)$$

As a result,

$$\theta = 0.2934, \quad \arctan \theta = 16.3 \text{ degrees} \quad (4.A.7)$$

Similarly, with the following equation proposed by Teng et al. (2006a),

$$f'_{cc} = f'_{co} + 3.5\sigma_l \quad (4.A.8)$$

it can be easily shown that

$$\theta = 0.2624, \quad \arctan \theta = 14.7 \text{ degrees} \quad (4.A.9)$$

## Appendix 4.2

The shear strength ratio between biaxial compression and triaxial compression can be calculated using the empirical equations for the strengths of concrete under biaxial compression and triaxial compression. For instance, if the biaxial compressive strength of concrete is assumed to be equal to 1.16 times the uniaxial compressive strength (Kupfter et al. 1969) and Richart et al.'s (1928) equation is adopted to calculate the strength of confined concrete, the shear strength ratio can be calculated to be 0.69, as shown below.

For concrete under triaxial compression, Eqns 4.A.1-4.A.3 can be used to obtain the peak stress and the corresponding stress invariants.

For concrete under biaxial compression:

$$I_1 = 2.32f'_{co} \quad (4.A.10)$$

$$\sqrt{J_2} = \frac{1.16f'_{co}}{\sqrt{3}} \quad (4.A.11)$$

Imposing the condition that the values of  $I_1$  for the two cases are the same using Eqn 4.A.2 and Eqn 4.A.10, one obtains

$$\sigma_l = 0.22f'_{co} \quad (4.A.12)$$

Therefore the shear strength ratio of concrete under biaxial compression to that under triaxial compression is equal to

$$\frac{1.16f'_{co}}{f'_{co} + 3.1 * 0.22f'_{co}} = 0.69 \quad (4.A.13)$$

Similarly, if Eqn 4.A.8 proposed by Teng et al. (2006a) is adopted, the shear strength ratio is found to be 0.725.

Table 4.1 Summary of existing D-P type models for FRP-confined concrete

D-P type model	Yield criterion	Hardening rule		Flow rule
		Including strain hardening/softening?	Related to the confining pressure?	
Fang (1999)	Eqn 4.1	No	/	Associated flow rule
Mahfouz et al. (2001)	Eqn 4.1	Yes	No	Associated flow rule
Lan (1998)	Eqn 4.1	Yes	Yes (via experimental stress-strain curves of actively-confined concrete)	Associated flow rule
Karabinis and Kiousis (1994)	Eqn 4.1	Yes	Yes (via Eqn 4.6)	Non-associated flow rule with a constant dilation angle
Karabinis and Kiousis (1996)	Including the third deviatoric stress invariant	Yes	Yes (via Eqn 4.6)	Non-associated flow rule with a constant dilation angle
Karabinis and Rousakis (2002)	Eqn 4.1	Yes	Yes (via Eqn 4.6)	Non-associated flow rule with a dilation angle varying with the plastic deformation
Mirmiran et al. (2000) Shahawy et al. (2000)	Eqn 4.1	No	/	Non-associated flow rule with a constant dilation angle
Oh (2002)	Eqn 4.1	Yes	Yes (via empirical equations for actively-confined concrete)	Non-associated flow rule with a dilation angle varying with both the plastic deformation and the confining pressure

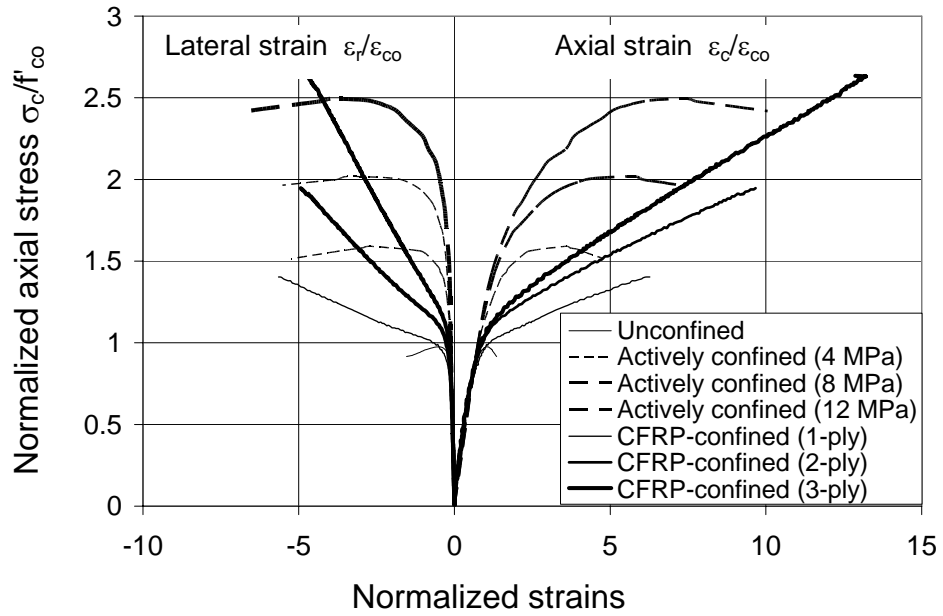
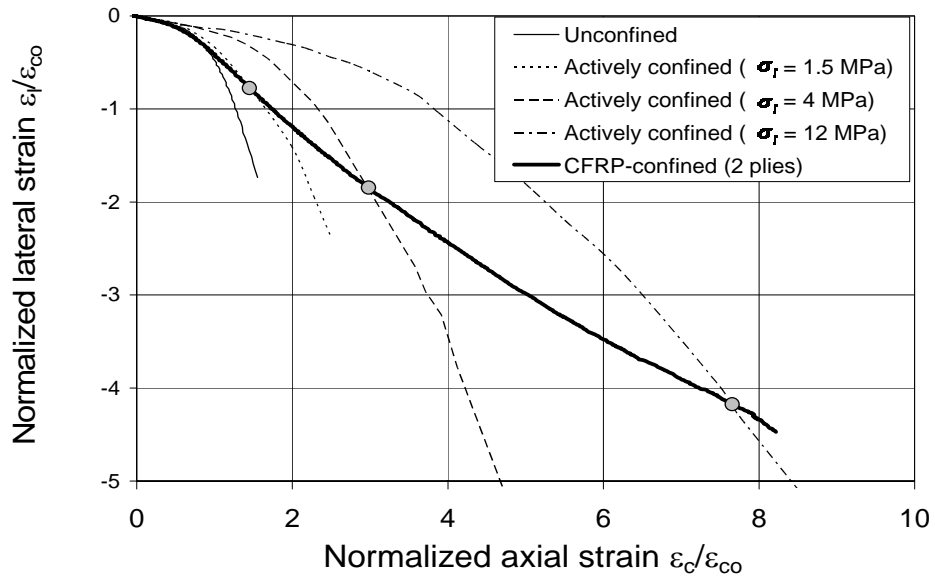
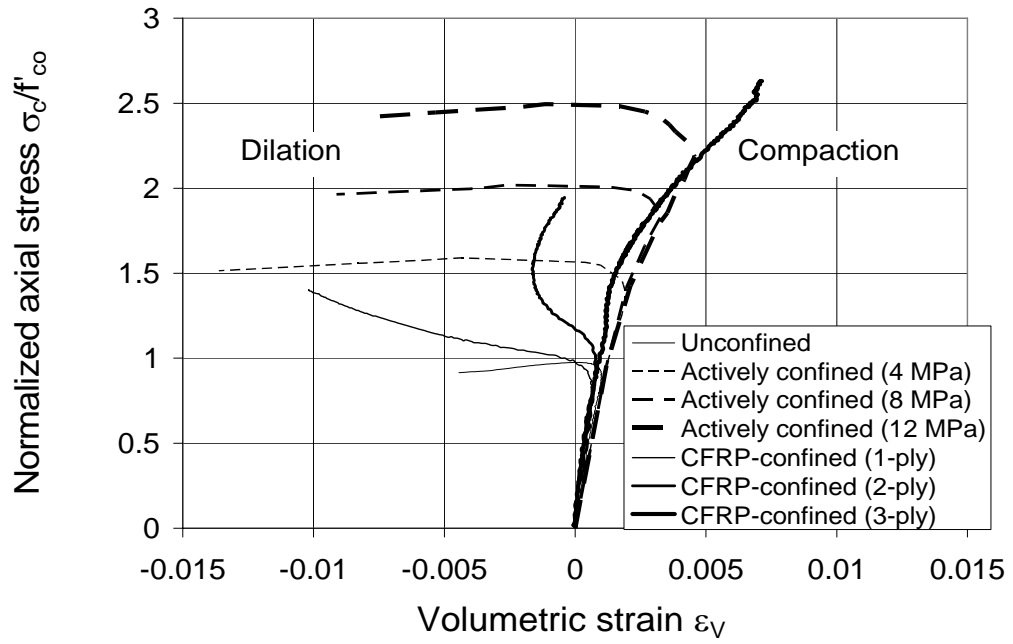


Figure 4.1 Stress-strain curves of confined concrete (Teng and Lam 2004)



(a) Lateral strain-axial strain responses of unconfined and confined concrete (Teng et al. 2006a)

Figure 4.2 Dilation properties of confined concrete



(b) Stress-volumetric strain responses of confined concrete  
(Teng and Lam 2004)

Figure 4.2 Dilation properties of confined concrete (Cont'd)

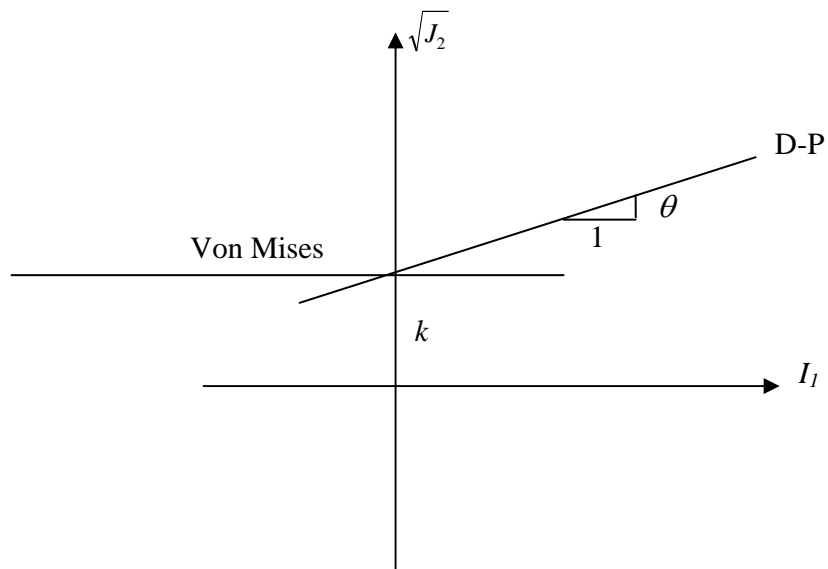


Figure 4.3 Drucker-Prager yield surface in the meridian plane

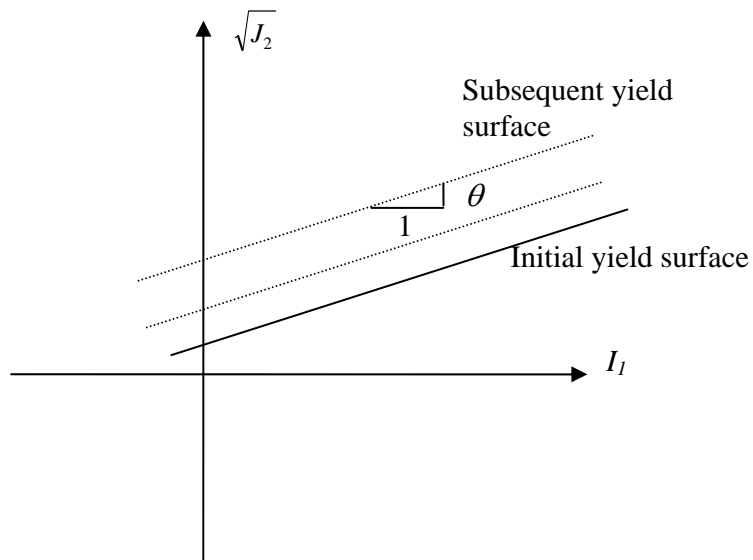


Figure 4.4 Initial and subsequent yield surfaces in the meridian plane

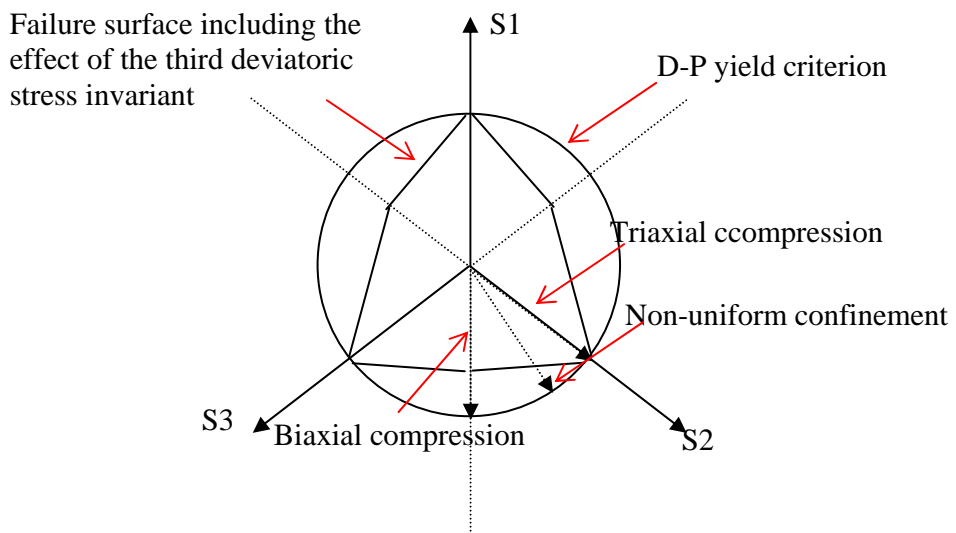


Figure 4.5 Failure surfaces in the deviatoric plane

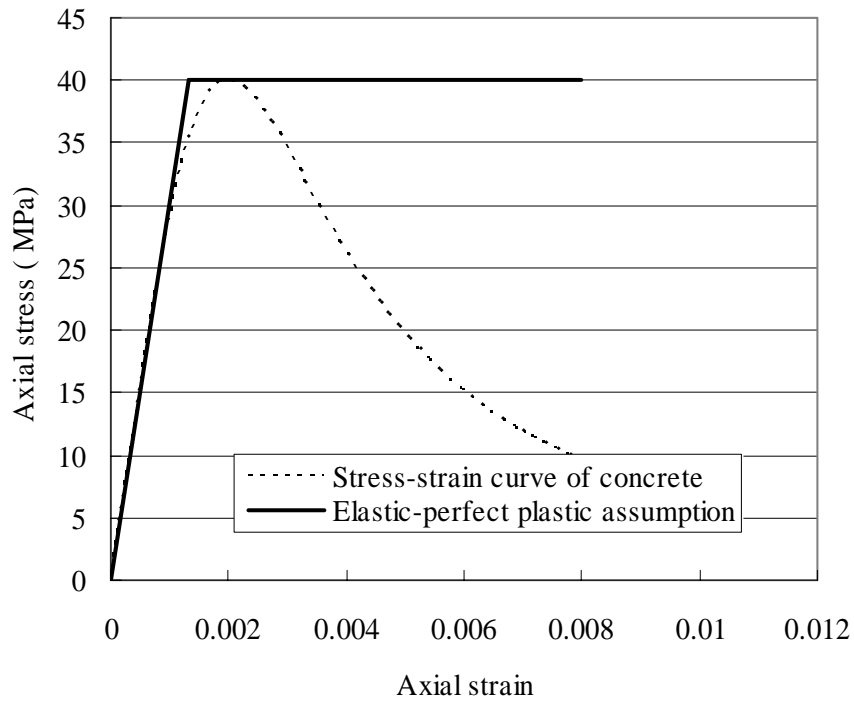


Figure 4.6 Axial stress-strain curve of concrete under uniaxial compression

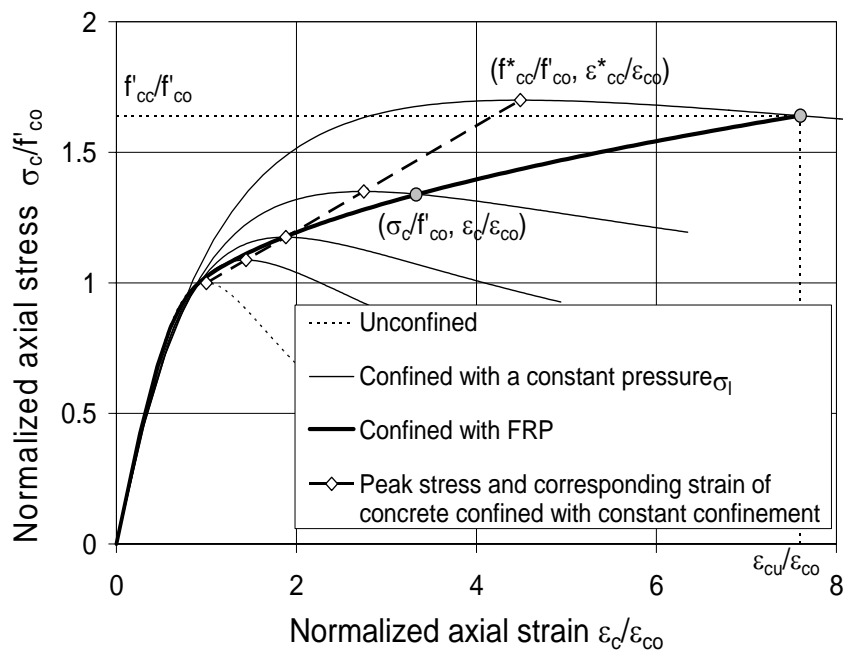


Figure 4.7 Theoretical stress-strain curves of FRP- and actively-confined concrete (Teng et al. 2006a)

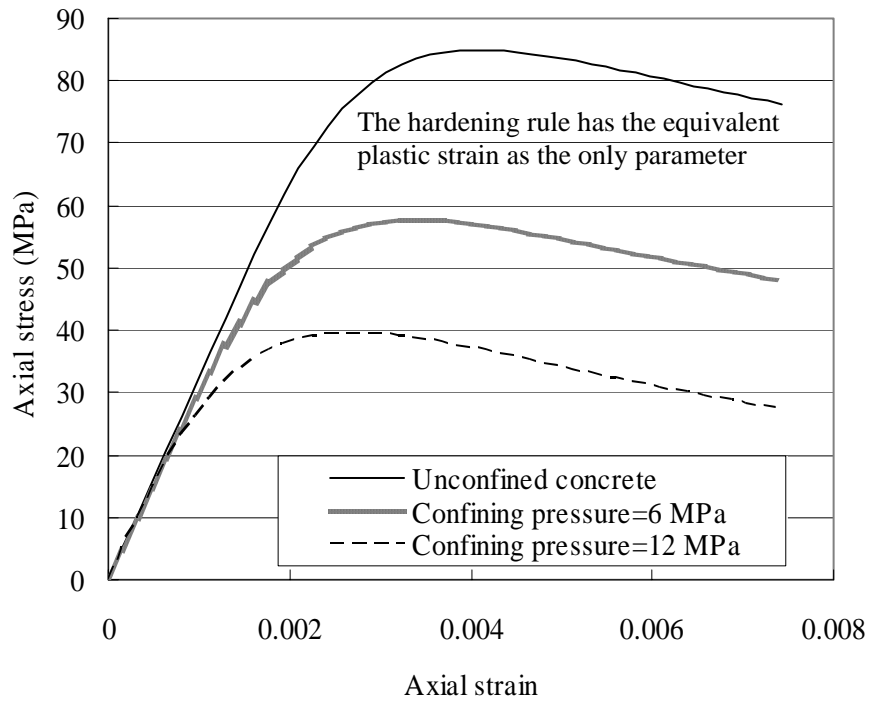


Figure 4.8 Theoretical axial stress-strain curves of unconfined and confined concrete

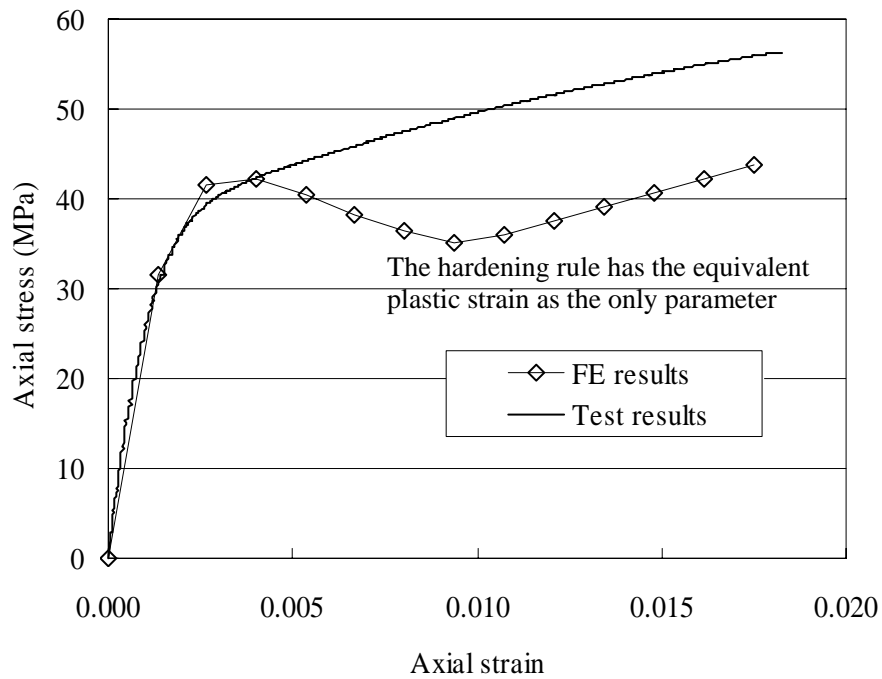


Figure 4.9 Axial stress-strain curves of FRP-confined concrete

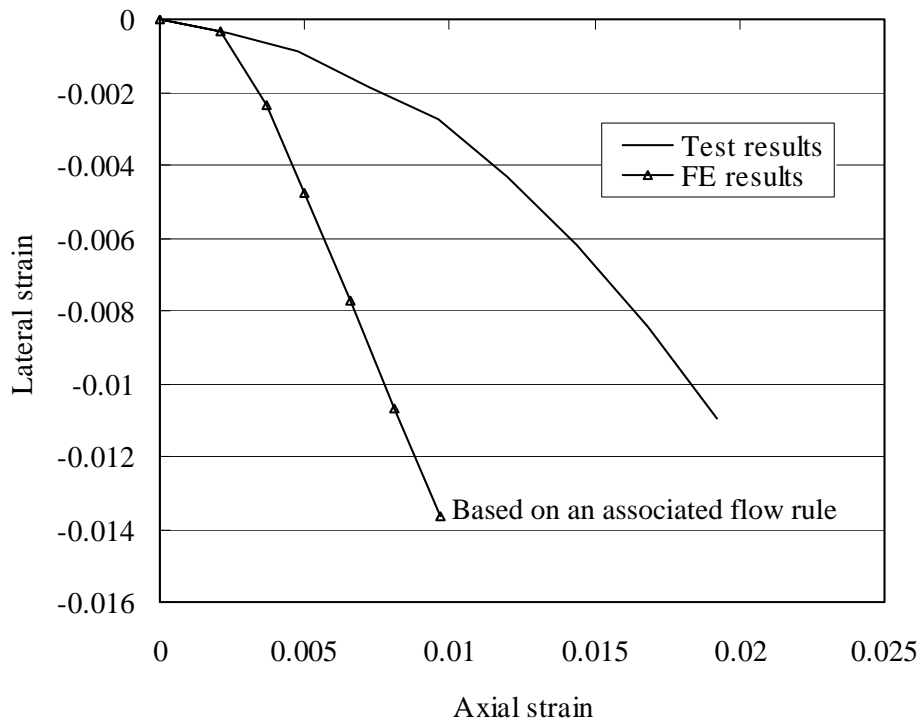


Figure 4.10 Theoretical axial-lateral strain curves of actively-confined concrete

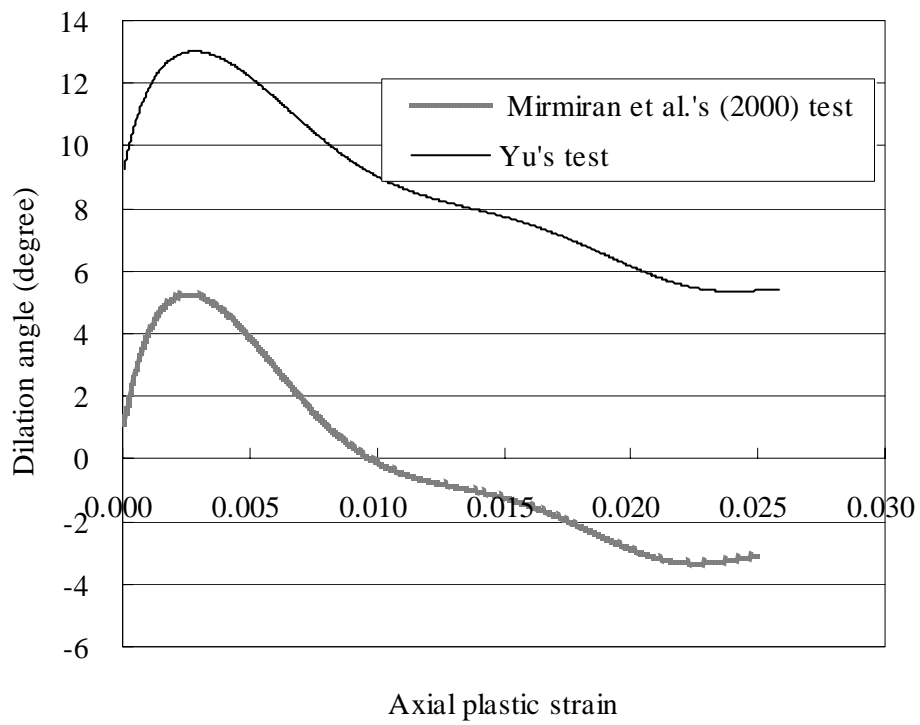
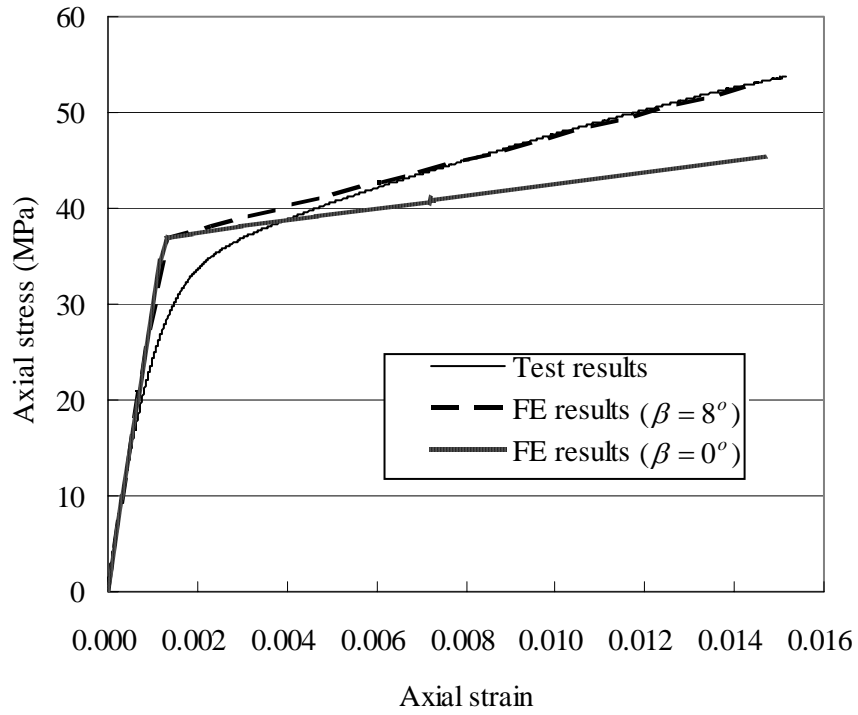
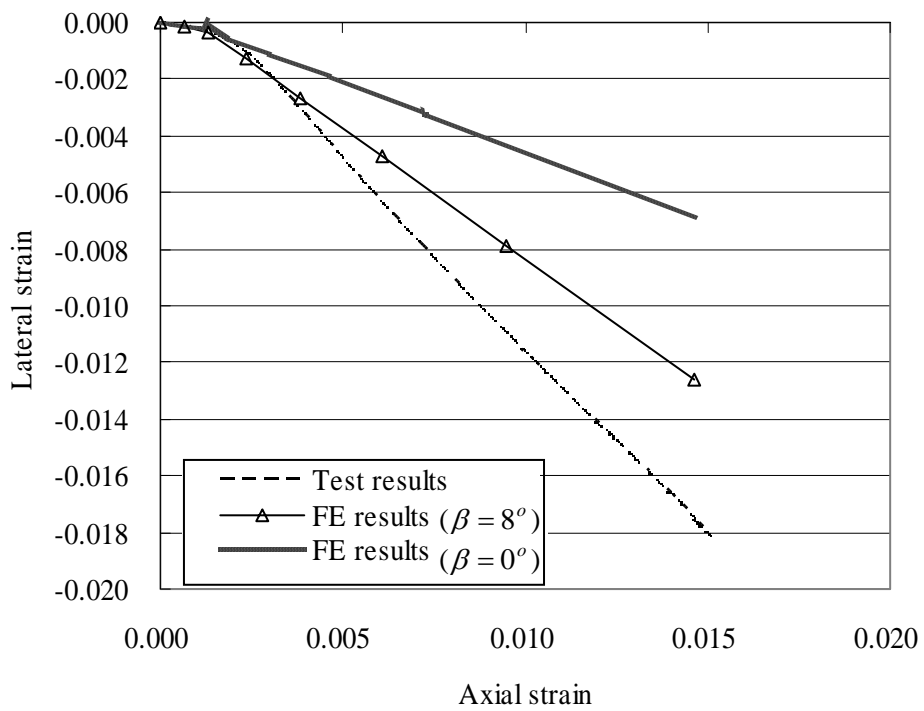


Figure 4.11 Dilation angle of FRP-confined concrete from Teng et al.'s (2006a) model



(a) Axial stress-strain curves



(b) Axial-lateral strain curves

Figure 4.12 FE results from a D-P model with a constant dilation angle for Yu's test

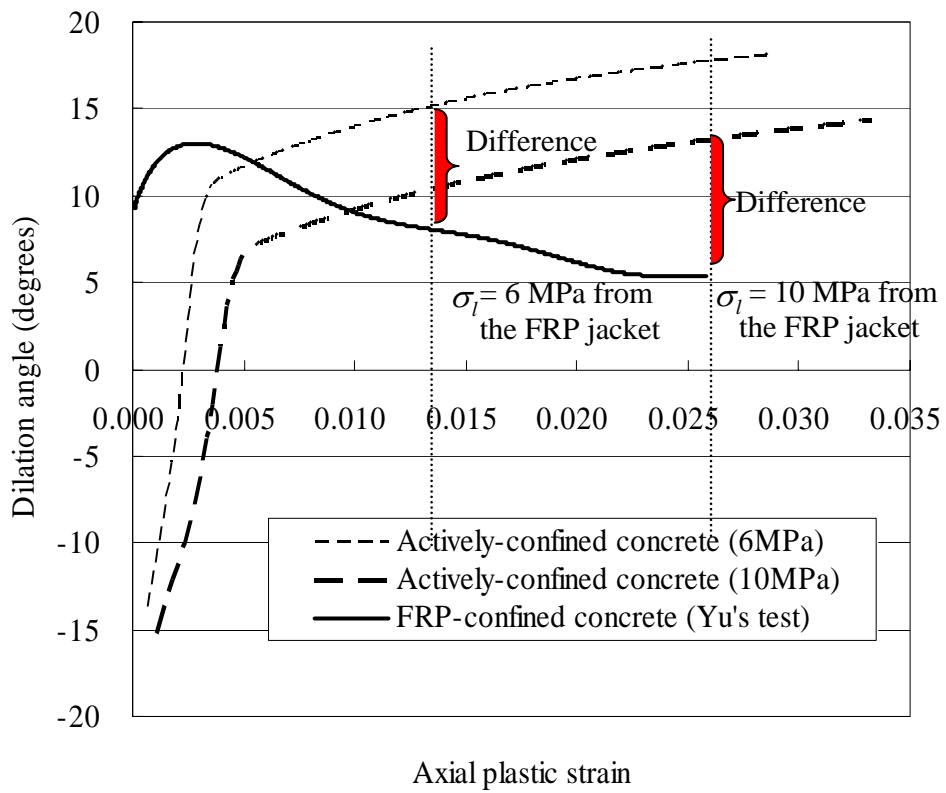
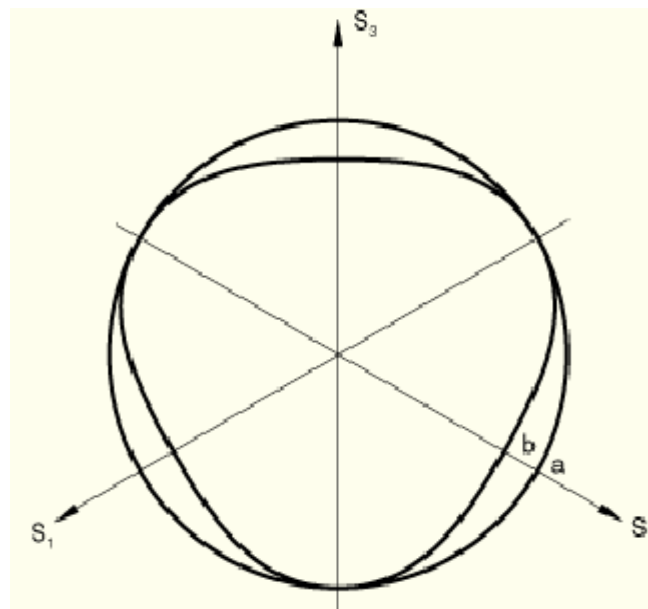
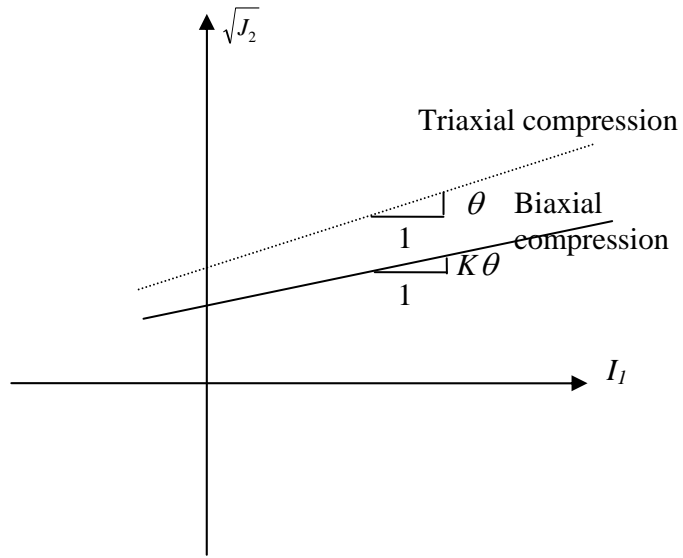


Figure 4.13 Comparison between actively-confined and FRP-confined concrete



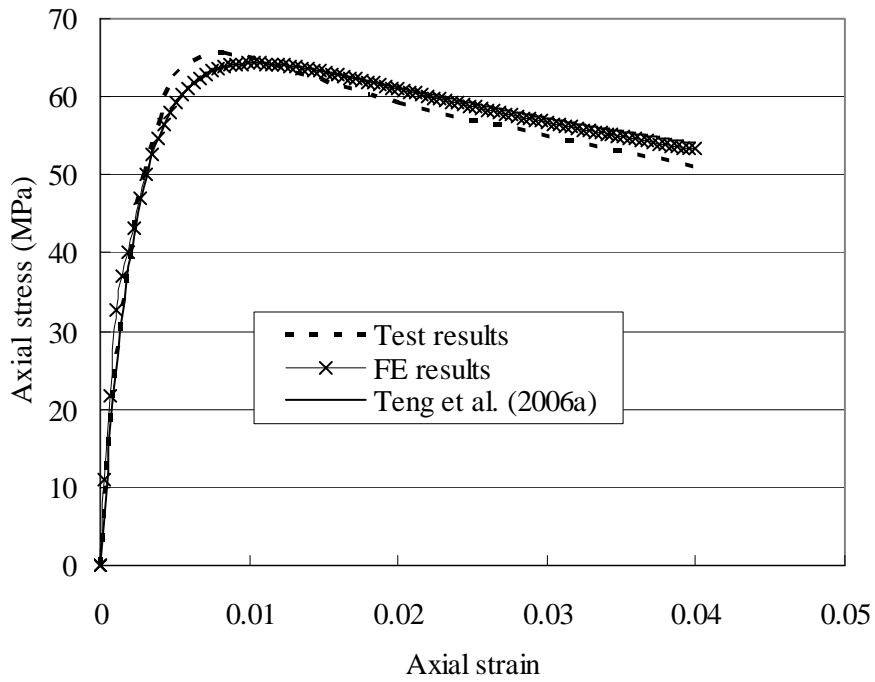
(a) Failure surface in the deviatoric plane (ABAQUS 2004)

Figure 4.14 Failure surface of the Extended Drucker-Prager Model in ABAQUS



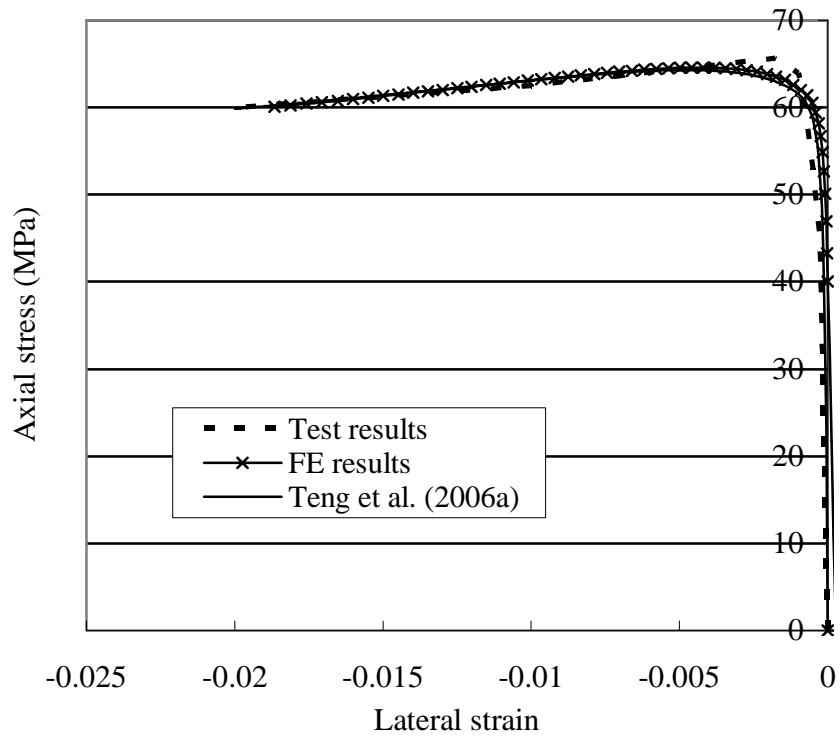
(b) Failure curve in the meridian plane

Figure 4.14 Failure surface of the Extended Drucker-Prager Model in ABAQUS  
(Cont'd)

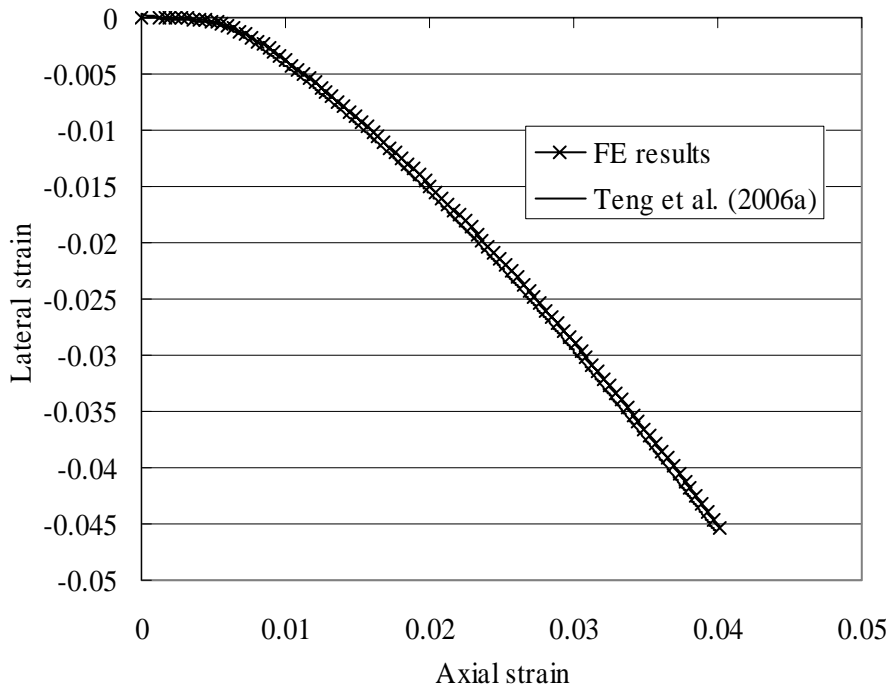


(a) Axial stress-strain curves

Figure 4.15 FE results for actively-confined concrete from numerical test I

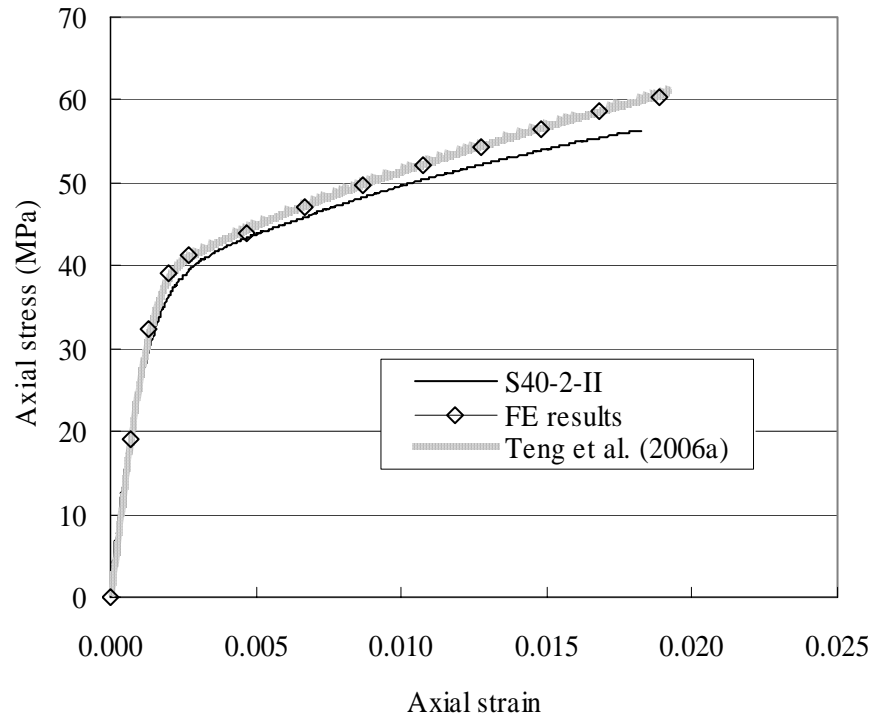


(b) Axial stress-lateral strain curves

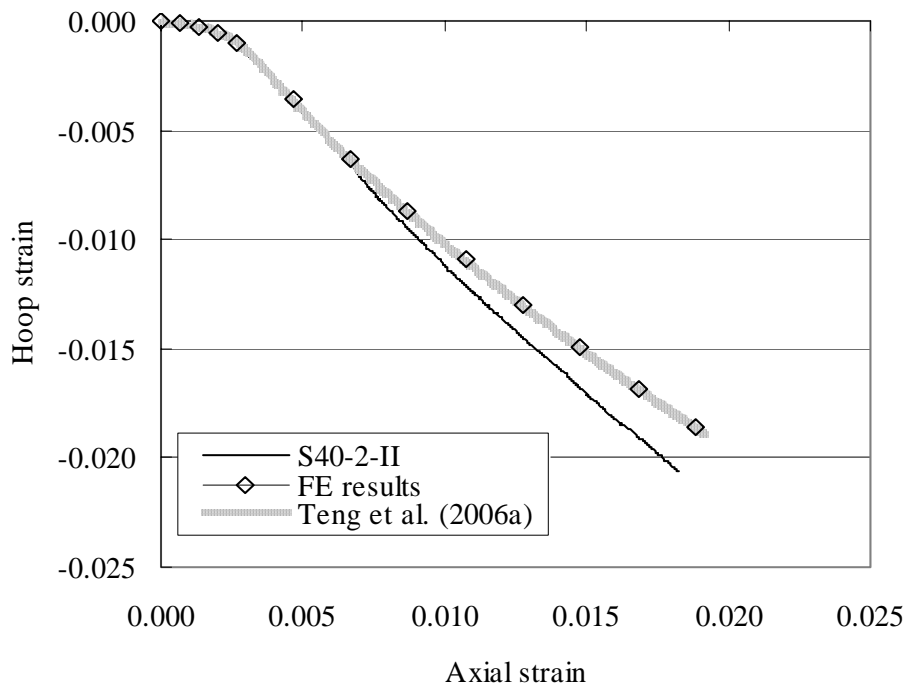


(c) Lateral strain-axial strain curves

Figure 4.15 FE results for actively-confined concrete from numerical test I (Cont'd)

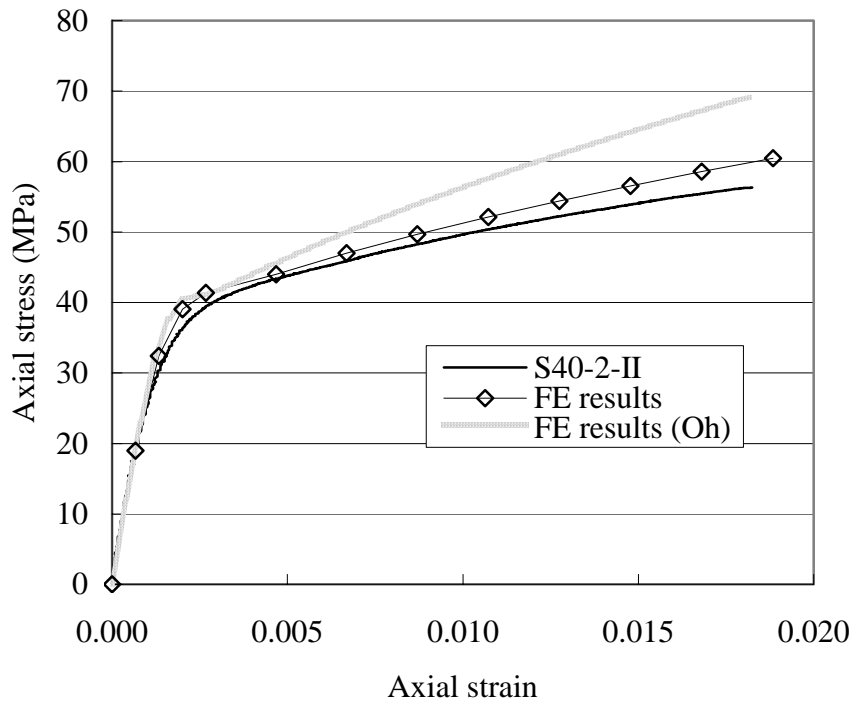


(a) Axial stress-strain curves

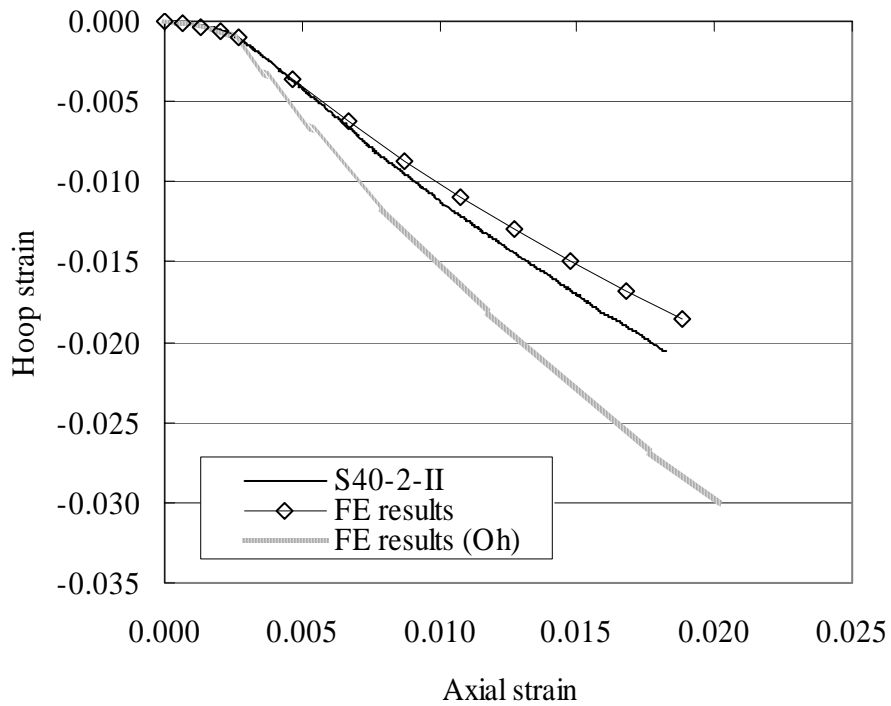


(b) Hoop strain-axial strain curves

Figure 4.16 FE results for FRP-confined concrete from numerical test II



(a) Axial stress-strain curves



(b) Hoop strain-axial strain curves

Figure 4.17 FE results for FRP-confined concrete from numerical test III

# **CHAPTER 5**

## **FINITE ELEMENT MODELING OF HYBRID DSTCS**

### **5.1 INTRODUCTION**

It was concluded in Chapter 4 that a D-P type plasticity model leading to close predictions of the behavior of confined concrete, including actively-confined concrete and FRP-confined concrete, should include a strain-hardening/softening rule and a flow rule that are both confinement-dependent, and a yield criterion dependent on the third deviatoric stress invariant.

In this chapter, an improved constitutive model, which takes due account of the conclusions reached in Chapter 4 on concrete plasticity, confinement-dependent damage and other distinct characteristics of non-uniformly confined concrete, is first discussed. The inclusion of damage is to simulate the elastic stiffness reduction of concrete while the inclusion of the other distinct characteristics of non-uniformly confined concrete is also necessary as is discussed later. Verification of the model with test results of concrete under both uniform and non-uniform confinement is then presented.

A finite element (FE) analysis is next presented for hybrid DTSCs under axial compression, using the proposed constitutive model. The predictions by the FE model are compared with the test results of such columns presented in Chapter 3. Finally, a parametric study is presented based on which a design-oriented stress-strain model is proposed.

## **5.2 IMPROVED CONSTITUTIVE MODEL FOR CONCRETE**

### **5.2.1 Introduction**

In general, the nonlinearity of concrete under compression can be modeled by approaches based on the concept of either damage or plasticity, or both (Maekawa et al. 2003). Plasticity is generally defined as the unrecoverable deformation of concrete after all loads have been removed. Damage is generally characterized by the reduction of elastic constants and capacity of absorbing elastic strain energy. Both the reduction of unloading stiffness and unrecoverable deformation have been clearly observed in real concrete compression tests (Oshima and Hashimoto 1984; Maekawa et al. 2003) as shown in Figure 5.1, which suggests that the concept of plasticity should be combined with the concept of damage to correctly represent the nonlinear behavior of concrete.

In this section, an improved constitutive model for concrete, which is within the theoretical framework of the Concrete Damaged Plasticity Model (CDPM) provided in ABAQUS but includes necessary modifications to reflect the properties of confined concrete, is discussed. The proposed modifications include modifications to the plasticity part and the damage variable, and modifications to

reflect the characteristics of concrete under non-uniform confinement. The modifications to the plasticity part are similar to those introduced in the previous chapter. The dependence of the damage variable on the confining pressure is included. The unique properties of concrete under non-uniform confinement are also appropriately considered.

### 5.2.2 Concrete Damaged Plasticity Model (CDPM) in ABAQUS

The Concrete Damaged Plasticity Model in ABAQUS provides a general capability for modeling concrete in all types of structures (beams, trusses, shells and solids). It uses concepts of isotropic damage in combination with isotropic tensile and compressive plasticity to represent the inelastic behavior of concrete, and is designed for applications in which concrete is subjected to monotonic, cyclic and/or dynamic loadings (ABAQUS 2004). The key aspects of this model in terms of the compressive behavior of concrete, including the damage variable, the yield criterion, the hardening rule, and the flow rule, are summarized as follows. In this chapter, compressive stresses/strains are defined to be positive while tensile strains/stresses are defined to be negative, unless otherwise specified.

#### 5.2.2.1 Damage

The scalar damaged elasticity equation is adopted, which takes the following form:

$$\sigma_{ij} = (1 - d)D_{ijkl}^e (\varepsilon_{ij} - \varepsilon_{ij}^p) \quad (5.1)$$

where  $\sigma_{ij}$  is the stress tensor,  $\varepsilon_{ij}$  and  $\varepsilon_{ij}^p$  are the strain tensor and the plastic strain tensor respectively,  $D_{ijkl}^e$  is the initial (undamaged) elasticity matrix and  $d$  is the damage variable which characterizes the degradation of the elastic stiffness.

In general, the scalar damage variable is determined by a series of equations which take into account the effect of both tensile and compressive damage, and the effect of stiffness recovery which is associated with stress reversals in cases of cyclic loading. When concrete is subjected to uniaxial monotonic compression, Eqn 5.1 is simplified to:

$$\sigma_1 = (1 - d) E_c (\varepsilon_1 - \varepsilon_1^p) \quad (5.2)$$

where  $\sigma_1$  and  $\varepsilon_1$  are the compressive stress and strain of concrete in the loading direction respectively;  $\varepsilon_1^p$  is the plastic strain in the loading direction;  $E_c$  is the initial elastic modulus of concrete.

The effective stress  $\bar{\sigma}_1$  is defined as:

$$\bar{\sigma}_1 = \frac{\sigma_1}{1 - d} \quad (5.3)$$

Similarly, the first effective stress invariant  $\bar{I}_1$  and the second effective deviatoric stress invariant  $\bar{J}_2$  are defined in terms of the effective stress tensor.

$$\bar{I}_1 = \bar{\sigma}_{ii} \quad (5.4)$$

$$\bar{J}_2 = \frac{1}{2} \bar{S}_{ij} \bar{S}_{ij} \quad (5.5)$$

where  $\bar{S}_{ij}$  is the effective deviatoric stress tensor.

### 5.2.2.2 Yield criterion

The model adopts the yield function proposed by Lubliner et al. (1989) and modified by Lee and Fenves (1998). In terms of effective stresses, the yield function takes the following form.

$$F = \frac{1}{1-A} (\sqrt{3J_2} - A\bar{I}_1 + B(\tilde{\varepsilon}_p) \langle -\bar{\sigma}_{\min} \rangle - C \langle \bar{\sigma}_{\min} \rangle) - \bar{\sigma}_{cn}(\tilde{\varepsilon}_{pc}) = 0 \quad (5.6)$$

with

$$A = \frac{f'_b / f'_{co} - 1}{2f'_b / f'_{co} - 1}; \quad 0 \leq A \leq 0.5, \quad (5.7)$$

$$B = \frac{\bar{\sigma}_{cn}(\tilde{\varepsilon}_{pc})}{\sigma_m(\tilde{\varepsilon}_{pt})} (1-A) - (1+A), \quad (5.8)$$

$$C = \frac{3(1-K)}{2K-1}. \quad (5.9)$$

Here,

$\bar{\sigma}_{\min}$  is the minimum principal effective stress;

$f'_b$  is the concrete strength under biaxial compression;

$\bar{\sigma}_{cn}$  and  $\bar{\sigma}_m$  are the effective compressive and tensile cohesion stresses respectively;

$\tilde{\varepsilon}_{pc}$  and  $\tilde{\varepsilon}_{pt}$  are the equivalent compressive and tensile plastic strains respectively;

$K$  is the strength ratio of concrete under biaxial compression to triaxial compression

Typical yield surfaces in the deviatoric plane are shown in Figure 5.2(b) for different values of  $K$ .

For the case of triaxial compression, Eqn 5.6 reduces to the Drucker-Prager yield condition expressed in Eqn 5.10.

$$\left(\frac{1}{3}C + 1\right)\sqrt{3J_2} - \frac{(C + 3A)}{3}\bar{I}_1 = (1 - A)\bar{\sigma}_{cn} \quad (5.10)$$

Compared with Eqn 4.1, the friction parameter  $\theta$  and  $k$  in Eqn 4.1 can be expressed by:

$$\theta = \frac{\sqrt{3}(C + 3A)}{3(C + 3)} \quad (5.11)$$

$$k = \frac{\sqrt{3}(1 - A)}{C + 3}\bar{\sigma}_{cn} \quad (5.12)$$

Therefore, the value of  $C$  can be found based on the value of  $\theta$  which is related to the strength of concrete under triaxial compression (see Appendix 4.1), and the value of  $A$  which is related to the strength of concrete under biaxial compression (Eqn 5.7). The yield surface of concrete under compression (with the minimum principal stress larger than zero) can be represented in the meridian plane by a linear curve for the case of triaxial compression (Figure 5.2(a)) and in the deviatoric plane by a non-circular curve (Figure 5.2(b)).

### 5.2.2.3 Hardening rule

For concrete under uniaxial monotonic compression, the strain hardening/softening function can be defined in the CDPM by

$$\bar{\sigma}_{cn} = \bar{\sigma}_{cn}(\tilde{\epsilon}_p) \quad (5.13)$$

#### 5.2.2.4 Flow rule

A non-associated flow rule is assumed in the CDPM. The flow potential adopted in this model is the Drucker-Prager hyperbolic function (Eqn 5.14).

$$d\varepsilon_{ij}^p = \lambda \frac{\partial G}{\partial \sigma_{ij}}; \quad G = \sqrt{(\varepsilon \sigma_{to} \tan \psi)^2 + \bar{J}_2} - \bar{I}_1 \tan \psi \quad (5.14)$$

where  $\psi$  is the dilation angle measured in the meridian plane at high confining pressure;  $\sigma_{to}$  is the uniaxial tensile stress at failure;  $\varepsilon$ , referred to as the eccentricity, defines the rate at which the function approaches the asymptote. The flow potential tends to a straight line when the eccentricity  $\varepsilon$  is close to zero. A typical curve of the flow potential in the meridian plane is shown in Figure 5.3. It is seen (Figure 5.3) that the dilation angle is very close to  $\psi$  when the concrete is under compression.

### 5.2.3 Proposed Modifications

It was concluded in Chapter 4 that a plasticity model leading to close predictions for FRP-confined concrete should include a strain-hardening/softening rule and a flow rule that are both confinement-dependent, and a yield criterion that is dependent on the third deviatoric stress invariant. A confinement-dependent strain-hardening/softening rule is necessary to reflect the difference in the experimental stress-strain curve between confined concrete and unconfined concrete. A confinement-dependent flow rule, in which the dilation angle is related not only to the confining pressure but also to the rate of confining pressure increment, is required to capture the unique lateral expansion behavior of passively-confined concrete. A yield criterion dependent on the third deviatoric

stress invariant is necessary to simulate the experimental observation that the shear strength is different for concrete under biaxial compression and triaxial compression, even when the hydrostatic pressure is the same for both cases. In a plastic-damage model such as the CDPM in ABAQUS, a confinement-dependent damage variable also needs to be included, as strain softening is at least partially simulated by the scalar damage in such models. As the CDPM implicitly includes the effect of hydrostatic pressure and the third deviatoric stress invariant on the shear strength of concrete, modifications are proposed herein only for the hardening rule, the flow rule and the damage variable, based on the above discussions. In addition, the unique properties of concrete under non-uniform confinement are appropriately included, and are discussed later.

#### *5.2.3.1 Damage variable*

As explained earlier, concrete nonlinearity can be modeled as either damage or plasticity, or both. Different definitions of damage and plasticity lead to different plastic-damage models. When suitable material parameters are used, these different models may lead to the same prediction for concrete under monotonic loadings. However, predictions of cyclic loading tests depend significantly on how to differentiate the effects of damage and plasticity, as the definition of damage directly determines the stiffness of the unloading curve (Figure 5.1). To accurately reflect experimental observations, it is desirable to isolate the effect of damage using test results of concrete under cyclic loadings. In the present research, as only the simulation of monotonic loading tests is concerned, the following assumption is adopted for simplicity: concrete non-linearity before the peak stress is due only to concrete plasticity and strain hardening but there is no strain

hardening/softening after the peak stress has been reached. A similar assumption was adopted by Schwer (2003) and Murray and Lewis (1995) in their plastic-damage models. Besides its simplicity, the advantage of this assumption is that it simulates stress reductions after the peak stress by reductions in elastic constants instead of retractions of the yield surface in the stress space. Retractions of the yield surface are necessary to simulate the strain softening behavior in a concrete plasticity model and may cause numerical problems.

Similar to the strain hardening rule, the damage variable is assumed to be dependent on the confining pressure, as the descending branches of the stress-strain curves of confined and unconfined concrete have different slopes (see Section 4.2). Based on the assumption stated earlier, the damage variable is equal to zero before the peak stress and is given by the equations below after the peak stress.

For concrete under uniaxial compression,

$$d = 1 - \frac{\sigma_c}{f'_{co}} \quad (5.15)$$

in which  $\sigma_c$  is the axial stress of concrete on the descending branch and  $f'_{co}$  is the stress of concrete at the peak point.

For concrete with a constant confining pressure,

$$d = 1 - \frac{\sqrt{J_2} - \theta_{1c}}{\sqrt{J_{2c}} - \theta_{1c}} = 1 - \frac{\sigma_c - \frac{1+C+2A}{1-A}\sigma_l}{f'_{cc} - \frac{1+C+2A}{1-A}\sigma_l} \quad (5.16)$$

in which  $f_{cc}^*$  is the peak stress of concrete under a constant confining pressure;  $\sigma_l$  is the confining pressure;  $J_{2c}$  and  $J_2$  are the second deviatoric stress invariants corresponding to the peak stress point and a point on the descending branch respectively;  $I_{1c}$  and  $I_1$  are the first stress invariants corresponding to the peak stress point and a point on the descending branch respectively.

The confining pressure-dependent damage variable was implemented in ABAQUS through the following procedure: (1) obtain a series of axial stress-strain curves of concrete for various constant confining pressures using Teng et al.'s (2006a) model; (2) find the values of the damage variable corresponding to different axial strains and confining pressures using Eqns 5.15 and 5.16; (3) input these values for the damage variable into ABAQUS in the required format, in which the association of the damage variable with the confining pressure is defined through the SDFV option as described earlier in Chapter 4. A computer program was developed to produce the input material data.

### 5.2.3.2 Yield criterion

It is evident that the CDPM implicitly includes the effect of the first stress invariant and the third deviatoric stress invariant. The two controlling parameters of this model for concrete in compression are  $A$  and  $C$  in Eqn 5.10.

The constant  $A$  can be determined using Eqn 5.7 based on the experimental biaxial concrete strength. Kupfer et al. (1969) found from their tests that the ratio  $f_b' / f_{co}'$

is approximately 1.16, yielding a value of 0.12 for  $A$ . This value is adopted in the present research.

The constant  $C$  can be determined using Eqn 5.9 based on the experimental shear strength ratio of concrete between biaxial compression and triaxial compression. It has been shown in Appendix 4.2 that this ratio is equal to 0.725 based on empirical equations, yielding a value of 1.83 for  $C$ , which is used in the present research.

#### 5.2.3.3 Hardening rule

It has been made evident in Section 4.3 that the hardening rule should be related to the confining pressure. The equation below is adopted in the present research.

$$\bar{\sigma}_{cn} = \bar{\sigma}_{cn}(\tilde{\varepsilon}_p, \sigma_l) \quad (5.17)$$

According to the assumption stated in Subsection 5.2.3.1, the definition of strain hardening is the same as in a plasticity model (see Section 4.3) before the peak stress of concrete. Therefore, the procedure to produce the material data for ABAQUS are the same as that introduced in Subsection 4.3.3.3. After the peak stress has been reached, no strain hardening/softening is defined and the yield surface remains unchanged.

#### 5.2.3.4 Flow rule

The procedure to calculate the dilation angle is similar to that introduced in Subsection 4.3.3.3 for a concrete plasticity model, except that the equivalent plastic strain should be calculated based on Eqn 5.1 and the damage variable

obtained using Eqns 5.15 and 5.16. In addition, the Drucker-Prager hyperbolic function is adopted as the flow potential (Eqn 5.14) instead of Eqn 4.14. It is shown in Figure 5.3 that the dilation angle is close to  $\psi$  when  $I_1 > 0$ . Therefore, the calculated dilation angle is input as the  $\psi$  value for the CDPM, which is believed to have only minor effects on the calculated results.

#### *5.2.3.5 Concrete under non-uniform confinement*

Up to now, all the material parameters have been found from Teng et al.'s (2006a) analysis-oriented model, which is for FRP-confined circular concrete cylinders in which the concrete is under uniform confinement. It has been discussed earlier (Section 4.3) that the effect of the third deviatoric stress invariant should be taken into account in the yield criterion so that the strength of concrete under biaxial compression and non-uniform confinement can be accurately predicted. The CDPM implicitly includes this effect. The inclusion of this effect, however, does not necessarily mean that the deformation (e.g. the axial stress-strain curve and the lateral strain-axial strain curve) of concrete under non-uniform confinement can be closely simulated. The prediction of the axial stress-strain behavior depends significantly on the definition of the hardening rule, and the prediction of the lateral strain-axial strain behavior depends significantly on the definition of the flow rule, instead of the yield criterion.

The hardening rule is related to the confining pressure as explained earlier, but the definition of the confining pressure, which is equal to both of the two principal lateral stresses for concrete under uniform confinement, remains absent for concrete under non-uniform confinement. Therefore, an effective confining

pressure  $\sigma_{l,eff}$  should be defined for accurate predictions of the deformation of concrete under non-uniform confinement. To this end, the equation below is adopted in the present research for the effective confining pressure:

$$\sigma_{l,eff} = \frac{2(\sigma_2 + af'_{co})(\sigma_3 + af'_{co})}{(\sigma_2 + \sigma_3 + 2af'_{co})} - af'_{co} \quad (5.18)$$

where  $\sigma_2$  and  $\sigma_3$  are the two principal lateral stresses respectively;  $f'_{co}$  is the cylinder compressive strength of concrete; and  $a$  is a constant to be determined based on test results.

Eqn 5.18 can be regarded as a special case of the generalized  $f$ -mean in mathematics and statistics expressed by  $\sigma_{l,eff} = f^{-1}\left(\frac{f(\sigma_2) + f(\sigma_3)}{2}\right)$  with

$$f(x) = \frac{1}{x + af'_{co}}.$$

It is easy to see that Eqn 5.18 refers to the well-known harmonic mean when  $a=0$ . In addition,  $\sigma_{l,eff} = \sigma_2 = \sigma_3$  when the two lateral stresses are equal, no matter what the value of  $a$  is. The inclusion of an additional term  $af'_{co}$  in Eqn 5.18 for the effective confining pressure is mainly due to the experimental observation that the effectiveness of confinement depends partially on the unconfined concrete strength.

Kupfer et al. (1969) provided stress-strain curves for concrete under biaxial compression with different stress ratios. The test results provided by Kupfer et al.

(1969) have been extensively cited (e.g. Ahmad and Shah 1982; Maekawa et al. 2003) and were also employed in the present research for the calibration of the value of  $a$  in Eqn 5.18. Based on Kupfer et al.'s (1969) test results, the best-fit value for  $a$  is 0.039. Eqn 5.18 is then rewritten as

$$\sigma_{l,eff} = \frac{2(\sigma_2 + 0.039f'_{co})(\sigma_3 + 0.039f'_{co})}{(\sigma_2 + \sigma_3 + 0.078f'_{co})} - 0.039f'_{co} \quad (5.19)$$

For actively-confined concrete, the flow rule is related to the confining pressure (Eqn 4.20).  $\sigma_{l,eff}$  expressed by Eqn 5.19 is adopted in the present research as the effective confining pressure for Eqn 4.20. For FRP-confined concrete, the flow rule needs to be related to the ratio between the confining pressure and the lateral strain (Eqn 4.21). For FRP-confined concrete in a circular section, this ratio (i.e.  $\frac{\sigma_l}{\varepsilon_l}$ ) can be expressed in terms of the properties of the FRP outer tube as

$$\frac{\sigma_l}{\varepsilon_l} = \frac{E_{frp} t_{frp}}{R_o}, \text{ where } R_o \text{ is the outer diameter of the circular section. For}$$

FRP-confined concrete in non-circular sections, this ratio is however not readily available as the lateral stresses and the strains are unequal in different directions. In the present research, two methods were explored for the flow rule of confined concrete in such cases:

#### Method (1)

The first method is to make use of the flow rule for concrete in an equivalent FRP-confined circular section. For FRP-confined annular sections, the flow rule for concrete in an FRP-confined circular section with the same outer diameter and

FRP tube is adopted for the concrete, as for both cases the term  $\frac{E_{frp}t_{frp}}{R_o}$  directly relates the hoop expansion to the confining pressure provided by the FRP tube. For FRP-confined rectangular sections, the  $R_o$  value of an equivalent FCSC specimen, in which the same area of concrete is surrounded by the FRP tube, is used. It is obvious that when adopting this method, the flow rule is the same for concrete over the whole section.

### Method (2)

The second method is to make use of the effective confining pressure given by Eqn 5.19, together with the area strain, which is defined as the average of the two lateral strains, as the effective lateral strain. By doing so, Eqn 4.21 can be rewritten as

$$\beta = \beta\left(\frac{2\sigma_{l,eff}}{\varepsilon_2 + \varepsilon_3}, \tilde{\varepsilon}_p\right) \quad (5.20)$$

where  $\varepsilon_2$  and  $\varepsilon_3$  are the two principal lateral strains.

It is obvious that when adopting this method, the flow rule for concrete may be different for each point over a non-circular section.

### **5.2.4 Verifications of Improved Constitutive Model**

Using the constitutive model described above in this section, FE analyses were conducted for actively-confined concrete, FCSCs, concrete under biaxial compression and FRP-confined square concrete specimens. For both FCSC and FRP-confined square concrete specimens, the FE model was for a vertical slice of

the specimen and consisted of a single-layer of 8-node solid elements for the concrete tied to 4-node shell elements for the FRP jacket. For the concrete under biaxial compression and a uniform active confining pressure, only a single 8-node solid element was used.

Figure 5.4 shows a comparison between the predictions obtained from the proposed model and the test results reported by Sfer et al. (2002) for actively-confined concrete. The concrete had an unconfined strength of 32.8 MPa and a corresponding strain of 0.0018, and was confined by a constant pressure of 9 MPa. Predictions from Teng et al.'s (2006a) analysis-oriented model are also shown in Figure 5.4 for reference. It is evident that the FE analysis provides almost the same predictions as Teng et al.'s (2006a) model, which are reasonably close to the experimental stress-strain curve. The minor difference in the lateral-axial strain curve between the FE results and the predictions of Teng et al.'s (2006a) model is due to the limitation of the allowable values of the dilation angle in the CDPM in ABAQUS. The allowable values of the dilation angle of this model are limited between  $0^\circ$  and  $16^\circ$  in ABAQUS, while the calculated dilation angle in the proposed model is negative in the early loading stage. In order to make use of the theoretical framework of the CDPM model in ABAQUS, the negative values were replaced by  $0^\circ$  in the implementation. This consequently caused a small overestimation of the lateral strain in the early loading stage.

Figure 5.5 shows a comparison between the predictions of the proposed model and the test results of an FCSC specimen (specimen S40-2-II presented in Chapter 3). The concrete in this specimen had an unconfined strength of 39.6 MPa and a

corresponding strain of 0.00263. The cylinder had a diameter of 152.5 mm and a height of 305 mm, and was confined by a two-ply FRP tube with an elastic modulus of 80.1 GPa based on a nominal thickness of 0.17 mm per ply. As concrete is subjected to uniform confinement in this case, there is no difference in the predictions of using method (1) and method (2) for the flow rule of concrete. Results from Teng et al.'s (2006a) analysis-oriented model are also shown for reference. The FE results are almost the same as the predictions from Teng et al.'s (2006a) model, which are reasonably close to the test stress-strain curve.

Figure 5.6 shows a comparison between the FE results and the results of biaxial compression tests by Kupfer et al. (1969). The concrete had a uni-axial compressive strength of 32.0 MPa and a corresponding strain of 0.0021, and was subjected to biaxial compression with two different axial-to-lateral stress ratios, namely,  $\sigma_1 / \sigma_2 = 1$  and 0.5 respectively. Figure 5.6 shows that the FE results agree well with the test results.

Figure 5.7 shows comparisons between the FE predictions and the test results for an FRP-confined square concrete specimen with an unconfined concrete strength of 46.0 MPa and a corresponding strain of 0.0026 tested at The Hong Kong Polytechnic University. The specimen had a width of 150 mm and the four round corners had a rounded radius of 24 mm. It was wrapped with a two-ply CFRP jacket with an elastic modulus of 250,000 MPa based on a nominal thickness of 0.165 mm per ply. The comparisons are for both the average axial stress-axial strain curve and the corner hoop strain-axial strain curve. The average axial stress is defined as the load divided by the cross-sectional area of the concrete. The

experimental corner hoop strains were averaged from the readings of four strain gauges at the four corners. The curves denoted as “FE results I” in Figure 5.7 were obtained by using method (1) stated in Subsection 5.2.3.5 for the flow rule of concrete while those denoted as “FE results II” were obtained by using method (2). Figure 5.7 shows that the predictions by both methods of defining the flow rule for concrete are in reasonably close agreement with the test results.

## **5.3 MODELING OF HYBRID DSTCS**

### **5.3.1 Model Description**

FE models were developed for short DSTC specimens presented in Chapter 3. The specimens were tested under concentric axial compression.

In the tests, the two ends of a short column were constrained by the loading platens, but these constraints were assumed to have little effects on the behavior in the mid-height region of the column with a length equal to twice the diameter. Consequently, the FE model employed in this study consisted of one layer of finite elements spanning a one-degree circumferential segment (Figure 5.8). The finite element model was assigned boundary conditions representing axis-symmetric behavior (Figure 5.8). This simple model was aimed to provide close predictions of the behavior of the mid-height region of hybrid DSTCs.

The FRP tube was simulated to behave in a linear elastic manner with stiffness in the hoop direction only. The stiffness of the FRP tube in the longitudinal direction is very small and was neglected in the model. The tensile rupture behaviour of the

FRP in the hoop direction was not included in the model, but strains developed in the FRP tube could be compared with the ultimate tensile strain of the FRP tube to estimate the occurrence of FRP rupture. In the FE analysis the rupture strain of FRP was set to be the average experimental value of two identical hybrid DSTC specimens. The average stress-strain curve of the steel from tensile tests was represented with a number of data points. The  $J_2$  flow theory was employed to model the plastic behavior of the steel. The concrete was modeled by the modified CDPM introduced earlier.

The Mesh Tie Constraint option of ABAQUS was adopted in the model to simulate the interaction between the FRP and the concrete. Using these constraints, a node on the FRP tube was tied to a corresponding node on the outer edge of the concrete infill so that the two nodes were forced to experience the same translations. The Contact Pairs option of ABAQUS was adopted to simulate the interaction between the steel tube and the concrete. In the radial direction, the so-called “hard” contact, which allows the two surfaces to separate from each other, was specified. The contact pressure was automatically calculated by the program when the two surfaces were in contact. On the contrary, if the surfaces were not in contact, the pressure became zero. In the tangential direction, a friction coefficient was specified but this friction coefficient was not expected to affect the predictions as no slips were expected between the steel tube and the concrete infill due to the axis-symmetric nature of the FE model.

### 5.3.2 Mesh Convergence Study

A mesh convergence study was conducted, arriving at an appropriate mesh for the subsequent finite element modeling work presented in this chapter. A commonly-used approach for mesh convergence studies is to find a mesh which provides almost the same results as those from a further refined mesh. It was found by trying several different meshes that the element size of 1.6 mm in the radial direction was fine enough. Figure 5.9 shows a comparison between the predictions of FE models with two different meshes, for the average axial stress-strain curves of specimen D37-C2-I (see Chapter 3 for specimen details). The comparison shown in Figure 5.9 were obtained using a flow rule based on method (1), but the comparison based on method (2) are similar. The element size of the coarser mesh in Figure 5.9 is 1.6 mm while that of the refined mesh is 0.8 mm. As they give almost the same predictions, the element size of 1.6 mm was adopted in the subsequent finite element modeling work.

### 5.3.3 Results and Discussions

#### 5.3.3.1 Comparison with test results

Figure 5.10 shows comparisons between the FE results and the experimental results for all 18 DSTC specimens presented in Chapter 3, in terms of the axial stress-strain curves. Some simple descriptions of the specimens are also included in Figure 5.10, while further specimen details are available in Chapter 3. As stated in Chapter 3, the experimental axial stress of the concrete in the DSTCs is defined as the load carried by the annular concrete section divided by its cross-sectional area. The load carried by the concrete section is assumed to be the difference

between the load carried by the DSTC specimen and the load carried by the steel tube at the same axial strain. The latter was found from the compression tests of hollow steel tubes. When the axial strain of a DSTC specimen exceeds the buckling strain of the corresponding hollow steel tube, it is assumed that the load resisted by the steel inner tube is equal to  $P_s$ , which is the ultimate load from the compression tests of hollow steel tubes. Similarly, the axial stress of concrete from the FE results is defined as the predicted load carried by the annular concrete section divided by its cross-sectional area. Again, the curves denoted as “FE results I” in Figure 5.10 were obtained using method (1) stated in Subsection 5.2.3.5 for defining the flow rule while those denoted as “FE results II” were obtained using method (2). It is evident from Figure 5.10 that the FE models based on both methods of defining the flow rule for concrete provide reasonably close predictions for all test specimens except the one-ply specimens. The only obvious difference between the predictions due to the two methods of defining the flow rule appears to occur for specimens D40-B3 and D37-C3 (Figures 5.9(e) and (h)). For specimens D40-B3 and D37-C3, the curves predicted by method (2) are slightly higher as the interaction between the concrete and the steel tube was predicted to begin at a smaller axial strain. When using method (1), such interaction was predicted to begin at an axial strain slightly higher than the experimental ultimate strain. For the one-ply specimens (Figures 5.9(b) and (f)), both FE models overestimate the test results by predicting a monotonically ascending curve. This overestimation is believed to be due to Teng et al’s (2006a) analysis-oriented model which was adopted to produce material parameters for the constitutive model. Teng et al. (2006a) pointed out that although their model provided accurate predictions to numerous independent test data of FRP-confined

concrete, it might overestimate the axial resistance of concrete confined by a weak FRP jacket (such as a one-ply FRP jacket herein). Therefore, future improvements to the proposed FE model may be made when a more accurate analysis-oriented stress-strain model is available.

Figure 5.11 shows comparisons between the FE and experimental results, in terms of the hoop strain-axial strain curves. The experimental strains were obtained from several strain rosettes located at the mid-height of the outer FRP tube. The predictions are seen to be in close agreement with all test results.

#### *5.3.3.2 Stress distribution in the radial direction*

Figure 5.12 shows the predicted axial stress distribution in the radial direction for specimen D37-C2-I. It is obvious that, although a different definition of the flow rule makes only minor difference in the predicted axial stress-strain curve and hoop strain-axial strain curve (Figures 5.9 and 5.10), it leads to significant difference in the axial stress distribution over the section. When method (2) is used to define the flow rule, the stress variation is more rapid near the inner edge but slower near the outer edge, compared with the results based on using method (1). It is also obvious from Figure 5.12 that the axial stress varies significantly in the radial direction. The axial stress reduces with the distance from the outer edge, and the rate of variation is more significant near the inner edge. This could be explained by the fact that the two lateral stresses are more non-uniform near the inner edge as shown in Figure 5.13, leading to a smaller effective confining stress and a less significant confining effect. The ability to predict stress variations over

the section is one of the advantages of a three-dimensional FE model over a one-dimensional analysis-oriented model such as Teng et al.'s (2006a) model.

#### *5.3.3.3 Interaction between the concrete and the steel tube*

Under axial compression, the interaction between the concrete and the steel inner tube is dictated by the difference in the radial displacements (or the lateral expansions) of the two components. The lateral expansion of the steel tube is controlled by the Poisson's ratio of steel which is around 0.3 in the elastic range and is around 0.5 in the perfectly-plastic range. In the strain hardening range, the Poisson's ratio of steel is between 0.3 and 0.5. The lateral expansion of concrete is controlled by a Poisson's ratio of around 0.18 in the elastic range, but this ratio varies in a complicated manner in the inelastic range. For uniformly confined concrete, the lateral expansion of concrete can be predicted by an analysis-oriented model such as the one proposed by Teng et al. (2006a). For non-uniformly confined concrete, the lateral expansion of concrete, however, is non-uniform over the section and a three-dimensional constitutive model, such as the one adopted in the present research, needs to be employed for close predictions. Generally, concrete confined by a stronger FRP jacket has less lateral expansion corresponding to a given axial strain (Teng et al. 2006a).

Figure 5.14(b) shows the radial displacement of the steel tube versus that of the concrete inner edge for specimens D40-B1-I, D40-B2-I, D40-B3-I; the flow rule was defined using method (2). The only differences between these specimens are the FRP outer tubes, which are one-ply, two-ply and three-ply tubes respectively. The FE results show that in the initial stage, the radial displacements of both

components are equal for all the three specimens, because the initial Poisson's ratio of concrete is smaller than that of steel and the steel tube moves outward faster than the concrete, so the two components remain in contact. After the elastic range, the concrete begins to deform faster and separates from the steel tube. The distance between the two components, as indicated in Figure 5.14(b), then continues to increase with loading for the one-ply specimen, keeps almost constant in the final loading stage for the two-ply specimen, but begins to decrease after a certain axial strain for the three-ply specimen. This distance does not disappear for the specimens with a one-ply or a two-ply FRP tube until the ultimate limit state, indicating that there is no interaction between the concrete and the steel tube throughout the loading process. For the specimen with a three-ply FRP tube, this distance disappears in the final stage, indicating that interaction between the concrete and the steel tube exists in this stage. This finding is consistent with the experimental results given in Chapter 3.

Figure 5.14(a) shows the corresponding predictions when the flow rule is defined by method (1). Similar observations can be made about these predictions. The only difference is that by using method (1) the predicted interaction between the steel tube and concrete occurs at a larger axial strain, as also seen in the predicted axial stress-strain curves (Figure 5.10).

#### *5.3.3.4 Comparison between FCSC and DSTC specimens*

The differences between FCSC and DSTC specimens are obvious when examining the stress distribution over the cross section. In an FCSC specimen, the stresses, including both axial and lateral stresses, are uniform over the section.

However, in a DSTC specimen, the axial stresses are highly non-uniform in the radial direction, as shown in Figure 5.12. In addition, the two lateral stresses (i.e. the radial stress and the circumferential stress) are equal to each other over the whole section of an FCSC specimen, but are quite different over the section of a DSTC specimen, as shown in Figure 5.13. The unequal lateral stresses reduce the confinement effectiveness, as discussed in Chapter 4.

Despite the obvious differences pointed out above, the overall behavior of FCSC specimens and that of DSTC specimens can be compared using the axial stress-strain curves and the hoop strain-axial strain curves. Due to the axial stress variation over the section, the axial stress of a DSTC specimen refers to the average axial stress, and is defined as the load carried by the annular concrete section divided by its cross-sectional area, as stated earlier. The hoop strain refers to the hoop strain developed on the FRP outer tube. Figure 5.15 shows comparisons of FE results of an FCSC and two different DSTCs. The FE results were obtained using a flow rule based on method (1), but the FE results based on method (2) are similar. The geometric and material parameters, including the unconfined concrete properties, the outer diameter and the FRP outer tube, are all the same for each pair of FCSC and DSTC specimens.

It can be seen from Figures 5.14(c) and (d) that when the void ratio is relatively small the DSTC specimen has almost the same behavior as the corresponding FCSC specimen, in terms of the average axial stress-strain curve and hoop strain-axial strain curve. However, when the void ratio is relatively large, Figures 5.14(a) and (b) show that there are some differences between these two kinds of

specimens: (1) the axial stress-strain curve of the DSTC specimen has a smaller slope for its second branch, which however ends at a larger axial strain; (2) the radial expansion of the outer FRP tube of the DSTC specimen is less than that of the FCSC specimen for the same axial strain. These findings are consistent with the experimental observations presented in Chapter 3.

#### *5.3.3.5 Concluding remarks*

The following concluding remarks can be made based on the above discussions.

- (1) The FE results, based on either method for the definition of the flow rule for concrete are in reasonably close agreement with the test results, in terms of the general structural behavior, including the axial stress-strain behavior and the hoop strain-axial strain behavior.
- (2) The FE models are superior to analysis-oriented models due to their ability to predict both the stress variation over the section and the interaction between the steel tube and the concrete.
- (3) The differences between the predictions corresponding to the two different methods for defining the flow rule for concrete lie mainly in the axial stress distribution and the strain level at which the interaction between the concrete and the steel inner tube occurs.

As in general there is no significant difference between the predictions of the two methods for defining the flow rule of concrete, in terms of the general structural behavior, the parametric study presented in the following section was conducted

employing method (1) which appears to be simpler, despite that method (2) appears to be more reasonable in that it takes into account the different flow rule for each point over a non-circular section. The parametric study was aimed at not only a good understanding of the effects of different parameters on the structural behavior of hybrid DSTCs, but also the development of a simple design-oriented model.

## 5.4 PARAMETRIC STUDY

### 5.4.1 Introduction

From the test results presented in Chapter 3 and the FE results presented earlier in this chapter, the main parameters affecting the behavior of concrete in a DSTC specimen in contrast to an FCSC can be identified to be the void ratio and the confinement stiffness  $\frac{E_{frp}t_{frp}}{R_o}$ , where  $E_{frp}$  and  $t_{frp}$  are respectively the elastic modulus and the thickness of the FRP outer tube and  $R_o$  is the outer diameter of the cylinder. It is shown in Subsection 5.3.3.3 that significant interaction between the concrete and the steel tube exists when the FRP outer tube is sufficiently strong. In such cases, the stiffness of the steel inner tube may also affect the behavior of concrete. The ultimate condition of concrete is also significantly affected by the rupture strain of the FRP outer tube, as explained earlier. In addition, the properties of unconfined concrete are also significant parameters affecting the behavior of confined concrete. These two factors are important for FCSCs as well.

The unconfined concrete properties are not taken as significant parameters in this parametric study. Although they may affect the effectiveness of confinement, this effect is very limited on the stress-strain curve of FRP-confined concrete when the axial stress and the axial strain are normalized by the peak stress of unconfined concrete strength and the corresponding strain respectively, provided that normal strength concrete is used. In this parametric study, the concrete has an unconfined strength of 40 MPa and a corresponding strain of 0.0026. It was explained in Chapter 1 that it is desirable that the FRP outer tube does not significantly enhance the load-carrying capacity of the new hybrid DSTCs. Based on this consideration, the stiffness of the FRP outer tube should not be too large. It has been shown that the load capacity of a three-ply DSTC specimen (e.g. specimen D40-C3-I in Chapter 3) was enhanced by 62% due to the presence of the FRP tube. In practical applications, it is reasonable to employ suitable FRP tubes so that the confinement stiffness is smaller than that of the three-ply DSTC specimens. The confinement stiffness, however, should not be too small as otherwise there may be a descending branch in the stress-strain curve of confined concrete. It has been shown that the one-ply DSTC specimens (e.g. specimen D40-B1-I in Chapter 3) had an almost elastic-perfectly plastic stress-strain curve. Therefore, it is reasonable to take the confinement stiffness of specimen D40-B1-I as the lower limit for practical use. Based on the above considerations, the confinement stiffness adopted in this parametric study ranges from 200 MPa ( $>178.6$  MPa which is the confinement stiffness of specimen D40-B1-I) to 500 MPa ( $<535.8$  MPa which is the confinement stiffness for specimen D40-C3-I). Four values were adopted, which are 200 MPa, 300 MPa, 400 MPa and 500 MPa respectively. Two rupture strain values, namely, 0.01 and 0.02, were selected in

the parametric study for the FRP outer tube. The former value is close to the rupture strain of commonly used CFRP while the latter value is close to that of commonly used GFRP. Three void ratios, namely, 0.25, 0.5 and 0.75, were adopted in the parametric study. The  $D_s/t_s$  ratio of the steel inner tube was set to be 25 unless otherwise specified.

#### **5.4.2 Interaction between the Concrete and the Steel Tube**

It was found from the FE analysis that there is no interaction between the concrete and the steel tube for all cases when the FRP rupture strain is 0.01. When the FRP rupture strain is 0.02, however, this interaction appears in the final stage of deformation for specimens with a void ratio of 0.75 and a confinement stiffness of 400 MPa or 500 MPa, and specimens with a void ratio of 0.5 and a confinement stiffness of 500 MPa (Figures 5.18 and 5.19). It is noted that this interaction tends to appear earlier for specimens with a larger void ratio or with a larger confinement stiffness, or both.

Due to the existence of interaction, the  $D_s/t_s$  ratio of the steel inner tube may also be expected to affect the behavior of concrete. In order to clarify this point, different steel tubes were employed in the specimens with a void ratio of 0.75 and a confinement stiffness of 400 MPa or 500 MPa in the parametric study. The  $D_s/t_s$  ratio of the steel inner tube varies from 10 to 50. Figure 5.16 shows the FE results for different  $D_s/t_s$  ratios. It is evident that the  $D_s/t_s$  ratio of the steel tube has only a small effect on the stress-strain behavior of the concrete in DSTCs. Therefore, it needs not be taken as a significant parameter in the present parametric study. All

other FE results of this parametric study are for a steel tube with a  $D_s/t_s$  ratio of 25.

### **5.4.3 Compressive Strength**

Figure 5.17 shows the compressive strengths (i.e. the ultimate stresses) of concrete for all the cases analyzed. Each case represents a specimen with one combination of the three key parameters of void ratio, confinement stiffness and FRP rupture strain. Each group of three points with the same shape (triangle or rectangular) and the same confinement stiffness in Figure 5.17 represents the results for specimens with the three void ratios of 0.25, 0.5 and 0.75 respectively. It is clear that the three points in each group are very close to each other except the two solid points. These two higher solid points are for specimens in which there is significant interaction between the concrete and the steel tube. It may therefore be concluded that the void ratio has only a small effect on the compressive strength of concrete in DSTCs, when there is no interaction between the concrete and the steel tube. On the contrary, the FRP rupture strain and the confinement stiffness both have a significant effect on the compressive strength of concrete, as shown in Figure 5.17.

### **5.4.4 Ultimate Axial Strain**

Figure 5.18(a) shows the ultimate axial strains for all the analyzed cases. It is evident that the ultimate axial strain increases with the FRP rupture strain or the confinement stiffness, or both. It is also noted that the effect of the void ratio cannot be neglected. Figure 5.18(b) shows the variation of the ultimate axial strain

with the void ratio for specimens with a FRP rupture strain of 0.02. Different from the conclusions drawn for the compressive strength of concrete, it is clear from Figure 5.18(b) that the ultimate axial strain increases considerably with the void ratio.

#### **5.4.5 Axial Stress-Strain Curves**

Figure 5.19 shows the predicted axial stress-strain curves of all analyzed cases with a void ratio of 0.5. It can be seen that the curves remain almost identical until the axial stress reaches about the unconfined concrete strength, significant differences between these curves are seen afterwards. The specimen with a larger confinement stiffness exhibits a second branch which is with a larger slope and ends at a larger ultimate axial strain. In addition, when the confinement stiffness is large enough, significant interaction between the concrete and the steel tube appears in the final stage.

Figure 5.20(a) shows the predicted axial stress-strain curves of all specimens with a confinement stiffness of 300 MPa. No interaction between the steel and the concrete can be seen in the final stage for all these specimens. The specimen with a larger void ratio has a shallower second branch which however ends at a larger ultimate axial strain. Despite these differences, all these specimens have approximately the same compressive strength of concrete. Figure 5.20(b) shows the predicted axial stress-strain curves of all specimens with a confinement stiffness of 500 MPa. Similar to Figure 5.20(a), the specimen with a larger void ratio exhibits a longer stress-strain curve with a larger ultimate axial strain. In

addition, because of the interaction between the concrete and the steel tube in the final stage, the ultimate strength of the specimen with the largest void ratio is also significantly larger than those of the other two specimens.

## **5.5 DESIGN-ORIENTED STRESS-STRAIN MODEL**

### **5.5.1 Introduction**

As mentioned in Chapter 2, Lam and Teng's (2003a) design-oriented model can closely predict the axial stress-strain curves of FRP-confined solid concrete cylinders (FCSCs). A refined version (Teng et al. 2006b) of this model has recently been proposed and been shown to provide more accurate predictions than the original model (Lam and Teng 2003a), especially for weakly-confined concrete. Lam and Teng's (2003a) design-oriented model was described in detail in Subsection 2.2.3.2 and is described by Eqns 2.12-2.19. Teng et al.'s (2006b) proposed new equations for the compressive strength and the ultimate axial strain of FRP-confined concrete (i.e. Eqns 2.20 and 2.21). While Teng et al.'s (2006b) model provides close predictions for FCSCs, it cannot be directly applied to concrete in DSTCs. The behavior of concrete in DSTCs is more complicated and depends on more parameters, such as the void ratio, besides the properties of FRP and unconfined concrete. The effects of these parameters have been clarified in the parametric study presented in Section 5.4. In this section, suitable modifications to Teng et al.'s (2006b) refined model are proposed, based on the results from the parametric study, leading to a design-oriented model for the prediction of the average axial stress-strain curves of the concrete in the new hybrid DSTCs.

### 5.5.2 Modifications to Teng et al.'s (2006b) Model

Based on the results from the parametric study (see Subsection 5.4.3), it is clear that the compressive strength of concrete in hybrid DSTCs is mainly related to the confinement stiffness and the FRP rupture strain but not the void ratio, when significant interaction between the concrete and the steel inner tube does not exist. When such interaction exists, the compressive strength of concrete may be significantly enhanced. The effects of these two parameters are appropriately considered in Teng et al.'s (2006b) model for concrete uniformly confined with FRP (solid cylinders with the void ratio equal to zero) (Eqn 2.20). Therefore, Eqn 2.20 is directly adopted here for the compressive strength of the concrete in hybrid DSTCs. Figure 5.21 shows that Eqn 2.20 provides reasonably accurate predictions when there is no interaction between the concrete and the steel inner tube. When such interaction exists, Eqn 2.20 provides less accurate but safer predictions.

The parametric study also showed that the ultimate strain is related not only to the confinement stiffness and the FRP rupture strain, but also to the void ratio. Therefore, Eqn 2.21 needs to be modified to include the effect of the void ratio. The equation below is proposed in which  $\phi$  is the void ratio:

$$\frac{\varepsilon_{cu}}{\varepsilon_{co}} = 1.75 + 6.5 \rho_K^{0.8} \rho_\varepsilon^{1.45} (1 - \phi)^x \quad (5.21)$$

Based on the results from the parametric study, the best-fit value for  $x$  is -0.22.

Therefore, Eqn 5.21 becomes,

$$\frac{\varepsilon_{cu}}{\varepsilon_{co}} = 1.75 + 6.5 \rho_K^{0.8} \rho_\varepsilon^{1.45} (1 - \phi)^{-0.22} \quad (5.22)$$

Figure 5.22 shows the comparison between the results from Eqn 5.22 and those from the parametric study. It is evident that they are in close agreement.

To summarize, the proposed design-oriented stress-strain model for concrete in hybrid DSTCs includes Eqns 2.12-2.15 proposed by Lam and Teng (2003a), Eqn 2.20 from Teng et al. (2006b) for the compressive strength and Eqn. 5.22 for the ultimate axial strain.

Comparisons between the predictions of the proposed stress-strain model and the test results are given in Figure 5.10. This design-oriented model is seen to provide reasonably close but conservative predictions. The conservativeness arises mainly from the conservative nature of Eqn 2.20 for such concrete.

## **5.6 CONCLUDING REMARKS AND DESIGN**

### **RECOMMENDATIONS**

#### **5.6.1 General**

This chapter has presented a modified plastic-damage model within the theoretical framework of the Concrete Damaged Plasticity Model (CDPM) in ABAQUS (2004) for the modeling of FRP-confined concrete. The proposed modifications include a damage variable, a strain-hardening rule and a flow rule, all of which are confinement-dependent, following the conclusions drawn in Chapter 4. The unique deformation characteristics of non-uniformly confined concrete are also included in the modified model. The validity of the proposed model has been

demonstrated through comparisons with test results of actively-confined concrete, FRP-confined concrete in a circular section and that in a rectangular section, and concrete under biaxial compression. Using this modified plastic-damage model for concrete, a finite element model was developed for hybrid DSTCs. Results from this finite element model are in reasonably close agreement with test results. A parametric study using this FE model was also presented which led not only to a good understanding of the behavior of hybrid DSTCs but also to a design-oriented model.

### 5.6.2 Design Recommendations

The design-oriented stress-strain model described in Section 5.5 was proposed based on an FE parametric study and was demonstrated by comparisons with test results to be reasonably accurate and safe. Consequently, this simple stress-strain model is recommended for design use.

The parametric study showed that the confinement stiffness  $\frac{E_{frp} t_{frp}}{R_o}$  of the FRP outer tube affected the behavior of hybrid DSTCs significantly. For practical use, the FRP outer tube should satisfy two requirements: (1) it is not too stiff and does not significantly enhance the load-carrying capacity of hybrid DSTCs; (2) it is sufficiently stiff to avoid a descending branch in the stress-strain curve of confined concrete.

The parametric study showed that the void ratio also significantly affects the behavior of hybrid DSTCs, especially the deformation behavior. For practical use, a void ratio within the range of 0.6 to 0.75 is recommended due to the following reasons: (1) the void ratio should be sufficiently large so that the advantages of hybrid DSTCs, such as their light-weight and good ductility, become obvious; (2) the void ratio should not be too large, so that the section still contains a sufficient amount of concrete for resisting compressive stresses.

The steel inner tube was shown to have a small effect on the stress-strain behavior of the concrete. It however significantly affects the overall load-carrying capacity of hybrid DSTCs, especially when the void ratio is large. In addition, the  $D_s/t_s$  ratio of the steel tube needs to be limited so that local buckling does not become a significant concern. Based on the present test results, an upper limit of 40 for the  $D_s/t_s$  ratio may be recommended for practical applications.

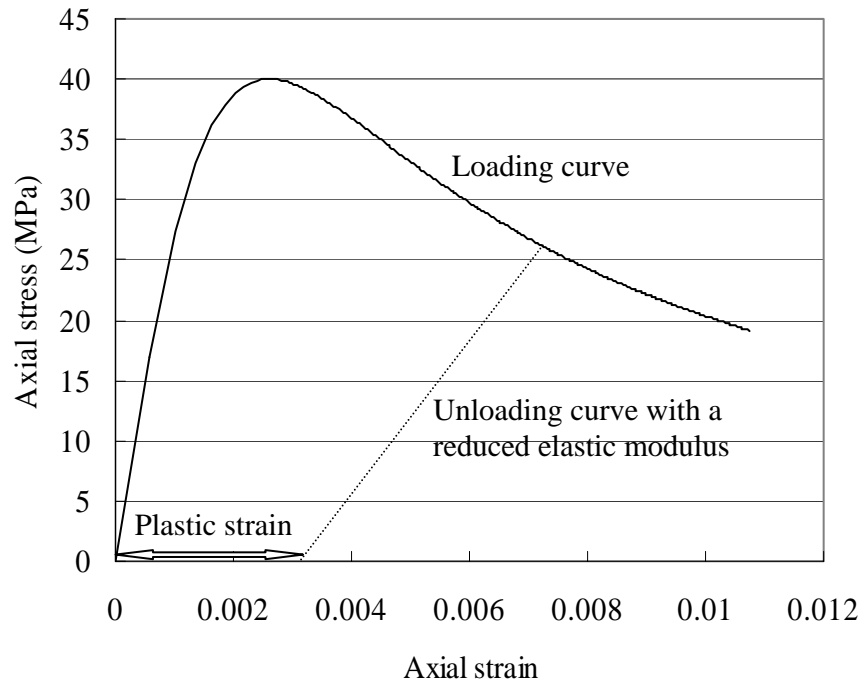
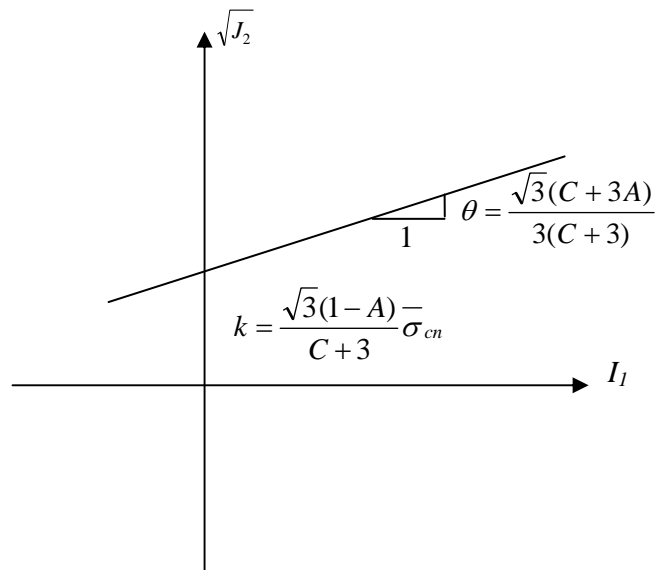
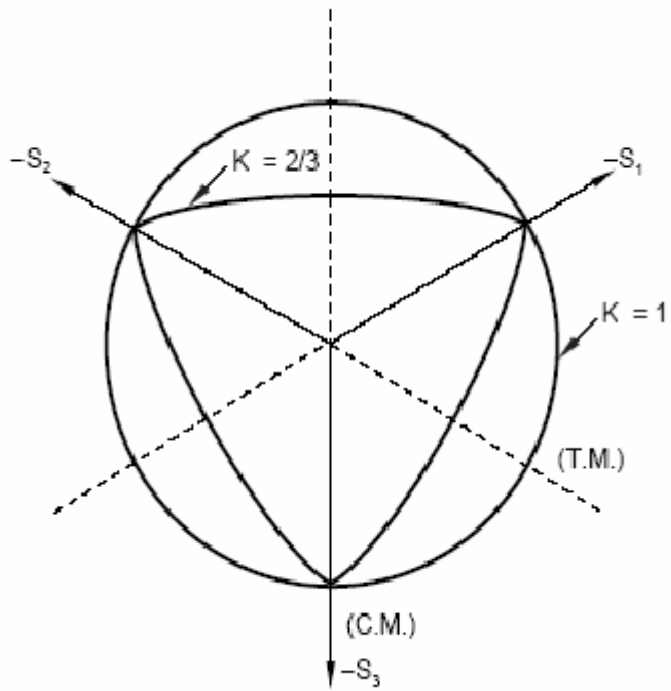


Figure 5.1 Typical stress-strain curve of concrete under compression



(a) Yield surface in the meridian plane for triaxial compression

Figure 5.2 Yield surface of Concrete Damaged Plasticity Model in ABAQUS



(b) Yield surfaces in the deviatoric plane (ABAQUS 2004)

Figure 5.2 Yield surface of Concrete Damaged Plasticity Model in ABAQUS (Cont'd)

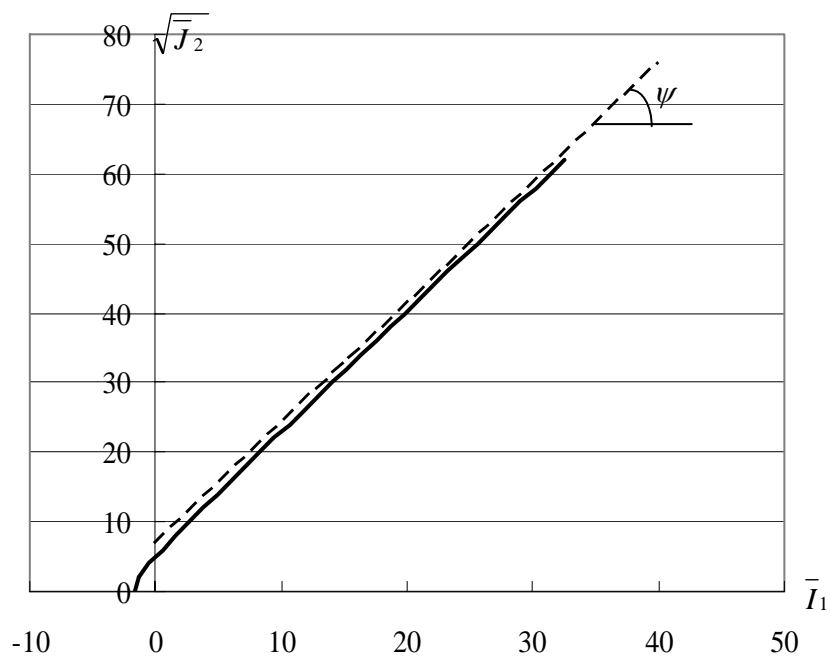
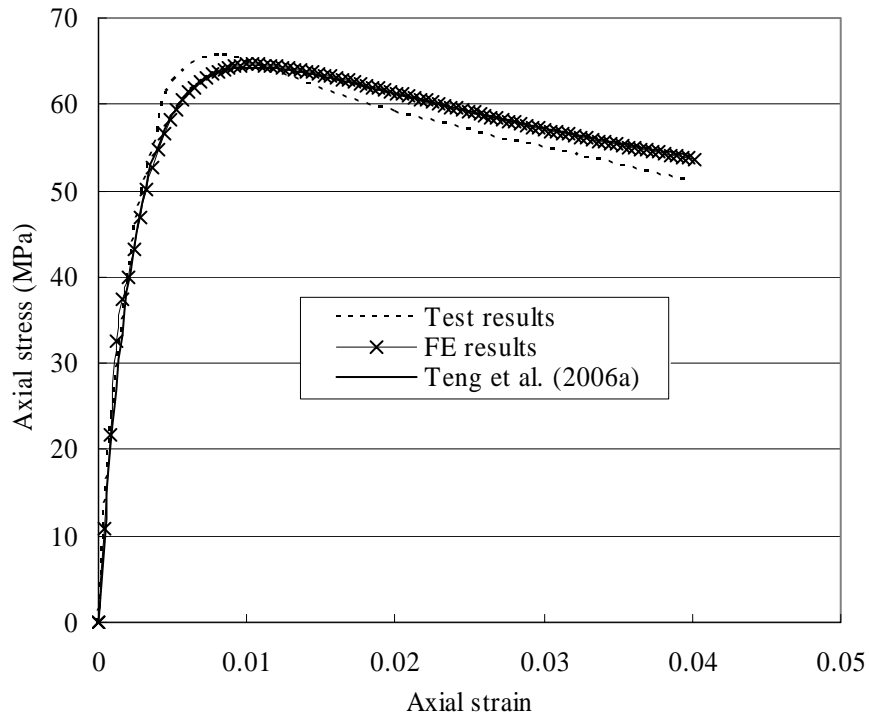
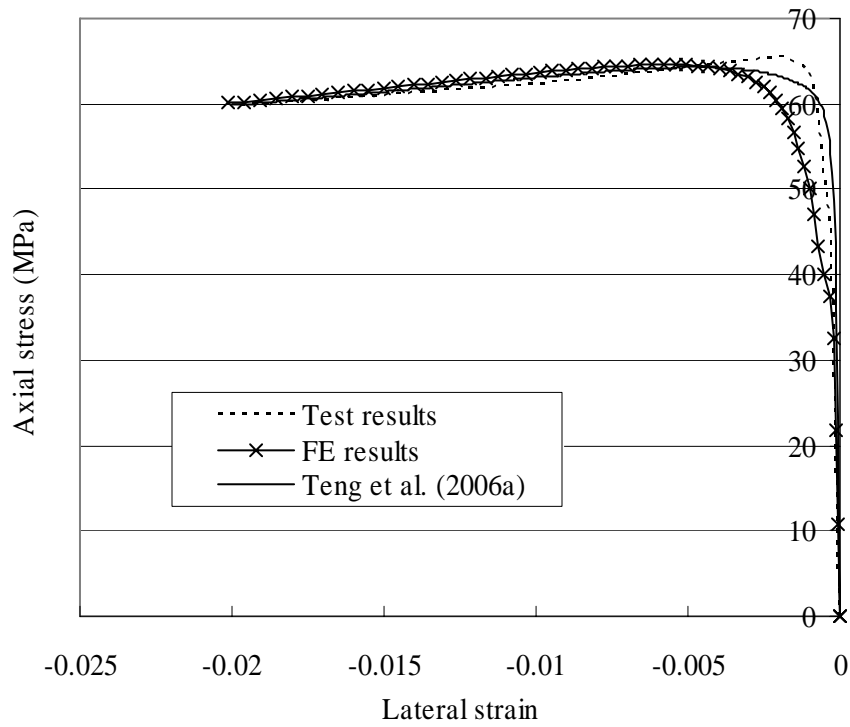


Figure 5.3. D-P hyperbolic flow potential in the meridian plane

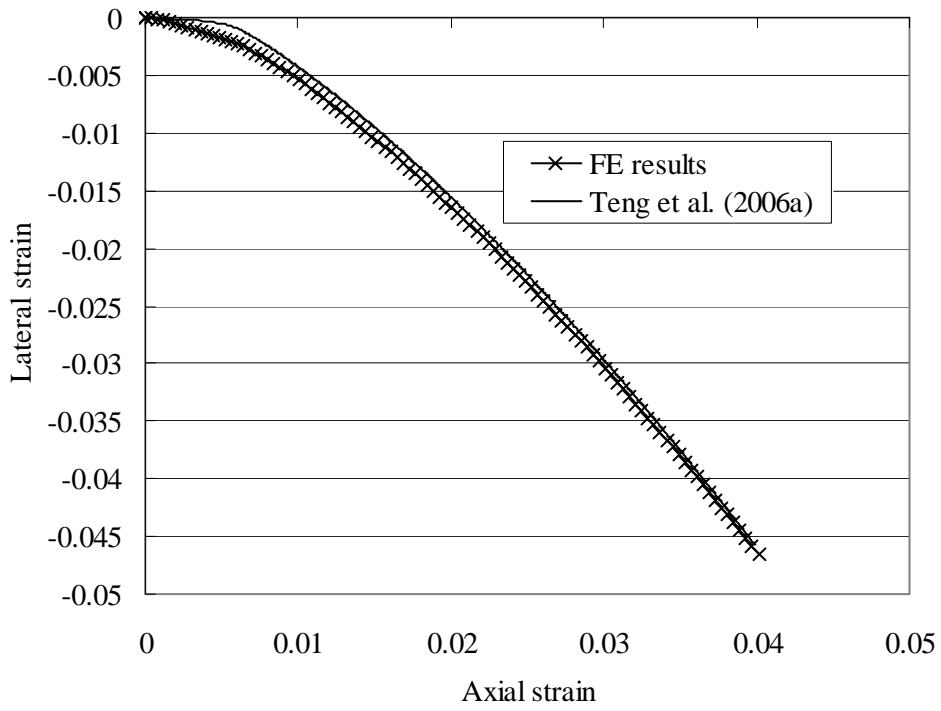


(a) Axial stress-strain curves



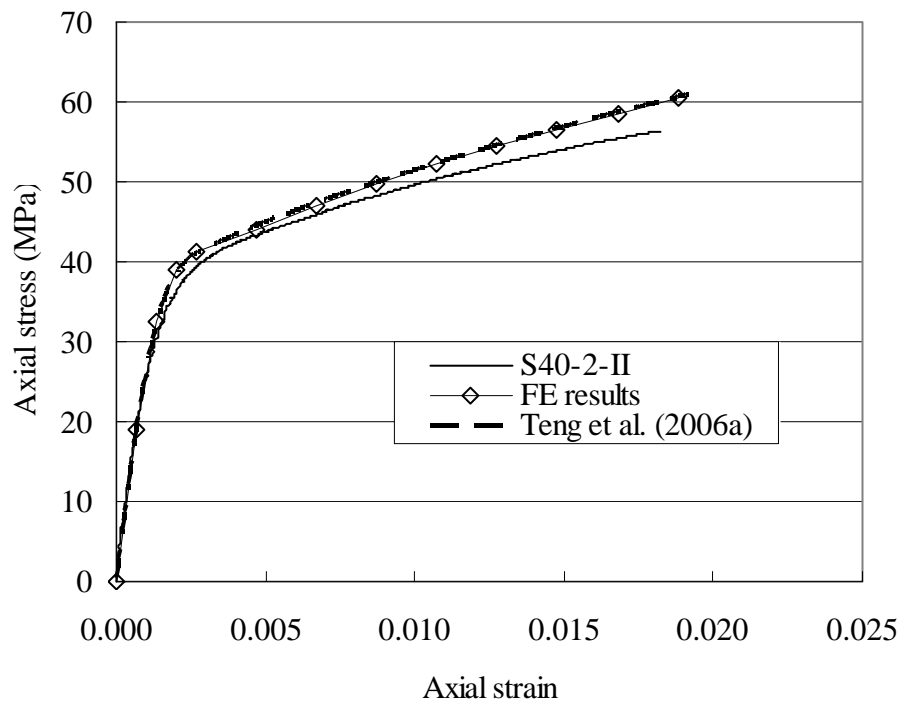
(b) Axial stress-lateral strain curves

Figure 5.4 Actively-confined concrete



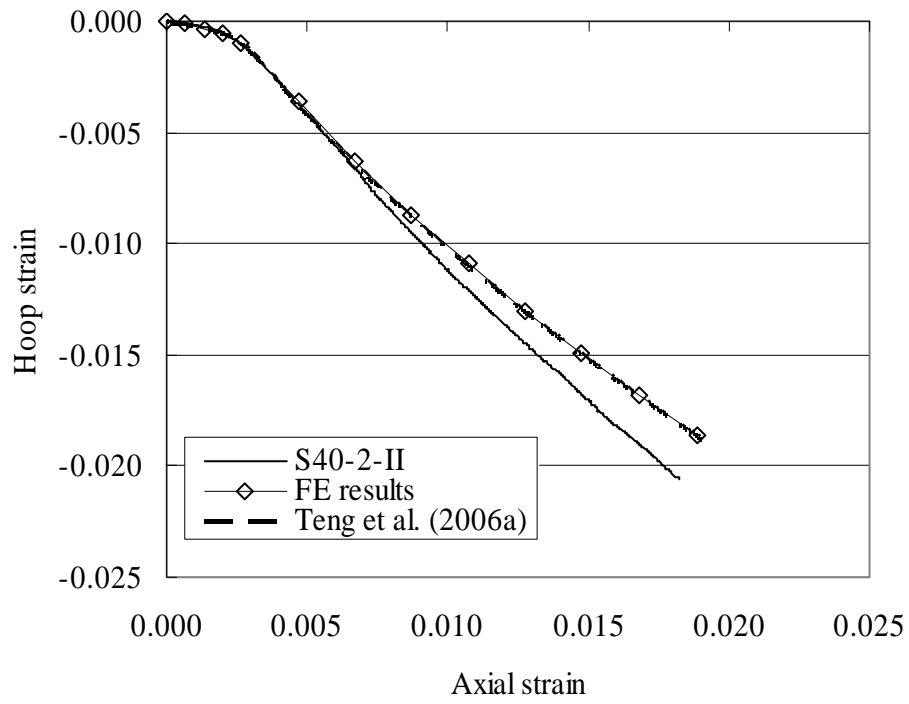
(c) Lateral strain-axial strain curves

Figure 5.4 Actively-confined concrete (Cont'd)



(a) Axial stress-strain curves

Figure 5.5 FRP-confined circular concrete cylinders



(b) Hoop strain-axial strain curves

Figure 5.5 FRP-confined circular concrete cylinders (Cont'd)

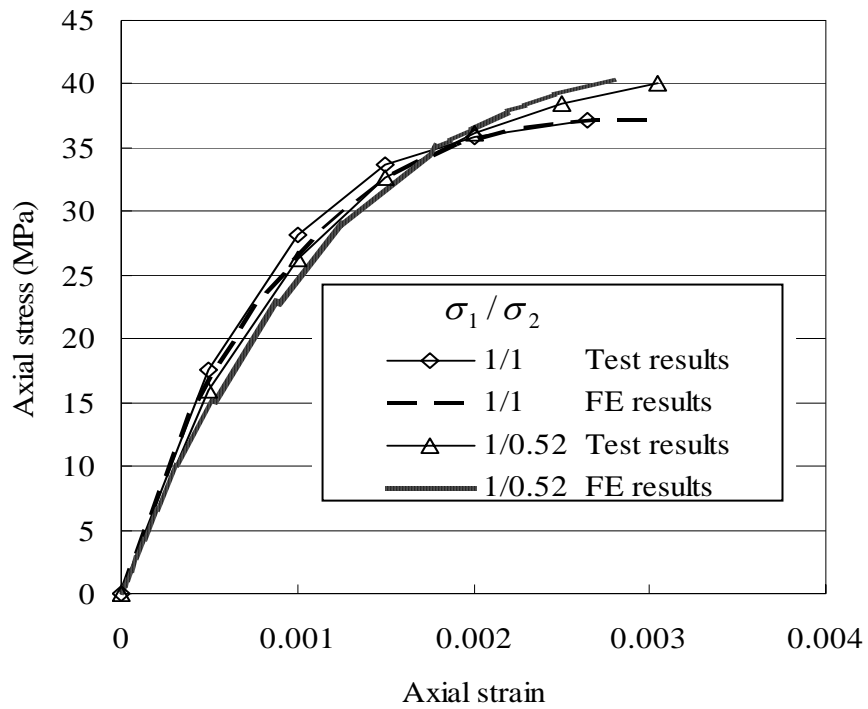
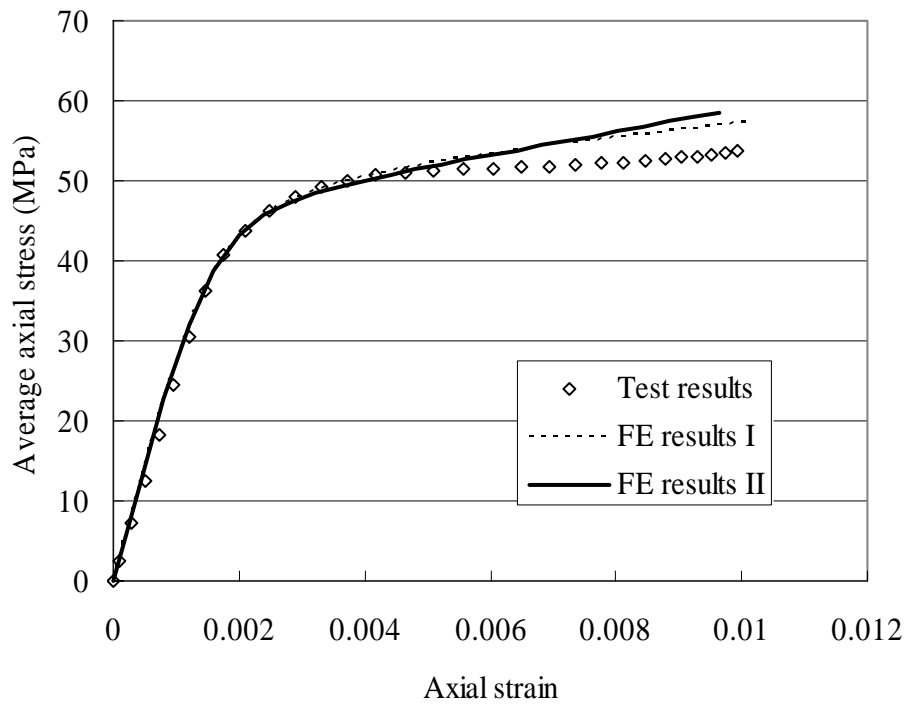
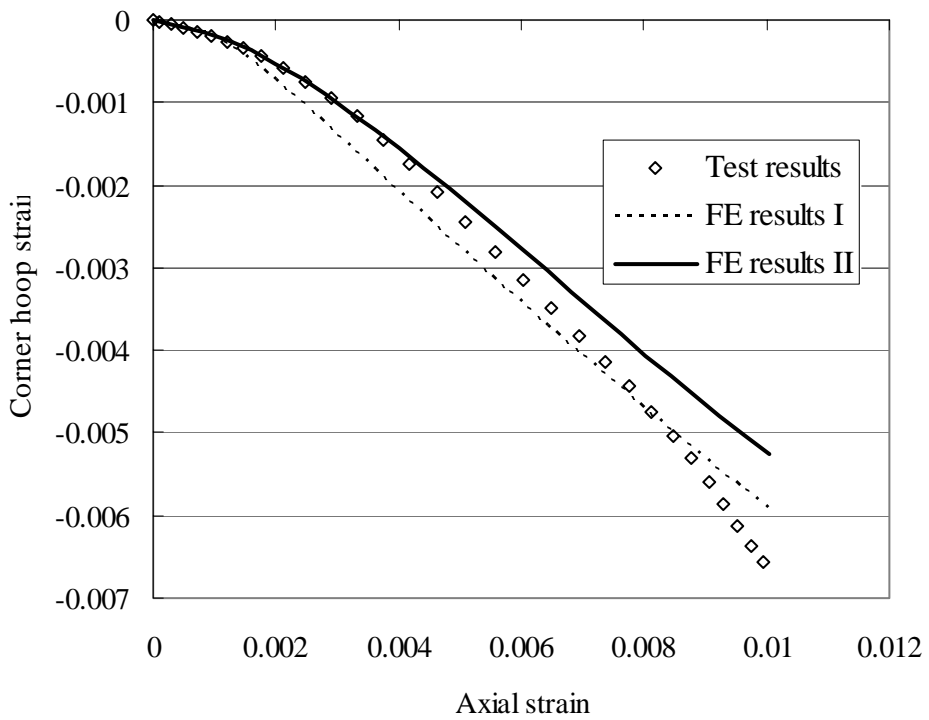


Figure 5.6 Concrete under biaxial compression



(a) Average axial stress-axial strain curve



(b) Corner hoop strain-axial strain curve

Figure 5.7 FRP-confined concrete in a square specimen

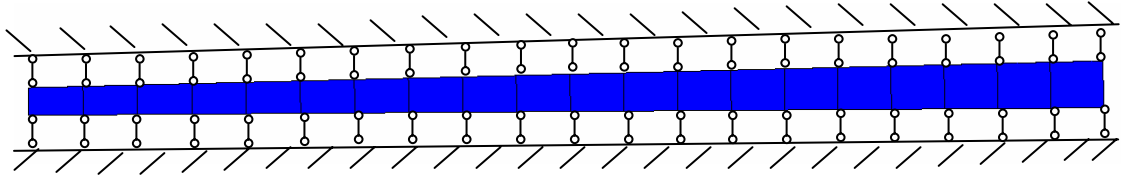


Figure 5.8 FE model for hybrid DSTCs

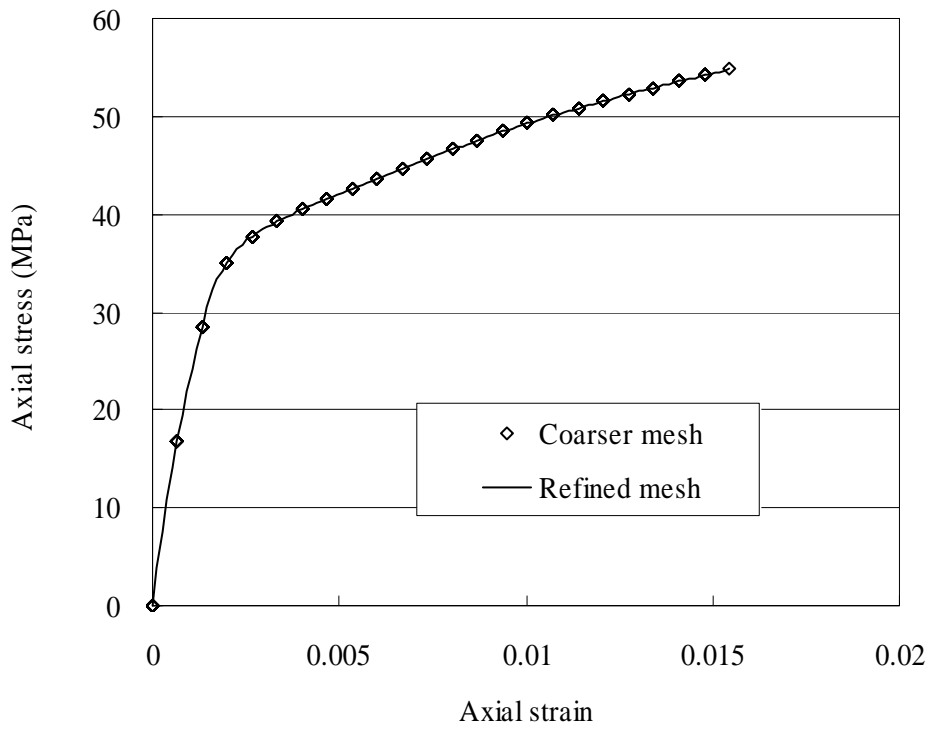
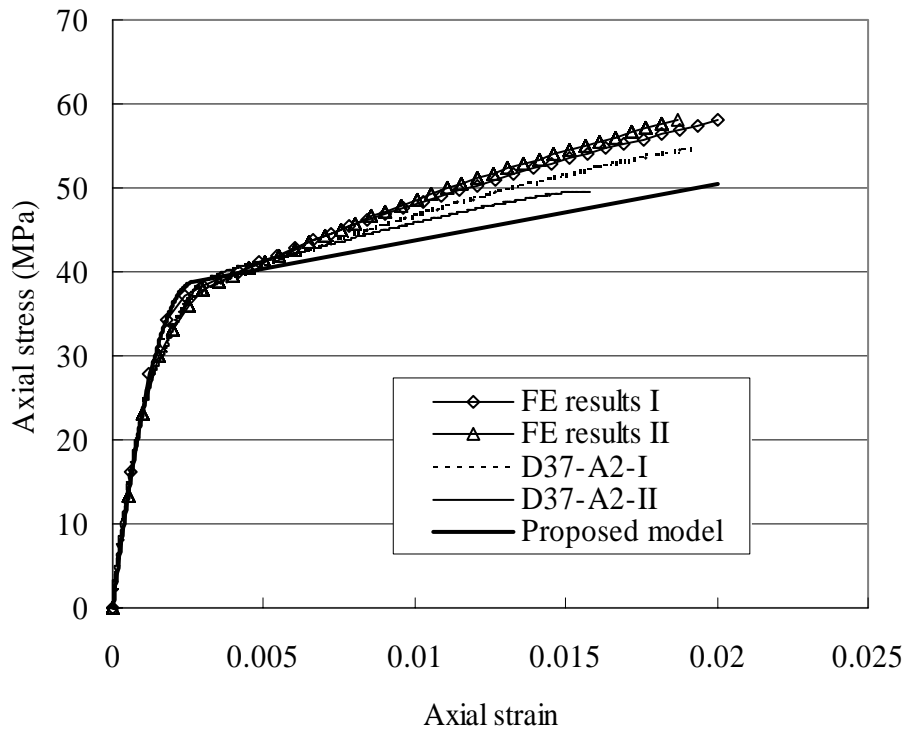
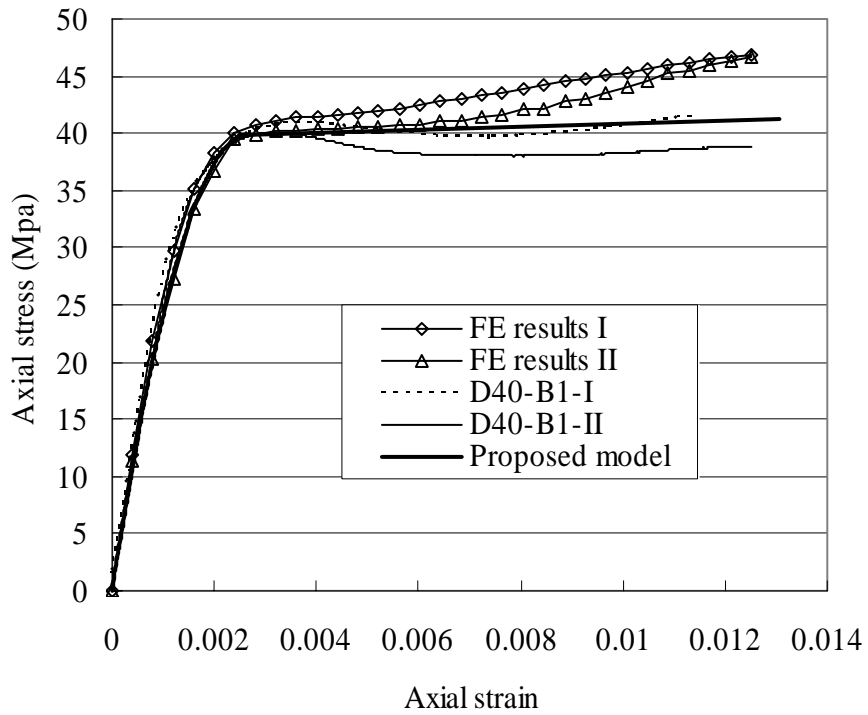


Figure 5.9 Results of mesh convergence study

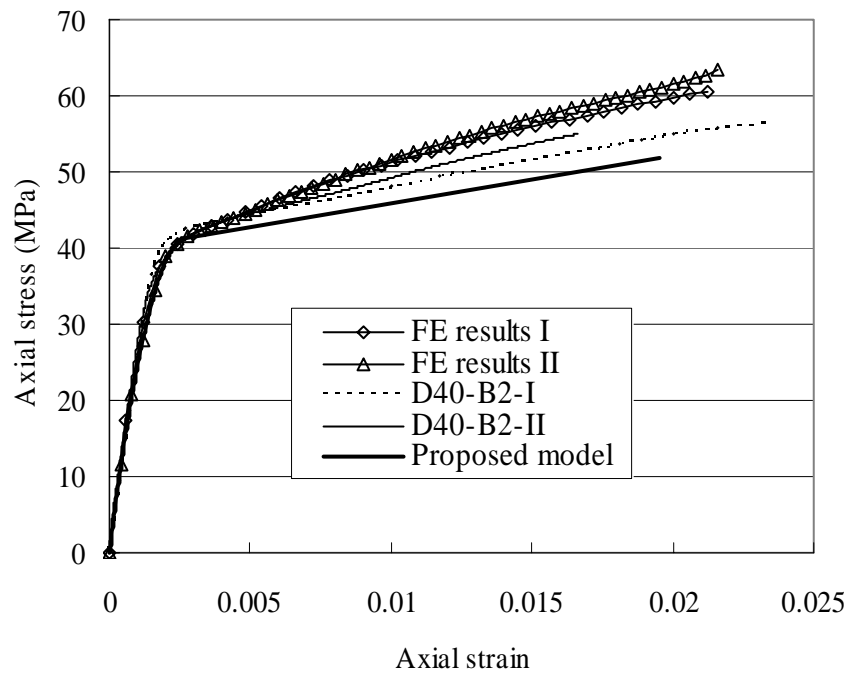


(a) Void ratio=0.28,  $f'_{co}$  =36.7 MPa, two-ply FRP

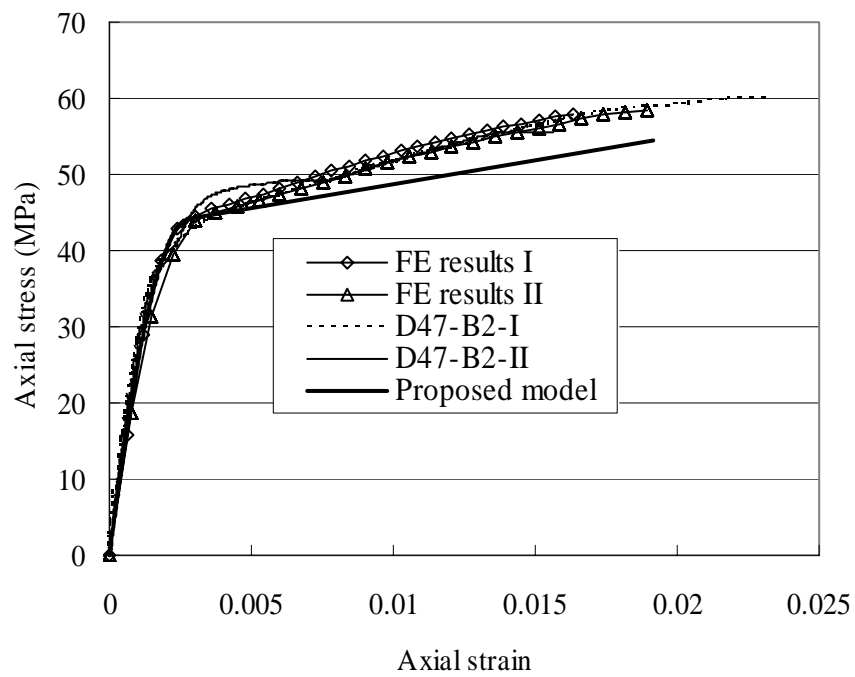


(b) Void ratio=0.5,  $f'_{co}$  =39.6 MPa, one-ply FRP

Figure 5.10 Axial stress-strain curves of concrete in DSTCs

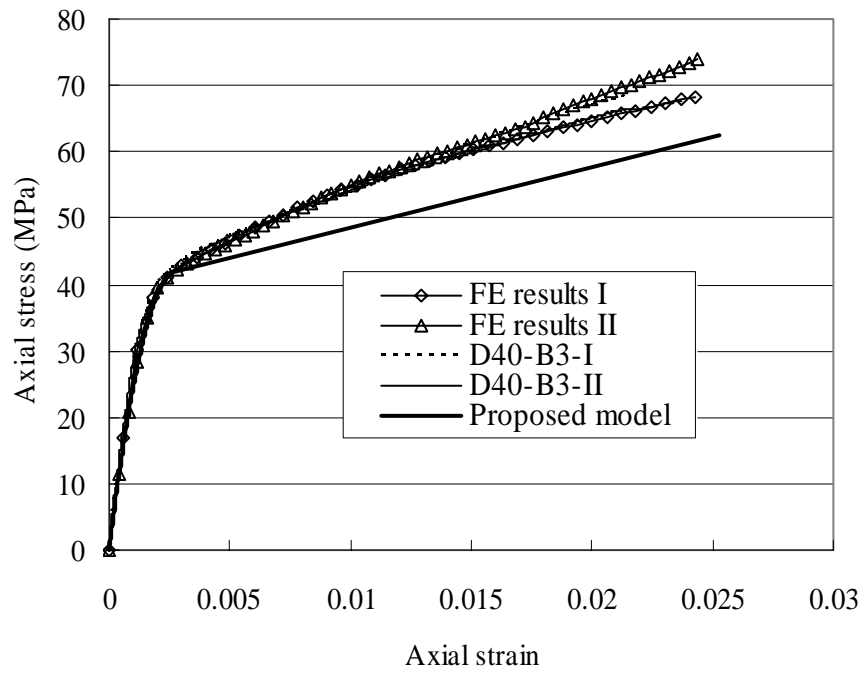


(c) Void ratio=0.5,  $f'_{co}$ =39.6 MPa, two-ply FRP

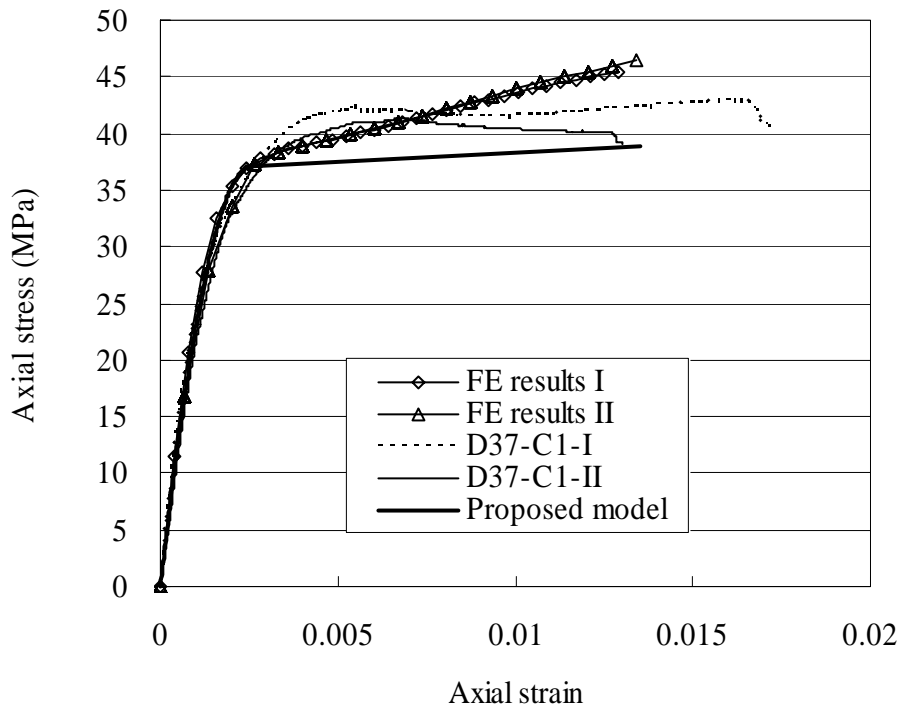


(d) Void ratio=0.5,  $f'_{co}$ =46.7 MPa, two-ply FRP

Figure 5.10 Axial stress-strain curves of concrete in DSTCs (Cont'd)

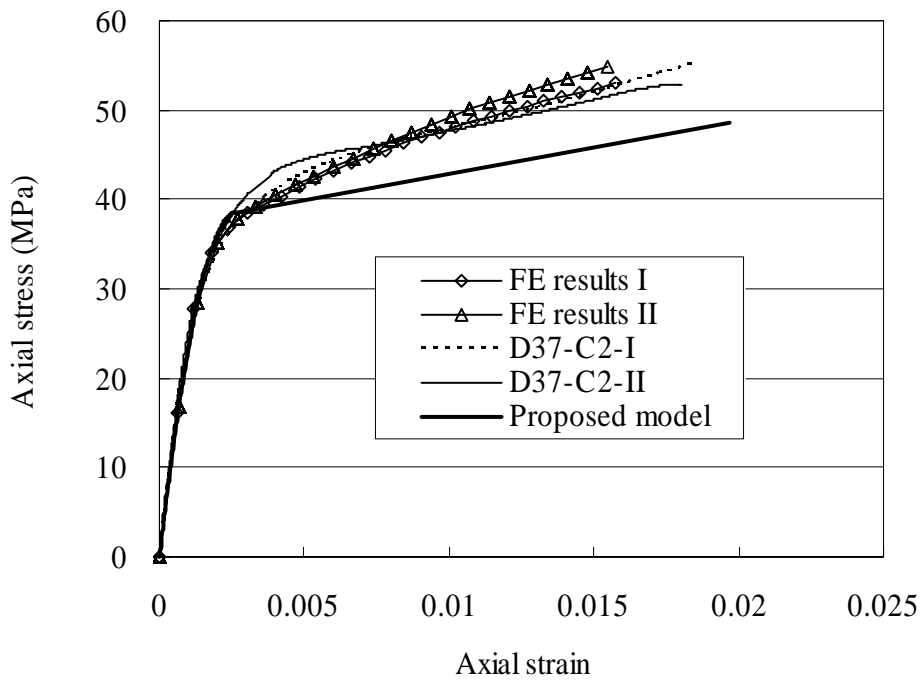


(e) Void ratio=0.5,  $f'_{co}$ =39.6 MPa, three-ply FRP

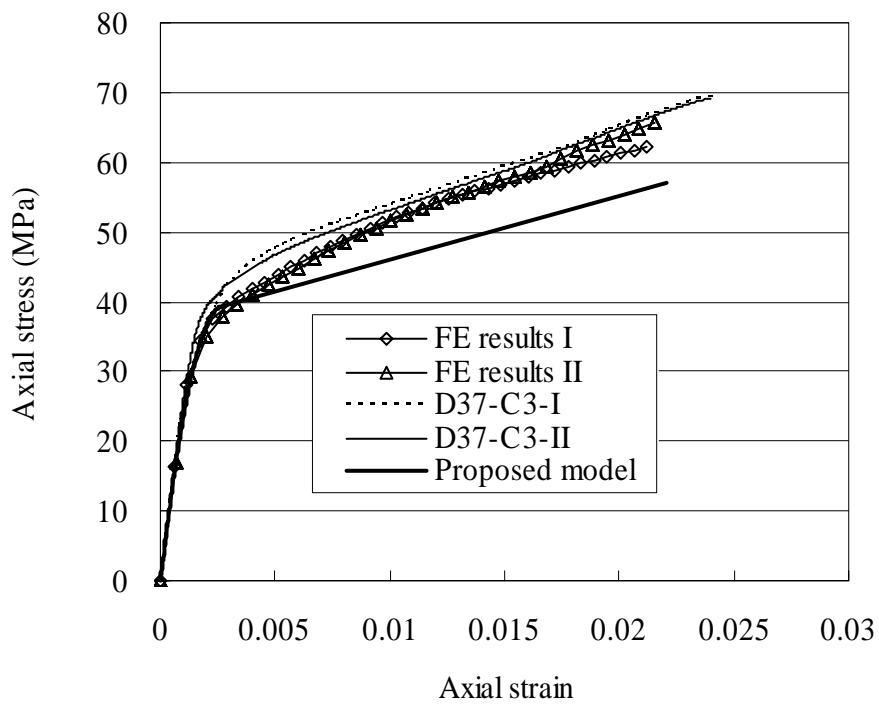


(f) Void ratio=0.58,  $f'_{co}$ =36.7 MPa, one-ply FRP

Figure 5.10 Axial stress-strain curves of concrete in DSTCs (Cont'd)

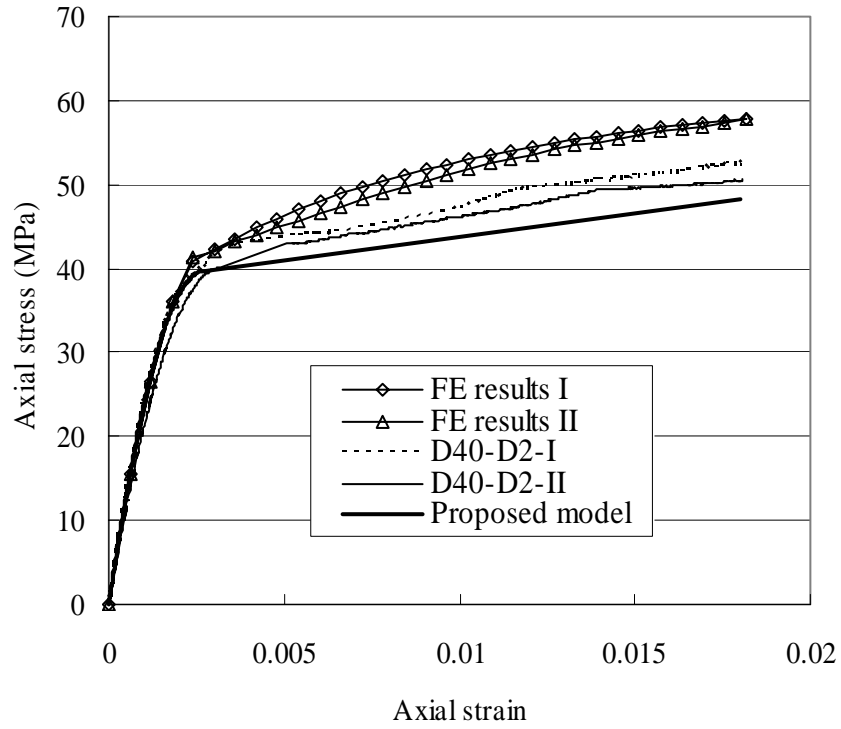


(g) Void ratio=0.58,  $f'_{co}$ =36.7 MPa, two-ply FRP



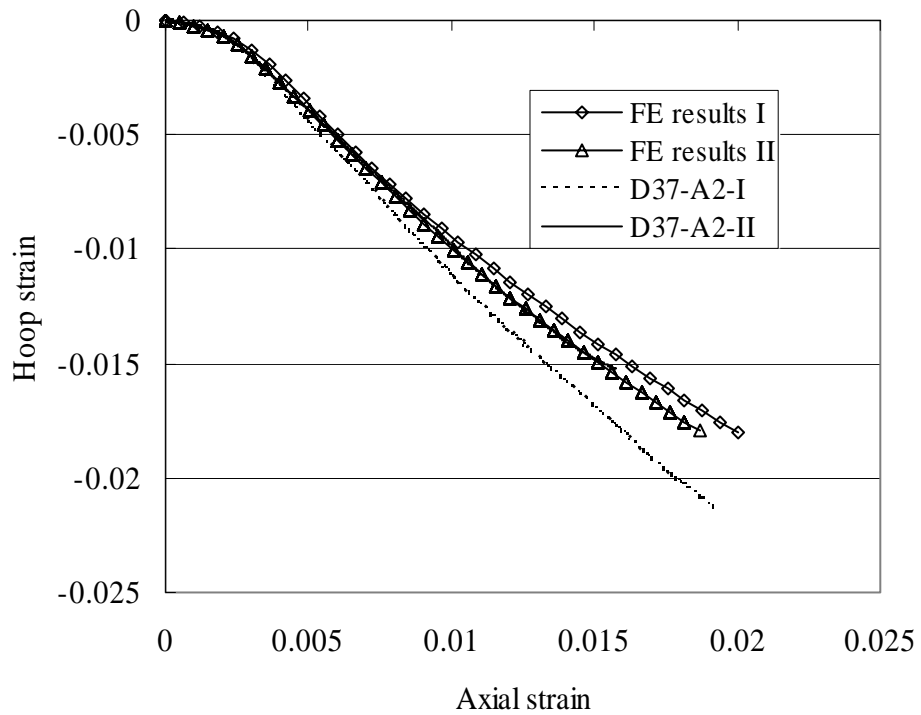
(h) Void ratio=0.58,  $f'_{co}$ =36.7 MPa, three-ply FRP

Figure 5.10 Axial stress-strain curves of concrete in DSTCs (Cont'd)



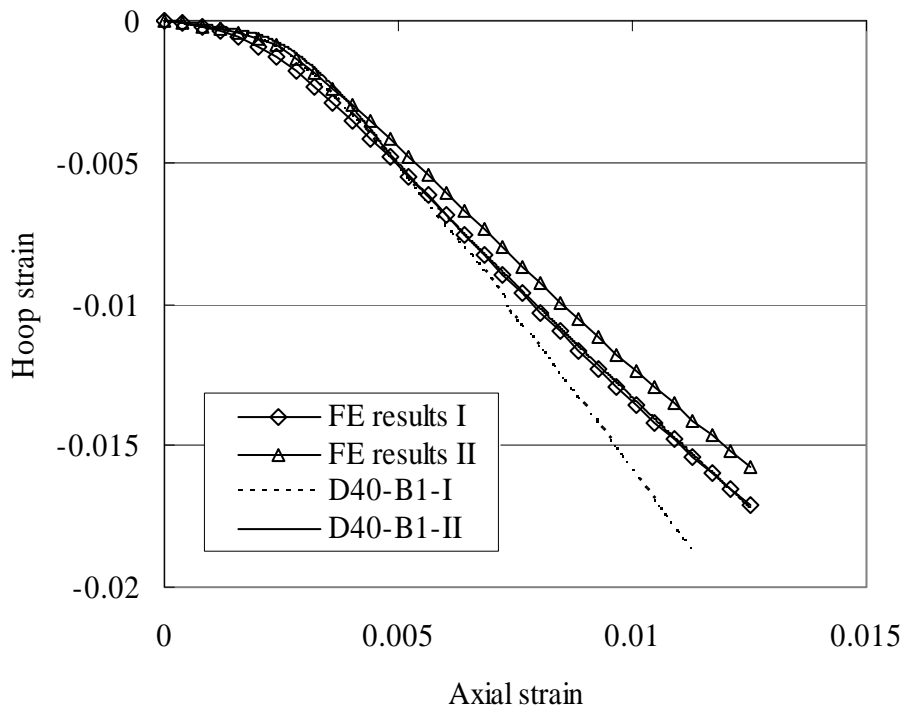
(i) Void ratio=0.75,  $f_{co}$ =40.1 MPa, two-ply FRP

Figure 5.10 Axial stress-strain curves of concrete in DSTCs (Cont'd)

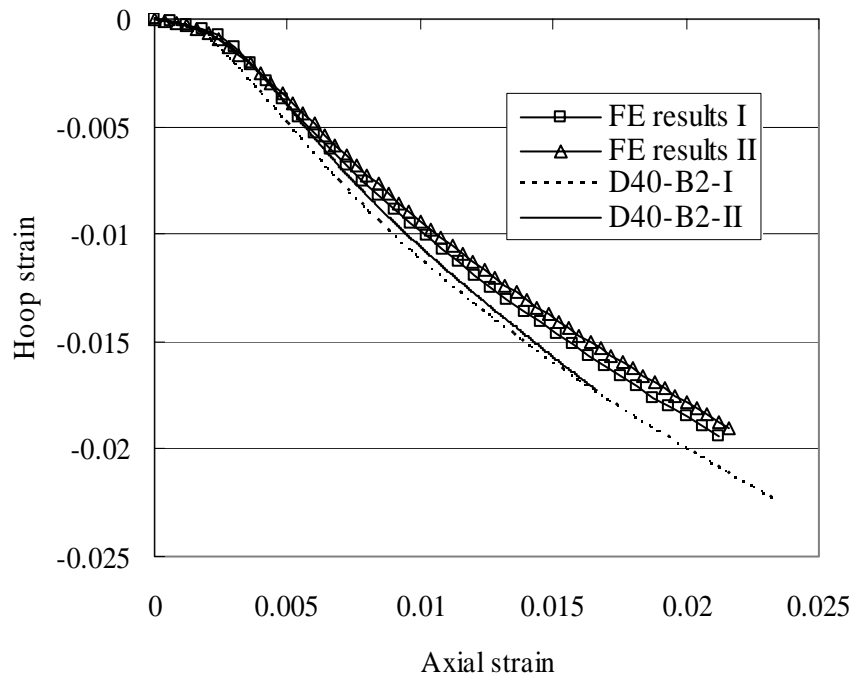


(a) Void ratio=0.28,  $f_{co}'$ =36.7 MPa, two-ply FRP

Figure 5.11 Hoop strain-axial strain curves of concrete in DSTCs

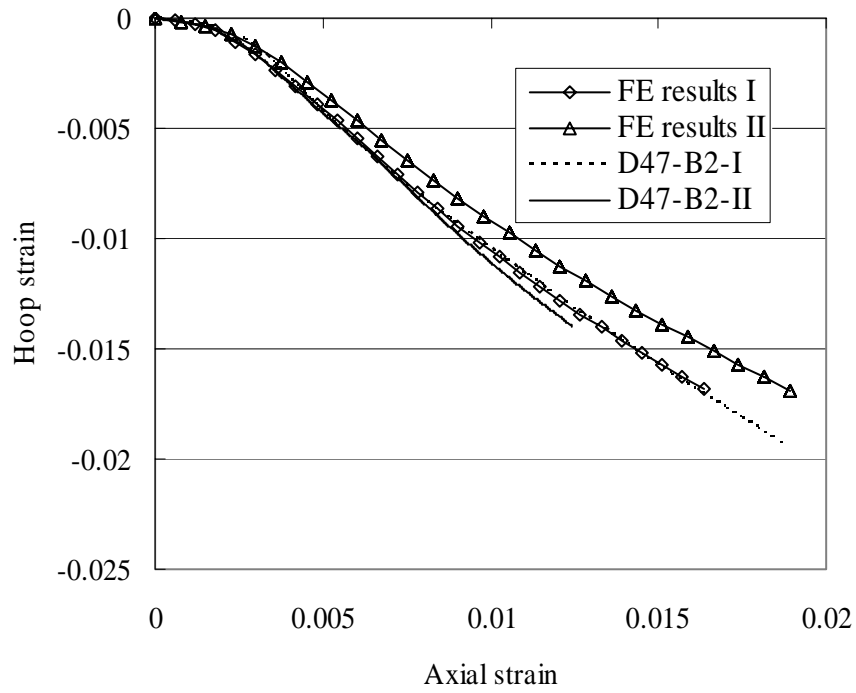


(b) Void ratio=0.5,  $f'_{co}$ =39.6 MPa, one-ply FRP

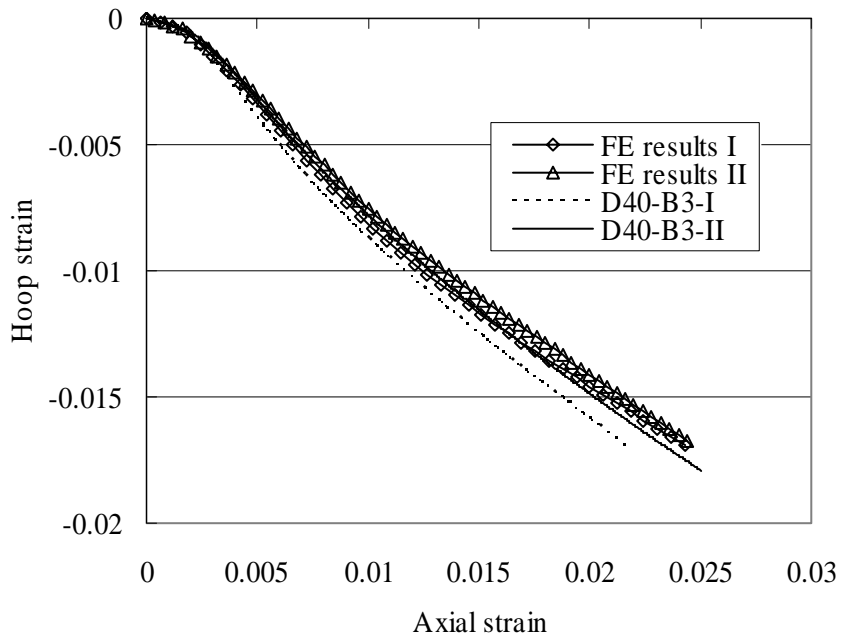


(c) Void ratio=0.5,  $f'_{co}$ =39.6 MPa, two-ply FRP

Figure 5.11 Hoop strain-axial strain curves of concrete in DSTCs (Cont'd)

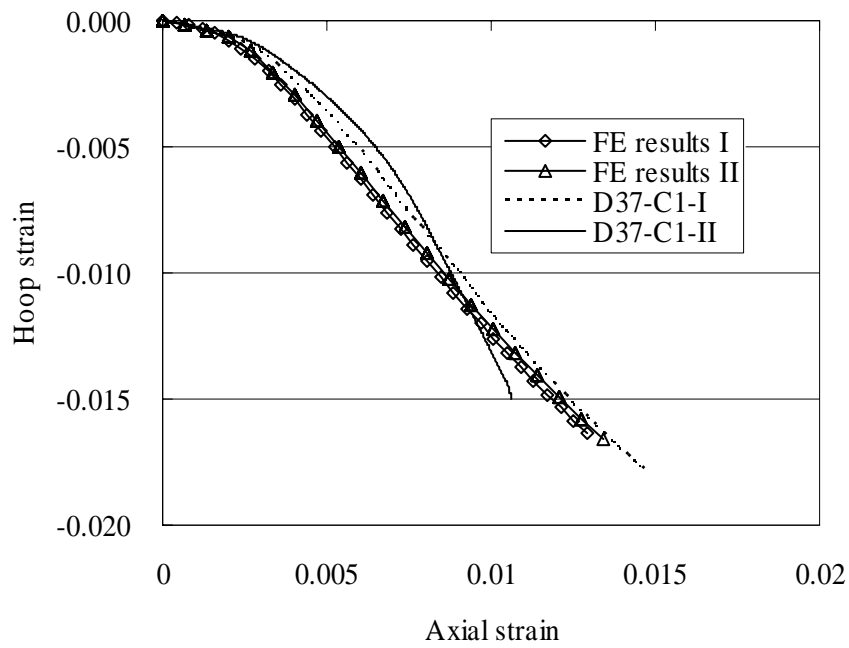


(d) Void ratio=0.5,  $f'_{co}$ =46.7 MPa, two-ply FRP

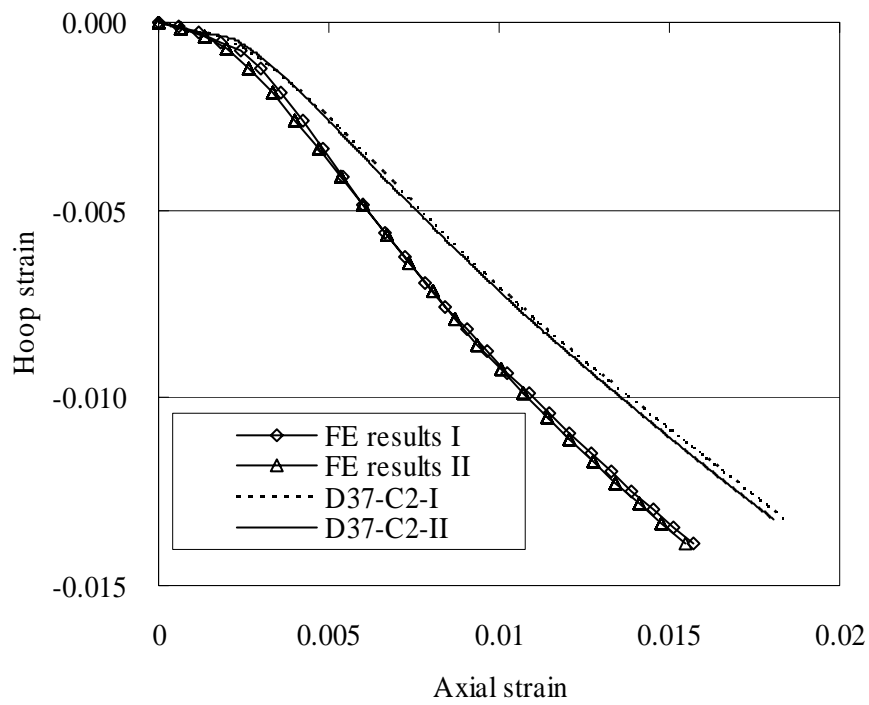


(e) Void ratio=0.5,  $f'_{co}$ =39.6 MPa, three-ply FRP

Figure 5.11 Hoop strain-axial strain curves of concrete in DSTCs (Cont'd)

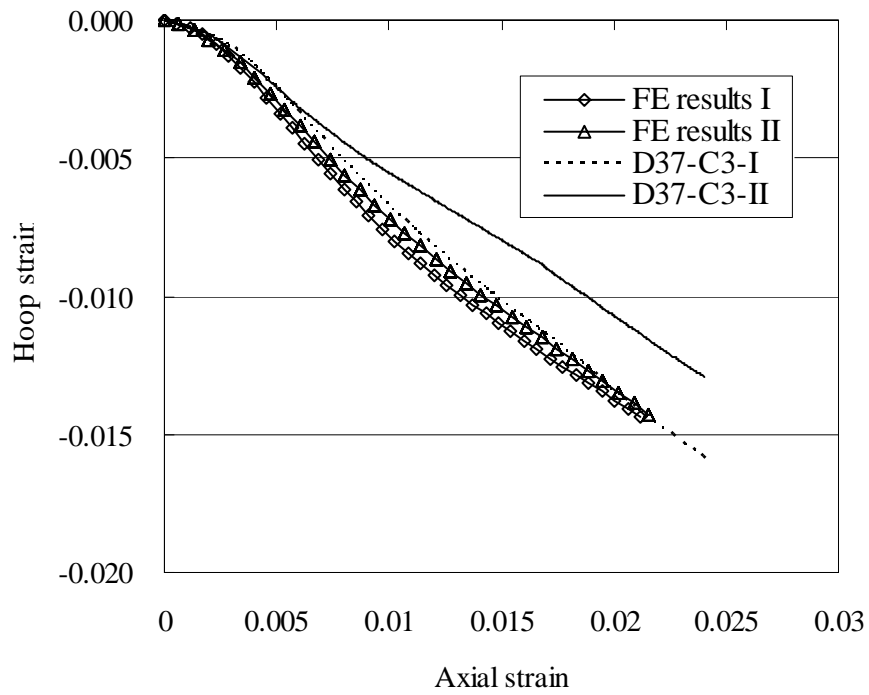


(f) Void ratio=0.58,  $f'_{co}$  =36.7 MPa, one-ply FRP

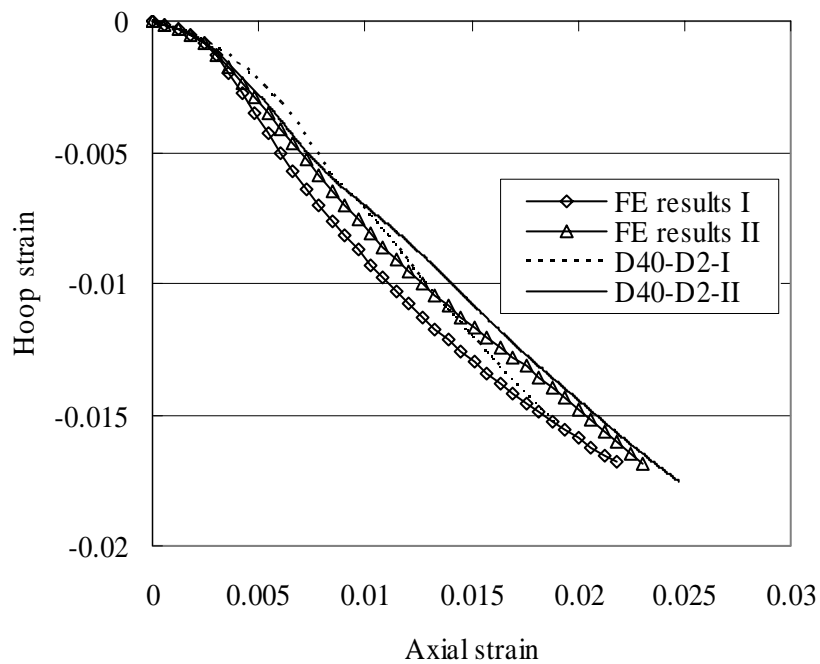


(g) Void ratio=0.58,  $f'_{co}$  =36.7 MPa, two-ply FRP

Figure 5.11 Hoop strain-axial strain curves of concrete in DSTCs (Cont'd)

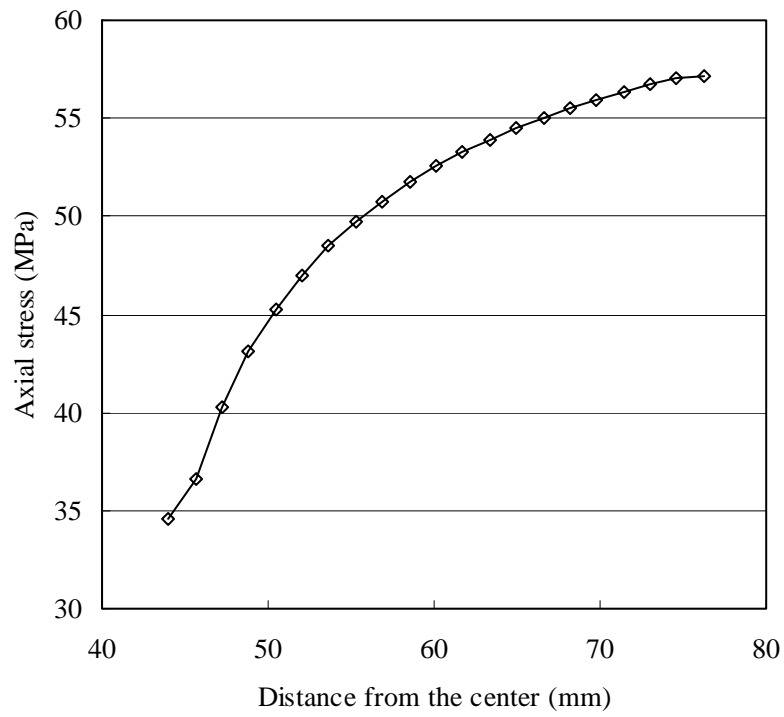


(h) Void ratio=0.58,  $f'_{co}$ =36.7 MPa, three-ply FRP

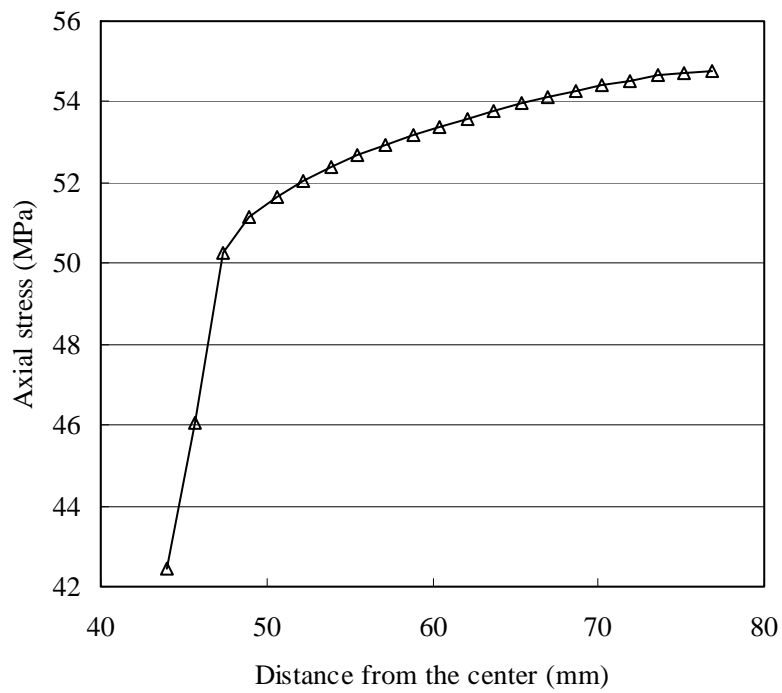


(i) Void ratio=0.75,  $f'_{co}$ =40.1 MPa, two-ply FRP

Figure 5.11 Hoop strain-axial strain curves of concrete in DSTCs (Cont'd)

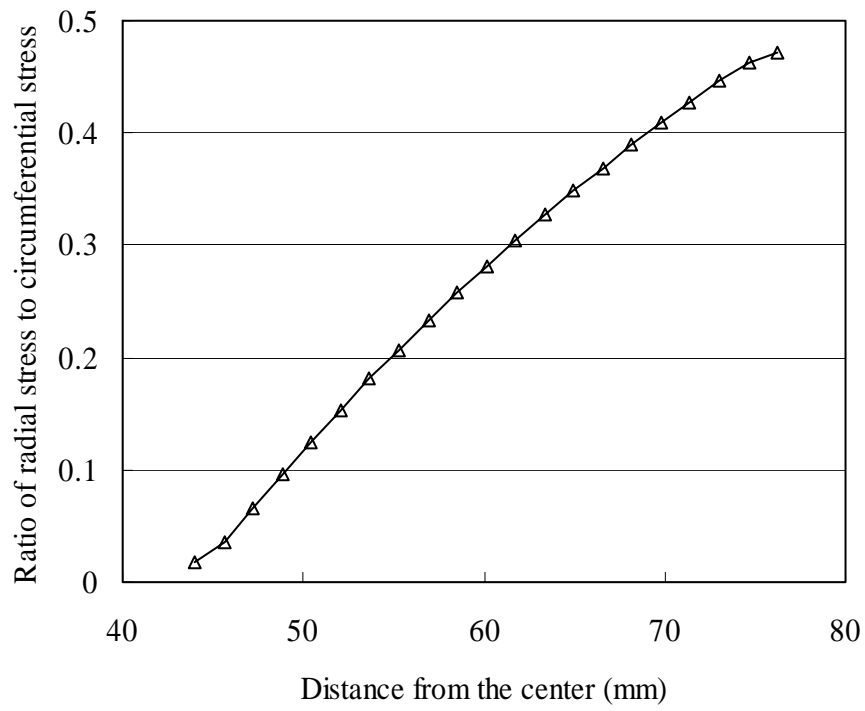


(a) Flow rule based on method (1)

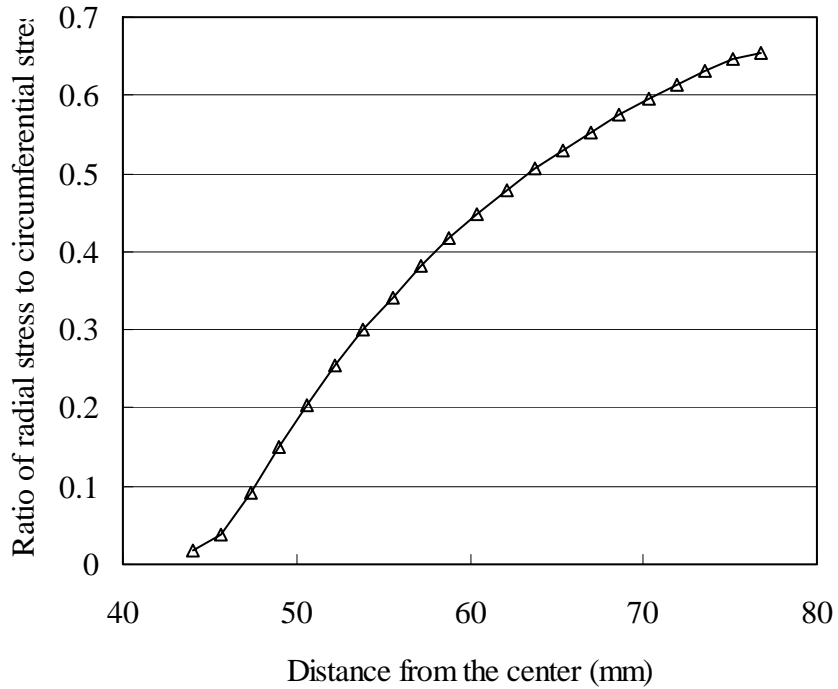


(b) Flow rule based on method (2)

Figure 5.12 Axial stress distribution in the radial direction

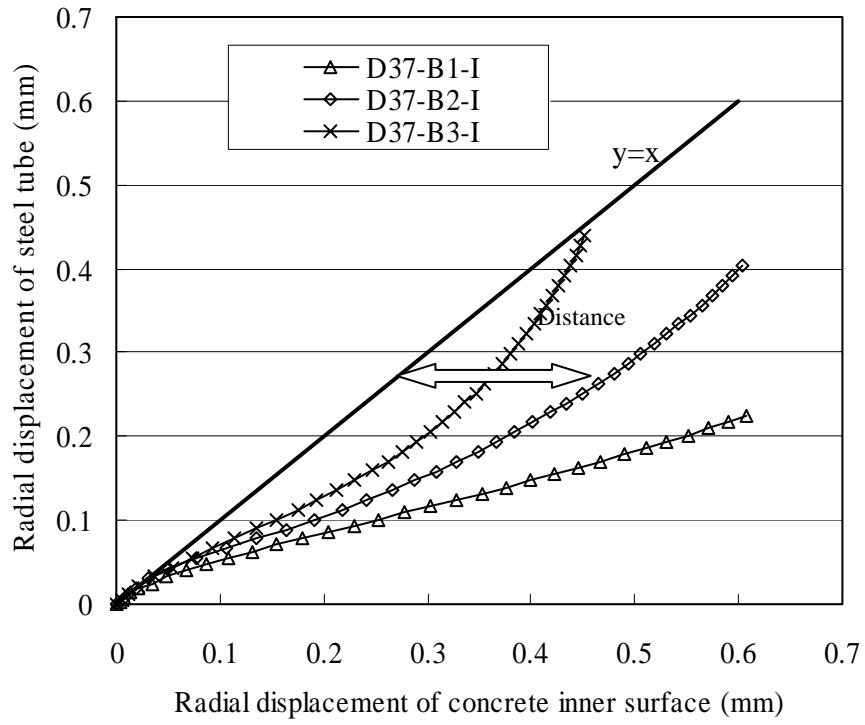


(a) Flow rule based on method (1)

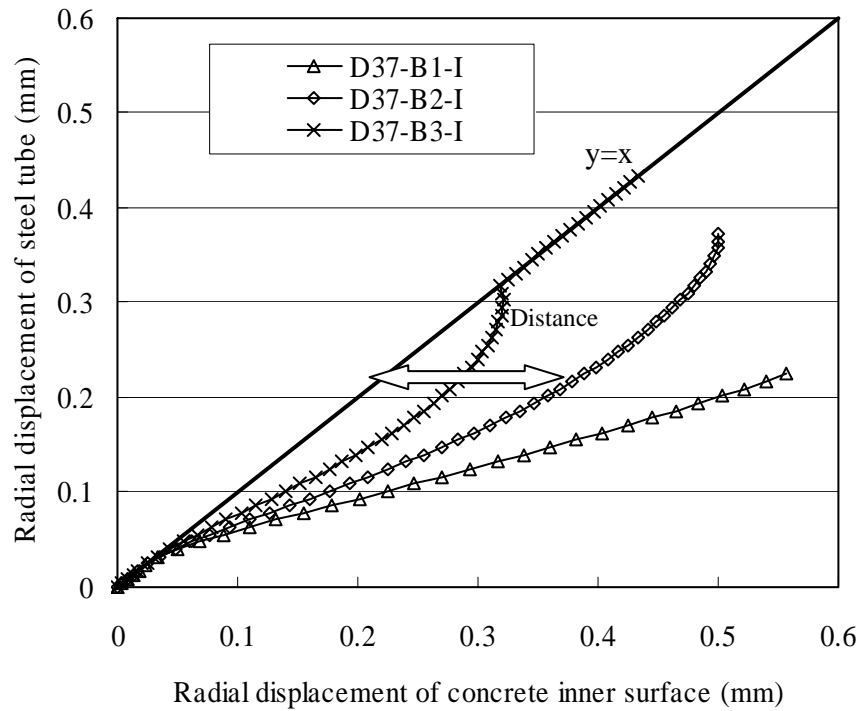


(b) Flow rule based on method (2)

Figure 5.13 Ratio of radial stress to circumferential stress

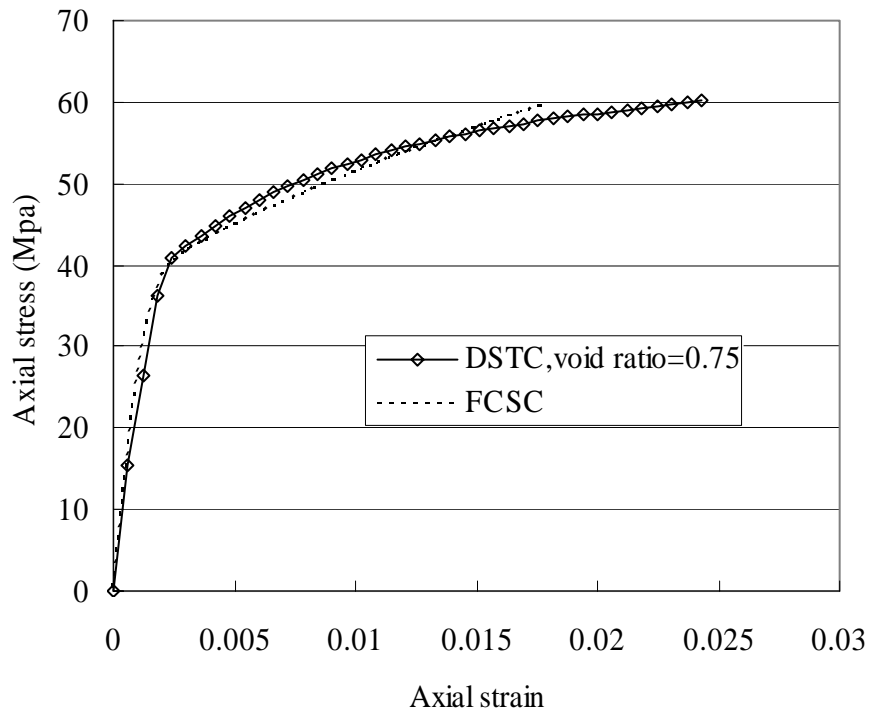


(a) Flow rule based on method (1)

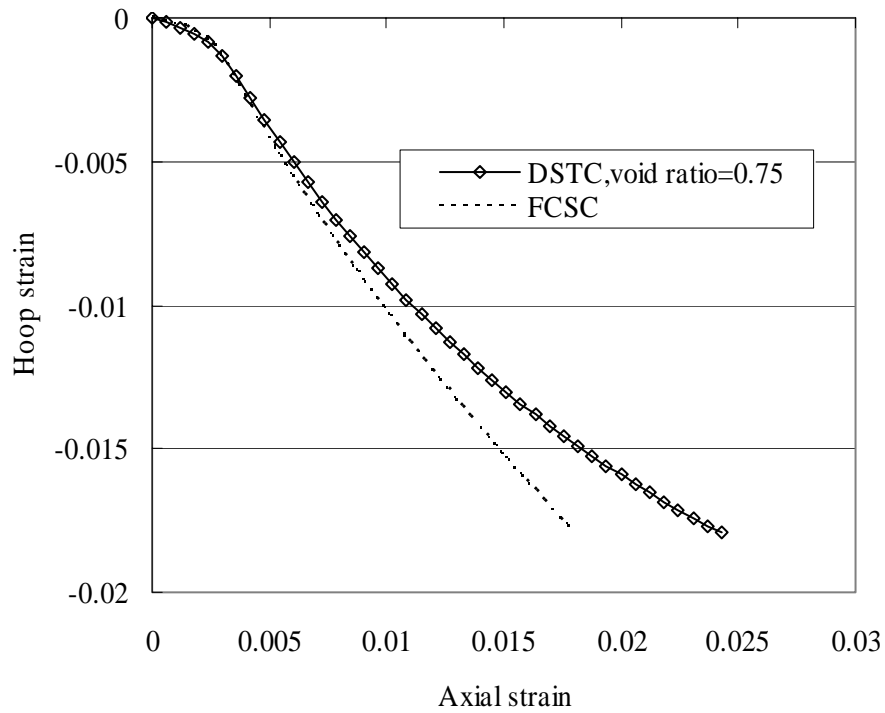


(b) Flow rule based on method (1)

Figure 5.14 Interaction between the steel tube and the concrete

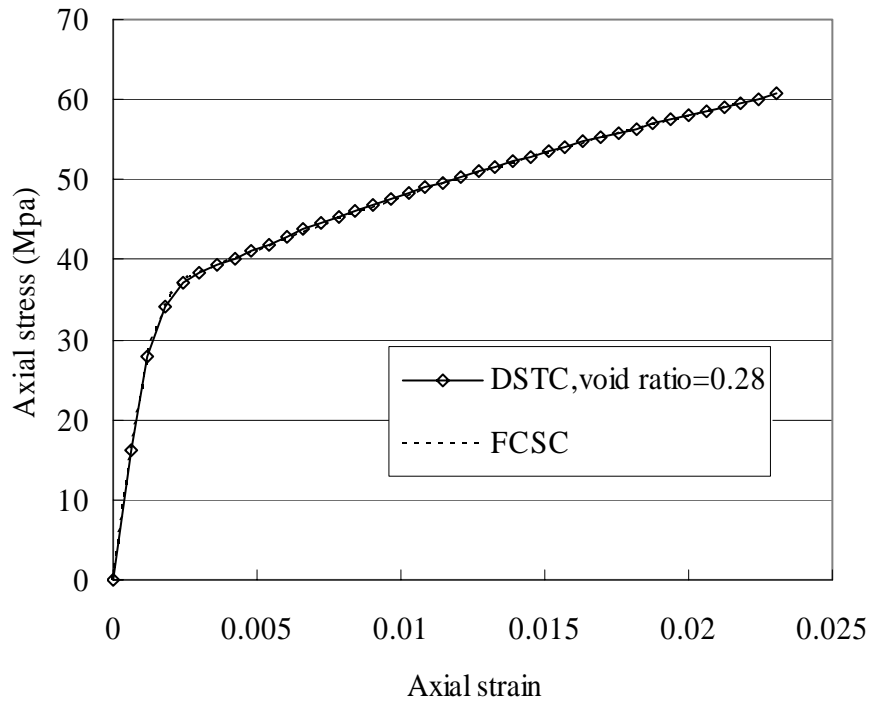


(a) Axial stress-strain curve, void ratio=0.75

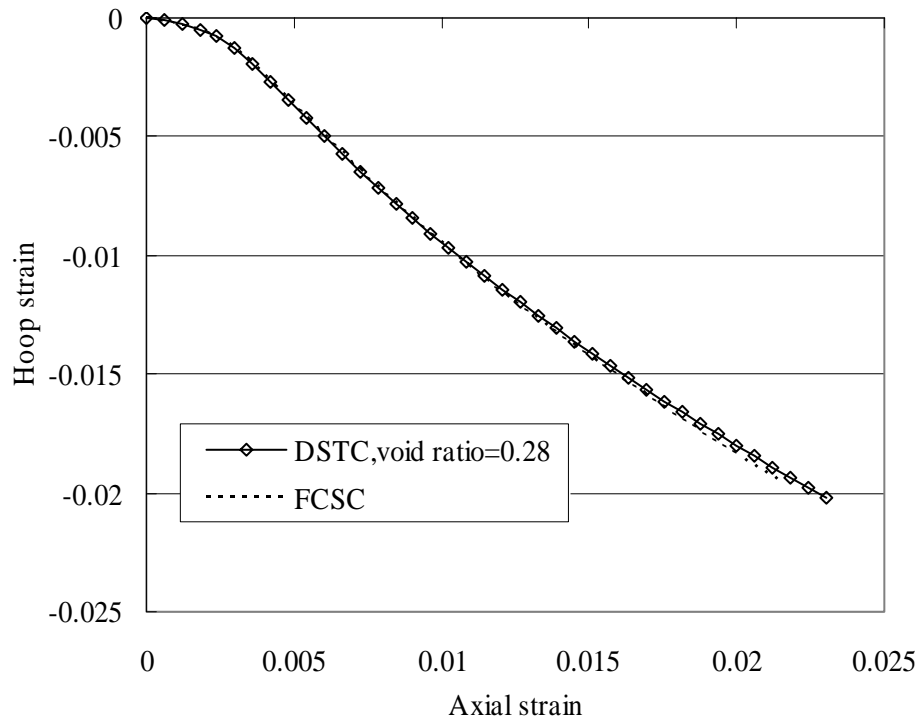


(b) Hoop strain-axial strain curve, void ratio=0.75

Figure 5.15 Comparison between FCSC and DSTC specimens

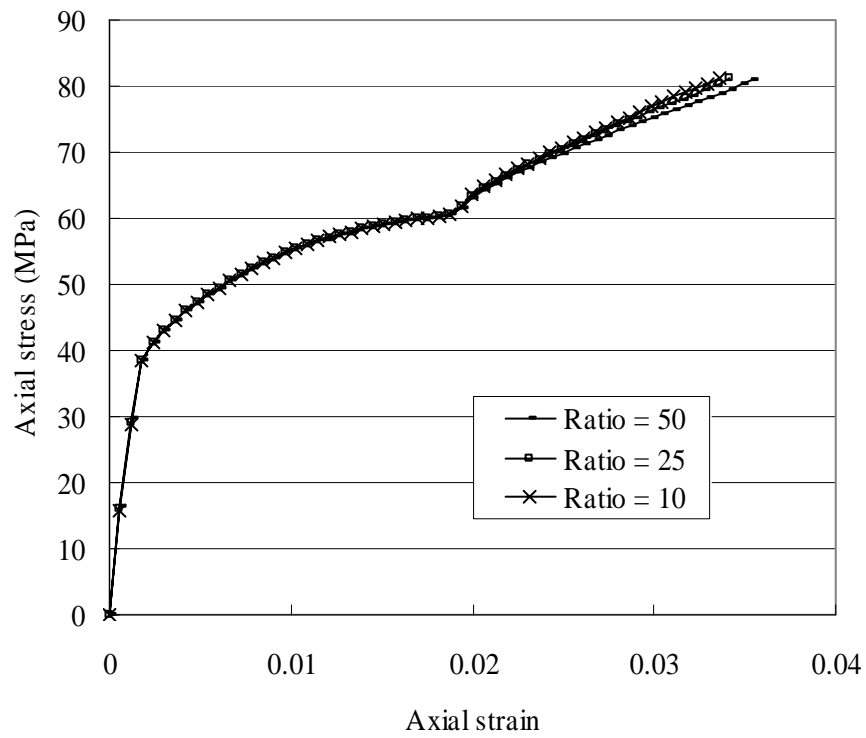


(c) Axial stress-strain curve, void ratio=0.28

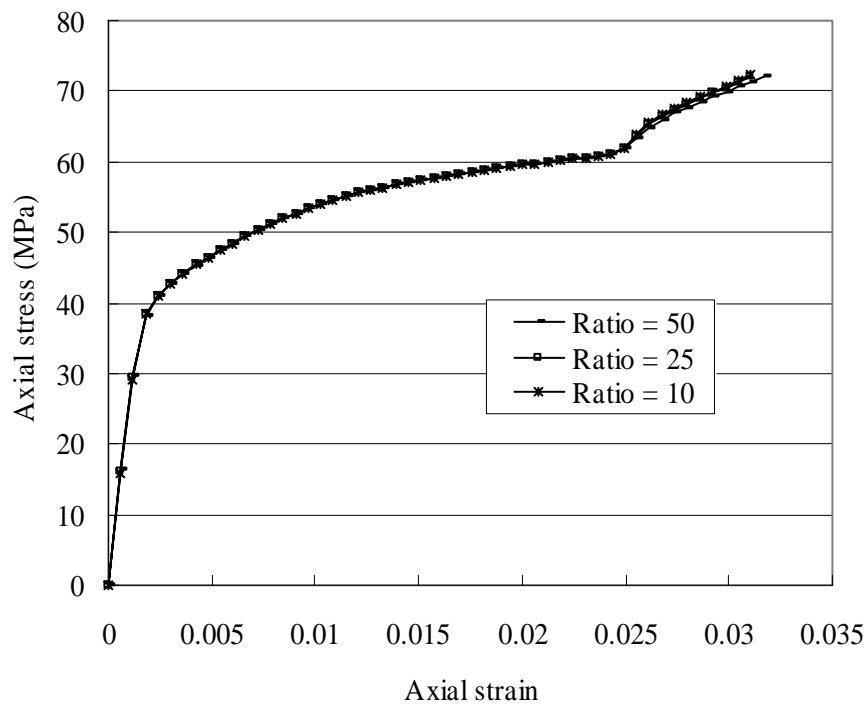


(d) Lateral-axial strain curve, void ratio=0.28

Figure 5.15 Comparison between FCSC and DSTC specimens (Cont'd)



(a) Confinement stiffness=500 MPa, FRP rupture strain=0.02



(b) Confinement stiffness=400 MPa, FRP rupture strain=0.02

Figure 5.16 Effect of  $D_s/t_s$  ratio of steel inner tube on stress-strain behavior

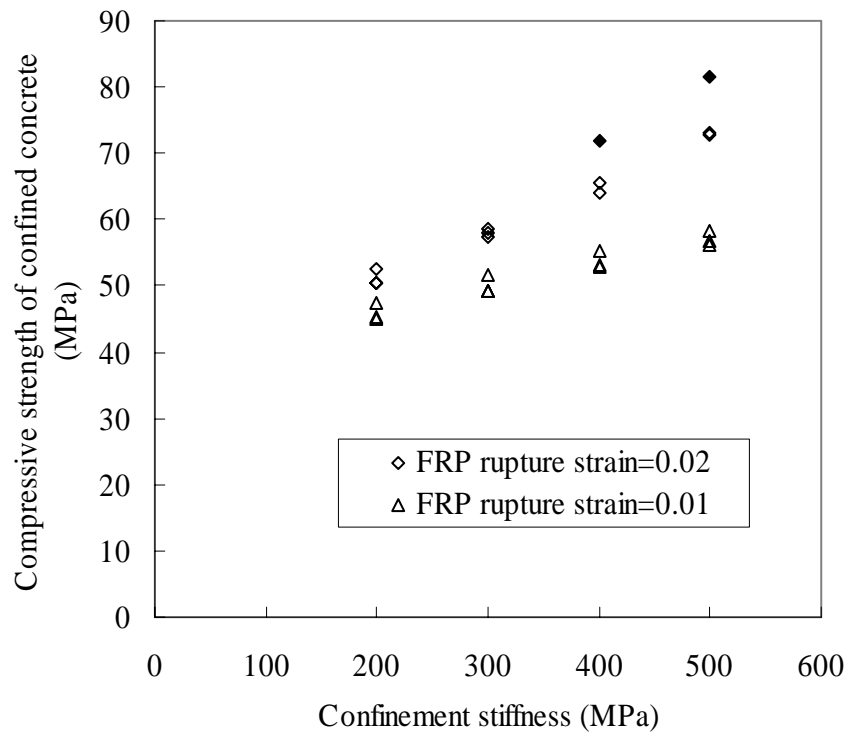
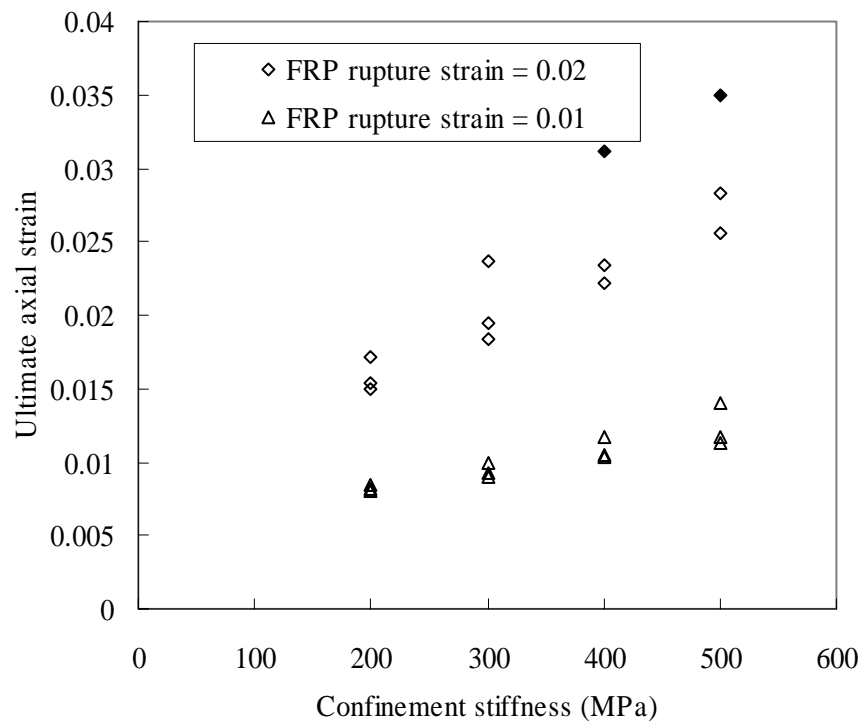
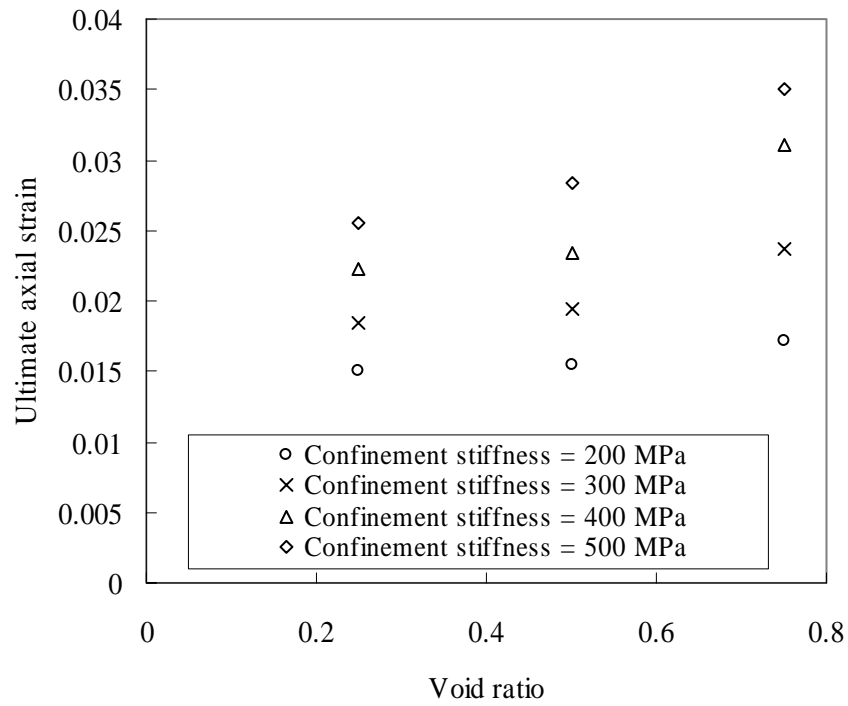


Figure 5.17 Compressive strength of concrete in DSTCs



(a) Effect of confinement stiffness on ultimate axial strain

Figure 5.18 Ultimate axial strain of concrete in DSTCs



(b) Effects of void ratio on ultimate axial strain

Figure 5.18 Ultimate axial strain of concrete in DSTCs (Cont'd)

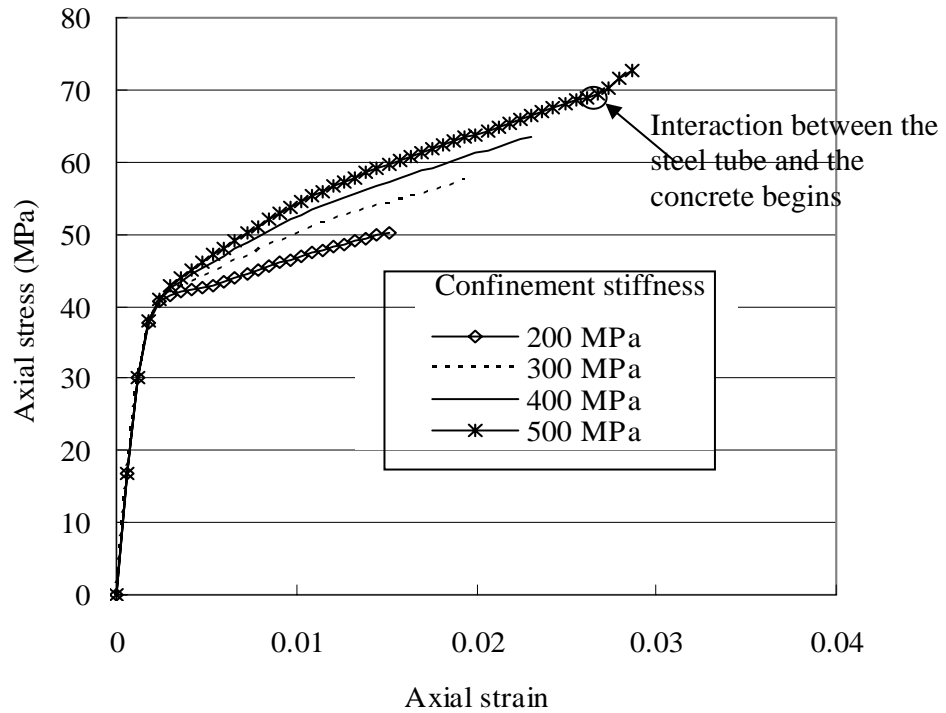
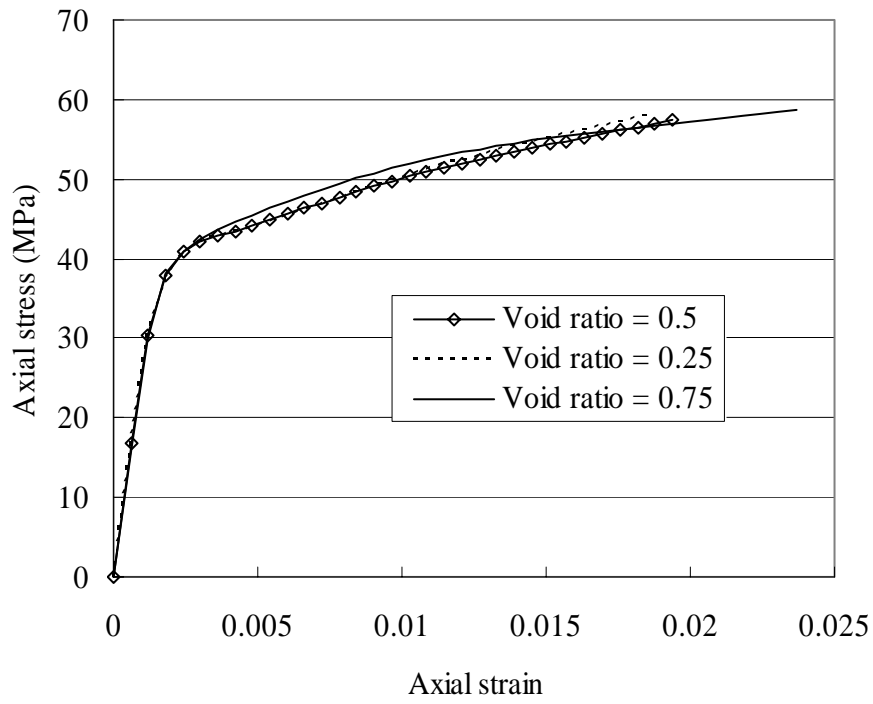
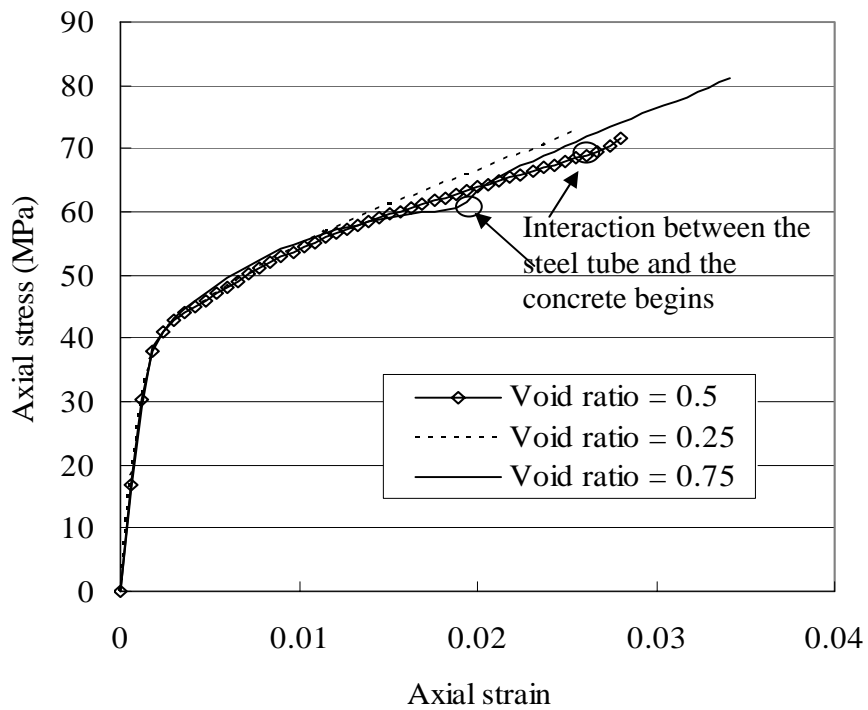


Figure 5.19 Effect of confinement stiffness on stress-strain behavior



(a) Confinement stiffness=300 MPa



(b) Confinement stiffness=500 MPa

Figure 5.20 Effect of void ratio on stress-strain behavior

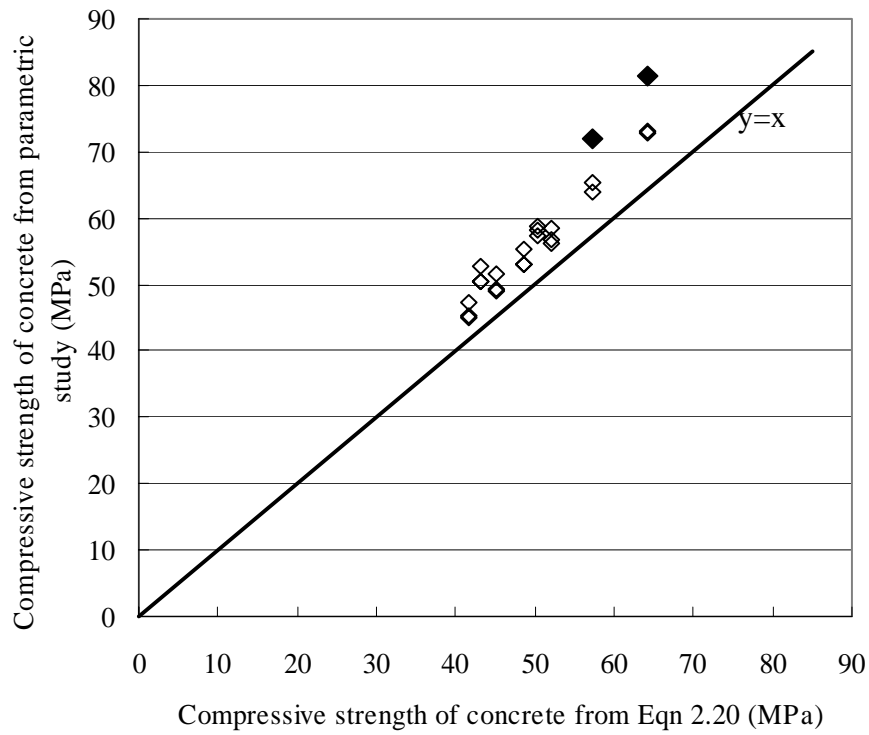


Figure 5.21 Compressive strength of concrete in DSTCs

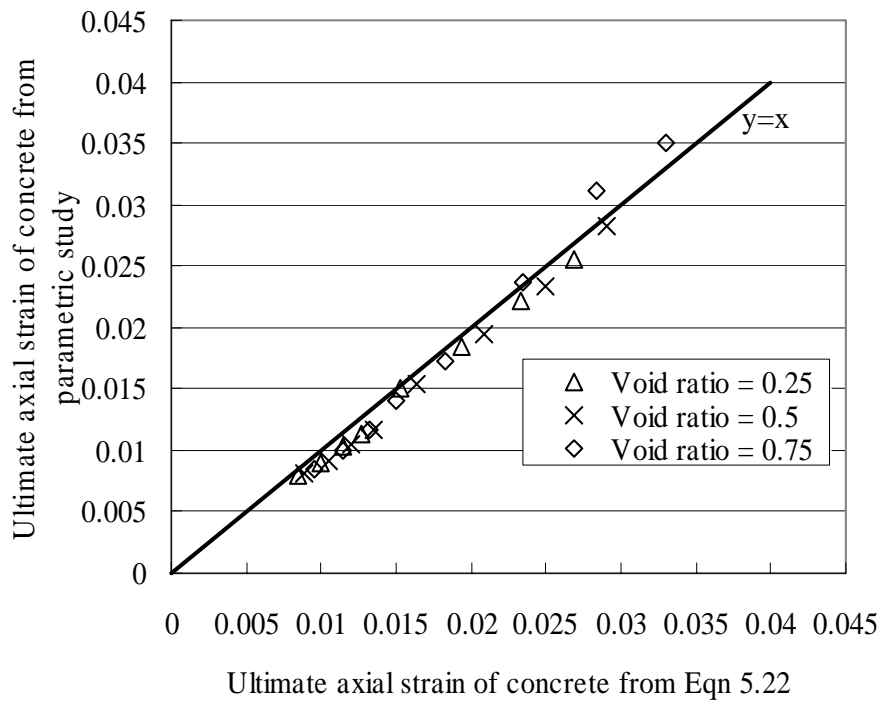


Figure 5.22 Ultimate axial strain of concrete in DSTCs

# **CHAPTER 6**

## **FLEXURAL BEHAVIOR OF HYBRID DSTCS**

### **6.1 INTRODUCTION**

This chapter examines the flexural behavior of the new hybrid FRP-concrete-steel double-skin tubular structural members. As columns are normally subjected to combined axial and lateral loads, their flexural behavior is important within the overall picture of their beam-column behavior. Furthermore, such hybrid members with an eccentric inner steel tube are highly attractive for use as beams (Figure 6.1), for which the flexural behavior is the main structural aspect to be understood.

In this chapter, a systematic experimental study on the flexural behavior of these hybrid members is firstly presented, which includes two series of four-point bending tests (14 beam specimens). The specimen details, material properties, preparation of specimens, test set-up and instrumentation are presented, followed by a detailed discussion of the experimental observations and results. Results from a theoretical model are also presented and compared with the test results. The theoretical model is based on the traditional section analysis employing the so-called fiber element approach. For simplicity, the test specimens are referred to

as beams hereafter in this chapter despite that the section form with a concentric inner tube is more suitable for columns.

## **6.2 BENDING TESTS**

### **6.2.1 Test Specimens**

In total, two series of four-point bending tests (Figure 6.2) on hybrid FRP-concrete-steel double-skin tubular beams (DSTBs) were conducted. The specimens all had an overall length of 1500 mm, an outer diameter of 152.5 mm, and an inner void with a diameter of about 69 mm. The first test series included eight specimens of axis-symmetric configuration (i.e. the outer FRP tube was concentric with the inner steel tube). Two of them were additionally reinforced with six 6 mm diameter longitudinal deformed FRP bars in contact with the inner surface of the FRP tube and evenly spaced around the circumference (Figure 6.3). These FRP bars were intended to increase the initial flexural stiffness of the beam and to delay the development of cracks in the beam.

The second test series included six specimens in which the inner steel tube was eccentrically placed, being shifted towards the tension zone of the beam section to improve the bending rigidity of the section (Figure 6.1). Details of all specimens are summarized in Table 6.1. In this table, the steel tube eccentricity is defined as the distance from the centre of the steel tube to the center of the concrete section (Figure 6.1), and  $D_s$  and  $t_s$  are the outer diameter and the thickness of the steel tube respectively. The variables studied include the concrete strength (from 26.1 MPa to 38.2 MPa), the thickness of the FRP tube (1 ply and 2 plies), the thickness

of the steel tube (from 2.7 mm to 4.3 mm), the provision of FRP bars (6 bars), and the eccentricity of the steel tube (18.2 mm and 32.2 mm). It should be noted that the two steel tube eccentricities were initially designed to correspond to 20 mm and 0 mm concrete covers on the tension side of the section respectively. While a 20 mm cover was achieved without difficulty, it was found to be difficult to produce specimens with the steel tube in contact with the FRP tube. Instead, the measured concrete covers of specimens B-E0-32, B-E1-32 and B-E2-32 were 4.5 mm, 5.5 mm and 6.5 mm respectively. As a result, a steel tube eccentricity of 32.2 mm (or 6 mm concrete cover) was adopted as the average value for the latter two specimens in making the theoretical predictions for these two specimens. Specimen naming uses the following convention: it starts with the letter “B” to indicate that this is a beam specimen, followed by a letter (from “A” to “E”) which represents one of the five types of steel tubes used, and then followed by a number which defines the number of plies of the FRP tube. For two of the specimens in series I, the letter “F” is added at the end to indicate the inclusion of FRP bars as additional longitudinal reinforcement. For series II specimens, a two-digit number is added at the end to define the eccentricity of the steel tube. For example, specimen B-E2-32 had a type E steel tube and a two-ply FRP tube, with the centre of the former being at 32.2 mm from that of the latter.

### **6.2.2 Material Properties**

Tensile tests on three steel coupons were conducted for each type of steel tubes. The coupons were cut along the longitudinal direction from a steel tube of the same type and were tested according to BS 18 (1987). The average experimental values of the elastic modulus ( $E_s$ ), yield strength ( $f_y$ ), and tensile strength ( $f_u$ ) for

each type of steel tubes are listed in Table 6.1. Four tensile tests for the FRP bars were also conducted basically following ACI 440.3R (2004), with two of the specimens failing near the ends and the other two failing away from the ends. The average elastic modulus from the 4 specimens was 54.5 GPa, while the average tensile strength from the two specimens failing away from the ends was 951.7 MPa. The elastic modulus is the more important parameter for the subsequent interpretation of the test results, as the rupture strains of FRP bars in the beam specimens were measured using strain gauges. Tensile tests showed that the GFRP for making the FRP tubes had an average strength of 1825.5 MPa, an average Young's modulus of 80.1 GPa, and an average rupture strain of 0.0228. These results were determined from tensile tests conducted following the ASTM standard (ASTM D3039/D3039M-00 2000) on six coupons and calculated using a nominal thickness 0.17 mm per ply. These properties are for the hoop direction of the FRP tubes where the FRP fibers were oriented in the hoop direction only. Three concrete cylinders (152.5 mm x 305 mm) were cast for each batch of concrete to determine the compressive strength. The mean concrete cylinder strength ( $f'_{co}$ ) for each batch is also given in Table 6.1.

### **6.2.3 Preparation of Specimens**

The preparation process of the DSTC specimens without FRP bars is similar to that introduced in Chapter 3 for the short column specimens, except that a longer formwork was needed for the beam specimens (Figure 6.4). The FRP tube was again formed by the wrapping and resin impregnation of fiber sheets on hardened concrete (Figure 6.5), due to the same reason as stated in Chapter 3. For

specimens with additional FRP bars (i.e. specimens B-D1-F and B-D2-F), the FRP bars were attached to the inner surface of the outer PVC tube at several points along their length using a sealant, before the casting of concrete.

#### **6.2.4 Experimental Set-up and Instrumentation**

The test set-up is shown in Figure 6.2. Except for the two specimens without an outer FRP tube (specimens B-E0-18 and B-E0-32), sixteen strain rosettes were installed, with 8 strain rosettes evenly distributed around the circumference of the FRP tube at each of sections 1 and 2 (Figure 6.2(a)). For those specimens with FRP bars, six additional uni-directional strain gauges (one for each bar) were installed on the FRP bars within the pure bending region. Five displacement transducers were provided at sections 1, 2 and 3 (Figure 6.2(a)) and the two loading sections (Figure 6.2(b)) to measure deflections, while two other displacement transducers were provided at each end of the specimen to measure the slips between the concrete and the steel tube and between the concrete and the FRP tube respectively (Figure 6.2(c)).

For the two specimens without an FRP tube, five uni-directional strain gauges were attached on the concrete surface at different heights of the mid-span section. The provision of displacement transducers differed in that only one displacement transducer was needed at each end to monitor the slip between the concrete and the steel tube. At each loading point, a load cell was used to measure the applied load  $P$ . The test data were collected by a data logger.

## **6.2.5 Test Results, Observations and Discussions**

### *6.2.5.1 General observations*

The load-deflection curves are shown in Figure 6.6, where the load  $P$  represents the average load recorded by the two load cells. It is clear that except specimens B-A1 and B-E2-32, the beam specimens without FRP bars exhibited a smooth load-deflection curve with large deflection ductility, with the mid-span deflection exceeding  $1/15$  of the span at a less than 10% reduction in the load carrying capacity. During the tests of B-A1 and B-E2-32, there was a sudden load drop accompanied by a loud noise, after which, however, the specimens could be reloaded to exceed the original load level.

The two specimens with FRP bars (B-D1-F and B-D2-F) also experienced sudden load drops during the tests. These load drops, which were due to the rupture of the FRP bars, were relatively small (about 19% of the peak load) and could not be subsequently recovered. After these load drops, the specimens could still sustain an almost constant load with increasing deformation.

For the specimens with an FRP tube but without FRP bars, the test was eventually terminated due to the headroom limitation of the loading frame. For the two specimens without an FRP tube, the test was terminated when many large cracks were found on the beam (due to the absence of an FRP tube outside) (Figure 6.7(c)) and the whole loading system became somewhat unstable. For the two specimens with FRP bars, the test was terminated when the beam became increasingly more asymmetric and unstable due to a major localized crack (Figure

6.7(b)). Specimens B-B1, B-D1-F and B-E0-18 after the tests are shown in Figure 6.7 to illustrate the typical deformation and crack patterns.

#### *6.2.5.2 Development of cracks*

During the tests, initial flexural cracks were found in the early stage of loading. For the DSTB specimens, these initial cracks were revealed by white patches on the FRP tube which appeared as a result of resin damage due to cracks in the concrete behind the tube. The initiation of cracks can also be identified from the readings of strain gauges. Figure 6.8 shows two typical compressive-tensile strain curves for two specimens, in which the compressive and tensile strains are from two strain gauges located at the top and bottom of the mid-span respectively. In both cases, the relationship between the two strains is initially linear, but after the tensile strain reaches about 0.00013, the tensile strain in specimen B-C1 increases much more rapidly than before, while the tensile strain in specimen B-B1 remains almost constant despite large increases of the compressive strain. This is because tensile cracks occurred within the gauge length of the strain gauge in the former case but outside the gauge length in the latter case. The end of the initial linear relationship corresponds to the occurrence of tensile cracks in the beam, which took place at about 15% of the peak load for those specimens without FRP bars and at about 20% of the peak load for those with FRP bars.

With further load increments, new cracks and extension of existing cracks were observed. At the end of each test, the mid-span deflection exceeded 1/15 of the span and wide cracks were found in the specimen. For the specimens with an outer FRP tube but without FRP bars, two major vertical cracks always formed

right below or very close to the two load positions, and other less prominent vertical cracks were randomly distributed within and outside the pure-bending region of the specimen (Figure 6.7(a)). For the specimens without an outer FRP tube, inclined shear cracks were found together with flexural cracks along the specimen (Figure 6.7(c)). For the specimens with FRP bars, no obvious cracks were found on the surface of the FRP tube before the peak load except some “white patches” which indicated the appearance of cracks in the concrete behind. After the attainment of the peak load (at a mid-span deflection of about 1/50 of the span) at the rupture of the FRP bar at the bottom of the beam, a major crack opened up at the location of rupture of the FRP bar within the pure bending region (Figure 6.7(b)).

#### *6.2.5.3 Effect of the FRP tube*

For the specimens in series I, in which the two tubes (the FRP tube and the steel tube) were concentrically placed, the thickness of the FRP tube had little effect on the stiffness and the ultimate load of the DSTB (Figure 6.6). However, local rupture of the FRP tube by hoop tension was found in the final stage of testing in some specimens with a one-ply FRP tube (Figure 6.9) but in none of the two-ply FRP tubes. This implies that a thicker FRP tube will lead to a more ductile response. In addition, specimens with an FRP tube can be expected to possess a superior performance to those without an FRP tube due to the confinement to concrete and the shear resistance provided by the FRP tube.

For the specimens in series II, which had an eccentrically placed steel tube, the one-ply FRP tube enhanced the ultimate load by over 20% for both steel tube

eccentricities. A thicker FRP tube also helped increase the ultimate load and the ductility; local FRP rupture was again found in both specimens with a one-ply FRP tube in the final stage of testing. Indeed, for specimens B-E1-18 and B-E1-32, the load began to drop in the final stage due to the rupture of the FRP tube (Figure 6.6(b)). In addition, shear cracks were found in the two specimens without an FRP tube (Figure 6.7(c)), but not in the other specimens with an FRP tube (Figure 6.7(a) and (b)), which were at least partially responsible for the poorer performance of the specimens without an FRP tube. The FRP tube clearly enhanced the shear resistance of the specimens. The shear resistance offered by the FRP tube is also confirmed by the development of significant hoop tensile strains (over 0.1%) at some locations (probably where the shear cracks in the concrete were located) in the lower part of the FRP tube as revealed by strain measurements.

#### *6.2.5.4 FRP confinement of concrete*

As there were only hoop fibers in the FRP tubes, their axial stiffness and strength were insignificant. The contribution of the FRP tube to the flexural behavior of a DSTB was mainly through the provision of confinement to the concrete. Axial compressive tests (Chapter 3) have shown that the confinement provided by the FRP tube to the concrete in such a double-skin section can improve the ductility or both the ductility and the strength of the concrete, depending on the thickness of the FRP tube. The benefit of confinement was also present in the test beams with an FRP tube (Figure 6.6 and Table 6.1).

The test results from series I indicate that the ultimate load was little affected by the thickness of the FRP tube. This observation may mean that in these test beams, the behavior of the concrete confined by a one-ply FRP tube did not differ significantly from that of the concrete confined by a two-ply FRP tube, which differs from the conclusion drawn from the axial compression test results on closely similar DSTC sections (Chapter 3). In the axial compression tests, the two-ply tube led to a significantly higher ultimate load and better ductility than those obtained for a one-ply tube. This difference in the effect of confinement between axial compression and flexural specimens may be due to two reasons: 1) the area of the compressive region of concrete is much smaller (less than half of the section) in the flexural specimens, so their ultimate loads are much less sensitive to the concrete strength; 2) the effect of confinement is reduced in a beam specimen due to the existence of a strain gradient over the beam section. Previous experimental work by other researchers on concrete-filled FRP tubes has shown that the effect of confinement on concrete is less significant for beams than for columns (Fam and Rizkalla 2002; Mirmiran et al. 1999).

The test results of specimens of series II clearly indicate the benefit of a thicker FRP tube. The ultimate load of specimen B-E2-18 is 7.69% higher than that of specimen B-E1-18, while the ultimate load of specimen B-E2-32 is 15.1% higher than that of specimen B-E1-32. The larger difference between the two B-E-32 specimens may be due to two reasons: 1) there was more concrete in the compressive region of the B-E-32 sections with a steel tube eccentricity of 32.2 mm than the B-E-18 sections with a steel tube eccentricity of 18.2 mm, so more benefit was derived from the FRP confinement; 2) the concrete in the B-E-32

specimens had a lower unconfined strength (26.1 MPa) (Table 6.1), which made the effect of FRP confinement more significant in terms of strength increases relative to the unconfined strength, as has been established in the existing literature (e.g. Teng and Lam 2004).

For the specimens in series I, although the thickness of the FRP tube had little effect on the ultimate load, it did lead to a clear difference in the axial strain-hoop strain behavior (at the top compressive fiber). Figure 6.10 shows two axial strain-hoop strain curves for specimens B-C1 and B-C2 with a one-ply FRP tube and a two-ply FRP tube respectively. Both curves indicate that as the axial strain increases, the rate of increase in the hoop strain (in terms of the absolute value) initially increases and then remains more or less constant. In the later stage of loading, at the same axial compressive strain, the hoop strain for the one-ply tube is about twice that for the two-ply tube, so the two tubes provided about the same amount of confinement as their thicknesses were different. For instance, at an axial compressive strain of 0.008, the hoop tensile strain is 0.0052 for B-C1 and 0.0029 for B-C2. This greater demand on the hoop deformation of the one-ply tube explains why some of the one-ply FRP tubes but none of the two-ply FRP tubes failed by rupture and why DSTBs with a thicker FRP tube can be expected to exhibit greater ductility.

#### *6.2.5.5 Slip between the concrete and the tubes*

The slip between the concrete and the FRP tube was insignificant (almost zero) in all cases except for B-E2-32 due to the small axial stiffness of the FRP tube. The slip between the concrete and the steel tube, however, was much larger (about 10

mm at the end of test for most of the specimens). The steel tube-to-concrete slip gradually increased with the mid-span deflection except for specimen B-A1.

During the test of specimen B-A1, there was a sudden load drop accompanied by a loud noise at a load  $P=26.1$  kN with a mid-span deflection of 54.1 mm. The LVDT readings at the two ends of the specimen revealed that there was a sudden increase in the slip between the concrete and the steel tube at the onset of this sudden load drop. It is believed that this sudden slip increase was due to at least a partial loss of the composite action between the concrete and the steel tube. This phenomenon indicates that an improvement to the bond between the concrete and the steel tube in such DSTBs may be needed.

During the test of specimen B-E2-32, there was also a sudden load drop with a loud noise at a load  $P=35.4$  kN with a mid-span deflection of 21.5 mm. The associated slip between the concrete and the FRP tube was about 0.65 mm. This suggests that the bond between the concrete and the FRP tube in such DSTBs may also need improvement, particularly if the FRP tube possesses significant axial stiffness.

It is evident from the test observations that improvements to the bond resistance at both interfaces are desirable. Roughening treatments on the tubes and the use of mechanical connectors are possible alternatives to achieve enhanced interfacial bond resistance.

#### *6.2.5.6 Effect of FRP bars*

Two of the beams (B-D1-F and B-D2-F) had FRP bars as additional longitudinal reinforcement. These FRP bars were provided to avoid the early development of cracks in the tensile concrete. The FRP bars enhanced both the stiffness and the ultimate load of the beam. These beams displayed almost linear load-deflection behavior up to a mid-span deflection of about 1/100 of the span (or about 80% of the ultimate load). Afterwards, the stiffness of the beam reduced continuously, while the load kept increasing until the ultimate load was reached at a mid-span deflection of about 1/50 of the span. No obvious cracks were found on the surface of the FRP tube before the peak load was reached. At the ultimate load, a sudden and large noise was heard and the load dropped abruptly to a lower level, accompanied by the opening-up of a major crack and a large increase of the mid-span deflection. This failure was due to the rupture of the FRP bar at the bottom of the beam, which was subjected to the largest tensile strain. After this large reduction in load, the specimen continued to sustain a considerable load in a ductile manner. Figure 6.6(a) shows a comparison of the load-deflection responses of specimens with or without FRP bars. It is clear that the provision of FRP bars provides an effective means to enhance the flexural stiffness and the ultimate load of the member, and to suppress early cracking.

#### *6.2.5.7 Effect of the steel tube*

In the present hybrid members, the steel tube is the sole longitudinal reinforcement, except when some FRP bars are also provided. The steel tube thus plays a very important role in resisting loading and ensuring a ductile response. With all other parameters being the same, a thicker steel tube leads to a higher

ultimate load, as can be seen by comparing the results for specimens with a 4.3 mm thick steel tube (specimens B-C1 and B-C2) to those for specimens with a 2.7 mm or 3.2 mm thick steel tube (specimens B-A1 and B-A2; and specimens B-B1 and B-B2) (Figure 6.6(a)). For the two groups of specimens with steel tube thicknesses of 2.7 mm and 3.2 mm respectively, the small benefit of the slightly thicker tube was offset by a lower yield stress, so the effect of steel tube thickness is unclear in Figure 6.6(a).

For the hybrid section to be employed in a beam, the flexural stiffness and strength of the beam can be enhanced by shifting the steel tube towards the tension side, which also places more concrete in the compression zone. The specimens in series II were tested to demonstrate the performance of DSTBs with an eccentrically placed steel tube. The test results show that the ultimate load of specimen B-E1-18 is about 40% higher than that of specimen B-B1 (Table 6.1), although the two specimens had similar steel tubes, FRP tubes and concrete. Specimen B-E1-18 also displayed a higher flexural stiffness than that of specimen B-B1 (Figure 6.6). Similar conclusions can be drawn by comparing the results of specimens B-E2-18 with B-B2. It can also be found that the ultimate loads of specimens B-E1-32 and B-E2-32 are higher than those of specimens B-E1-18 and B-E2-18 respectively (3.1% for one-ply tubes and 10.23% for two-ply tubes), although the unconfined concrete strength of the former two specimens is much lower (28%) than that of the latter two specimens. This is because the former two specimens had a larger steel tube eccentricity. It may also be noted that the difference in the ultimate load is larger between the two specimens with a two-ply

tube, which suggests that the effect of FRP confinement on the concrete is more significant for these specimens.

## **6.3 THEORETICAL ANALYSIS**

### **6.3.1 Analysis Model**

A traditional section analysis of the so-called fiber element approach was developed for the present DSTBs based on the plane section assumption and the assumption that all FRP bars become ineffective once rupture of the most highly stressed FRP bar occurs. The analytical procedure involves the determination of the position of the neutral axis for a given strain of the extreme compression fiber by force equilibrium and the evaluation of the bending moment by integrating the contributions of stresses over the section.

The stress-strain behavior of the steel tubes was modeled based on their tensile test results. For specimens in series I except specimens B-C1 and B-C2, an elastic-perfectly plastic stress-strain curve was adopted with the elastic modulus and the yield stress for each type of steel tube as given in Table 6.1. For specimens B-C1 and B-C2 and the specimens in series II, the experimental stress-strain curves did not show an elastic-perfectly plastic shape. A typical curve for the steel of specimens B-C1 and B-C2 is shown in Figure 6.11. For these specimens, the stress-strain curve for each type of steel tube was modeled by representing the average experimental stress-strain curve with a large number of data points.

A linear stress-strain curve was adopted for FRP bars based on the tensile test results. The contribution of the outer FRP tube in the longitudinal direction was neglected as it did not have longitudinal fibers.

The concrete was assumed to possess the same initial elastic modulus in both tension and compression. Tensile cracking was assumed to occur at a tensile strain of  $130 \mu\epsilon$  based on test observations (e.g. Figure 6.8(b)), and the concrete was assumed to resist no tensile stresses after cracking. The design-oriented stress-strain model (Eqns 2.12-2.15, 2.20 and 5.22) proposed in Chapter 5 was adopted to produce the stress-strain relationship of concrete in compression. For each specimen, the longitudinal strain at the extreme compression fiber of its FRP tube reached at the end of test was taken as the ultimate point of the stress-strain curve of its confined concrete.

### **6.3.2 Load-Strain Curves**

#### *6.3.2.1 Specimens without FRP bars*

Figures 6.12(a)-(f) show comparisons of predicted and experimental load-strain curves for specimens B-C1, B-C2, B-E1-18, B-E2-18, B-E1-32, and B-E2-32 respectively. The strain values shown are those of the extreme compressive fiber at the mid-span. These comparisons cover different section configurations, different steel tube eccentricities, and different FRP tube thicknesses.

It is evident that in general the theoretical results agree well with the test results for all specimens except specimen B-E2-32. Considerable errors exist for the

initial part of the load-strain curve of specimen B-E2-32 (Figure 6.12(f)). These errors may be attributed to slips between the FRP tube and the concrete which might have existed right from the beginning of loading due to the greater thickness of the FRP tube (i.e. greater axial rigidity) of specimen B-E2-32, so that the strains recorded on the FRP tube are smaller than predictions based on the plane section assumption. Indeed, the sudden slip found during the test of this specimen, but not in other specimens, supports this explanation.

It is also noted that the theoretical analysis provides better predictions for the specimens with a one-ply FRP tube (B-C1, B-E1-18 and B-E1-32) than for those with a two-ply FRP tube. For specimen B-E2-18 with a two-ply FRP tube and an eccentric steel tube, the ultimate load can be closely predicted, but errors exist in the predicted load-strain response. For specimen B-C2 which had a two-ply FRP tube and a concentric steel tube, the theoretical analysis overestimates both the ultimate load and load-strain response. This observation may be due to the fact that in a beam specimen the confining mechanism is different from that in a column specimen and the effect of confinement is reduced due to the existence of a strain gradient over the beam section.

Taking into consideration the above observation and the experimental finding that the experimental behavior of a beam with a one-ply tube differed from that of the corresponding beam with a two-ply tube (Figure 6.6) only slightly, the following simple compressive stress-strain curve with an approximately elastic-perfect plastic shape was assumed for concrete in DSTBs, regardless of the thickness of the FRP tube. This curve is close to that found from the design-oriented

stress-strain model for the one-ply DSTC specimens with a very small concrete strength increase (e.g. Figure 5.10(b)).

$$\sigma_c = E_c \varepsilon_c - \frac{E_c^2}{4f'_{co}} \varepsilon_c^2, \text{ when } 0 \leq \varepsilon_c \leq \frac{2f'_{co}}{E_c} \quad (6.1)$$

$$\sigma_c = f'_{co}, \text{ when } \varepsilon_c > \frac{2f'_{co}}{E_c} \quad (6.2)$$

in which  $\sigma_c$  and  $\varepsilon_c$  are the stress and strain of concrete respectively, whereas  $E_c$ ,  $f'_{co}$  and  $\varepsilon_{co}$  are the elastic modulus, the unconfined concrete cylinder strength and the corresponding strain respectively. It should be noted that the stress-strain curve represented by Eqns 6.1 and 6.2 can be regarded as a special case of the curves produced by the design-oriented stress-strain model presented in Chapter 5, with  $E_{2c} = 0$ . The results predicted by the section analysis using this modified stress-strain curve [denoted as “theoretical results (modified)”] are also compared with the test results in Figures 6.12(a)-(f). As expected, the modified theoretical results provide close predictions for specimens with two concentrically placed tubes, and safe and reasonable predictions for specimens with an eccentric steel tube.

It should be noted that the different confinement effects on the concrete in column and beam specimens have also been noted by previous researchers. Mirmiran et al. (1999) concluded from their beam and beam-column test results of concrete-filled FRP tubes that the confinement effect increases with the level of axial load. It is also suggested in Mirmiran et al. (1999) that the slope of the second linear part of the stress-strain curve, i.e.  $E_{2c}$ , of FRP-confined concrete should be a function of the axial load level. Rochette and Labossiere (1996) proposed a lower bound of 0

for  $E_{2c}$ . The proposed concrete stress-strain curve (Eqns 6.1 and 6.2) is similar to that proposed by Mirmiran et al. (1999) with the lower bound for  $E_{2c}$  proposed by Rochette and Labossiere (1996). A similar approach was suggested by Ziara et al. (1995) for conventional RC beams with considerable transverse reinforcement. Fam et al. (2003) also found that the confinement effect is less significant in beams than in columns, but suggested to use the unconfined stress-strain curve for concrete confined by an FRP tube when it is under pure flexure. The theoretical results obtained using the concrete stress-strain curve suggested in Fam et al. (2003) are also shown in Figures 6.12(a)-(b) for specimens B-C1 and B-C2. It is evident that the direct use of the unconfined concrete stress-strain curve led not only to an underestimation of the test results but also to a descending branch for the load-strain curves, which is not supported by the experimental observations.

#### 6.3.2.2 Specimens with FRP bars

Figure 6.12(g) shows a comparison of load-strain curves for one of the two specimens with FRP bars. Eqns 6.1 and 6.2 were used in the theoretical analysis. The comparison for the other specimen is similar. The theoretical load-strain curve follows the experimental curve closely but then exceeds it considerably with a significantly higher ultimate load. It was found that the rupture strain of FRP bar in the beam tests (0.011) was much lower (about 36%) than the rupture strain obtained from tensile tests (about 0.017), which was adopted in the analysis. The degradation of rupture strain of FRP bar in the beam tests may be due to the presence of bending deformation in the FRP bar. This reduction in the rupture strain explains the difference between the predicted and experimental load-strain curves. An alternative prediction, in which the reduced rupture strain observed in

the beam tests replaced that from the tensile tests, is also shown in Figure 6.12(g) [denoted as “theoretical results (modified)”]. This alternative prediction is in much closer agreement with the experimental curve.

### **6.3.3 Load-Deflection Curves**

The results from the section analysis can be integrated to predict the deflections of the beam. Figure 6.13 shows comparisons between the experimental and the predicted mid-span load-deflection curves for specimen B-E1-32, which had no FRP bars, and for specimen B-D1-F, which had FRP bars, respectively. The theoretical analysis again adopted Eqns 6.1 and 6.2 as the compressive stress-strain curve for concrete. For specimen B-E1-32, the theoretical results agree well with the test results up to a load level of about 1/3 of the ultimate load, after which the difference between the theoretical and test results becomes more significant. The differences are believed to be mainly due to the development of wide localized cracks in the beam and slips between the concrete and the tubes, both of which were not considered in the analysis. For specimen B-D1-F, the predicted curve ends at the rupture of the FRP bar at the bottom, as the accuracy of the section analysis further deteriorates due to the appearance of a wide crack at the location of FRP bar rupture immediately afterwards. It can be seen from Figure 6.13(b) that the prediction is more accurate than that for specimen B-E1-32. This is consistent with the test observation that no large cracks were found in specimen B-D1-F before the rupture of the bottom FRP bar. Some small differences between the test and predicted results still exist, which may be attributed to some slips between the concrete and the tubes (particularly the steel tube).

## 6.4 DESIGN RECOMMENDATIONS

It is shown in Section 6.3 that the proposed section analysis method with the compressive stress-strain curve of concrete defined by Eqns 6.1 and 6.2 provides reasonable and safe predictions of the behavior of DSTBs. This method is therefore recommended for design use.

The normalized hoop strain-axial strain curves of two DSTB specimens are compared with those of the corresponding DSTC specimens in Figure 6.14, where the hoop strain and axial strain are normalized by the strain corresponding to the peak stress of unconfined concrete. For DSTB specimens, the strain values were recorded by the strain gauge at the top of the specimen (i.e. the extreme compressive fiber). It can be found from Figure 6.14 that with the same concrete axial strain, the beam specimens (B-C1 and B-C2) are subjected to a smaller hoop strain than the corresponding column specimens (D40-B1-I and D40-B2-I respectively). This can be explained by the strain gradient developed over a beam section. Within the section, the concrete subjected to a larger axial strain (near the extreme compressive fiber) tends to expand more significantly, while the concrete subjected to a smaller axial strain expands less. Therefore, part of the expansion on the compression side is transferred to the rest of the section and the hoop strain experienced by the FRP outer tube is reduced.

Based on the above observation, it is safe to adopt the ultimate axial strain predicted by the design-oriented stress-strain model, which was proposed for

column specimens in section analysis of beam specimens. This ultimate axial strain is thus recommended for design use.

## **6.5 CONCLUSIONS**

This chapter has presented and interpreted the results of two series of 4-point bending tests on hybrid double-skin tubular beams (DSTBs). The main parameters examined in this study include the section configuration and the thicknesses of the steel tube and the FRP tube. A simple theoretical model based on the plane section assumption and the fiber element approach was also developed and employed to predict the responses of the test beams. Based on the test results and comparisons with the theoretical predictions, the following conclusions can be drawn.

- (1) Hybrid DSTBs possess a very ductile response. The FRP tube confines the concrete and provides additional shear resistance. The steel tube provides ductile longitudinal reinforcement.
- (2) A DSTB with an eccentric steel tube benefits more significantly from the outer FRP tube than a corresponding DSTB with a concentric steel tube, as in the former, a larger amount of concrete is in the compression zone.
- (3) Significant slips between the concrete and the two tubes, particularly the steel tube, and associated load fluctuations may occur. Improvements to the bond resistance at both interfaces are desirable.
- (4) The flexural response of a DSTB, including the flexural stiffness, ultimate load and cracking, can be substantially improved by shifting the inner steel

tube towards the tension region or by providing FRP bars as additional longitudinal reinforcement.

- (5) The effect of FRP confinement on concrete in beam specimens is less significant than that in column specimens of identical sections, because of the existence of a strain gradient and a relatively small concrete compression zone.
- (6) The predictions from the theoretical model are in reasonably close agreement with the test results. Differences arise from factors not considered in the theoretical model, including the concentrations of cracks and the slips between the concrete and the two tubes. The development of a more accurate model should take these factors into account.

Table 6.1 Details of specimens and measured load capacities

Specimen		FRP Tube	Steel tube eccentricity (mm)	FRP bars	Steel tube					Concrete cylinder strength $f'_{co}$ (MPa)	Ultimate Load P (kN)
					$D_s$ (mm)	$t_s$ (mm)	$E_s$ (MPa)	$f_y$ (MPa)	$f_u$ (MPa)		
Series I	B-A1	1 ply	No	No	76.1	2.7	201.5	381.5	421.5	38.2	27.26
	B-A2	2 plies									27.44
	B-B1	1 ply									25.09
	B-B2	2 plies								35.5	26.48
	B-C1	1 ply									39.36
	B-C2	2 plies									38.41
	B-D1-F	1 ply		Yes	76.1	3.5	198.7	406.2	475.5	27.8	46.28
	B-D2-F	2 plies		Yes							48.91
Series II	B-E0-18	No	18.2	No	76.1	3.5	208.6 <sup>#</sup>	340.3 <sup>*</sup>	444.5	33.4	28.90
	B-E1-18	1 ply									35.39
	B-E2-18	2 plies									38.11
	B-E0-32	No	32.2							26.1	27.11
	B-E1-32	1 ply									36.49
	B-E2-32	2 plies									42.01

<sup>#</sup> Initial elastic modulus

<sup>\*</sup> 0.2% proof stress

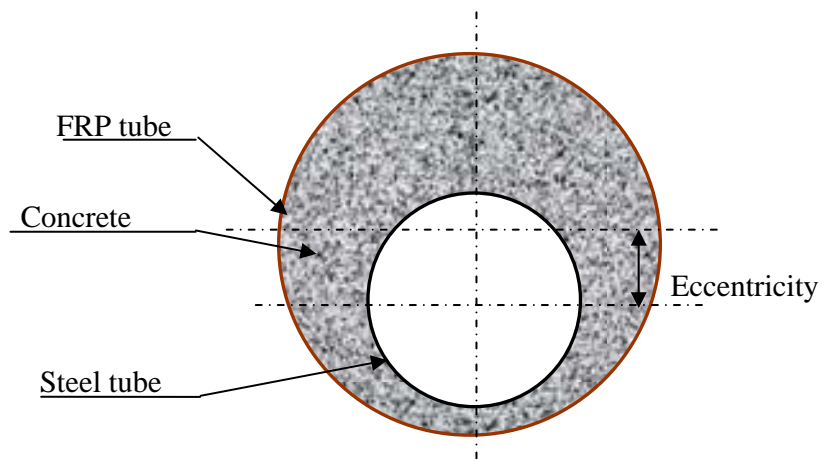
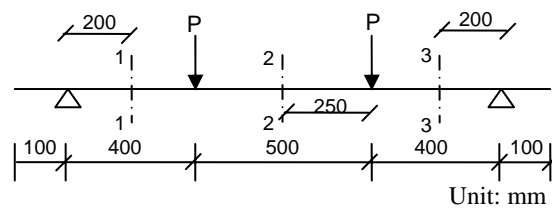


Figure 6.1 Double-skin tubular members with an eccentric steel tube



(a) Dimensions of test set-up



(b) Overview of test set-up



(c) End of specimen

Figure 6.2 Test set-up

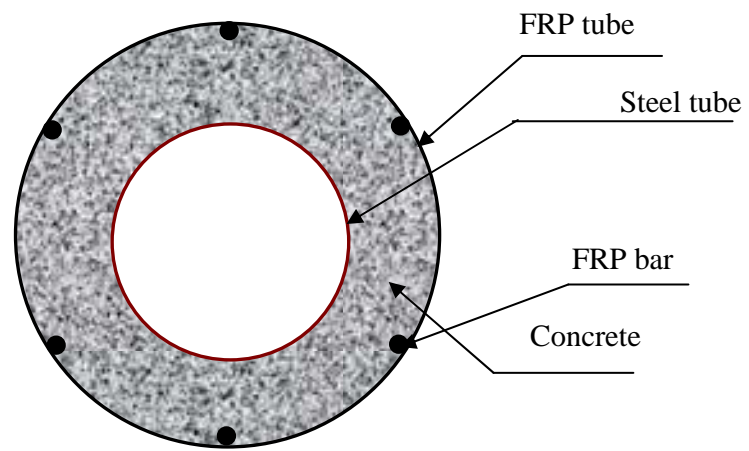


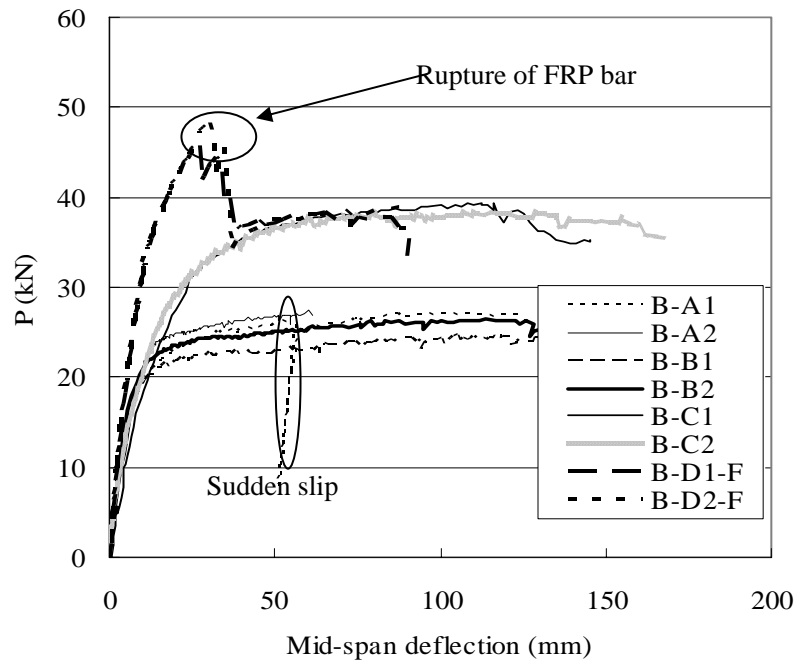
Figure 6.3 Cross-section of specimen with FRP bars



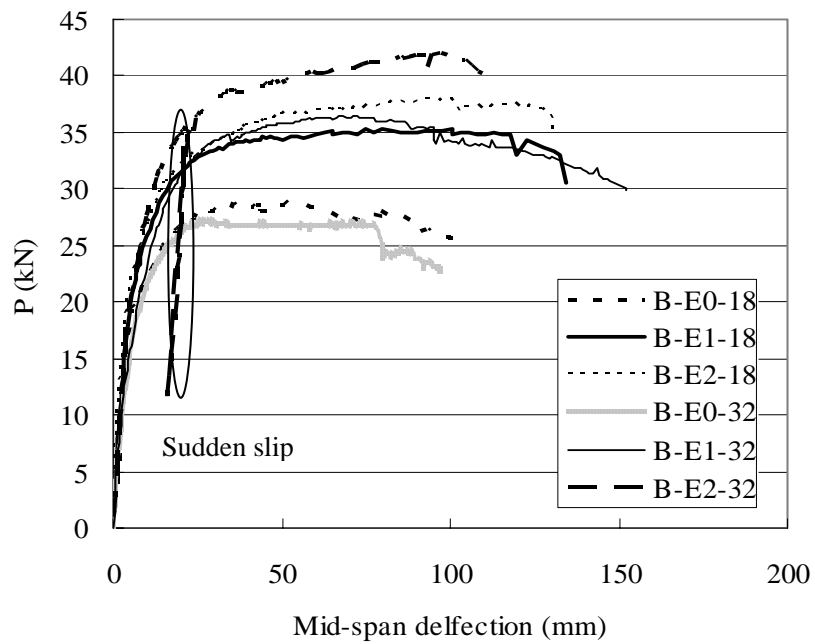
Figure 6.4 Formwork for casting concrete



Figure 6.5 Fabrication of FRP tube



(a) Series I



(a) Series II

Figure 6.6 Mid-span load-deflection curves



(a) Specimen B-B1

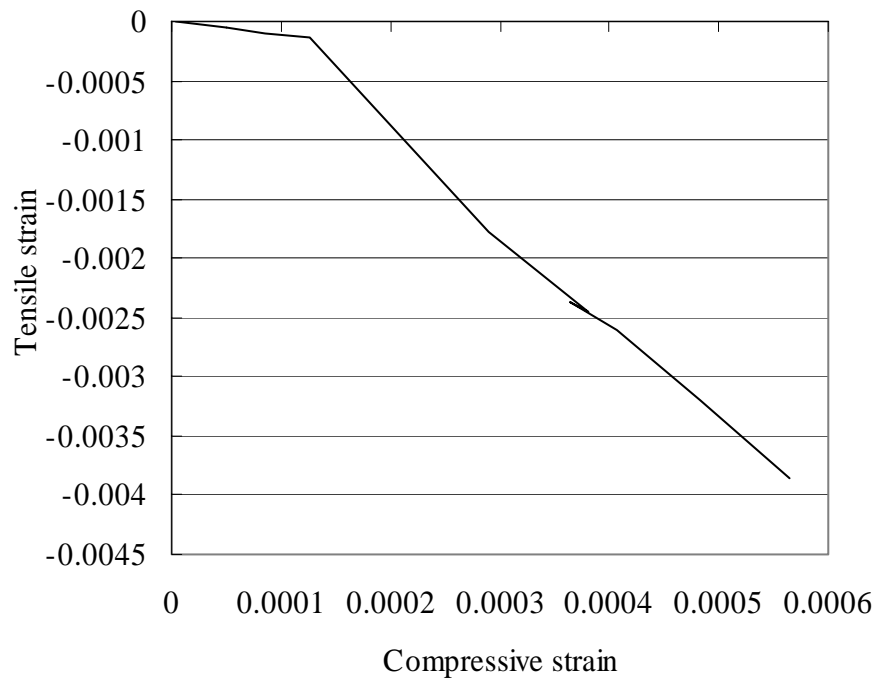


(b) Specimen B-D1-F

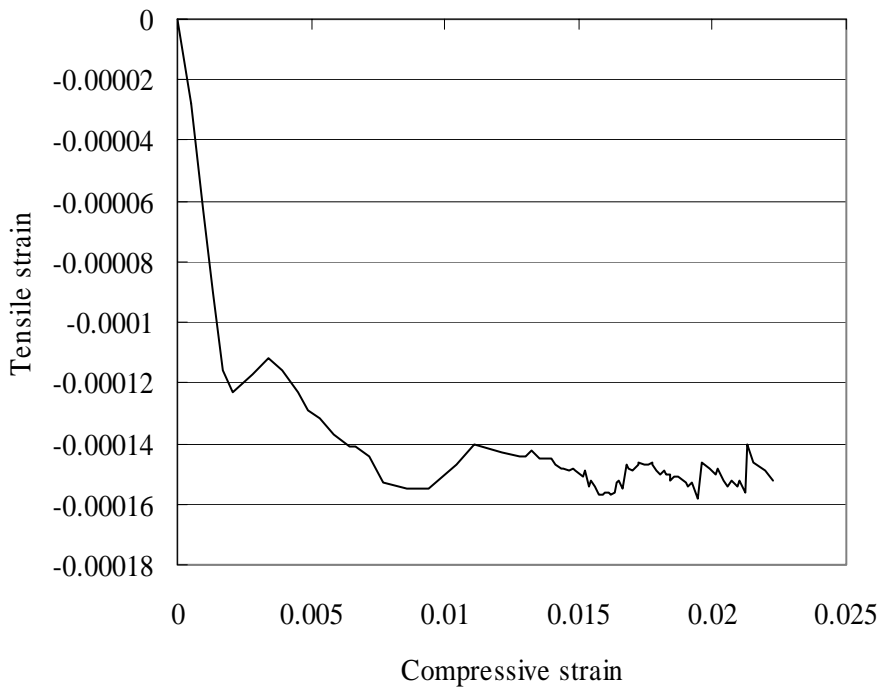


(c) Specimen B-E0-18

Figure 6.7 Specimens after testing



(a) Specimen B-C1



(b) Specimen B-B1

Figure 6.8 Compressive-tensile strain curves



Rupture of the FRP tube in the compression zone due mainly to hoop tension

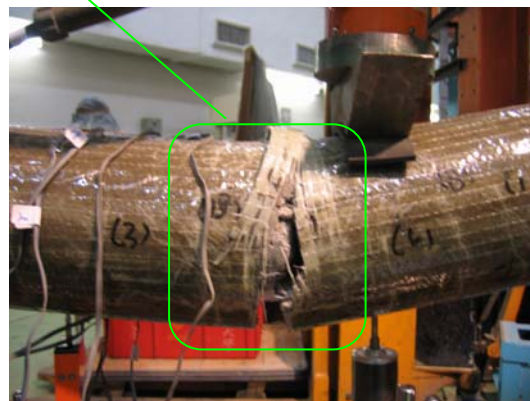


Figure 6.9 Specimen B-D1-F after testing

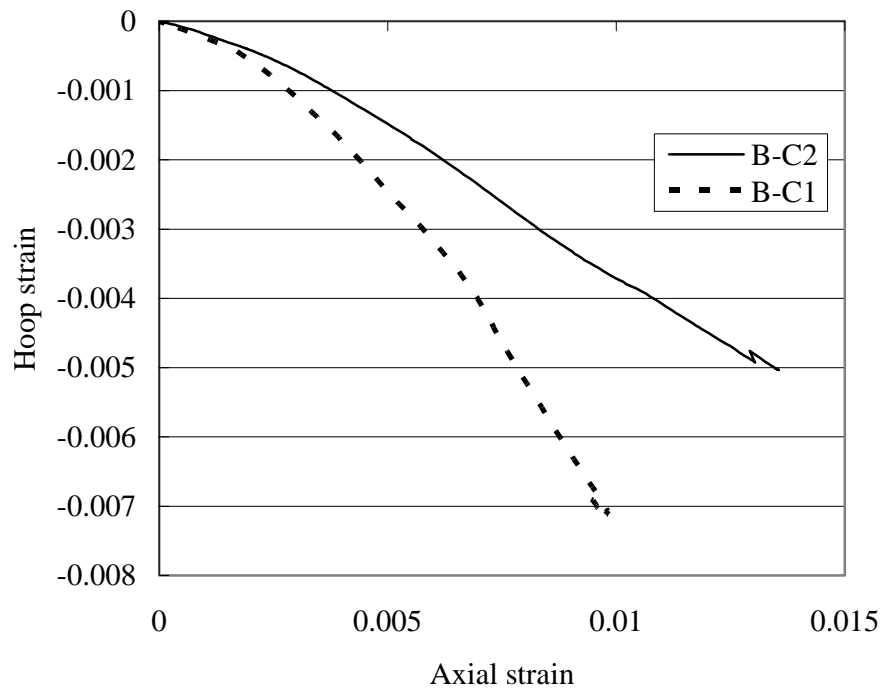


Figure 6.10 Axial-hoop strain behavior

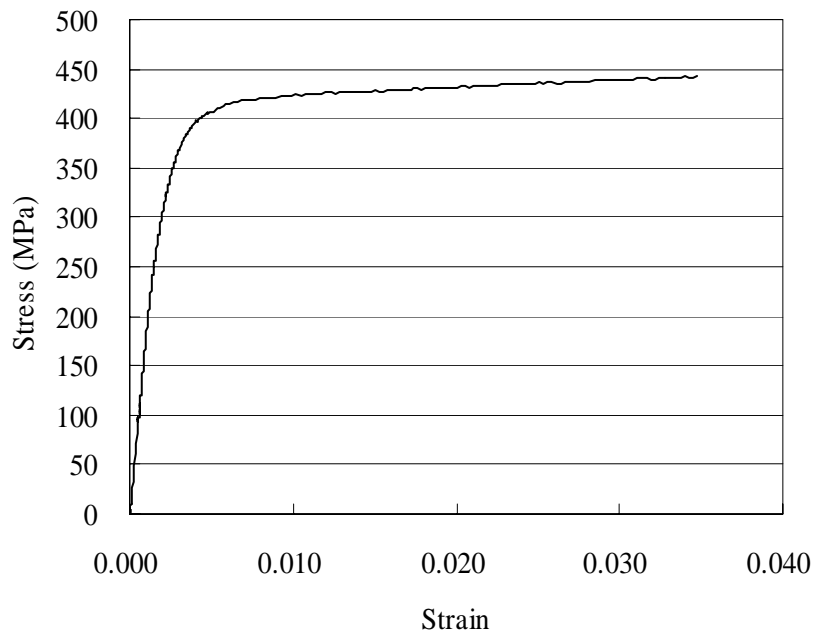
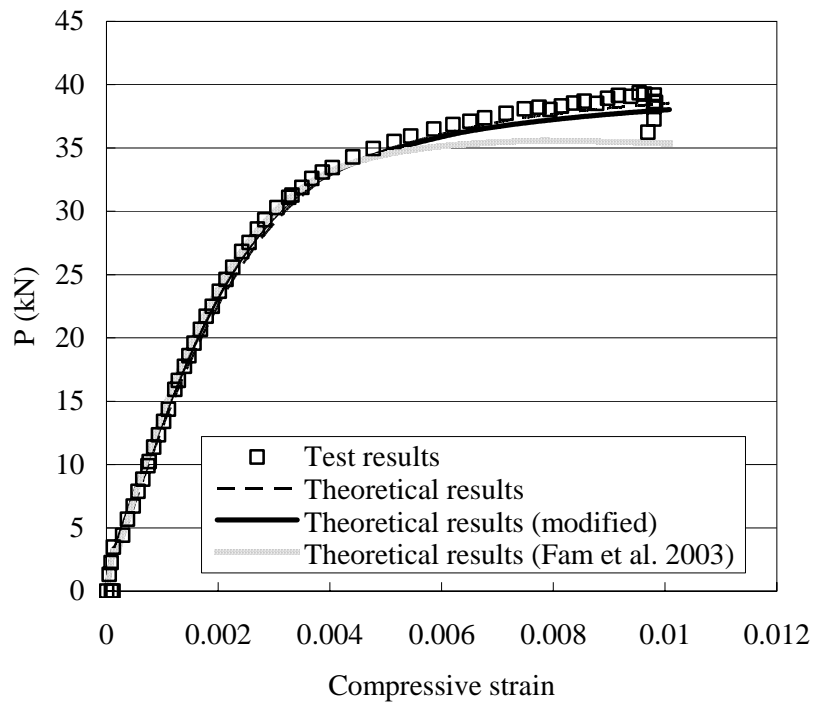
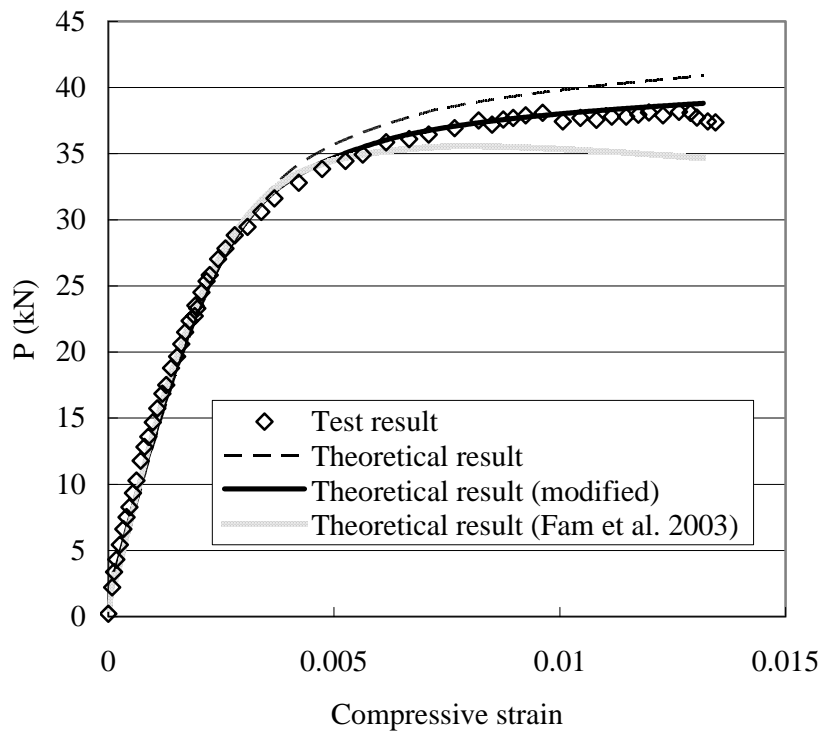


Figure 6.11 Typical stress-strain curve of steel tube in B-C1

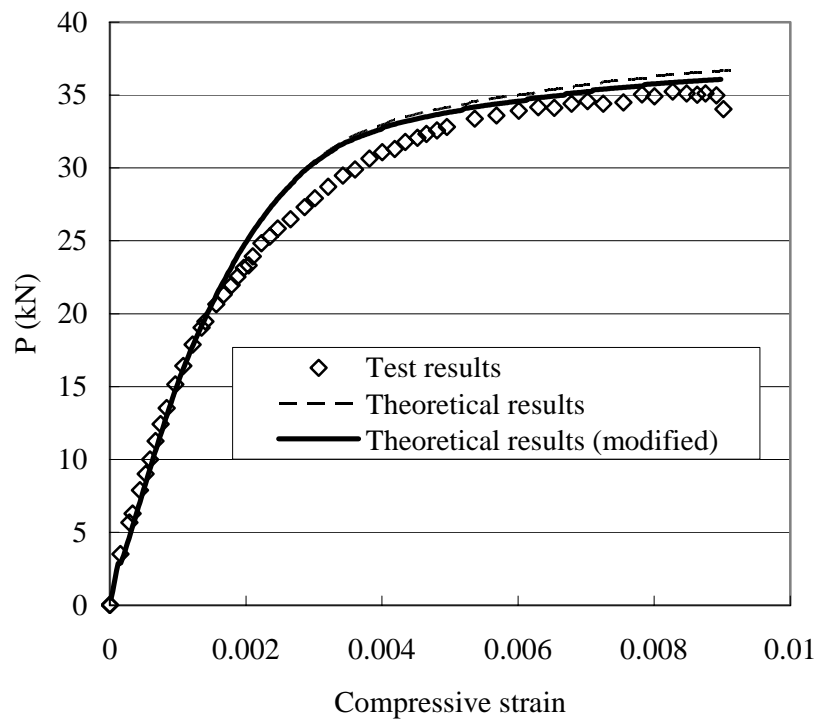


(a) Specimen B-C1

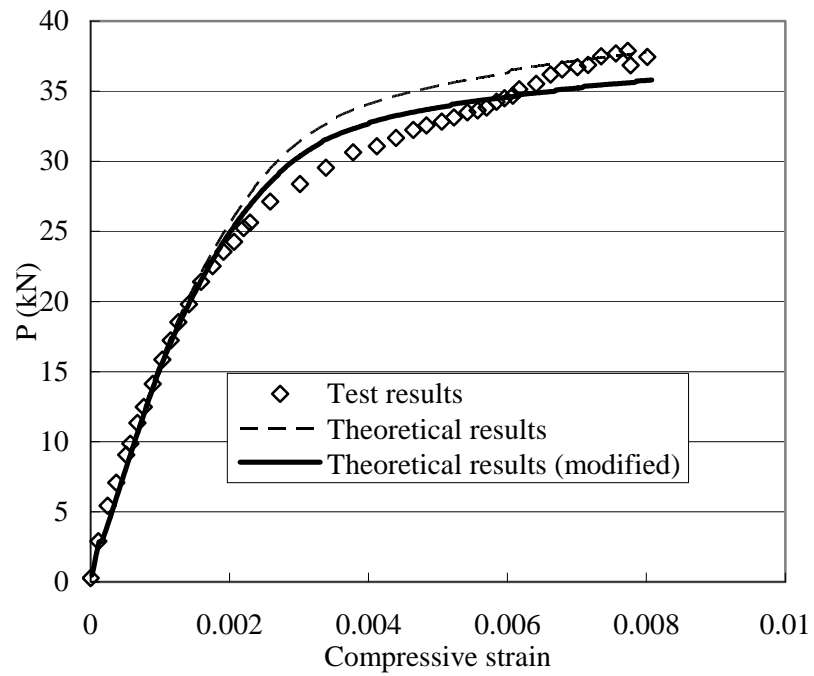


(b) Specimen B-C2

Figure 6.12 Comparison of load-compressive strain curves

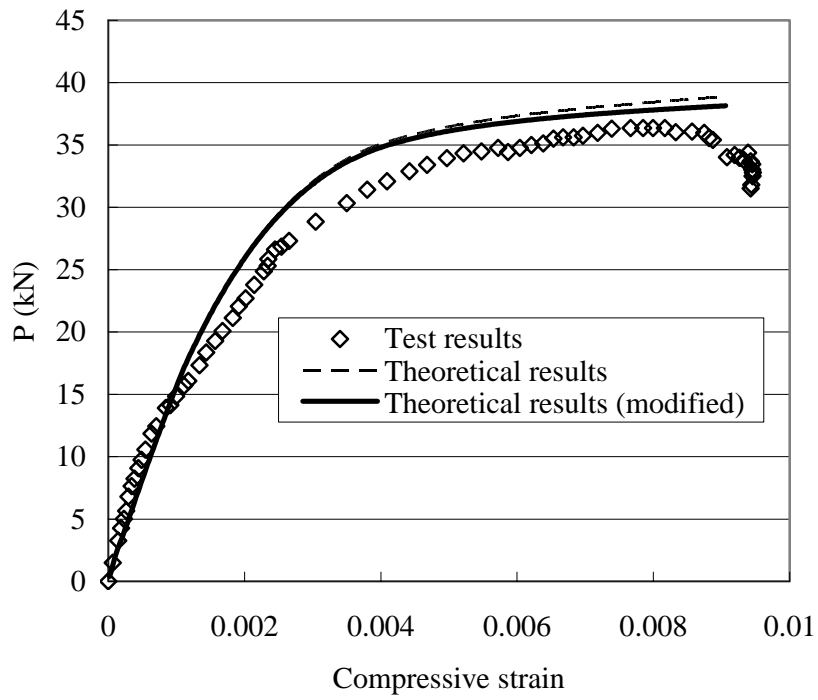


(c) Specimen B-E1-18

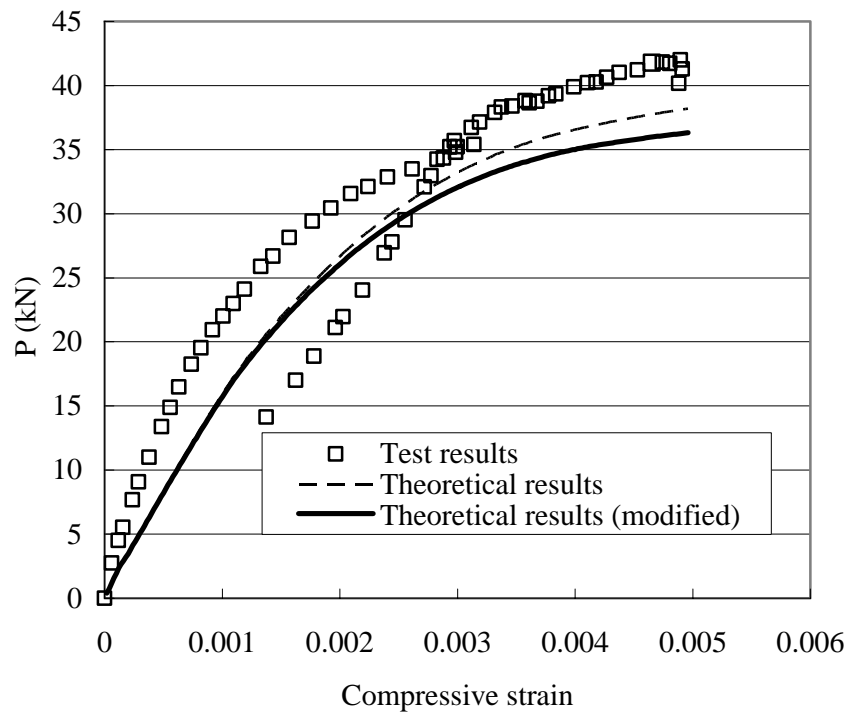


(d) Specimen B-E2-18

Figure 6.12 Comparison of load-compressive strain curves (Cont'd)

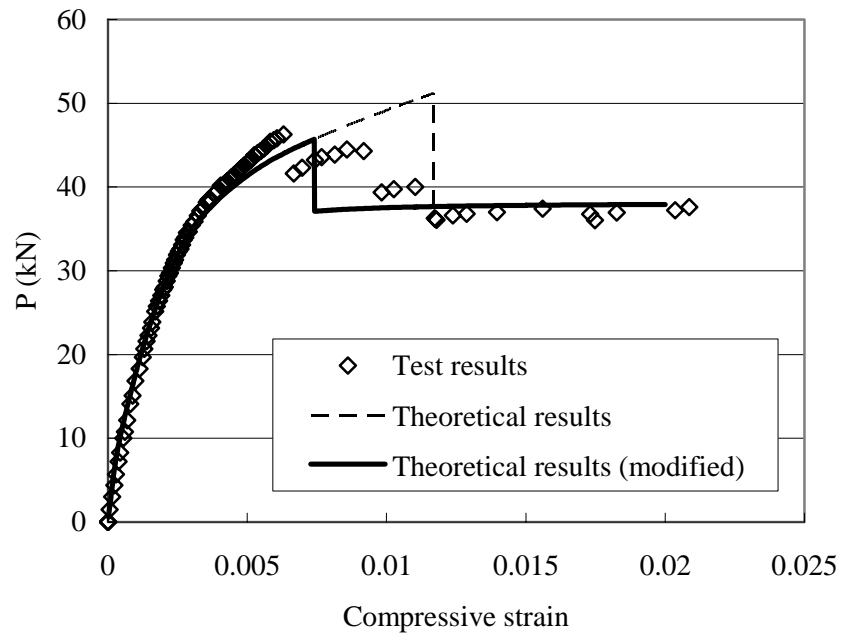


(e) Specimen B-E1-32



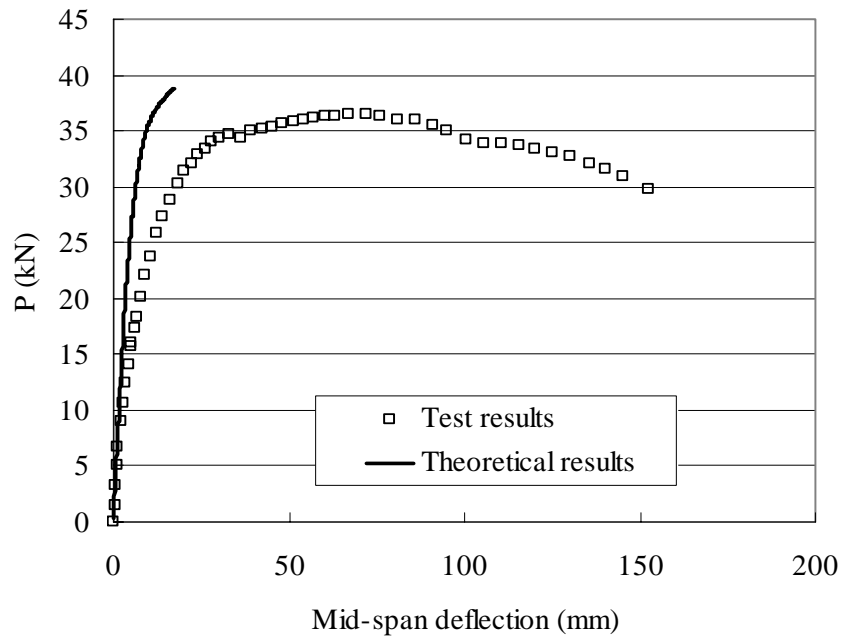
(f) Specimen B-E2-32

Figure 6.12 Comparison of load-compressive strain curves (Cont'd)



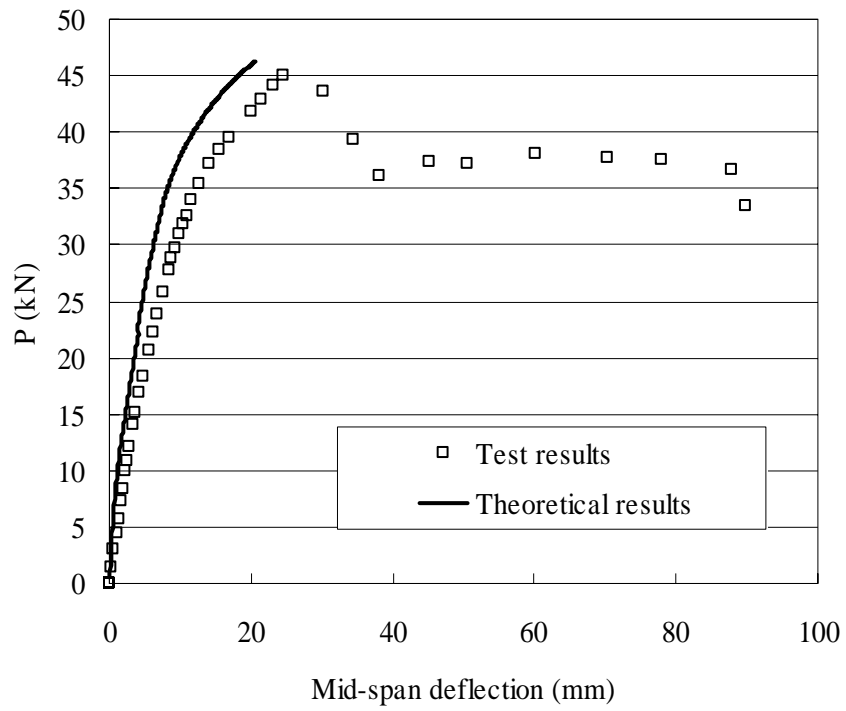
(g) Specimen B-D1-F

Figure 6.12 Comparison of load-compressive strain curves (Cont'd)



(a) Specimen B-E1-32

Figure 6.13 Comparison of mid-span load-deflection curves



(b) Specimen B-D1-F

Figure 6.13 Comparison of mid-span load-deflection curves (Cont'd)

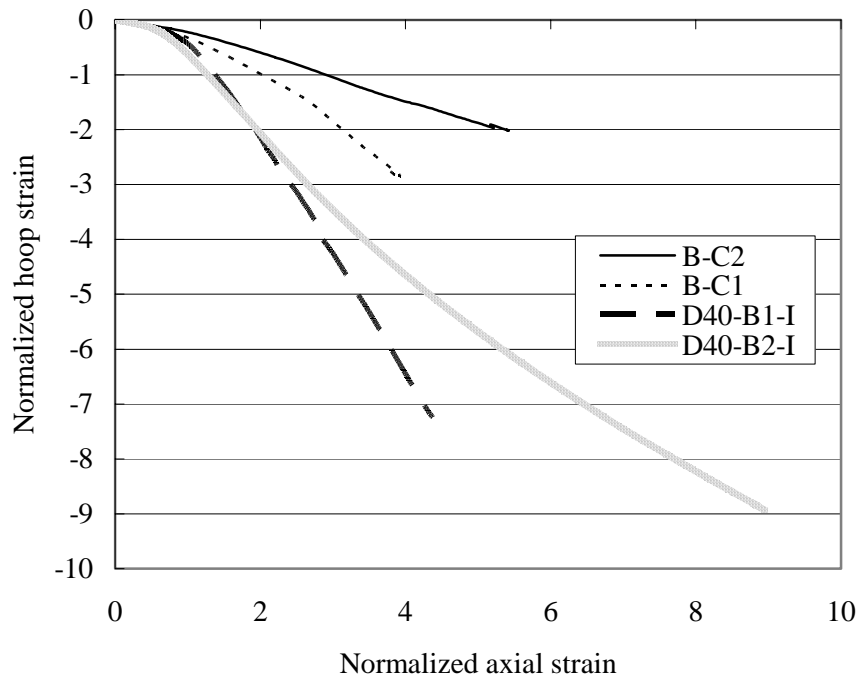


Figure 6.14 Comparison between hoop strain-axial strain curves of DSTBs and DSTCs

## **CHAPTER 7**

### **BEAM-COLUMN BEHAVIOR OF HYBIRD DSTCS**

#### **7.1 INTRODUCTION**

This chapter first presents an experimental study on the beam-column behavior of the new hybrid FRP-concrete-steel double-skin tubular columns (DSTCs). The beam-column behavior is important for design as columns are normally subjected to combined axial and lateral loads, such as wind and seismic loads.

The beam-column behavior of a composite column can be predicted by a traditional section analysis when the stress-strain relationship of each constituent material is known. In this chapter, results from such a section analysis method based on the design-oriented stress-strain model presented in Chapter 5 for the concrete in hybrid DSTCs are presented. The theoretical results are shown to be in close agreement with the experimental results reported earlier in this chapter.

## 7.2 EXPERIMENTAL STUDY

### 7.2.1 Specimen Details

In total, six identical DTSC specimens were prepared and tested under eccentric compression with three different eccentricities (0 mm, 9 mm and 18 mm); for each eccentricity value, two identical specimens were tested. All specimens had an outer diameter of 155 mm and a height of 465 mm, a steel inner tube with a  $D_s/t_s$  ratio of 76/3.7, and a one-ply FRP outer tube. It should be noted that the outer diameter of 155 mm refers to the concrete core and does not include the thickness of the FRP outer tube. The details of all these specimens are summarized in Table 7.1. Each specimen is identified by a naming system, which starts with a letter “E” indicating that this is a specimen belonging to the eccentric compression test series, followed by a number which defines the number of plies of the FRP tube and then followed by a two-digit number which defines the eccentricity of the compressive load. The last Roman digit “I” or “II” in the naming system is to differentiate the two specimens of a pair loaded at the same eccentricity.

The preparation procedure for these DSTC specimens is similar to that reported in Chapter 3 and included the following steps: (1) fabrication of the form, which consisted of a PVC tube outside and a steel tube inside; strain gauges on the steel tube were installed before the casting of concrete (Figure 7.1); (2) casting the

concrete; (3) wet-layup formation of the FRP tube after the concrete had hardened and the PVC form had been removed.

### **7.2.2 Material Properties**

The FRP used in the eccentric compression tests was the same as that used in the concentric compression tests presented in Chapter 3. Tensile coupon test results showed that the FRP had an average tensile strength of 1825.5 MPa and an average elastic modulus of 80.1 GPa, based on a nominal thickness of 0.17 mm per ply.

All steel tubes in these DSTCs came from the same long steel tube. Tensile tests on steel coupons cut from the same original steel tube were conducted to determine the material properties of the steel. These tests showed that the steel had a yield stress of 398.2 MPa, a tensile strength of 457.5 MPa, a Young's modulus of 199.7 GPa and a long plastic plateau after yielding. In addition, three hollow steel tubes nominally identical to those used in the DSTCs and also cut from the same long tube were tested under compression. The steel tubes showed large plastic deformation before failure occurred by a combination of overall buckling and local buckling, as shown in Figure 7.2. The average ultimate load of these tubes was 356.9 kN.

The elastic modulus, compressive strength and compressive strain at peak stress of the concrete averaged from three concrete cylinder tests (152.5 mm x 305 mm) were 31.8 GPa, 49.7 MPa and 0.00245 respectively.

### **7.2.3 Experimental Set-up and Instrumentation**

Eight strain rosettes with a gauge length of 20 mm were evenly distributed around the circumference at the mid-height of the FRP outer tube to measure the axial and hoop strains at different locations. Two strain rosettes were attached to the outer surface of steel inner tube at 180° apart. The locations of the strain rosettes are shown in Figure 7.3. The overlapping zone was placed farthest from the applied load.

All specimens were tested on an MTS machine with a ball joint at the top (Figure 7.4). The loading rate was 0.003 mm per second for all specimens. For the four specimens under eccentric compression, two steel plates were employed at the bottom. One of the steel plates had a V-block while the other had two V-shape grooves so that the desirable eccentricity (9 mm and 18 mm) could be accurately achieved. The eccentric compression test set-up is shown in Figure 7.4.

For the two specimens of this series tested under concentric compression (eccentricity = 0 mm), two linear variable displacement transducers (LVDTs)

were used to measure the axial deformation of the middle region of 120 mm for each specimen, as explained in Chapter 3. For the four specimens tested under eccentric compression, seven LVDTs were adopted to measure displacements at different locations and in different directions. Three LVDTs (LVDTs 1-3) were respectively installed at the mid-height, near the bottom and near the top of each specimen to measure the lateral deflections at different heights (Figure 7.4). Four LVDTs (LVDTs 4-7) were installed to measure the axial shortening of the specimen at different points (Figure 7.4).

#### **7.2.4 Experimental Observations and Interpretations**

The specimens were subjected to combined axial compression and flexure during eccentric compression tests. As expected, the deformations of the specimens included axial shortening and bending (Figure 7.5). Consequently, the LVDTs located at different distances from the applied load recorded different axial shortenings and the LVDTs located at different heights recorded different lateral deflections. As the curvature and the lateral deflection increased, the actual load eccentricity/bending moment varied along the height and deviated from the initial value. The bending moment was the largest where the largest lateral deflection occurred. Tensile cracks occurred on the side farthest from the load, although the eccentricities were designed to be small enough so that no tension would occur during the initial loading stage. These tensile cracks were initially revealed by

white patches on the FRP tube which appeared as a result of resin damage due to cracks in the concrete behind the tube. With the development of tensile cracks, the lateral deflection of the specimen increased more rapidly, which in turn increased the value of the actual loading eccentricity for sections away from the ends. The specimens reached their ultimate state by the rupture of the FRP outer tube (Figure 7.5(b)) on the side nearest to the applied load, due to the expansion of concrete in compression. The locations of the major tensile cracks and the rupture of the FRP tube were recorded in terms of the distances from the top of the specimen, as shown in Table 7.2, in which  $x_1$  and  $x_2$  are the respective distances of the tensile cracks and the FRP rupture from the top end. It can be seen from Table 7.2 that FRP rupture occurred at approximately the same height as the location of a major tensile crack on the opposite side. The major tensile cracks normally occurred at or near the mid-height except specimen E-1-18-I.

Figure 7.5 shows the specimens after test. It is not strange to find that the specimen tested under a larger eccentricity experienced a more significant rotation (Figure 7.5(a)). The FRP outer tubes of some of the specimens were removed after test to further examine the appearance of the concrete. It was found that there were many vertical cracks and a few inclined cracks in addition to the horizontal cracks described earlier (the cracks are marked in Figure 7.5(c)). These cracks were probably due to the expansion and bending of the inner steel tube. Concrete crushing was also found on the extreme compression side.

## 7.2.5 Experimental Results and Discussions

### 7.2.5.1 Axial strain distribution over the section

Eight strain rosettes were attached to the FRP outer tube and two strain rosettes were attached to the steel inner tube, to measure strains at different circumferential locations (Figure 7.3). The distribution of axial strain over the section is illustrated in Figure 7.6, in which the horizontal axis represents the distance to the center of the specimen and the vertical axis represents the axial strain value. For each specimen, several curves representing the strain distributions under different load or axial-shortening levels are shown. For instance, the curves denoted as “300 kN” and “1.5 mm” in Figure 7.6 represent the strain distributions under a load level of 300 kN and an axial-shortening level of 1.5 mm, respectively. The load and axial-shortening values were recorded by the MTS machine. Unless otherwise specified, a tensile strain is negative and a compressive strain is positive in this chapter. The following observations can be made from these figures.

- (1) Generally, the distribution of strains on the FRP outer tube remains approximately linear with the distance from the center of the section, especially in the initial stage of loading.
- (2) When the maximum compressive strain of the section exceeds 0.0025, which

is approximately equal to the axial strain at the peak stress of unconfined concrete, the strain distribution starts to become non-linear, as can be seen in Figures 7.6(b) and (d). This deviation may be a result of significant local damage of concrete after the strain exceeded 0.0025.

- (3) As the load increases, the neutral axis keeps moving toward the center of the section, resulting in the occurrence of tensile strains. Consequently, tensile cracks occurred on the side farthest from the loading point. Some strain gauges spanning over the cracks recorded large tensile strains, which deviate from the linear curve (Figures 7.6(a), (b) and (d)). It is also noted that the tensile strains of specimen E-1-18-I are relatively low (Figure 7.6(c)). It was found that in this specimen, no tensile crack crossed the strain gauges.
- (4) When the readings of the strain gauges on the steel tubes exceed a value of about 0.002, some of them deviate significantly from a linear strain distribution, as shown by the solid dots in Figures 7.6(b) and (d). These may be due to non-uniform plastic local deformation in the steel tube.

The axial strains at the two extreme locations are compared in Figure 7.7, where the horizontal axis represents the axial strain at the location farthest from the loading point (extreme tensile fiber) while the vertical axis represents that at the location nearest to the loading point (extreme compressive fiber). These comparisons are for specimens E-1-09-I and E-1-18-II. It can be seen that both strains increase and are linearly related in the initial stage, indicating that the

specimen was elastically deformed and the location of the neutral axis did not change. When the strain at the extreme compressive fiber reaches about 0.002, the curve begins to reverse. The compressive strain at the extreme tensile fiber becomes increasingly smaller and finally reverses to a tensile strain, indicating the movement of the neutral axis towards the center of the section with an increasing axial load. Beside the effect of a varying neutral axis, the occurrence of tensile cracks and the resulting deformation localization is another factor affecting the curves in Figure 7.7.

#### *7.2.5.2 Axial stress-strain curves of concrete in hybrid DSTCs under concentric compression*

The axial stress-strain curves of concrete in hybrid DSTC specimens under concentric compression (i.e. specimens E-1-00-I, II) are shown in Figure 7.8. The average axial stress in the concrete in the DSTCs was found by dividing the load acting on the concrete area by the cross-sectional area of the concrete section. The load carried by the concrete is assumed to be equal to the difference between the load carried by the DSTC specimen and the load carried by the steel tube at the same axial strain as found from the compression tests on hollow steel tubes. It is clear from Figure 7.8 that both experimental curves have an approximately elastic-perfectly plastic shape. The peak concrete stresses of these two specimens, however, are a little smaller (about 8%) than that of unconfined concrete. Despite this small strength difference, concrete in such DSTCs has a very good ductility

(the axial strain reaches about 1.5%) with very small stress decreases. The small strength difference may be due to the different slenderness ratio of the DSTC specimens compared to that of standard cylinders. Standard concrete cylinder specimens with a diameter of 152.5 mm and a height of 305 mm were tested to find the unconfined concrete strength. However, the concrete component in these hybrid DSTC specimens had an annular shape with a thickness of about 40 mm and a height of 465 mm. As discussed in Chapter 3, hollow concrete cylinders may have a smaller unconfined strength than solid concrete cylinders, especially when the unconfined concrete strength is high (e.g. Batch 4 in Table 3.2).

The results predicted by the design-oriented stress-strain model proposed in Chapter 5 are shown in Figure 7.8 for comparison, using the concrete cylinder strength from standard cylinder tests. It is evident that the design-oriented model overestimates the concrete strength. This overestimation comes from the concrete cylinder strength used which is greater than the unconfined concrete strength of hollow cylinders, as discussed earlier. To achieve a better prediction, a lower unconfined concrete strength (45.8 MPa) is input, which is equal to the average peak stress of specimens E-1-00-I and E-1-00-II. By doing so, the stress-strain curves of DSTCs can be closely predicted, as shown in Figure 7.8 by the curve denoted as “Design model (modified)”.

### *7.2.5.3 Axial load-shortening behavior*

The peak axial loads of all six specimens are summarized in Table 7.1. It is not surprising to find that the specimens loaded at a larger eccentricity have a smaller axial load capacity, due to the existence of a larger bending moment. For the two pairs of specimens with eccentricities of 0 mm and 9 mm respectively, there is only a very small difference between the two specimens of each pair. On the contrary, the two specimens with an eccentricity of 18 mm show a relatively large difference. The reason for this difference is explained later in this section.

There were two ways to obtain the axial-shortenings of the specimens. One was to take the average of readings from the four LVDTs measuring platen-to-platen deformations at two opposite sides of the specimen, while the other was to use the machine output values. The former represents the deformation of the center line of the specimen while the latter represents the relative movement between the two loading points. It is not difficult to find that the latter is in general larger than the former because of the rotation of the specimen. The problem is that the shortenings measured by the four LVDTs are not accurate enough to give a reliable measurement of the center-line shortening. For instance, in specimen E-1-18-II, the shortenings on the two sides were found to be approximately -13 and 10 mm using the LVDTs and the average shortening could be calculated to be about 3 mm. However, the difference between the readings of the two LVDTs at the same side (i.e. LVDTs 4, 5 in Figure 7.4) was about 1.5 mm, about 50% of the

obtained average shortening. Therefore, it is believed that the average shortening deduced from the LVDTs cannot accurately reflect the shortening of the center line of the specimen. The shortenings recorded by the MTS machine, however, are more reliable, although they include the deformation of the steel plates and as a result are expected to be slightly larger than the actual values. In addition, the initial part of the load-shortening curve is not linear when the machine readings are used, due to the contact problem, so the initial values need to be corrected. The corrected load-shortening curves, from which the deformation of the steel plates has been excluded, are shown in Figure 7.9.

It can be found from Figure 7.9 that those specimens tested at a larger eccentricity had a lower initial stiffness, although all of them had the same cross section. The reason is that the shortenings recorded by the machine include all deformation between the two loading points, so both the axial shortening and the flexural deformation of the specimen are included. The flexural component of deformation is larger for a specimen tested at a larger eccentricity. It can also be found from Figure 7.9 that all these specimens showed good ductility (the axial shortening reached about 1% of the height).

The two specimens (E-1-18-I, II) tested at the same designed eccentricity of 18 mm failed at quite different loads (709.31 kN and 588.79 kN). For clarification, the two specimens after test were carefully examined (Figure 7.10). It was noted

that the failure, involving the rupture of FRP on the compression side and tensile cracking of concrete on the tension side, took place near the mid-height of specimen E-1-18-II but near the upper quarter of specimen E-1-18-I (see also Table 7.2). It was also noted that there was large local deformation near the failure region due to the development of wide tensile cracks and the crushing of concrete under compression. It is explained in Subsection 7.2.4 that the actual eccentricity varied along the height of the specimen and deviated from the initial value as the load increased. The local deformation occurring near the failure region exacerbated the amplification of eccentricity. Consequently, the actual bending moment at the same load level varied along the height of the specimen and this variation may be different even for two identical specimens under compression at the same initial eccentricity. A section loaded at a larger actual eccentricity experiences a larger bending moment at the same axial load. It was found after tests that the lateral deflections recorded by LVDT 3 (Figure 7.4) was considerably larger for specimen E-1-18-I than for specimen E-1-18-II, indicating a larger actual eccentricity at the mid-height section of specimen E-1-18-I. As a result, the actual bending moment at the mid-height section corresponding to the peak load, which was calculated using the actual eccentricity, was found to be similar for the two specimens (13.9 kNm for specimen E-1-18-II and 13.2 kNm for specimen E-1-18-I), although their peak loads were quite different. In addition, it should be noted that the maximum bending moment along the height of specimen E-1-18-I took place near the upper quarter (the failure region) and was

higher than the value given above for the mid-height section. The exact value of this maximum bending moment is not available as the actual eccentricity for the upper quarter region was not measured. The discussions above explain why specimen E-1-18-I had a lower ultimate axial load.

#### *7.2.5.4 Hoop strain-axial strain behavior*

As mentioned earlier (Subsection 7.2.4), all the DSTC specimens tested under eccentric compression failed by the hoop rupture of FRP on the compression side. The relationship between hoop strain and axial strain is thus important to determine the ultimate axial strain and ductility of such specimens. Figure 7.11 shows the hoop strain-axial strain curves of selected specimens loaded at different eccentricities, in which the strain values were recorded by strain rosette SG5 (Figure 7.3) at the extreme compressive fiber for the two eccentric compression specimens. For specimen E-1-00-I which was loaded under concentric compression, the axial strain values were averaged from the readings of eight strain rosettes (SGs 1-8 in Figure 7.3) and the hoop strain values were averaged from the readings of the five strain rosettes (SGs 3-7) outside the overlapping zone. It can be seen from Figure 7.11 that in the initial stage, the curves of the eccentric compression specimens (i.e. specimens E-1-09-I and E-1-18-II) basically follow that of the concentric compression specimen (i.e. specimen E-1-00-I). With further increases in the axial strain, however, the hoop strains of specimens E-1-09-I and E-1-18-II become smaller than those of specimen

E-1-00-I. This could be explained by the following: (1) the strains of specimens under eccentric compression may include the effect of local damage which enlarged the strain values, while those of specimen E-1-00-I were average values over the section and basically without the influence of significant local damage; (2) the strain states in eccentric compression specimens were much more non-uniform (Figure 7.6). It can be expected that within an eccentric compression section, the concrete subjected to a larger axial strain tends to expand more significantly, while the remaining concrete subjected to smaller axial deformation does not have the same expansion. Therefore, part of the expansion on the extreme compression side is re-distributed to the rest of the section and the hoop strain recorded on the FRP outer tube is less. The higher hoop strain-axial strain curves of specimens under eccentric compression (Figure 7.11) consequently lead to a larger axial strain at the ultimate state for these specimens.

## **7.3 THEORETICAL ANALYSIS**

### **7.3.1 Analysis Model**

A traditional section analysis of the so-called fiber element approach was developed for the specimens under eccentric compression based on the plane section assumption. As explained in Subsection 7.2.5.1, the experimental axial strain distribution follows approximately the plane section assumption, except for some of the strains measured on the steel tubes (e.g. Figure 7.6(d)). Deviations of

strain values from the plane section assumption were found to be due to the localization of plastic deformation and occurred after the yielding of the steel tube when the stress level did not change significantly with the strain. Therefore, it can be expected that the plane section assumption can still be used for the prediction of the beam-column behavior and any errors are expected to be small. The analytical procedure is similar to that presented in Chapter 6 for flexural analysis. It involves the determination of the position of the neutral axis for a given strain of the extreme compression fiber by force equilibrium and the evaluation of the axial load and the bending moment by integrating the contributions of stresses over the section.

The stress-strain behavior of the steel tubes was modeled based on their tensile test results. An elastic-perfectly plastic stress-strain curve was adopted with the elastic modulus and the yield stress given in Subsection 7.2.2, as strain hardening took place at a relatively large axial strain exceeding those recorded on the steel tubes in the eccentric compression tests.

The concrete was assumed to possess the same initial elastic modulus in both tension and compression. Tensile cracking was assumed to occur at a tensile strain of  $130 \mu\epsilon$  based on the beam tests presented in Chapter 6 (e.g. Figure 6.8(b)), and the concrete was assumed to resist no tensile stresses after cracking.

It has been concluded in Chapter 6 that the effectiveness of FRP confinement of concrete is reduced in beam specimens compared to column specimens due to the existence of a strain gradient over the beam section. It can thus be expected that the confining effect in a beam-column specimen lies between those in a beam specimen and in a column specimen. Mirmiran et al. (1999) suggested that the slope of the second linear part of the stress-strain curve, i.e.  $E_{2c}$ , of FRP-confined concrete should be a function of the axial load level for beam-column specimens. Fam et al. (2003) believed that the stress-strain curve of FRP-confined concrete in beam-column specimens is dependent on the eccentricity of the applied load, and lies between that for column specimens and the unconfined concrete stress-strain curve. Fam et al. (2003) proposed concrete stress-strain curves which take into account the effect of strain gradient on the effectiveness of confinement. However, it has been shown in Chapter 6 that the direct use of the unconfined concrete stress-strain curve leads to unreasonable predictions of the test results of hybrid double-skin beams (Figures 6.12(a) and (b)). In Chapter 6, an approximately elastic-perfectly plastic compressive stress-strain curve was proposed for concrete in beam specimens regardless of the thickness of the FRP outer tube. The analysis model with such a concrete stress-strain curve has also been shown to provide reasonably accurate predictions of the test results of hybrid double-skin beams. As mentioned in Chapter 6, the only difference between the stress-strain curve for concrete in beam specimens and that produced from the design equations given in Chapter 5 for column specimens lies in the  $E_{2c}$  value. The  $E_{2c}$  value for

concrete in column specimens is dependent on the FRP jacket stiffness, while that for concrete in beam specimens is always equal to zero. Therefore, the following equations are proposed for the compressive stress-strain relationship of concrete in beam-column specimens, with a slope of the linear second portion which lies between that for column specimens and that for beam specimens and is denoted by  $E_{2ec}$ . In these equations, the effect of confinement on the concrete is related to the eccentricity of the applied load in a manner similar to that proposed by Fam et al. (2003).

$$\sigma_c = E_c \varepsilon_c - \frac{(E_c - E_{2ec})^2}{4f'_{co}} \varepsilon_c^2, \text{ when } 0 \leq \varepsilon_c \leq \varepsilon_t \quad (7.1)$$

$$\sigma_c = f'_{co} + E_{2ec} \varepsilon_c, \text{ when } \varepsilon_t \leq \varepsilon_c \quad (7.2)$$

$$\varepsilon_t = \frac{2f'_{co}}{(E_c - E_{2ec})} \quad (7.3)$$

where  $E_{2ec}$  is the slope of the linear second portion of the stress-strain curve and is determined by

$$E_{2ec} = E_{2c} \frac{D_o}{D_o + e} \quad (7.4)$$

where  $E_{2c}$  is from the design-oriented stress-strain model presented in Chapter 5 (Eqns 2.12-2.15, 2.20, 5.22);  $D_o$  is the outer diameter of the specimens and  $e$  is the eccentricity of loading. For the case of concentric compression,  $e = 0$  and  $E_{2ec} = E_{2c}$ ; for the case of pure bending,  $e = \infty$  and  $E_{2ec} = 0$ .

As discussed in Subsection 7.2.5.2, the concrete cylinder strength from standard solid cylinder specimens tends to overestimate the strength of concrete in hybrid DSTCs. On the contrary, the design-oriented stress-strain model with a lower (by about 8%) concrete strength (45.8 MPa) can provide good predictions of the behavior of specimens under concentric compression. Consequently, this unconfined concrete strength value (45.8 MPa) was adopted in the present section analysis. For each specimen, the longitudinal strain of the extreme compression fiber at the mid-height of the FRP tube at the end of the test was taken as the ultimate point of the stress-strain curve of its confined concrete. This experimental value of ultimate axial strain was higher than that of the corresponding column specimen, as explained in Subsection 7.2.5.4. Due to this reason, the ultimate axial strain from the design-oriented stress-strain model presented in Chapter 5 was not directly used herein.

### **7.3.2 Comparison with Test Results**

Figure 7.12 shows the comparisons of the predicted and experimental load-strain curves for all four specimens under eccentric compression. The strain values shown are those of the extreme compressive fiber at the mid-height (i.e. readings of SG5 in Figure 7.3).

It is evident from Figure 7.12 that the theoretical predictions agree well with the test results for all specimens except specimen E-1-18-I. The considerably lower load capacity of specimen E-1-18-I is believed to be due to a localized major tensile crack in the upper quarter region of the specimen, as discussed in Subsection 7.2.5. For the other three specimens, although the theoretical analysis provides reasonably good predictions of the ultimate loads, it cannot predict the descending branch of the experimental curves. This may be attributed to the fact that the section analysis was conducted assuming a constant load eccentricity, and the effect of lateral deflection on eccentricity (i.e. second order effect) was ignored.

### **7.3.3 Interaction Diagram**

The eccentricities of loading examined in the experimental program cover only a narrow range (from 6% to 12% of the outer diameter of the specimen). Section analyses were thus conducted to cover the full range, with the eccentricity of loading ranging from zero (concentric compression) to infinity (pure bending). The same section configuration and material properties as the test specimens were employed in these section analyses. The ultimate concrete strain was found from the design-oriented stress-strain model presented in Chapter 5 in all section analyses presented in this and the next subsection. It is shown in Subsection 7.2.5.4 that the ultimate axial strain of concrete in specimens under eccentric

compression is generally higher than that in specimens under concentric compression (Figure 7.11). However, it is believed that this assumption for the ultimate strain has only a small effect on the ultimate load of specimens under eccentric compression, as the stress-strain curve of concrete in hybrid DSTCs has a small slope in the second region (e.g. Figure 7.8).

The results from these section analyses and those from the experiments are shown in Figure 7.13. The vertical axis of Figure 7.13 represents the ultimate load while the horizontal axis represents the ultimate moment. Figure 7.13 is commonly known as an interaction diagram. It is a representation of all combinations of axial load and moment for a given column cross-section. In Figure 7.13, any point on the solid line represents the ultimate limit for a specific combination of axial load and moment; straight lines from the origin represent various eccentricities. It can be found that the shape of this interaction diagram is similar to that of a traditional reinforced concrete column (e.g. Spiegel and Limbrunner 2003). It can also be seen from Figure 7.13 that the few experimental results lie close to the predicted interaction diagram.

#### **7.3.4 Parametric Study**

A parametric study was conducted using the developed section analysis to investigate the effect of confinement stiffness and void ratio on the beam-column behavior of hybrid DSTCs.

The first series of analyses was concerned with DSTC specimens which had the same section configuration, unconfined concrete properties and steel tube as the test specimens but had a stronger FRP jacket with the confinement stiffness being 500 MPa. The load eccentricity in this series of analyses ranged from zero (concentric compression) to infinity (pure bending). Figure 7.14 shows a comparison of two interaction diagrams. It can be seen that when the load eccentricity is not large, the ultimate load and moment are significantly increased with an increase in the confinement stiffness of the FRP outer tube. For a larger load eccentricity, however, this moment capacity increase becomes increasingly smaller until it disappears when the specimen is under pure flexure. This is a natural result of the stress-strain curve for concrete adopted in the theoretical analysis.

The DSTC specimens examined in the second series of analyses had the same outer diameter, unconfined concrete properties and FRP outer tube as the test specimens but had a larger void ratio of 0.75. The steel tubes in these specimens

had the same cross-section area and stress-strain relationship as those in the test specimens. Figure 7.15 shows a comparison of the interaction diagram between this series of analyses and the test specimens. It can be found that a specimen with a larger void ratio has a smaller load capacity when subjected to concentric compression but has a larger moment capacity when subjected to pure flexure. This is easy to understand as a specimen with a larger void ratio has the same steel area as but a smaller concrete area than that with a small void ratio. On the other hand, the steel tube is located farther from the center in a specimen with a larger void ratio.

## **7.4 CONCLUSIONS AND DESIGN RECOMMENDATIONS**

This chapter has presented and interpreted the results of a series of eccentric compression tests on hybrid double-skin tubular columns (DSTCs). A simple theoretical model based on the plane section assumption and the fiber element approach was also developed and employed to predict the responses of the test columns and to conduct a parametric study. Based on the results from the experiments and those from the theoretical analysis, the following conclusions can be drawn.

- (1) Hybrid DSTCs possess a very ductile response when loaded under combined flexure and axial compression.

- (2) A load eccentricity leads to a significant reduction in the axial load capacity of DSTCs.
- (3) The strain distribution over the section generally conforms to the plane section assumption. Deviations from this assumption may occur for the strains on the steel tube after the yielding of steel and for those within the tensile region after the cracking of concrete.
- (4) The shape of interaction diagrams of hybrid DSTCs is similar to that of traditional reinforced concrete (RC) columns.
- (5) The effect of FRP confinement on the concrete in beam specimens is less significant than that in column specimens, while that in beam-column specimens lies in between.
- (6) In DSTCs with a larger void ratio, the steel tube is positioned farther from the center, leading to a more efficient use of the steel tube in resisting bending.

The predictions from the theoretical model are in close agreement with the test results. This section analysis method is thus recommended for design use. The simple concrete stress-strain curve represented by Eqns 7.1-7.4 takes into account both the effects of confinement stiffness and strain gradient, and is also recommended for design use. As evident from Figure 7.11, the ultimate axial strain of a corresponding column may be used directly in such section analyses, as it leads to conservative predictions for beams and beam-columns. This ultimate strain value, which can be found from the design-oriented stress-strain model

presented in Chapter 5, is recommended for design use. Figure 7.16 provides a summary of the stress-strain model recommended for use in the design of columns, beam-columns and beams.

Table 7.1 Details of test specimens

Specimen	FRP Tube	Concrete cylinder strength (MPa)	Diameter (thickness) of steel tube (mm)	Eccentricity (mm)	Axial load capacity (kN)
E-1-00-I	1 Ply	49.7	76(3.7)	0	955.4
E-1-00-II					980.7
E-1-09-I				9	868.5
E-1-09-II					839.0
E-1-18-I				18	588.8
E-1-18-II					709.3

Table 7.2 Locations of tensile cracks and FRP rupture

Specimen	$x_1$ (mm)	Length of the tensile cracks (mm)	$x_2$ (mm)	Width of the FRP rupture zone (mm)
E-1-09-I	205	130	170	105
E-1-09-II	205	100	185	100
	255	150		
E-1-18-I	80	100	140	85
	145	120		
	190	170		
E-1-18-II	230	130	220	130

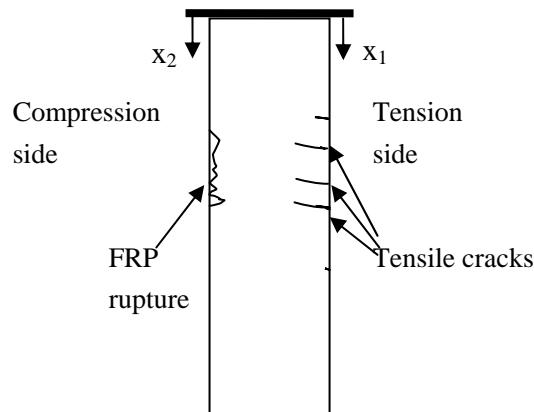




Figure 7.1 Form for casting concrete



Figure 7.2 Buckling of hollow steel tube

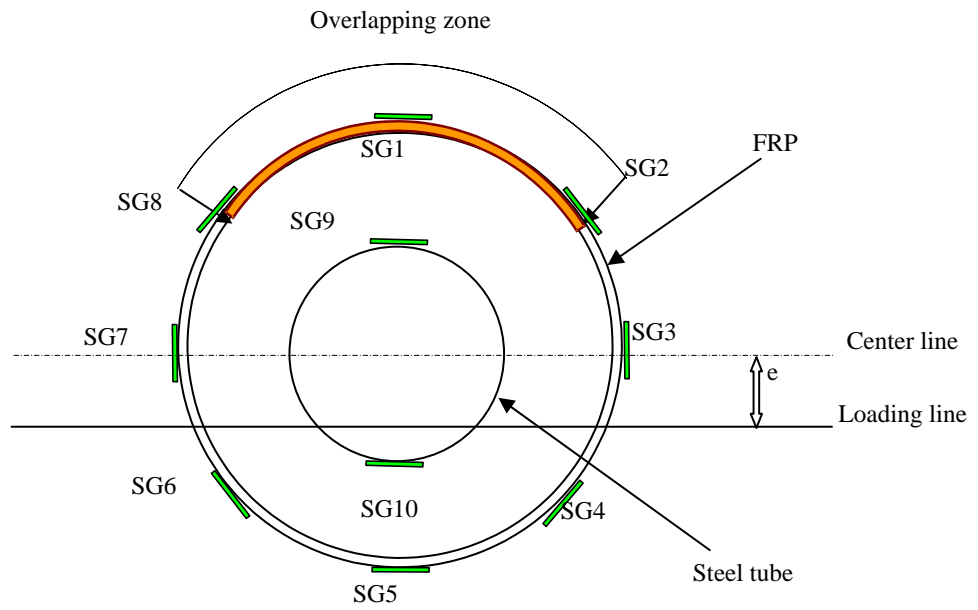
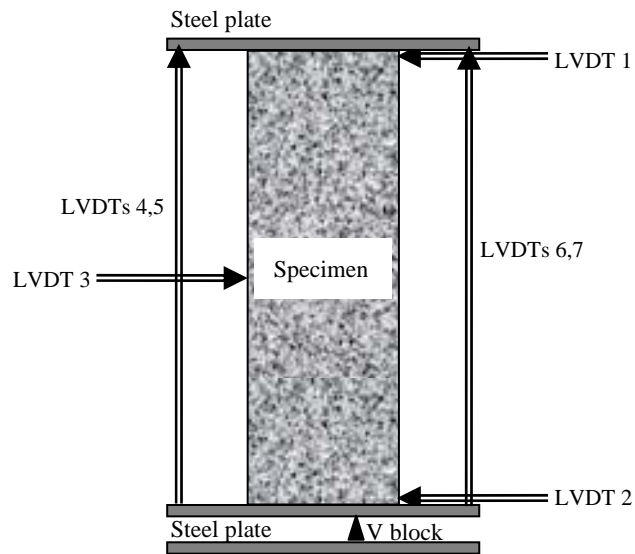


Figure 7.3 Layout of strain gauges



(a) Schematic diagram

Figure 7.4 Set-up for eccentric compression tests



(b) Test photo

Figure 7.4 Set-up for eccentric compression tests (Cont'd)



(a) Overview



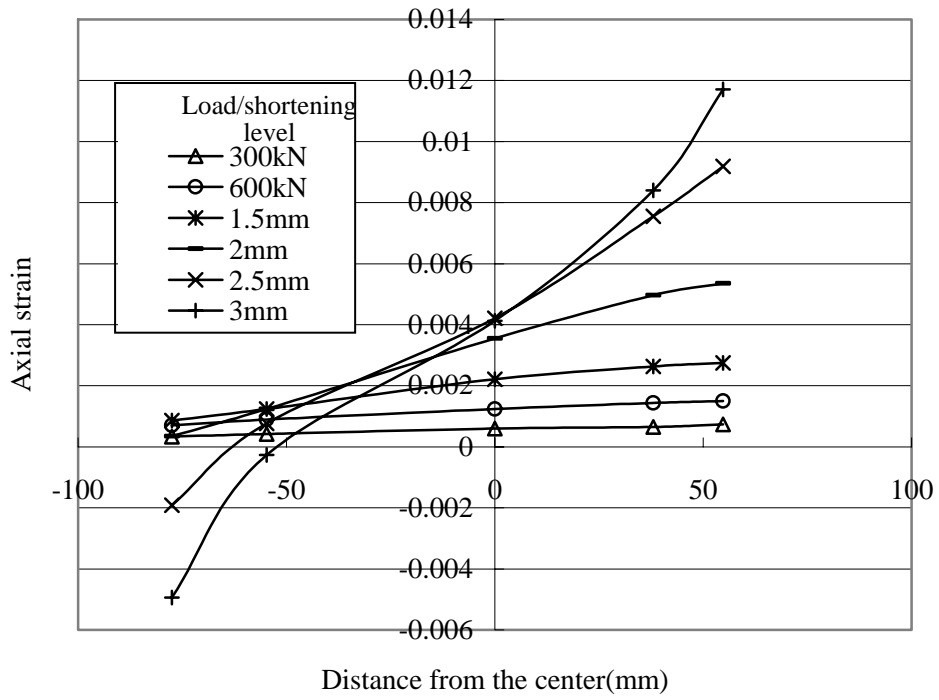
(b) Compression side

Figure 7.5 Specimens after test

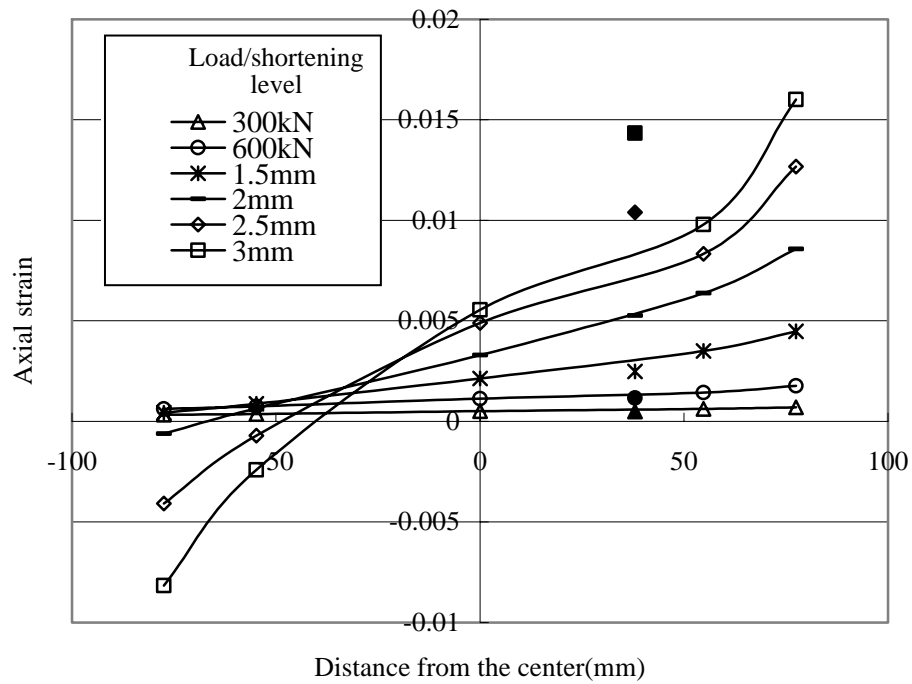


(c) Cracks on tension side

Figure 7.5 Specimens after test (Cont'd)

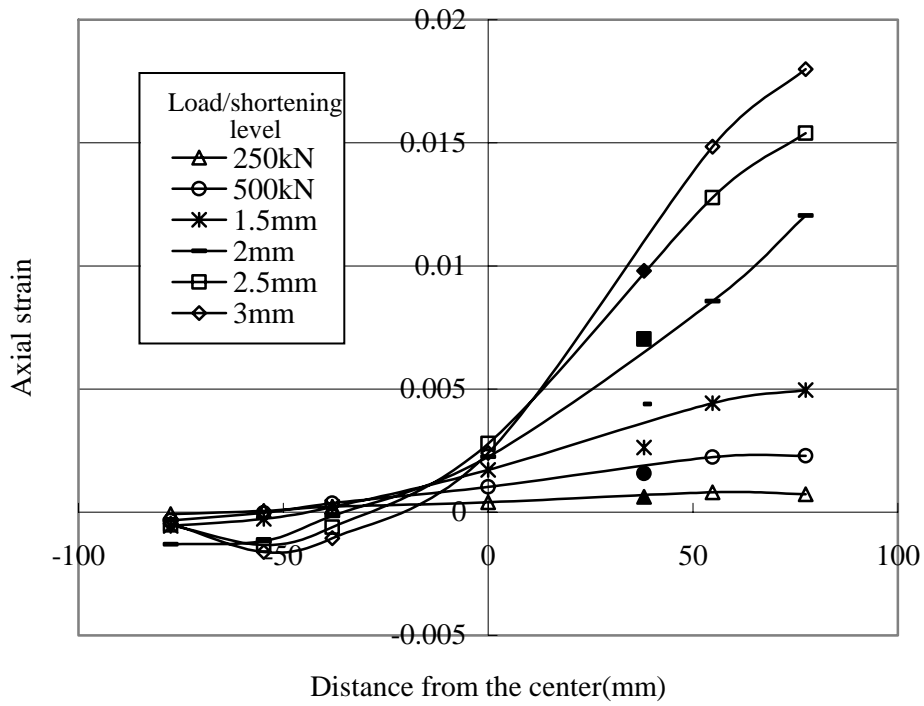


(a) Specimen E-1-09-I

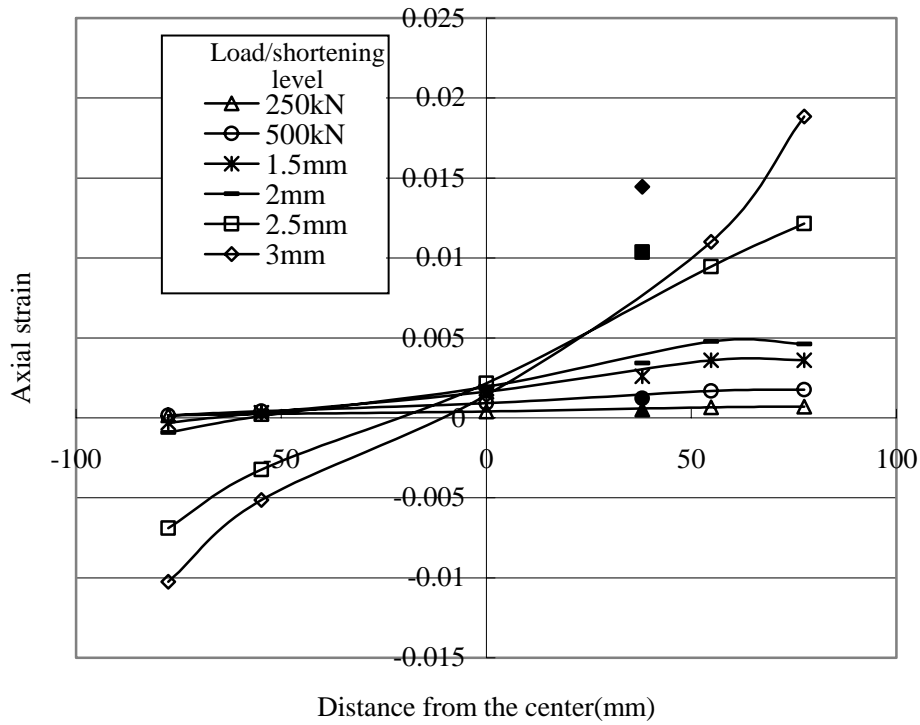


(b) Specimen E-1-09-II

Figure 7.6 Axial strain distributions of specimens under eccentric compression

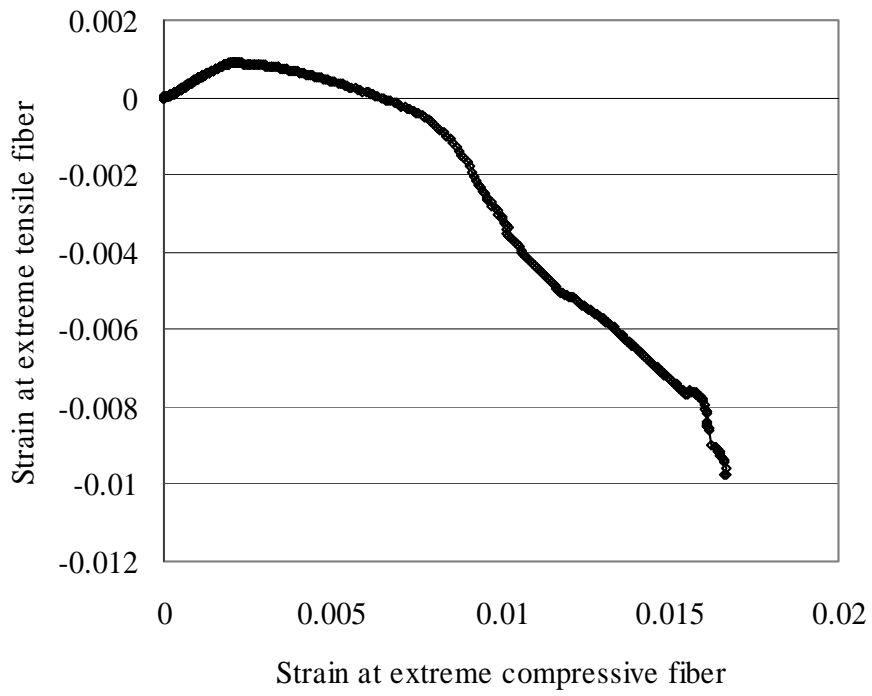


(c) Specimen E-1-18-I

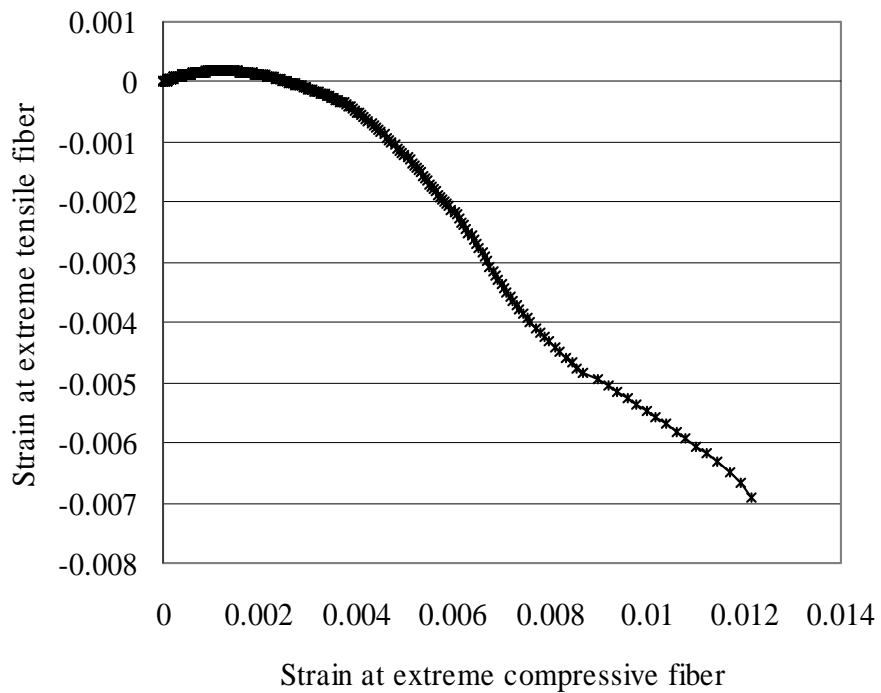


(d) Specimen E-1-18-II

Figure 7.6 Axial strain distributions of specimens under eccentric compression(Cont'd)



(a) Specimen E-1-09-I



(b) Specimen E-1-09-II

Figure 7.7 Comparisons between measured axial strains at extreme tensile and compressive fibers

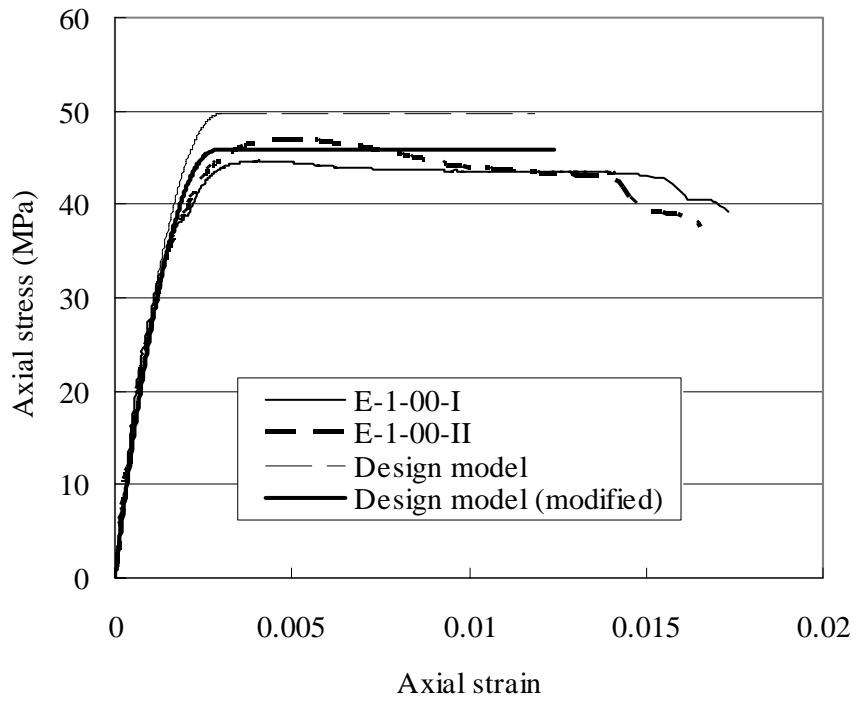


Figure 7.8 Axial stress-strain curves of concrete

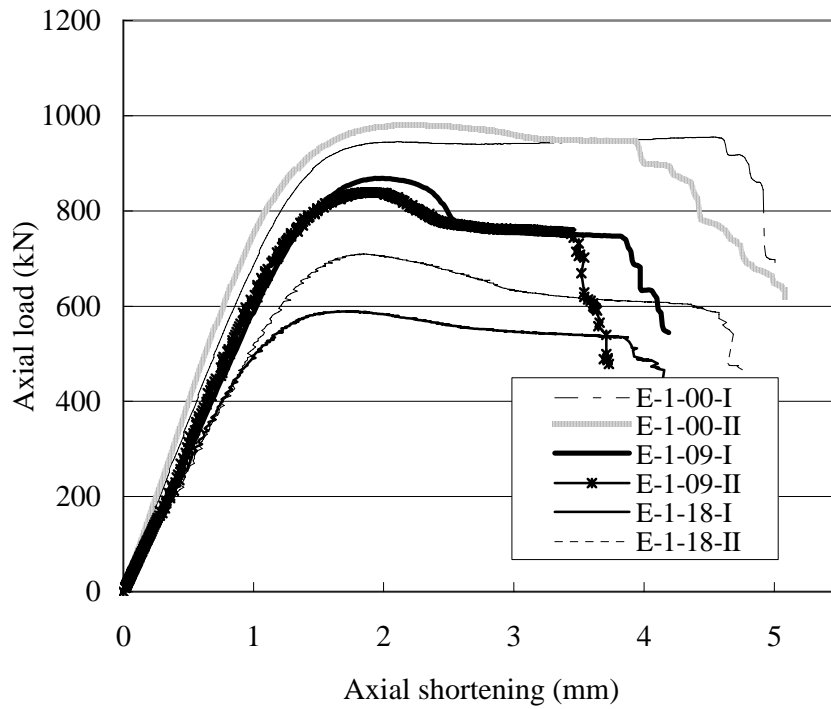


Figure 7.9 Experimental axial load-shortening curves of hybrid DSTCs



(a) Compression side



(b) Tension side

Figure 7.10 Comparison between specimens E-1-18-I and II

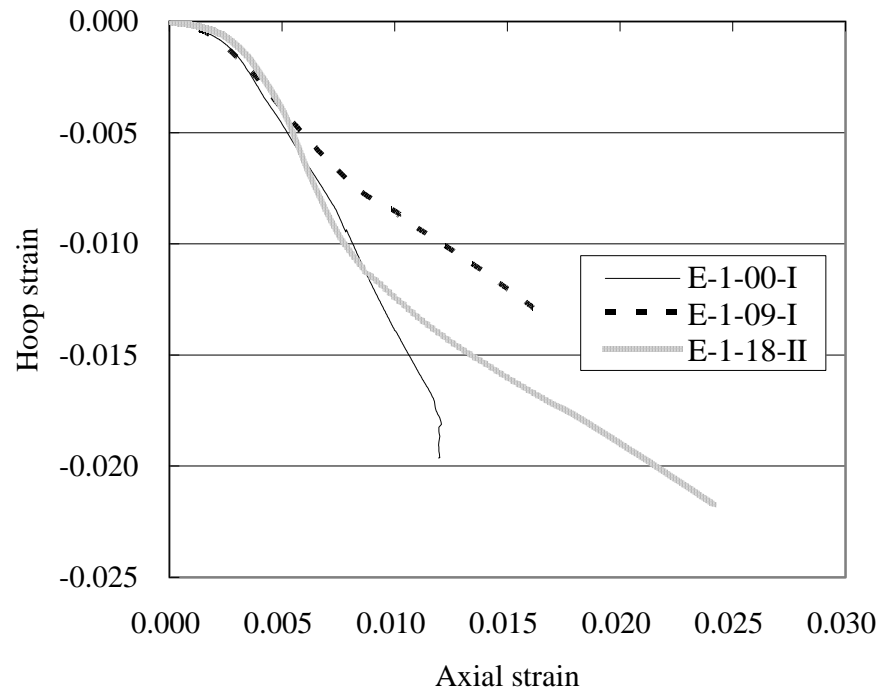
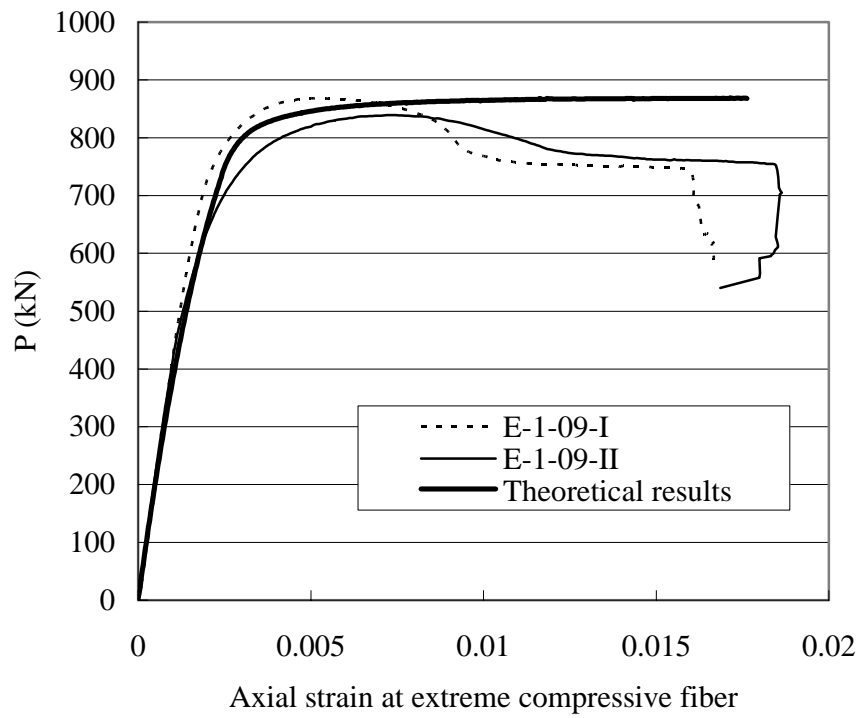
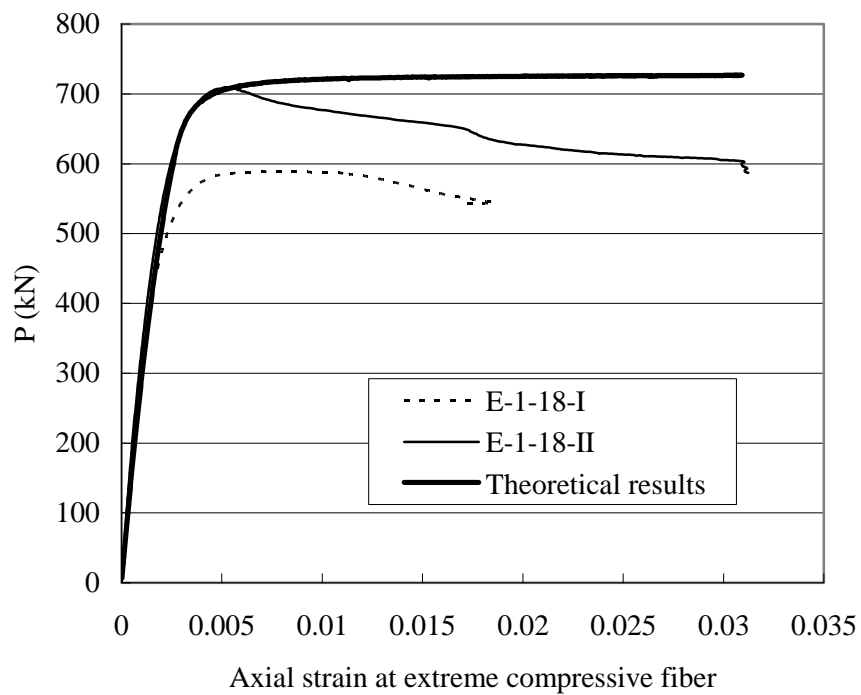


Figure 7.11 Hoop strain-axial strain curves



(a) Loading eccentricity = 9 mm



(b) Loading eccentricity = 18 mm

Figure 7.12 Comparisons between experimental and theoretical results

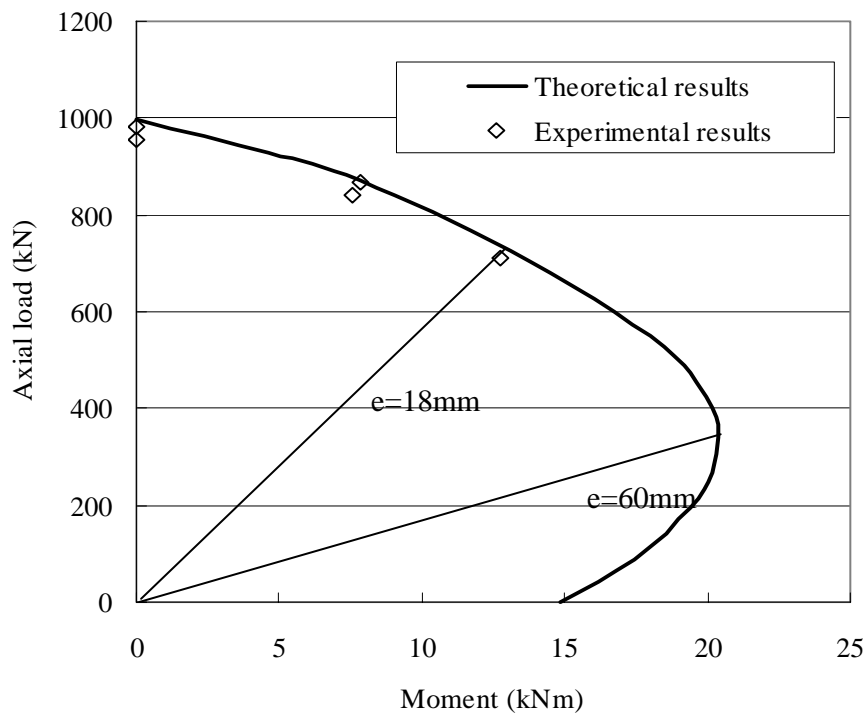


Figure 7.13 Column interaction diagram

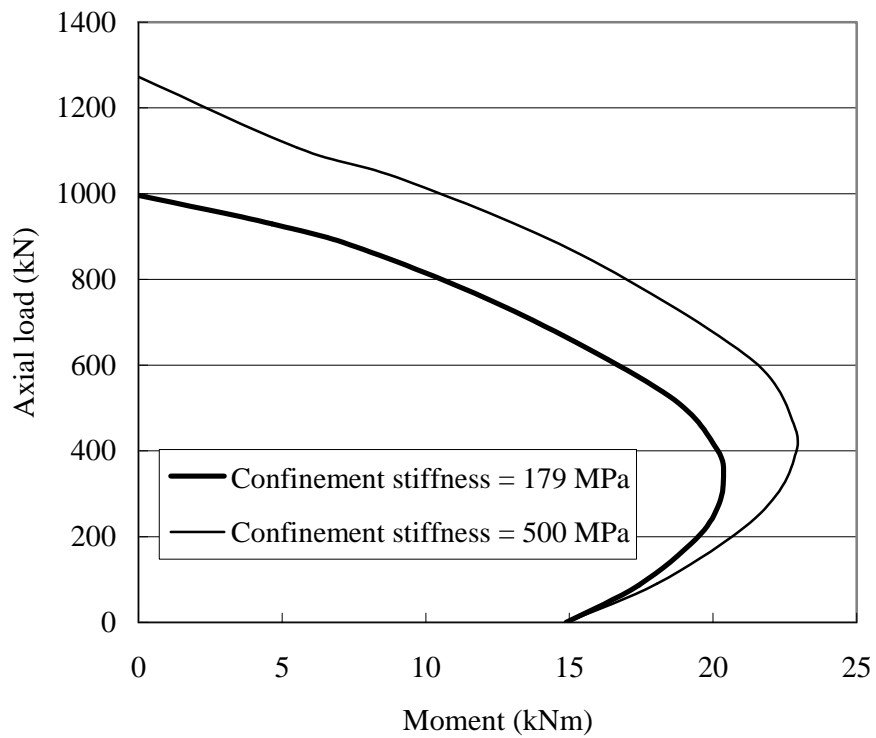


Figure 7.14 Effect of confinement stiffness

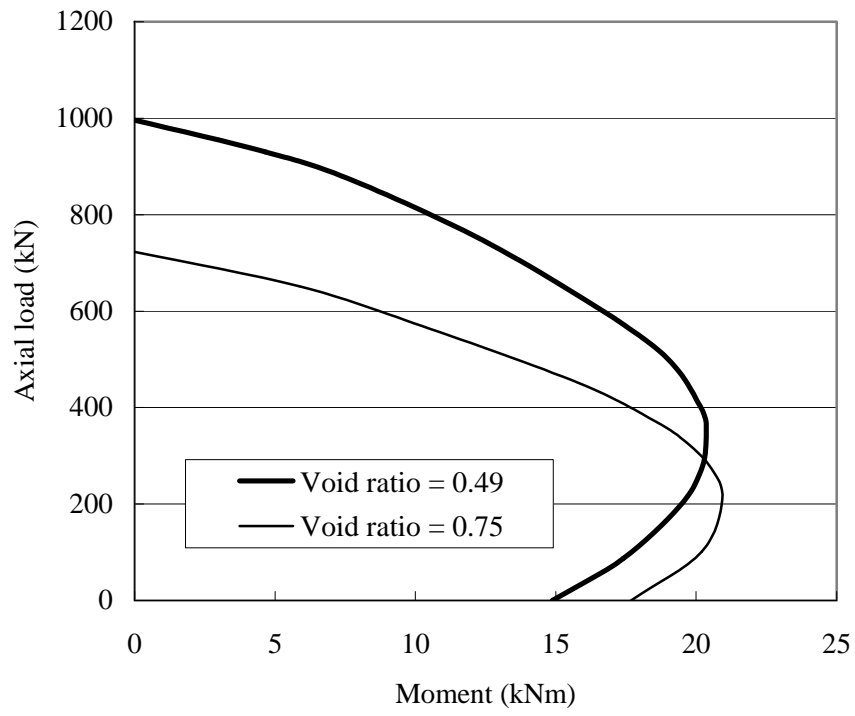


Figure 7.15 Effect of void ratio

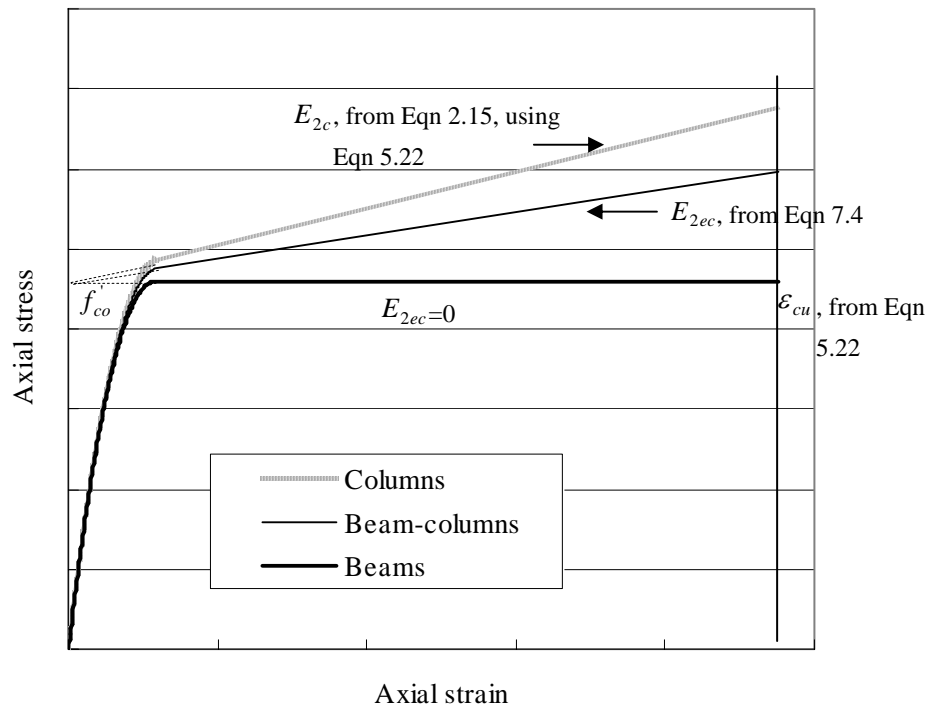


Figure 7.16 Design stress-strain curve for concrete in hybrid DSTCs

## **CHAPTER 8**

### **CONCLUSIONS**

#### **8.1 INTRODUCTION**

This thesis has presented a study into the structural behavior and modeling of a new form of hybrid structural members, namely hybrid FRP-concrete-steel double-skin tubular columns (DSTCs). The new hybrid column consists of an outer tube made of fiber-reinforced polymer (FRP) and an inner tube made of steel, with the space between filled with concrete. In this new hybrid column, the three constituent materials are optimally combined to achieve several advantages over existing columns. These advantages include good ductility, corrosion resistance and ease for construction. In addition, fire protection is not needed as the FRP outer tube is sacrificial during a fire.

A large amount of experimental work has been presented in this thesis, involving laboratory tests of hybrid DSTCs under axial compression, bending and eccentric compression to study the compressive, flexural and beam-column behavior of the new hybrid column. In addition to axial compression tests on short hybrid DSTCs, tests on stub columns of circular solid and annular concrete sections confined with

an FRP outer tube have also been presented, to gain a better understanding of how the three components in a hybrid DSTC interact under axial compression. These test results provided not only the first insight into the structural behavior of hybrid DSTCs but also the means for verifying theoretical models.

Apart from the experimental study, finite element (FE) analysis of hybrid DSTCs under axial compression has also been presented. As a basis for the FE model, an assessment of existing Drucker-Prager (D-P) type concrete plasticity models for confined concrete was first presented. A constitutive model for concrete which takes into account the conclusions drawn from this assessment and other distinct characteristics of non-uniformly confined concrete was proposed and verified with test results. A parametric study by the FE model incorporating this constitutive model was then presented, from which a simple one-dimensional stress-strain model for the concrete in hybrid DSTCs for design use was formulated.

Making use of the proposed one-dimensional stress-strain model of concrete, a simple theoretical method based on section analysis has also been developed for hybrid DSTCs under flexure or combined axial compression and flexure, and verified with test results.

## 8.2 AXIAL COMPRESSIVE BEHAVIOR

The advantages of this new structural form are most obvious when used as a column, for which the axial compressive behavior is the main structural aspect to be understood. Chapter 3 presented a systematic experimental study on the compressive behavior of these hybrid members. In addition, compressive tests on specimens of other similar section forms were also presented in Chapter 3 for comparison, in order to reach a better understanding of the structural behavior and confining mechanism of this new hybrid member. The column forms examined include FRP-confined solid cylinders (FCSCs) which consist of a circular solid concrete column confined with FRP, and FRP-confined hollow cylinders (FCHCs) in which a circular concrete column with a circular inner void is confined with FRP. The main parameters examined included the section configuration, the void ratio, the diameter-to-thickness ratio of the steel inner tube, and the thickness of the FRP outer tube. Based on the test results and discussions, the following conclusions were drawn:

- (1) The concrete in hybrid DSTCs is very effectively confined by the two tubes, and local buckling of the steel inner tube is either delayed or suppressed by the surrounding concrete, leading to a very ductile response. The axial load-shortening behavior of hybrid DSTCs is very similar to FCSCs, which

exhibits an approximately bilinear shape when the confinement of the FRP outer tube exceeds a certain threshold value.

- (2) DSTCs are superior to FCHCs in both the general behavior and the effectiveness of confinement of concrete. The steel inner tube plays an important role by preventing the concrete near the inner surface from inward spalling.
- (3) The behavior of FCHCs, including their stress-strain curves, deformation properties and failure mechanisms, depends significantly on the void ratio. Specimens with a small void ratio exhibit similar behavior to that of the FCSC and DSTC specimens while the failure mechanism of specimens with a relatively large void ratio may be the inward spalling of concrete instead of the rupture of the FRP outer tube.
- (4) The behavior of concrete in hybrid DSTCs is generally similar to that in FCSCs provided the void ratio and the diameter-to-thickness ratio of the steel inner tube are within a reasonable range.
- (5) The behavior of concrete in FCSCs and DSTCs, including the stress-strain behavior and the ultimate strength and strain, depends significantly on the confinement stiffness of the FRP outer tube. The FCSCs or DSTCs with a stronger FRP outer tube possess a larger ultimate strength and strain, and a stress-strain curve with a larger slope of the second linear part. By contrast, the confinement stiffness of the FRP outer tube has a smaller significant effect on the behavior of concrete in FCHCs, especially when the void ratio is large.

When the void ratio is sufficiently large, the confining effect on the concrete in FCHCs may even become negligible.

- (6) The behavior of concrete in hybrid DSTCs, although in general similar to that in FCSCs, depends significantly on the void ratio. The concrete in hybrid DSTCs with a larger void ratio appears to possess a larger ultimate axial strain, and a stress-strain curve with a smaller slope of the second linear part.

### **8.3 FLEXURAL BEHAVIOR**

As columns are normally subjected to combined axial and lateral loads, the flexural behavior is important within the overall picture of the beam-column behavior of the new form of hybrid members. Furthermore, such hybrid sections with an eccentric inner steel tube are particularly suitable for use in beams, for which the flexural behavior is the main structural aspect to be understood. Chapter 6 presented a systematic experimental study on the flexural behavior of the new form of hybrid members. The main parameters examined in this study included the section configuration and the thicknesses of the steel inner tube and the FRP outer tube. The following conclusions were drawn based on the test results and discussions:

- (1) Hybrid DSTCs possess a very ductile response under pure flexure. The FRP tube confines the concrete and provides additional shear resistance. The steel tube provides ductile longitudinal reinforcement.
- (2) A DSTC with an eccentric steel tube benefits more significantly from the FRP outer tube than a corresponding DSTC with a concentric steel tube, as in the former, a larger amount of concrete is in the compression zone.
- (3) Significant slips between the concrete and the two tubes, particularly the steel tube, and associated load fluctuations may occur. Improvements to the bond resistance at both interfaces are desirable.
- (4) The flexural response of a DSTC, including the flexural stiffness, ultimate load and cracking, can be substantially improved by shifting the inner steel tube towards the tension region or providing FRP bars as additional longitudinal reinforcement.
- (5) The effect of FRP confinement on concrete in beam specimens is less significant than that in column specimens of identical sections, because of the existence of a strain gradient and a relatively small concrete compression zone.

## **8.4 BEAM-COLUMN BEHAVIOR**

The beam-column behavior is the main aspect of concern when columns are subjected to combined axial and lateral loads. Chapter 7 presented and interpreted

the results of a series of eccentric compression tests on hybrid DSTCs. The following conclusions were drawn from the test results and discussions:

- (1) Hybrid DSTCs possess a very ductile response when loaded under combined flexure and axial compression.
- (2) A load eccentricity leads to a significant reduction in the axial load capacity of DSTCs.
- (3) The strain distribution over the section generally conforms to the plane section assumption. Deviations from this assumption may occur for the strains on the steel tube after the yielding of steel and for those within the tensile region after the cracking of concrete.
- (4) The shape of interaction diagrams of hybrid DSTCs is similar to that of traditional reinforced concrete (RC) columns.
- (5) The effect of FRP confinement on the concrete in beam specimens is less significant than that in column specimens, while that in beam-column specimens lies in between.
- (6) In DSTCs with a larger void ratio, the steel tube is positioned farther from the center, leading to a more efficient use of the steel tube in resisting bending.

## 8.5 THEORETICAL MODELING

As the proposed hybrid section has three components, it is important to understand the interaction between them, based on which a reasonable method of prediction may then be developed. In addition, the stress state of a hybrid DSTC section is highly non-uniform. In order to predict the stress variation over the annular section and the interaction between the different components, a three-dimensional finite element (FE) model was presented in Chapter 5 for hybrid DSTCs under concentric axial compression. As a basis for the FE modeling of hybrid DSTCs, existing Drucker-Prager (D-P) type concrete plasticity models for confined concrete were first assessed in Chapter 4.

Based on the assessment presented in Chapter 4, it was concluded that a plasticity model can be expected to give reasonably accurate prediction of test results only if the following conditions are met: (a) a hardening rule and a flow rule that are both confinement-dependent, and (b) a pressure-dependent yield criterion which includes the effect of the third deviatoric stress invariant. A confinement-dependent hardening rule is necessary to reflect the difference in the experimental stress-strain curve between confined concrete and unconfined concrete, as the axial stress-strain curve of confined concrete has a more gradual descending branch than that of unconfined concrete. A confinement-dependent flow rule, in which the dilation angle is related not only to the confining pressure

but also to the rate of confining pressure increment, is required to capture the unique lateral expansion behavior of passively-confined concrete. A pressure-dependent yield criterion is necessary to simulate the experimental observation that the shear strength of concrete increases with increases in the hydrostatic pressure. The inclusion of the third deviatoric stress invariant in the yield criterion is necessary to reflect the shear strength difference between concrete under biaxial compression and that under triaxial compression. In Chapter 4, it was also shown that a D-P type plasticity model with all the above modifications, in which the material parameters were produced based on Teng et al.'s (2006a) analysis-oriented model, led to reasonably close predictions for confined concrete of different types.

Despite the modifications explained above, a concrete plasticity model still suffers from a number of problems, including the inability to model the stiffness degradation of concrete and the possible numerical difficulty when modeling the softening behavior of concrete. The introduction of a damage variable to account for stiffness degradation in a plasticity model can overcome these problems. A modified plastic-damage model within the theoretical framework of the Concrete Damaged Plasticity Model (CDPM) in ABAQUS was thus proposed in Chapter 5. In this plastic-damage model, the conclusions drawn in Chapter 4 for concrete plasticity models were taken into account, together with the distinct deformation characteristics of non-uniformly confined concrete. With this plastic-damage

model, FE models were developed and verified with test results of concrete under active confinement and passive confinement, and those of hybrid DSTCs obtained in the present project. Using the verified FE models, a parametric study was then conducted to further investigate the behavior of hybrid DSTCs, including the interaction between the three components (i.e. FRP outer tube, concrete and steel outer tube) and the effect of several parameters, such as the confinement stiffness and rupture strain of the FRP outer tube, the void ratio and the  $D_s/t_s$  ratio of the steel inner tube. The parametric study showed that although the void ratio does not significantly affect the compressive strength of concrete in hybrid DSTCs, it has a considerable effect on the ultimate axial strain. A simple one-dimensional stress-strain model for the concrete in hybrid DSTCs was also formulated for design use, based on this parametric study.

Sectional analysis method has also been developed for the prediction of flexural and beam-column behavior of hybrid DSTCs, based on the so-called fiber element approach. The analytical procedure involves the determination of the position of the neutral axis for a given strain of the extreme compression fiber by force equilibrium and the evaluation of the bending moment by integrating the contributions of stresses over the section. It is known that the key point determining the success of such sectional analysis of a hybrid structural member is the stress-strain model adopted for each constituent material. A simple stress-strain model was presented in Chapter 5 for the confined concrete in hybrid

DSTCs under pure axial compression. It was however found from the bending tests presented in Chapter 6 that the confinement is less effective when hybrid DSTCs are under bending, mainly due to the strain gradient over the section. This finding is similar to that observed for the concrete in concrete-filled FRP tubes (CFFTs) by previous researchers. Therefore, the so-called “variable confinement model” was adopted for the concrete in hybrid DSTCs. In this variable confinement model, the effect of strain gradient on the confinement effectiveness is included by relating the slope of second linear portion of the concrete stress-strain curve (i.e.  $E_{2c}$  for columns or  $E_{2ec}$  for beam-columns) to the eccentricity of loading. For columns in which the load eccentricity is equal to zero, the  $E_{2c}$  value calculated from the stress-strain model presented in Chapter 5 can be directly adopted, producing the upper bound of the variable confinement model. For beams in which the load eccentricity is infinite, the  $E_{2ec}$  value is assumed to be zero, producing the lower bound of the variable confinement model. With this variable confinement model, the section analysis method was verified with test results presented in Chapters 6 and 7 and adopted to conduct a parametric study.

## **8.6 FURTHER RESEARCH**

This thesis has primarily been concerned with the static structural behavior of hybrid FRP-concrete-steel double-skin tubular columns and the theoretical modeling of this behavior. This research has led to a good understanding of the

structural behavior of this hybrid structural member, including the compressive, flexural and beam-column behavior. A finite element model has been developed for the compressive behavior, and a section analysis method has been developed for the flexural and beam-column behavior of hybrid DSTCs. Both modeling methods have been verified with test results. The results presented in this thesis represent a major step forward on the road towards the practical application of this new form of structural members and facilitate further research on the following issues.

Experiments on hybrid DSTCs have so far been limited to small scale specimens. Differences in behavior may exist between these small scale specimens and full-scale specimens in real construction. Testing of large or full-scale specimens should be carried out in the future. The section analysis method proposed in this thesis has been verified with results from bending tests and eccentric compressive tests with small load eccentricities. Its applicability in modeling hybrid DSTCs under compression with large load eccentricities is yet to be verified. The effect of column slenderness should also be examined. The long-term behavior of hybrid DSTCs is another important issue. For example, the long-term durability of the FRP outer tube and the column as a whole should be investigated. Finally, the seismic response of hybrid DSTCs needs to be studied.

The present research has identified attributes which are necessary for a plasticity model to yield reasonably close predictions for confined concrete and led to a modified constitutive model for concrete. FE analyses of confined concrete using the proposed constitutive model were also conducted. Despite the close agreement between the FE and the test results, it is important to note that while the proposed constitutive model has a rigorous basis for uniformly confined concrete (confined concrete in solid circular sections), it has to rely on assumptions derived from empirical evidence for confined concrete in non-circular sections. While this approach represents a significant improvement to existing modeling approaches for FRP-confined concrete in non-circular sections as discussed in Chapter 5, further research is still needed to verify the proposed approach more fully or to develop a more rigorous treatment.

Apart from further research, the practical application of this new form of structural members should be actively sought. The present research has provided an adequate technical basis for the design of real hybrid DSTCs, while the long-term health of the structural member can be monitored with modern technology. During practical applications, reliable construction details such as connections between hybrid DSTCs and beams and footings should also be developed.

## REFERENCES

ABAQUS (2004). *ABAQUS Analysis User's Manual*, version 6.5.

ACI 318-95 (1999). *Building Code Requirements for Structural Concrete (318-95) and Commentary (318R-95)*, American Concrete Institute (ACI), Fifth Printing, Farmington Hills, Michigan, USA.

ACI 440.3R (2004). *Guide Test Methods for Fiber-Reinforced Polymers (FRPs) for Reinforcing or Strengthening Concrete Structures*, ACI Committee 440, Michigan, USA.

Ahmad, S.H. and Shah, S.P. (1982). "Complete triaxial stress-strain curves for concrete", *Journal of the Structural Division*, ASCE, Vol. 108, No. ST4, pp. 728-742.

ASTM D2290-00 (2000). *Standard Test Method for Apparent Hoop Tensile Strength of Plastic or Reinforced Plastic Pipe by Split Disk Method*, American Society for Testing and Materials (ASTM), Philadelphia, USA.

ASTM D3039/D3039M-00 (2000). *Standard Test Method for Tensile Properties of Polymer Matrix Composite Materials*, American Society for Testing and Materials (ASTM), Philadelphia, USA.

ASTM D3410/D3410M-95 (1995). *Standard Test Method for Compressive Properties of Polymer Matrix Composite Materials with Unsupported Gage*

*Section by Shear Loading*, American Society for Testing and Materials (ASTM), Philadelphia, USA.

ASTM D3518/D3518M-94 (1994). *Standard Test Method for In-Plane Shear Response of Polymer Matrix Composite Materials by Tensile Test of a  $\pm 45^\circ$  Laminate*, American Society for Testing and Materials (ASTM), Philadelphia, USA.

ASTM D695-02a (2002). *Standard Test Method for Compressive Properties of Rigid Plastics*, American Society for Testing and Materials (ASTM), Philadelphia, USA.

Becque, J. (2000). *Analytical Model of Concrete Columns Confined by FRP*, MSc Thesis, Department of Civil and Geological Engineering, The University of Manitoba, Winnipeg, Manitoba.

Becque, J., Patnaik, A.K. and Rizkalla, S.H. (2003). "Analytical models for concrete confined with FRP tubes", *Journal of Composites for Construction*, Vol. 7, No. 1, pp. 1-8.

Bhide, K.M. (2002). *Shear Response of Concrete Filled Circular Fiber-reinforced-polymer Composites Tubes*, MSc Thesis, Michigan State University.

BS 18 (1987). *Tensile Testing of Metals (including Aerospace Materials)*, British Standards Institution, London, UK.

BS 8110. (1997). *Structural Use of Concrete, Part 1, Code of Practice for Design and Construction*, London, UK: British Standards Institution.

Burgueno, R., Davol, A., Zhao, L., Seible, F. and Karbhari, V.M. (2004). "Flexural behavior of hybrid fiber-reinforced polymer/concrete beam/slab bridge component", *ACI Structural Journal*, Vol. 101, No. 2, pp. 228-236.

Candappa, D.C., Sanjayan, J.G. and Setung, S. (2001) "Complete triaxial stress-strain curves of high-strength concrete", *Journal of Materials in Civil Engineering*, ASCE, 13(3), 209-215.

Carreira, D. J. and Chu, K.-H. (1985). "Stress-strain relationship for plain concrete in compression." *ACI Journal*, Vol. 82, No. 6, pp. 797-804.

Cervera, M., Oliver, J. and Faria, R. (1995). "Seismic evaluation of concrete dams via continuum damage models", *Earthquake Engineering and Structural Dynamics*, Vol. 24, pp. 1225-1245.

Chen, W.F. (1982). *Plasticity in Reinforced Concrete*, McGraw-Hill Book Company, New York, N.Y.

Chen, W.F. and Lan, Y.M. (2004). "Finite element study of confined concrete", in *Proceedings of International Symposium on Confined Concrete*, in CD-Rom format, Changsha, China.

Chun, S.S. and Park H.C. (2002). "Load carrying capacity and ductility of RC columns confined by carbon fiber reinforced polymer", *Proceedings, Third International Conference on Composites in Infrastructure*, in CD-Rom format.

Daniel, I.M. and Ishai, O. (1994). *Engineering Mechanics of Composite Materials*, Oxford University Press, Oxford.

Davol, A. (1998). *Structural Characterization of Concrete Filled Fiber Reinforced Shells*, PhD Thesis, University of California, San Diego, USA.

Davol, A., Burgueno, R. and Seible, F. (2001). “Flexural behavior of circular concrete filled FRP shells”, *Journal of Structural Engineering*, ASCE, Vol. 127, No. 7, pp. 810-817.

Drucker, D. C. and Prager, W. (1952). “Soil mechanics and plastic analysis or limit design”, *Quart Applied Mechanics*, Vol. 10, No. 2, pp. 157-165.

Elchalakani, M., Zhao, X.L. and Grzebieta, R. (2002). “Tests on concrete filled double-skin (CHS outer and SHS inner) composite short columns under axial compression”, *Thin-walled Structures*, Vol. 40, No. 5, pp. 415-441.

ENV 1992-1-1. Eurocode 2 (1992): *Design of Concrete Structures—Part 1: General Rules and Rules for Buildings*, European Committee for Standardization, Brussels.

Fam, A.Z. (2000). *Concrete-filled Fiber-Reinforced Polymer Tubes for Axial and Flexural Structural Members*, PhD Thesis, Department of Civil and Geological Engineering, The University of Manitoba, Winnipeg, Manitoba.

Fam, A. Z., Flisak, B. and Rizkalla, S. (2003). “Experimental and analytical modelling of concrete-filled fiber-reinforced polymer tubes subjected to combined bending and axial loads”, *ACI Structural Journal*, Vol. 100, No. 4, pp. 499-509.

Fam A.Z. and Rizkalla S.H. (2001a). “Confinement model for axially loaded concrete confined by circular fiber-reinforced polymer tubes”, *ACI Structural Journal*, Vol. 98, No. 4, pp. 451-461.

Fam, A.Z. and Rizkalla, S.H. (2001b). "Behavior of axially loaded concrete-filled circular fiber-reinforced polymer tubes", *ACI Structural Journal*, Vol. 98, No. 3, pp. 280-289.

Fam, A.Z. and Rizkalla, S.H. (2002). "Flexural behavior of concrete-filled fiber-reinforced polymer circular tubes", *Journal of Composites for Construction*, Vol. 6, No. 2, pp. 123-132.

Fang, J.H. (1999). *Finite Element Analysis of FRP-Retrofitted RC Beams*, Master Thesis, Department of Civil Engineering, National Taiwan University (in Chinese).

Fardis, M.N. and Khalili, H. (1981). "Concrete encased in fiberglass-reinforced plastic", *ACI Journal*, Vol. 78, No. 6, pp. 440-446.

Flisak, B. (2004). *Concrete Filled Fiber Reinforced Polymer Tubes for Structural Members*, MSc Thesis, University of Manitoba.

Flisak, B., Fam, A.Z. and Rizkalla, S.H. (2001). "FRP tubes filled with concrete and subjected to combined axial and flexural loads", *Proceedings of the Second Congress of Construction and Materials*, Houston, Texas, Oct 10-13.

Gerstle, K.H. (1981a) "Simple formulation of biaxial concrete behavior", *ACI Journal*, Vol. 78, No. 1, pp. 62-68.

Gerstle, K.H. (1981b) "Simple formulation of triaxial concrete behavior", *ACI Journal*, Vol. 78, No. 5, pp. 382-387.

Gardner, N.J. (1969). "Triaxial behaviour of concrete", *ACI Journal*, Vol. 66, No. 2, pp. 136-146.

Gopalaratnam, V.S. and Shah, S.P. (1985). "Softening response of plain concrete in direct tension", *ACI Journal*, Vol. 82, No. 3, pp. 310-323.

Hahn, H. and Tsai, S. (1973). "Nonlinear elastic behavior of unidirectional composite laminae", *Journal of Composite Materials*, Vol. 7, January, pp. 102-118.

Haj-Ali, R. and Kilic, H. (2002). "Nonlinear behavior of pultruded FRP composites", *Composites Part B: Engineering*, Elsevier, Vol. 33, pp. 173-191.

Han, B., Xia, J. and Zhao, J. (1995). "The strength of concrete filled double-skin steel tubes under axial compression", *Journal of Shijiazhuang Railway Institute*, Vol. 8, No. 3, pp.75-80

Han, L.H., Tao, Z., Huang, H. and Zhao, X.L. (2004). "Concrete-filled double skin (SHS outer and CHS inner) steel tubular beam-columns", *Thin-Walled Structures*, Vol. 42, No. 9, pp. 1329-1355.

Harries, K.A. and Kharel, G. (2002). "Behavior and modeling of concrete subject to variable confining pressure", *ACI Materials Journal*, Vol. 99, No. 2, pp. 180-189.

Hong, W.K., Kim, H.C. and Yoon, S.H. (2002). "Experiment of compressive strength enhancement of circular concrete column confined by carbon tubes", *KCI Concrete Journal*, Vol. 14, No. 4, pp. 139-144.

Huang, Y.L. (2005). *Analysis-oriented and Constitutive Modeling of FRP-Confined Concrete*, Master Degree Thesis, Tsing-Hua University (in Chinese).

Karabinis, A.I. and Kiouisis, P.D. (1994). "Effects of confinement on concrete columns: plasticity approach", *Journal of Structural Engineering*, ASCE, Vol. 120, No. 9, pp. 2747-2766.

Karabinis, A.I. and Kiouisis, P.D. (1996). "Strength and ductility of rectangular concrete columns: a plasticity approach", *Journal of Structural Engineering*, ASCE, Vol. 122, No. 3, pp. 267-274.

Karabinis, A.I. and Rousakis, T.C. (2002). "Concrete confined by FRP material: a plasticity approach", *Engineering Structures*, Vol. 24, pp. 923-932.

Karsan, I.D. and Jirsa, J.O. (1969). "Behavior of concrete under compressive loadings", *Journal of the Structural Division*, ASCE, Vol. 95, No. 12, pp. 2535-2563.

Kupfer, H., Hilsdorf, H.K. and Rusch, H. (1969). "Behavior of concrete under biaxial stresses", *ACI Journal*, Vol. 66, pp. 656-666.

Lam, L. and Teng, J.G. (2003a). "Design-oriented stress-strain model for FRP-confined concrete", *Construction and Building Materials*, Vol. 17, pp. 471-489.

Lam, L. and Teng, J.G. (2003b). "Design-oriented stress-strain model for FRP-confined concrete in rectangular columns", *Journal of Reinforced Plastics and Composites*, Vol. 22, No. 13, pp. 1149-1186.

Lam, L. and Teng, J.G. (2004) "Ultimate condition of FRP-confined concrete", *Journal of Composites for Construction* ASCE, Vol. 8, No. 6, pp. 539-548.

Lan, Y.M. (1998). *Finite Element Study of Concrete Columns with Fiber Composite Jackets*, PhD Dissertation, School of Civil Engineering, Purdue University.

Lee, J. and Fenves, G.L. (1998). "Plastic-damage model for cyclic loading of concrete structures", *Journal of Engineering Mechanics*, ASCE, Vol. 124, No. 8, pp. 892-900.

Lifshitz, J. (1988) "Determination of nonlinear shear modulus of a fiber-reinforced lamina from the axial behavior of ( $\pm 45$ )s specimens", *Journal of Composites Technology & Research*, Vol. 10, No. 4, pp. 146-150.

Lubliner, J., Oliver, J., Oller, S. and Onate, E. (1989). "A plastic-damage model for concrete", *International Journal of Solids and Structures*, Vol. 25, pp. 299-329.

Luccioni, B.M. and Rougier, V.C. (2005). "A plastic damage approach for confined concrete", *Computers and Structures*, Vol. 83, pp. 2238-2256.

Maekawa, K., Pimanmas, A. and Okamura, H. (2003). *Nonlinear Mechanics of Reinforced Concrete*, Spon Press.

Mahfouz, I., Rizk, T. and Sarkani, S. (2001). "An innovative FRP confining system for repairing rectangular columns", *Construction and Materials Issues 2001, Proceedings of the Second Congress*, ASCE and Construction Institute, pp. 16-25.

Mander, J.B., Priestley, M.J.N. and Park, R. (1988) "Theoretical stress-strain model for confined concrete", *Journal of Structural Engineering*, ASCE, Vol. 114, No. 8, pp. 1804-1826.

Mazars, J. (1986). "A model of a unilateral elastic damageable material and its application to concrete", *Fracture Toughness and Fracture Energy of Concrete*, F.H. Wittmann, ed., Elsevier Science Publishers, Amsterdam, The Netherlands, pp. 61-71.

Mirmiran, A. (2003). "Stay-in-place FRP form for concrete columns", *Advances in Structural Engineering*, Vol. 6, No. 3, pp. 231-241.

Mirmiran, A. and Shahawy, M. (1996). "A new concrete-filled hollow FRP composite column", *Composites Part B: Engineering*, Vol. 27B, No. 3-4, pp. 263-268.

Mirmiran, A. and Shahawy, M. (1997). "Behavior of concrete columns confined by fiber composites", *Journal of Structural Engineering*, ASCE, Vol. 123, No. 5, pp. 583-590.

Mirmiran, A., Shahawy, M. and Samaan, M. (1999). "Strength and ductility of hybrid FRP-concrete beam-columns", *Journal of Structural Engineering*, ASCE, Vol. 125, No. 10, pp. 1085-1093.

Mirmiran, A., Zagers, K. and Yuan, W.Q. (2000). "Nonlinear finite element modeling of concrete confined by fiber composites", *Finite Elements in Analysis and Design*, Vol. 35, pp. 79-96.

Murray, Y.D. and Lewis, B.A. (1995). *Numerical Simulation of Damage in Concrete*, APTEK technical report to the Defense Nuclear Agency, Contract No. DNA001-91-C-0075, Report No. DNA-TR-94-190.

Nordin, H. and Taljsten, B. (2004). "Testing of hybrid FRP composite beams in bending", *Composites Part B: Engineering*, Vol. 35, No. 1, pp. 27-33.

Oh, B. (2002). *A Plasticity Model for Confined Concrete under Uniaxial Loading*, PhD Thesis, Lehigh University.

Oshima, M. and Hashimoto, C. (1984). "Mechanical properties of concrete confined by steel rings", *Summaries of the 39<sup>th</sup> Annual Convention*, Vol. V, Japan Society of Civil Engineers.

Parvin, A. and Wang, W. (2001). "Behavior of FRP jacketed concrete columns under eccentric loading", *Journal of Composites for Construction*, ASCE, Vol. 5, No. 3, pp. 146-152.

Popovics, S. (1973). "Numerical approach to the complete stress-strain relation for concrete", *Cement and Concrete Research*, Vol. 3, No. 5, pp. 583-599.

Reinhardt, H.W. (1984). "Fracture mechanics of an elastic softening material like concrete", *Heron*, Vol. 29, No. 2, pp. 1-42.

Richart, F.E., Brandtzaeg, A. and Brown, R.L. (1928) *A Study of the Failure of Concrete under Combined Compressive Stresses*, Bulletin No. 185, Engineering Experiment Station, University of Illinois, Urbana, U.S.A.

Rochette, P. and Labossiere, P. (1996). "A plasticity approach for concrete columns confined with composite materials", *Proceedings of Conference on Advanced Composite Materials in Bridges and Structures*, M. El-Badry, ed., Canadian Society of Civil Engineers, Montreal, Canada, pp. 359-366.

Saafi, M., Toutanji, H.A., and Li, Z. (1999). "Behavior of concrete columns confined with fiber reinforced polymer tubes," *ACI Materials Journal*, Vol. 96, No. 4, pp. 500-509.

Samaan, M.S. (1997). *An Analytical and Experimental Investigation of Concrete-filled Fiber Reinforced Plastic (FRP) Tubes*, PhD Thesis, Departmental of Civil and Environmental Engineering, The University of Central Florida, Orlando, Florida.

Samaan, M., Mirmiran, A. and Shahawy, M. (1998). "Model of concrete confined by fiber composite", *Journal of Structural Engineering*, ASCE, Vol. 124, No. 9, pp. 1025-1031.

Schwer, L. (2003) *Geomaterial Modeling with LS-DYNA*, short course notes, organized by Livermore Software Technology Corporation.

Sfer, D., Carol, I., Gettu, R. and Etse, G.. (2002). "Study of the behavior of concrete under triaxial compression", *Journal of Engineering Mechanics*, ASCE, Vol. 128, No. 2, pp. 156-163.

Shahawy M., Mirmiran A. and Beitelman T. (2000). "Tests and modeling of carbon-wrapped concrete columns", *Composites: Part B-Engineering*, Vol. 31, Nos. 6 & 7, pp. 471-480.

Shakir-Khalil, H. (1991). "Composite columns of double-skinned shells", *Journal of Constructional Steel Research*, Vol. 19, No. 2, pp. 133-152.

Shakir-Khalil, H. and Illouli, S. (1987). "Composite columns of concentric steel tubes", In *Proceedings, Conference on the Design and Construction of Non-Conventional Structures*, Vol. 1, London, pp. 73-82.

Shao, Y. T. (2003). *Behavior of FRP-Concrete Beam-Columns under Cyclic Loadings*, PhD Thesis, North Carolina State University.

Simo, J.C. and Ju, J.W. (1987). "Stress and strain based continuum damage models-I. formulation", *Internal Journal of Solids and Structures*, Vol. 23, pp. 821-840.

Spiegel, L. and Limbrunner, G.F. (2003). *Reinforced Concrete Design*, 5<sup>th</sup> edition, Upper Saddle River, N.J. : Prentice Hall.

Spoelstra, M. and Monti, G. (1999), "FRP-confined concrete model", *Journal of Composites for Construction*, ASCE, Vol. 3, No. 3, pp. 143-150.

Tao, Z., Han, L.H. and Huang, H. (2003). "Concrete-filled double skin steel tubular column with square section under eccentric loads", *China Civil Engineering Journal*, Vol. 36, No. 2, pp. 33-40.

Teng, J.G., Chen, J.F., Smith, S.T. and Lam, L. (2002) *FRP Strengthened RC Structures*, John Wiley & Sons, Ltd.

Teng, J.G., Chen, J.F., Smith, S.T. and Lam, L. (2003). "Behaviour and strength of FRP-strengthened RC structures: a state-of-the-art review", *ICE Proceedings: Structures and Buildings*, Vol. 156, No. 1, pp. 51-62.

Teng, J.G., Huang, Y.L., Lam, L and Ye, L.P. (2006a). "Theoretical model for fiber reinforced polymer-confined concrete", *Journal of Composites for Construction*, ASCE, in press.

Teng, J.G., Jiang, T. , Lam, L. and Luo, Y.Z. (2006b). "Refinement of Lam and Teng's design-oriented stress-strain model for FRP-confined concrete", *Proceedings of IABSE Symposium*, Budapest, Hungary, September 13-15, 2006.

Teng, J.G. and Lam, L. (2004). "Behavior and modeling of FRP-confined concrete", *Journal of Structural Engineering*, ASCE, Vol. 130, No. 11, pp. 1713-1723.

Toutanji, H.A. (1999). "Stress-strain characteristics of concrete columns externally confined with advanced fiber composite sheets", *ACI Materials Journal*, Vol. 96, No. 3, pp. 397-404.

Wei S., Mau S.T., Vipulanandan C. and Mantrala, S.K. (1995a). "Performance of new sandwich tube under axial loading: analysis" *Journal of structural Engineering*, ASCE, Vol. 121, No. 12, pp. 1815-1821.

Wei S., Mau S.T., Vipulanandan C. and Mantrala, S.K. (1995b). "Performance of new sandwich tube under axial loading: experiment" *Journal of structural Engineering*, ASCE, Vol. 121, No. 12, pp. 1806-1814.

Xiao, Y. (2004). "Applications of FRP composites in concrete column", *Advances in Structural Engineering*, Vol. 7, No. 4, pp. 335-343.

Xiao, Y and Wu, H. (2000). "Compressive behavior of concrete confined by carbon fiber composite jackets", *Journal of Materials in Civil Engineering*, ASCE, pp. 139-146.

Xiao, Y. and Wu, H. (2003). "Compressive behavior of concrete confined by various types of FRP composites jackets", *Journal of Reinforced Plastics and Composites*, Vol. 22, No. 13, pp. 1187-1202.

Yagishita, F., Kitoh, H., Sugimoto, M., Tanihira, T. and Sonoda, K. (2000). "Double skin composite tubular columns subjected to cyclic horizontal force and

constant axial force”, *Proceedings of the Sixth ASCCS International Conference on Steel-Concrete Composite Structures*, pp. 497-503.

Yuan, H., Xue, Y., Li, X. and Zhang, M. (2002). “Study on a novel hybrid GFRP/CFRP composite beam”, *Proceedings of 2nd National Conference on Application Technology of FRP Materials in Civil Engineering*, Tsinghua University Publication, Beijing.

Zhang, D.X., Huang, L.N., Wang, R.G. and Zhao, J.H. (2000). “Experimental research on the mechanical properties of concrete filled FRP tubular column”, *Journal of Harbin University of Civil Engineering and Architecture*, Vol. 1, No. 33, pp. 73-76.

Zhao X.L. and Grzebieta R. (2002). “Strength and ductility of concrete filled double skin (SHS inner and SHS outer) tubes”, *Thin-Walled Structures*, Vol. 40, No. 2, pp. 199-213.

Zhao, X.L., Grzebieta, R. and Elchalakani, M. (2002). “Tests of concrete-filled double skin CHS composite stub columns”, *Steel and Composite Structures*, Vol. 2, No. 2, pp. 129-146.

Zhu, Z.Y. (2004). *Joint Construction and Seismic Performance of Concrete-filled Fiber Reinforced Polymer Tubes*, PhD Thesis, North Carolina State University.

Ziara, M.M., Haldane, D. and Kuttab, A.S. (1995). “Flexural behaviour of beams with confinement”, *ACI Structural Journal*, Vol. 92, No. 1, pp. 103-114.